5 PT

NASA CR-159420

(NASA-CR-159420) SPECIFIC SPACECRAFT EVALUATION: SPECIAL REPORT Special Report, 1 Nov. 1977 - 1 Jun. 1978 (TRW Defense and Space Systems Group) 211 p HC A10/MF A01 CSCL 21H G3/20

N80-11137

Unclas
39636

SPECIFIC SPACECRAFT EVALUATION

SPECIAL REPORT

UNDER

INVESTIGATION AND EVALUATION OF EFFLUX/SPACECRAFT INTERACTION

Prepared for

NATIONAL AERONAUTICS AND SPACE ADMINISTRATION
Lewis Research Center
Cleveland, Ohio

CONTRACT NAS 3-21047

NOVEMBER 1, 1978

TRW
DEFENSE AND SPACE SYSTEMS GROUP
ONE SPACE PARK · REDONDO BEACH · CALIFORNIA

SPECIFIC SPACECRAFT EVALUATION

SPECIAL REPORT

November 1, 1978

Prepared by

J.M. Sellen, Jr.

for

NASA-LeRC

Under Contract NAS3-21047

The results of the Study are based on simulated space environment and any interpretation of that data requires experimental confirmation in the space test environment.

TRW
DEFENSE AND SPACE SYSTEMS GROUP

CONTENTS

1. INTRODUCTION

This special report will examine the material transport interactive effects between an 8 cm mercury ion thruster and the P 80-1 spacecraft. The P 80-1 spacecraft has an auxiliary electric thruster complement of two 8 cm electron bombardment mercury ion engines. In the configuration to be examined here, one of these thrusters will be on the zenith (upper) surface of the spacecraft, while the second thruster will be on the rear facing surface. The P 80-1 spacecraft also has in its payload the Teal Ruby sensor, on the "left" facing surface, and the ECOM-501 sensors, on the zenith and nadir surfaces. There are no experiment payloads on the front and "right" face surfaces. The solar array and its supporting rotational mounting fixture are placed on the "right," sun-facing, side of the spacecraft.

The configuration of the P 80-1 spacecraft and its various elements and various payload experiments will not be illustrated here. Reference is made to the Rockwell International P 80-1 Spacecraft Familiarization Briefing, presented March 7 and 8, 1978 at Seal Beach, California for the specific configurational placement of the thrusters, the thruster sputter shields, the spacecraft surfaces, the solar array, and the various entrance apertures of the ECOM-501 and Teal Ruby sensors.

The examination of material transport effects will consider both neutral and charged particle species. For the neutral species, only the line-of-sight material transport mode is possible. For charged particles, both line-of-sight and nonline-of-sight material transport must be considered. Because of the thruster placements on the spacecraft and the configuration of the sputter shields, line-of-sight transport of particles is either eliminated or is reduced to extremely low levels. The predominant concern, thus, will be with nonline-of-sight ion motion and deposition. It will be shown that this process is, in the main, concerned with the weakly energetic ions released by the thruster rather than the energetic (thrust) ions. Because the weakly energetic ions constitute only a minor fraction of the total charged particle release by the thruster, deposition of ions on spacecraft surfaces will be at extremely low levels. It is believed that these deposition levels are sufficiently reduced to satisfy even the most stringent requirements of spacecraft surface material accumulation.

Because of the comparative importance of the nonline-of-sight transport of weakly energetic ions, this process will be discussed first (in Section 2). Sections 3 and 4 will discuss the line-of-sight transport of neutral and charged particles. Section 5 will discuss aspects of the phenomena which influence the accumulation and removal of material when material arrival rates are at very low levels, and Section 6 will discuss the effects of electron deposition. A final section, 7, will summarize the findings of this Special Report.

This report also contains two appendices. Appendix A reviews the efflux measurements of charged particles from an 8-centimeter mercury ion thruster, and Appendix B examines the recirculation of electic thruster ions in the magnetic field of the earth, with possible reinterception on spacecraft surfaces.

2. NONLINE-OF-SIGHT TRANSPORT OF WEAKLY ENERGETIC IONS

2.1 ION TRANSPORT VIA $\vec{v}_+ \times \vec{B}_e$ RECIRCULATION

An Hg^+ ion released from the ion thruster will be acted upon by both electric and magnetic fields as it moves through the ambient space plasma. For near-earth orbits, electric fields in the ionospheric plasma are generally at very low levels, and, even if present, may be either temporally or spatially varying in a period of time or space at such rates that cause effective cancellation of the $q_+\vec{E}$ forces on an ion. The magnetic field force on the ion (given by $q_+\vec{v}_+ \times \vec{B}_e$ where q_+ is ion charge, $\vec{v}_+$ is ion vector velocity, and $\vec{B}_e$ is the Earth's magnetic field), will, generally, exert a coherent bending force on the ion motion. This bending force causes the ion to move in a helical path, and, for certain orientations of $\vec{v}_+$, $\vec{B}_e$, and $\vec{v}_s$ (the spacecraft vector velocity), it is possible for the (helical) path of the ion to reintercept the spacecraft surface.

At any point in the motion of a spacecraft along its orbit it is possible to examine the various ion release trajectories and to determine if recirculation of the ion in the $\vec{v}_+ \times \vec{B}_e$ force and reinterception of the spacecraft surface is dynamically forbidden or dynamically allowed. If recirculation/reinterception is dynamically allowed, it is then possible to determine the required magnitude of v_+ and the required orientation of $\vec{v}_+$ relative to $\vec{v}_s$ and $\vec{B}_e$ for this reinterception to occur. Because the spacecraft has a finite size, the recirculation/reinterception conditions can be satisfied, if dynamically allowed, throughout a narrow range in magnitude in $\vec{v}_+$ and throughout a narrow cone of directions of $\vec{v}_+$ relative to $\vec{v}_s$ and $\vec{B}_e$.

Appendix B to this special report provides a detailed description of the dynamically allowed and forbidden regions of the spacecraft orbit for ion recirculation/reinterception, derives the "point-to-point focus conditions," and calculates the various dispersion coefficients of the ion point of impact for various small incremental parameter changes around the focus conditions. When these dispersion relations are used with estimated forms of the ion release distribution function (in energy and in angle) it is possible to calculate the rate of ion deposition on spacecraft surfaces as a result of ion recirculation in $\vec{B}_e$.

In Appendix B the specific case of the top mounted ion thruster was examined and calculations were presented of the ion deposition on the spacecraft zenith surface for several $\vec{v}_s$, $\vec{B}_e$ arrangements. The results, expressed in a normalized efflux coefficient, ε, whose units are cm^{-2}, and the total mission atom throughput in thruster propellant, N, allow the determination of εN, in mercury ions deposited on 1 square centimeter of spacecraft surface.

The values of ε calculated in Appendix B will depend upon some assumptions in the ion release distribution. Because the recirculation/reinterception reaction has its maximum likelihood for "weakly energetic" ions (where "weakly energetic" will generally range from 0 to ∿50 eV), and because the ion energy spectrum and ion angular distributions for these weakly energetic particles are not known with the precision of (for example) the thrust ion release properties, some assumptions will be required in the calculations of the normalized efflux coefficients. For an assumed release distribution function in weakly energetic ions corresponding to the present available experimental data on the ion thruster plasma plume, the normalized efflux coefficient is $\sim 5 \times 10^{-14}$ cm^{-2}. Using this ε value and for 10,000 hours of thruster operation (2 x [illegible]^{5} thrust ion throughput), the total ion deposition over the entire operational period is 10^{12} per square centimeter, which corresponds to 0.001 monolayers.

The extraordinarily low levels of deposition described above have been examined for other orientations of $\vec{v}_s$, $\vec{B}_e$, for interception on other spacecraft surfaces, and for various assumptions relative to the weakly energetic ion release distribution. The result of the more general examination follows the result of the specific configuration described above. Depositions for the 10,000-hour example of ion thruster operation remain at very small fractions of a monolayer for the entirety of the mission. As a result of these studies, it has been concluded that recirculation of ions in the magnetic field of the earth results in negligible levels of material transport for the surfaces of the spacecraft and its various sensors.

2.2 ION TRANSPORT VIA ELECTRIC FIELD REFRACTION

2.2.1 General Considerations

Section 2.1 has noted that both electric and magnetic fields are present in the space plasma and may act on an ion moving through that medium. It has been pointed out, however, that electric fields in the space plasma are at very weak levels and, even if present, do not act in general to produce coherent refraction in the trajectories of ions.

The interest of this Section will be electric field refraction of the ion velocity. The electric fields of interest, however, are not within the space plasma but are, instead, within the plasma plume of the ion thruster and between the plasma plume and the various material surfaces of the spacecraft and the thruster.

The focus of interest will be, again, upon the trajectories of weakly energetic ions. The approach to trajectory refraction of such ions by electric fields has been both analytical and experimental.

Appendix A of this Special Report, presents a detailed description of the experiments and analyses on ion refraction. Three conditions of ion thruster operation were examined. These conditions were:

(1) Operation of the thruster plasma discharge neutralizer only

(2) Operation of the thruster discharge and the thruster neutralizer discharge (but without the application the ion engine acceleration voltages)

(3) Operation of the complete thruster (FULL BEAM ON)

These various operational conditions will be discussed in Sections 2.2.2, 2.2.3, and 2.2.4.

2.2.2 Ion Transport for Operation of the Neutralizer Discharge Only

For nominal thruster neutralizer operation, a mercury injection of $\sim$6 milliamperes (equivalent) of Hg^0 is directed into the hollow cathode discharge. The hollow cathode discharge is maintained by a keeper electrode, maintained at $\sim$18 volts positive with respect to neutralizer cathode common and drawing a discharge current of $\sim$0.5 amperes. The passage of the discharge current creates an ion release current of

$\sim$300 μA Hg^+. These Hg^+ ions expand with the plasma plume electrons in an ambipolar diffusion. Because the neutralizer plume expansion causes a plasma density drop-off, and because of the finite electron temperature in the plume, the plasma has an electric field structure within it. The Hg^+ ions are accelerated by these electric fields and the ions gain energies which are generally "large" ($\cong$10) compared to kT_e, where k is Boltzmann's constant and T_e is electron temperature.

When the neutralizer plasma plume, in its expansion, encounters a material boundary, the plasma will, in general, establish an electric field between the boundary and the plume. For insulating materials, these electric fields are several times kT_e/e (in units of volts) divided by the sheath thickness. A plasma plume Hg^+ ion moving in this region of the plasma sheath can be refracted by this electric field and nonline-of-sight ion transport results.

For experiments with the neutralizer discharge only, a series of probe measurements was carried out in regions which can directly view the neutralizer and also in regions which are in the "shadows" (for optical transmission) created by various material boundaries for a point light source at the neutralizer location. It was determined that, in general, the "shadows" cast in the neutralizer plasma plume by the material boundaries are comparatively sharp. Some refraction of the ions is observed. This refraction is not large for insulating boundaries provided that the plasma has undergone a high degree of expansion from the neutralizer orifice before encountering the boundary. For conducting boundaries, the refraction can be increased by the deliberate creation of electric fields between the plasma and the boundary. For these conducting boundaries, however, the refraction of the ions may also be reduced by varying the boundary potential to reduce (or eliminate) the electric field between the plasma and the boundary.

From the above observations, it follows that the ion flux levels in the umbra region of the thruster sputter shield will be very greatly reduced from flux levels in the unshielded regions, and flux levels in the unshielded regions are given approximately by $I_+/2\pi R^2$ where I_+ is the ion release current ($\sim$0.3 milliamperes) and R is the distance from the neutralizer to the point of observation. For R $\sim$1 meter, flux levels of the order of 10^{10} ions/cm^2/sec are obtained in the unshielded regions leading to total ion arrival of $\sim$1 monolayer per day. For the shielded regions, the flux densities can be greatly reduced depending upon the point of location in the umbra and upon electric field conditions at the material boundary.

The explanation of the comparatively sharp shadows in the plasma plume cast by material boundaries is that the ion energies in the plume are sufficiently larger than kT_e/e so that $kT_e/e\lambda$ electric fields (where is a sheath thickness between a material boundary and the plasma plume) cause only minor bending of the trajectory.

In examining possible interactive effects of these ion fluxes with P 80-1 surfaces and sensors, there are three areas of principal concern. These areas are the Teal Ruby sensor, the ECOM-501 sensor, and the P 80-1 surface on that face of the spacecraft bearing the ion thruster. The first element to examine is the Teal Ruby sensor. The orientation of the thruster sputter shield is such that the Teal Ruby sensor lies in the umbra of this sputter shield. For an Hg^+ to move to the vicinity of the Teal Ruby sensor, it must first expand over the sputter shield, must refract by $\sim$90 degress, and must then travel a distance of $\sim$1 meter. At this juncture the ion must expand over the edge of the spacecraft (connecting the upper spacecraft face with the right facing surface of the Teal Ruby sensor) to encounter the exterior of the Teal Ruby sensor. For an ion to reach the interior of the Teal Ruby sensor it must then continue its movement but in a comparatively tortuous path, involving plural refractions of the ion. Experiments with Faraday cups (described in Appendix A) were carried to determine the extent of ion transport into collecting surfaces for a plural refraction requirement. These experiments were unable to detect such transport because the signal levels had diminished below the noise levels in the measuring circuits. These probes were capable of detecting mercury ion arrival at $\sim$1 monolayer per 10^7 seconds ($\sim$115 days, $\sim$2800 hours of thruster operation).

In summary for the data above and for the Teal Ruby sensor it may be concluded that Hg^+ ion transport into the sensor is at negligibly small levels (less than 1 monolayer per 10,000 hours of operation). Even at the edge of the spacecraft and for the exterior of the sensor it may be estimated that ion flux is less than 1 monolayer per 10^7 seconds of operation in this condition. For a thruster mission in which the total operation in all modes is 10,000 hours, operation in the neutralizer discharge only condition may be estimated at less than 10% of this time, and even this 10% figure would be obtained only for a large number of engine turn-on cycles with only comparatively brief periods of full-up thrusting. In overall summary, then, ion deposition levels are below 1 monolayer per mission at the sensor exterior and are (probably) many orders of magnitude below the monolayer per mission level for the sensor interior.

The second areea of concern for this neutralizer plasma plume flux is the top-mounted ECOM-501 sensor. This top-mounted sensor occupies the same surface as the top-mounted thruster and must be examined for possible material transport effects. There is no significant material transport to the top-mounted ECOM-501 sensor and the rear face thruster, and the nadir mounted ECOM-501 sensor has no significant material transport from either the top face or rear face thrusters.

The ECOM-501 sensor has a zenith pointing opening which is located in the "backward hemisphere" of the ion thruster (polar angle ∿120 degrees) and at a (polar coordinate system) radial separation distance of ∿1 meter. There is no direct line-of-sight from the thruster neutralizer to the entrance aperture of ECOM-501 and ions in the neutralizer plume can reach the ECOM entrance only by a trajectory refraction. The placement of the thruster sputter shield having been made so as to cast the umbra toward the Teal Ruby sensor results in a condition where the umbra region for the ECOM sensor is cast by the outer front ring of the mercury ion engine. Refraction of ions must occur, then, in the electric fields between the neutralizer plasma plume and the body of the thruster. The bending of the ions as the ions expand over the thruster edge must be somewhat above 30 degrees for the (now altered) trajectory to be in the direction of the ECOM-501 entrance aperture.

Measurements of the neutralizer plasma plume expansion over the thruster edge were not carried out in the experimental portion of the program described in Appendix A because of the placement of other material surfaces in the test configuration and because of the allowable range of probe positions in the presence of those boundaries. There are, however, several features in the ion motion and in the sensor entrance aperture which lead to a conclusion of very low levels of transport into the sensor interior. The first aspect of this transport is that the weakly energetic ions moving toward the ECOM-501 sensor aperture will encounter that aperture at an angle with respect to the sensor axis of ~60 degrees. For a line of sight particle to enter the sensor interior requires a comparatively small angle between the particle velocity and the sensor axis. The ion, thus, will encounter the edge of the entrance aperture near the entrance plane. If the ion should be more severely refracted via some other trajectory and have an entrance along the sensor axis, the particle will then be subject to a transverse magnetic field of several hundred gauss (placed at the entrance to prevent the ions and electrons of the ambient space plasma from entering the sensor). A final feature to note here is that the entrance aperture temperatures are sufficiently elevated that mercury accumulation on the entrance surfaces will not result. The likely action is that a mercury ion incident on the surface will accommodate to the surface for only a brief period before re-evaporation.

Of final interest here are the spacecraft surfaces including the spacecraft body surface and the rear face of the solar array. For the top mounted thruster, ion deposition on the rear surfaces of the solar array may occur via line-of-sight transport for ions emerging near a polar angle of 90 degrees from the thruster axis. Because this line-of-sight transport is similar to the ion transport to the rear side of the solar array for the combined discharge operation and for the fully operational thruster, a single discussion of ion arrival to the solar array rear face will be given in Section 4.

The remaining nonline-of-sight transport of ions to the spacecraft body surfaces occurs as a result of ion refraction over the edge of the thruster front ring, which has been previously examined as a material transport effect for the ECOM-501 sensor. For ions to encounter spacecraft body surfaces requires refraction in the range of 30 degrees or more and only selected azimuthal portions of the thruster periphery (∿50%) may contribute to this flow because of the presence of the thruster sputter shield. As noted previously, ion refraction effects over this portion of the thruster edge were not capable of being measured in the experimental configuration. Relative to ion deposition effects on spacecraft surfaces, however, it should be noted that these spacecraft surfaces are not at unusually low temperatures. The surfaces also have rather conventional solar absorptivities ($\alpha \sim 0.4$), so that the total spacecraft operation is not faced with the problem of maintaining extraordinarily low solar absorptivities (such as OSRs). Because the surfaces move in a modest temperature range (minimum temperatures of $\sim 0^{o}C$), and because the arrival rates of any refracted ions are at such low levels, it may be concluded that no significant surface alterations will occur.

2.2.3 Ion Transport for Operation of the Neutralizer Discharge and the Thruster Discharge

For the "combined discharge" plasma plume condition the thruster discharge is operated at nominal mass injection rate and nominal discharge currents and voltages and the neutralizer discharge is continued in the operation described earlier in Section 2.2.2. Ion acceleration voltages are not applied to the screen and accelerator electrodes and the thruster discharge cathode common remains at V = 0, the chamber ground potential.

Although the bulk of the injected Hg^{o} is ionized in the thruster discharge, the absence of the large ion acceleration potentials prevents the release of the majority of the created ions. A small current (∿2 to 3 milliamperes) of Hg^{+} can be transported in the potential fall between the thruster discharge plasma potential (given approximately by the discharge anode potential) and the screen electrode. The remainder of the injected mercury emerges, ultimately, in Hg^{o} atoms.

In the region outside of the thruster, the Hg^+ ions moving from the thruster discharge are neutralized by the thruster discharge neutralizer plasma. The comparatively low level of required neutralizer electron current to match the emerging Hg^+ does not cause the plasma plume potential to rise appreciably and the potential in this plume remains at a few volts positive with respect to the chamber walls. The Hg^+ ions created by the thruster neutralizer continue to be released, thus, and have kinetic energies of approximately the 10 eV for the previously discussed case of the neutralizer discharge only.

Retarding potential analyses of the ions moving from the thruster into the exterior plume reveal that these ions have kinetic energies of $\sim$20 to 30 eV which represents the potential fall between the initial region of ion generation and the exterior plasma. The current of these more energetic ions is approximately 10 times the current of ions created by the neutralizer plasma discharge.

The presence of larger ion release currents might be taken to indicate that increased levels of deposition might be encountered on spacecraft surfaces. These additional ions, however, are more energetic and are even less easily refracted in electric fields than the ion discussed in Section 2.2.2. Measurements of the electric fields in the plasma plume of the combined discharge operation condition reveal the electric field structure in this latter case is essentially the same as in the earlier, neutralizer discharge only, case. This electric field structure situation will be greatly altered, as will be seen, for the plasma plume of the fully operational thruster (Section 2.2.4).

In the present condition of operation, the released ion current has increased by approximately one order of magnitude compared to the neutralizer discharge only, the additional ions are more energetic (20 to 30 eV compared to $\sim$10 eV in the earlier case), the ion release profile is more sharply peaked along the thruster axis (constituting a weakly energetic ion beam), and refracting electric fields in the plasma plume and between the plasma plume and the material boundaries as essentially unchanged from the fields present in the earlier, neutralizer discharge only, case. From these several features of the plasma plume it will be concluded that ion deposition effects for the combined plasma discharge case are below levels of significance as was concluded earlier for the neutralizer plasma plume. These conclusions apply to the ion transport to the regions of the Teal Ruby Sensor, the regions of the ECOM-501 sensor, and to the surfaces on the spacecraft. Faraday cup measurements of these ion currents in the umbra regions of material boundaries confirm these conclusions in the geometries for which probe measurements were possible. There remain some questions, as before, on the extent of the refraction of weakly energetic ions over the front ring edge of the ion thruster.

A final observation for this combined discharge plasma plume operation condition relates to the expected on-orbit fraction of all thruster operational time in which these combined discharges are present but ion acceleration voltage is not applied. For a series of possible mission operational profiles (thruster close-downs, thruster restarts, and steady state thrusting), it may be estimated that less than 5% of the total period will be in the combined discharge condition. This has the further effect of reducing ion deposition levels below detectability in even the most sensitive of surfaces and sensors.

2.2.4 Ion Transport for the Fully Operational Ion Thruster

With the application of ion acceleration voltages to the screen and accelerator electrodes, the Hg^+ formed in the thruster discharge may now be extracted and accelerated into the ion thrust beam. The Hg^0 release from the ion thruster diminishes by approximately one order of magnitude and the ion release current increases to approximately 74 milliamperes. Because the thrust ions now require matching currents of electrons from the neutralizer, the potential gradient conditions in the region of the neutralizer now reverse direction, from that condition observed in the earlier two operational conditions. It is believed that this reversal of potential gradient causes a suppression of the weakly energetic ions created by the neutralizer discharge. Weakly energetic ions will continue to emerge from the thruster plasma plume, but the mechanism producing these ions and the energies and release directions of the ions will be different in the fully operational thruster than from either the neutralizer discharge only condition or the combined plasma discharge condition.

The electric fields required to extract the neutralizing electrons from the discharge neutralizer to the thrust beam plasma result in potential increments (between the neutralizer and the plasma plume axis) of up to 50 volts. Details of these potential profiles in the full thrust beam are given in Appendix A and in the references cited there. Within the plasma column these fields may reach levels of 20 volts/cm with the predominant electric fields in the high polar angle ($\theta \sim 90$ degrees) directions.

The Hg^0 release by the thruster and the Hg^+ thrust ions can react via the (Hg^0, Hg^+) charge transfer reaction to produce an (initially) very low-energy ion and an energetic neutral. The charge exchange ion then acquires kinetic energy in the electric fields in the plasma, as discussed above. These "Group IV" ions have a production rate of approximately 300 microamperes for a nominal operation condition of an 8-cm thruster at FULL BEAM ON. In addition to the charge exchange ions, there are also Hg^+ ions formed by the ionization of Hg^0 by the beam neutralization electrons, a fraction of which have sufficient injection energies to cause the ionization to occur. The properties of these electron-impact-ionization produced ions cannot be distinguished from the Group IV, charge exchange, ions and the 300 μA production rate cited above include ions produced by both charge transfer and by electron impact ionization.

The principal concern for nonline-of-sight ion transport for the fully operational thruster is in the motion of the weakly energetic ions in the electric fields of the thruster plasma plume and in the electric fields between this plasma plume and various material boundaries. As noted above, the weakly energetic ions now have kinetic energies ranging to approximately 50 eV. The electric fields in the plasma and between the plasma and the boundary are, however, also increased in magnitude from the previously examined operational condition, so that refraction of the "weakly energetic" ions may be through comparable angles in all of these operational conditions.

Details of the experiments with the fully operational ion thruster are given in Appendix A and in the references cited there. An important distinction must be made, however, between the measurements for the fully operational beam and the measurements for the neutralizer and thruster discharges. This distinction is that the presence of the energetic thrust ions in the testing chamber creates a series of facility effects reactions and charged particle fluxes which are not present in the previous two operational conditions. These facility effects have been known from previous experiments so that their presence in these more recent experiments was not unexpected. The measurements were carried out, however, to extract as much information as is possible on the "genuine" ion flux signals, and also as a continuing effort toward the reduction of the "facility effect" effluxes. As the discussion to follow will note, there are important remaining questions on the weakly energetic ion fluxes for this fully operational thruster condition.

The primary concern of the interactive effects analysis is, as before, ion transport to the Teal Ruby sensor. Following this, the concern shifts to possible ion transport to ECOM-501, with the remaining concern for ion transport to spacecraft surfaces.

For a Group IV ion to move to the regions of the Teal Ruby sensor, that ion must be created in the plasma thrust beam and must then move under the action of the plume electric fields and plume-to-material boundary electric fields in a trajectory which proceeds into the region occupied by the sensor. If the Group IV ion is created near the ion thruster (within a few centimeters of the accelerator grid plane), the ion must first move in the downstream axial direction (in addition to its radially outward motion, where the radial direction is now defined in a cylindrical coordinate system) in order to avoid the sputter shield, for assumed ion transport to the Teal Ruby sensor region. For this ion to then proceed toward the Teal Ruby sensor, trajectory bending of the order of 90 degrees may be required in the sheath fields between the sputter shield and the thrust beam plasma. Such high angle bending is not likely considering the general range of Group IV ion kinetic energies. It is possible that some lower energy Group IV ions, created near the edge of the thrust beam plasma and accelerated by the (now) weaker electric fields in these plasma edge regions, will be more easily refracted. The plasma edge regions will, however, have either reduced (or possibly reversed) axial electric fields and it will, thus, be difficult to satisfy the joint requirements of downstream motion (to clear the sputter shield) followed by high angle refraction. For Group IV ions created near the thruster accelerator plane, then, transport over the edge of the sputter shield and into the sputter shield umbra regions occupied by the Teal Ruby sensor appears an extremely low level process.

An important distinction concerning the Group IV ions in this fully operational thruster condition and the weakly energetic ions for the previous two operational conditions is that the Group IV ions are produced throughout the thrust beam plasma, while the weakly energetic ions examined earlier are created in easily described (and well proscribed) volumetric regions. The bulk of the Group IV ions are, of course, created near the accelerator grid plane where the densities of Hg^0 and Hg^+ are at maximum levels. There will be, however, continued charge exchange reactions throughout the thrust beam plasma, albeit at reduced volumetric rates. The discussion will now examine the Group IV ions made in the downstream region.

If a Group IV ion is made at a sufficiently removed downstream location, the view factor from that location point can include the Teal Ruby sensor. The question then becomes one of determining electric field structure in the plasma plume to determine if the electric fields can permit the created Group IV ion to move into the region of the Teal Ruby sensor. Some measurements of these plasma plume electric fields are described in Appendix A and field orientations at 120 degree polar angle have been observed in the outer edges of the plasma. A charge exchange ion created at such a plasma location point (and neglecting previous Hg^0 velocity) would move toward the Teal Ruby sensor. A principal question then becomes the possible volumetric ion creation rates for an ion thruster in space. The in-space distinction is made here in that weakly energetic facility effect ion fluxes are known to exist for the chamber measurements and tend to dominate any measurements of ion fluxes in these regions. Even the electric field structure described above may be affected by facility wall presence. Based on estimates of plume thrust ion and mercury atom densities, however, and allowing these downstream Group IV ions to expand cylindrically leads to deposition rates in the range from 10^8 ions/cm^2/sec to a few times 10^8 ions/cm^2/sec in the vicinity of the Teal Ruby sensor. These deposition rates are at approximately 1 monolayer in 10^7 seconds at the exterior of the Teal Ruby sensor. Reductions of deposition rates by many orders of magnitude for interior portions of the sensor are expected because of the requirements of plural ion refraction to enter these sensor regions. There would appear to be, thus, comforting evidence that the expansion of Group IV ions created in downstream regions and expanding outward into the regions of the Teal Ruby sensor will be at acceptably low levels. In confirmation of this conclusion, ion collection in Faraday cups in the testing facility and for the fully operational thruster (and in spite of the presence of facility effect fluxes) have demonstrated extremely low levels of ion transport, provided that plural ion refraction is required to enter the ion sensing device. These experiments are described in Appendix A.

The second area of concern for Group IV ion transport is for the ECOM-501 sensor. This sensor aperture is placed on the same surface of the spacecraft as the thruster for the case of interest. Previous sections have described how, for ion transport toward this device, the ions may be refracted over the thruster front edge. That previous discussion has also noted that experimental determinations of ion refraction in these regions has not been carried out because of constraints on probe motion by the boundaries present in the testing facility.

For the fully operational ion thruster and for electric field refraction over the thruster front edge, the ions of interest are the Group IV ions created near the accelerator grid plane and moving radially out of the thrust beam plasma. The electric fields of interest are the electric fields between the plasma plume of the thrust beam and the ion thruster front plate housing. Because the plasma densities are comparatively high in these regions and because plasma potentials in these regions are also at elevated values (up to 50 volts with respect to the thruster), the electric fields may be comparatively strong and refraction of the Group IV ions over the thruster front face edge should be expected to some degree. It is not immediately evident as to what the extent of this refraction will be and additional in-chamber measurements for this area would appear to be warranted, in spite of the potential problems facing such measurements because of facility effect fluxes. Appendix A provides some additional discussion regarding possible methods for reducing the levels of facility effect fluxes compared to fluxes of genuine Group IV particles (where genuine here is intended to denote those charge exchange particles which would be present for an ion thruster in space).

The deposition of ions over the surface of the spacecraft and the deposition of ions at the entrance aperture of the ECOM-501 sensor are, as previously noted, related in that both processes are the result of Group IV refraction over the thruster front plate edge, with possible additions from Group IV ions created near the edge of the plasma plume and launched into the backward hemisphere of directions by the electric fields present in these plasma plume edge regions. An earlier estimate of these fluxes of ions, after expansion to distances of approximately 1 meter from the thrust beam axis is of the order of 10^8 ions/cm^2/sec to a few times 10^8 ions/cm^2/sec. For the spacecraft upper surfaces, these very low arrival rates are considered not to be of concern, in view of the surface temperatures and the generally modest solar absorptivities required to those surfaces. The ECOM-501 sensor has a series of geometrical protection factors and a magnetic field protection factor which will act to reduce material transport into the sensor itself. The present analyses would tend to indicate that neither the spacecraft surfaces nor the ECOM-501 sensor will have any significant effects because of mercury ion deposition. This Special Report will, however, recommend that continued experimental determinations of these ion fluxes be carried out with a particular emphasis on weakly energetic ion refraction over the thruster front plate edge.

3. LINE-OF-SIGHT TRANSPORT OF NEUTRAL PARTICLES

The neutral particles emitted by the ion thruster are Hg^o atoms from the thruster and neutralizer discharges, sputtered metal atoms from the accelerator electrode, the neutralizer housing and thruster front ring, and sputtered atoms from the thruster sputter shield. All of these particles move in straight line trajectories. The surfaces on which these particles may deposit (for operation of the top-mounted thruster) are the rear face of the solar array, the zenith face of spacecraft, and that ECOM-501 sensor which is mounted on the spacecraft zenith face. The Teal Ruby sensor cannot be intercepted by thruster emitted neutrals because of the umbra cast by the thruster sputter shield.

Hg^o emitted by the thruster and sputtered metal atoms from the thruster cannot deposit on the spacecraft upper face as a primary material transport, where primary is intended to denote material transport from the thruster to the deposition surface of interest with no intervening surface contact. The limitation of primary material transport of Hg^o and sputtered metal atoms to only the rear surface of the solar array results from the raised configuration of the thruster mounting from the zenith surface of the spacecraft. Hg^o and sputtered metal atoms from the thruster may deposit on the spacecraft upper face as a secondary material, for those neutrals which moved initially to the sputter shield and were subsequently resputtered from the sputter shield. The sputter shield does have a view factor to the spacecraft upper surface over the thruster front ring. In keeping with present definitions, material from the sputter shield proper which is sputtered by thrust ion impact will be termed a primary material transport, and geometrical factors allow this sputtered beam shield material to deposit on the rear of the solar array and on the spacecraft upper surface.

The series of experimental measurements described in Appendix A have examined charged particle transport only and no information was obtained there on the deposition patterns of Hg^o, sputtered thruster metal atoms, or sputtered beam shield material. In the absence of experimental data there are two possible approaches which the analysis here may take. The first is to postulate a total material release in either one or another of the mass transports identified above and to also postulate the angular distribution function of that release pattern. In some cases (for example, Hg^0 release magnitudes at small polar angles and sputtered thruster metal atoms at small polar angles) this approach can probably provide comparatively good estimates of the actual mass transports. Such postulated distributions are probably not representative of actual conditions, however, for material which emerges at high polar angles (and also in the backward hemisphere of directions), and these are the mass transport regimes of interest here.

A second approach which the analysis may take is to identify the specific mass transport species and angular directions of interest and to recommend the experimental determination of those mass fluxes in those directions. This is the approach which will be taken.

The two mass transport species and angular ranges of interest are:

(1) Sputtered metal atoms from the thruster in the polar angle range from $\sim$70 to 90 degrees

(2) Sputtered beam shield atoms in the polar angle range from $\sim$70 to $\sim$135 degrees, where the polar angle direction, $\theta = 0$ deg, is (in both 2 and 1) the thrust beam axis.

Determination of Hg^0 at polar angles near 90 degrees has not been listed here because of the belief that the rear face of the solar array will be capable of thermal re-evaporation of Hg^0 at sufficient rates to prevent a buildup of any arriving Hg^0. The terms of interest above, then, are products with expected high probability of sticking and very low thermal re-evaporation rates.

The action of deposited sputter shield material and sputtered metal atoms on the rear face of the solar array cannot be estimated here in view of the uncertainty in the relative magnitudes of the two groups of particles and because of uncertainties in the species makeup in the material sputtered from the beam shield. The recommended approach for the in-chamber experimental determinations of these flux levels and species is deposition plates with extreme care being given in the deposition plate holder configuration in order to suppress the facility generated metal atom flux.

4. LINE-OF-SIGHT TRANSPORT OF CHARGED PARTICLES

The remaining particle species and transport mode of interest (with the exception of plasma plume electrons, discussed in Section 6) will be charged particles in line-of-sight transport. The particular charge species of interest here is the Group II Hg^+ and Group IV Hg^+ in the polar angle regions near 90 degrees. Both of these species can, if emitted in the proper direction, intercept the rear face of the solar array.

Group II Hg^+ ions are the result of charge transfer reactions in the screen grid-to-accelerator grid interspace. Because the resultant charge exchange ion does not move along the total path of the thrust ions, some fraction of the particles may emerge at high polar angles. The energies of these Group II ions ranges between the upper end point of the Group IV ions and the thrust ion energies. Group II ions can, thus, cause sputtering upon impact with a surface.

The numbers of Group II ions have been examined in previous laboratory measurements. For polar angle near 90 degrees and for separation distances of ~ 2 meters, the flux of Group II ions from a fully operational ion thruster is $\sim 5 \times 10^{11}$ ions/cm^2/sec. Because the energies of these particles are somewhat reduced from Group I ions, sputtering ratios are reduced and the material removal of their impact can be estimated as ~ 2 to 4×10^{11} particles/cm^2/sec. This would cause a removal of one monolayer of material from the back surface of the solar array in a period of approximately 1 day.

From the calculation above it cannot be concluded that a net material removal from the back surface of the array will occur. As was pointed out in Section 3, both sputtered metal atoms from the thruster and sputtered material from the beam shield can deposit on the solar array back surface. The estimates of the neutral material transport at large polar angles generally exceed the Group II ion flux. The likely result, then, is that some material accumulation on the back surface of the solar array will result but that accumulation will be somewhat less because of the "scrubbing" action of the Group II ions moving to these surfaces.

A final particle flow of interest is the Group IV flux which moves at polar angles near 90 degrees. This flux is approximately one order of magnitude above the Group II flux levels at these angles. Because of the lower energy range of these ions, their impact on the surface will not lead to sputtering of the surface. The expected temperatures of the solar array back surface, moreover, are expected to be sufficient to cause the thermal re-evaporation of those Group IV Hg^+ ions which stick to the surface upon impact. From these several factors, then, the arrival of Group IV ions at the rear surface of the solar array is not expected to cause any interactive effects of significance.

5. VERY LOW ARRIVAL RATE MATERIAL ACCUMULATION AND REMOVAL PHENOMENA

In the discussion of the preceding sections, the material accumulated on a surface element has been considered the material flux to the surface element integrated over the total period of such transport. This assumption of complete sticking for an encounter of a particle with a surface is clearly an upper bound to the material accumulation as a result of this particular mass transport. The discussion in this section will consider the various processes which make the actual material accumulation less than this "complete sticking" upper bound.

Many of the material transport fluxes considered in the previous sections are weakly energetic particles where "weakly energetic" may range from a few eV to a few tens of eV. Expressed in terms of temperature, these are, then, particles with kinetic temperatures ranging from a few tens of thousands of degrees Kelvin to a few hundreds of thousands of degrees Kelvin. The encounter of particles at these gas temperatures with a surface does not, in actuality, lead to complete sticking, irrespective of surface temperature, because the instantaneous "temperature" at the point of impact of the incident particle with the surface derives from both the initial atomic temperatures there and the (very high) temperatures of the arriving particles. Not only may the sticking be less than complete, the weakly energetic particle may also cause the removal of a surface particle.

While both surface accommodation and surface sputtering for the arrival of these weakly energetic ions and neutrals are possible reactions, it is not possible, in practice, to assign accurate values to these reaction cross sections for regimes in which the mass transport is at very low arrival rates. It is also required to consider material removal through thermal re-evaporation. An important overall feature to recognize here is that many possible reactions can be of importance when transport rates of monolayers in megaseconds (or longer) are involved. From a point of perspective, surface accumulation and surface evaporations at one monolayer per second correspond to "pressures" of 10^{-6} torr. Arrival rates quoted in the discussion of some of the previous sections at 1 monolayer per 10^7 and 10^8 seconds correspond, thus, to "pressures" of 10^{-13} and 10^{-14} torr.

It becomes a reasonable question, then, as to whether the vapor pressures of materials are known in these very low pressure regimes. A typical practice is to assign vapor pressures on the basis of a material evaporating from a substrate of its own material (for example, mercury being evaporated from a mercury base). When dealing with small fractions of a monolayer, however, these "same material" assumptions are not valid, and the important question becomes the rate of material evaporation from a differing material substrate. To complicate any analysis there are questions relating to the actual material in the upper monolayers of any material which has been in residence in (for example) room air. Careful analyses of such material surfaces reveal that the upper 10 to 100 Å contains many contaminant materials including waters of hydration and adsorbed contaminant gases. For spacecraft surfaces, the strictest control measures through spacecraft preparation and launch can still result in 10 to 20 Å of contaminant material. Spacecraft being launched via the Space Transportation System Shuttle may have even more in contaminant layer thickness.

From the above discussion several qualitative conclusions may be stated. The first conclusion is that there is no rigorous knowledge of the material state for the uppermost layers of spacecraft surfaces and their payload surfaces. Unknown contaminant materials may be present to depths of at least 10 monolayers. A second conclusion is that very low arrival rate sticking coefficients and very low departure evaporation rates cannot be stated with accuracy because of both the unknown nature of the substrate monolayers and the fractional monolayer coverage of the arriving (and possibly evaporating) materials. An assumption of complete sticking is, clearly, a method for getting upper bound estimates on material accumulation. Actual accumulations, however, may be much lower.

A final observation on surface material accumulation is to note that orbiting spacecraft are continuously impacted by the neutral and charged particles in the ambient atmosphere and ionosphere. Space plasma ion arrival rates may range from 10^{10} to 10^{12} particles/cm^2/sec for spacecraft near-earth orbit. Space plasma ion energies on impact range from a few eV to ~15 eV. For these weakly energetic impacts the sputtering ratios are not large. However, a sputtering ratio of 10^{-4} would result in a monolayer of surface removal in a period ranging from 10^7 to 10^9 seconds depending upon the ion flux density assumed. Assignment of a sputtering ratio of 10^{-3} would lead to monolayer removal from the surface in periods ranging from 10^6 to 10^8 seconds. These surface removal rates lie in the same regimes as many of the mercury ion and mercury neutral rates of transport from the ion thruster to spacecraft. It is possible, thus, that even such weakly erosive forces as surface scrubbing by the impact of the ionospheric and atmospheric fluxes may act to remove mercury accumulation on surfaces. From these several considerations, then, the most likely situation is that the actual accumulations of Hg^+ and Hg^0 on spacecraft surfaces and sensor surfaces will be even less than those extremely small levels derived from the "total sticking" assumptions which have been an implicit portion of all of the analysis in this Special Report.

6. ELECTRON DEPOSITION EFFECTS

The previous sections have been concerned with the deposition effects of the neutral particles and ions released by the ion thruster. The ion currents from the thruster are, however, also accompanied by an equal charge density of electrons in the thruster plasma plume and the deposition of these electrons at spacecraft and sensor surfaces can produce interactive effects. The physical act of electron impact on surfaces is generally not of concern. If, however, the point of electron drainage is at a positive voltage, the electron moving to the drainage point will acquire a kinetic energy $e\Delta V$, where e is electron charge and ΔV is the potential difference between the plasma plume of the thruster and the drainage point. The power loss associated with the total drainage current, $I_e\Delta V$, can affect the electrical efficiency of the circuit in question and the heat input into the drainage point from $I_e\Delta V$ can, under some circumstances, cause material damage. The electrical equilibration of spacecraft with the thruster plasma plume and with the ambient space plasma may also be affected by these electron drainage currents.

The specific areas of interest in this section will be the possible electron drainage effects to operating subsystems of the Teal Ruby sensor and the ECOM-501 sensor and to the solar array of the P 80-1 spacecraft. The concern for electron movement from the thruster plasma plume into the interior of the spacecraft experiment sensors with subsequent drainage to positive voltages (on exposed elements) of the sensor subsystems may be dismissed entirely if the spacecraft operational schedule does not call for simulataneous operation of the ion engine and the experiment sensors. This is the most probable operational schedule. On the other hand, it is of possible future benefit to establish the feasibility of simultaneous operation in view of future spacecraft mission requirements in which sensor operation and thrusting of the ion engine may be required on a joint, rather than on an exclusive, basis.

The rates of ion movement into the regions of the exterior of the Teal Ruby sensor have been estimated previously (Section 2.2.4) to be in the range from 1 to 3 x 10^8 ions/cm^2/sec (fully operational thruster case). Because electron mobilities are larger than ion mobilities by the ratio of $(M_+/m_e)^{1/2}$, where M_+ and m_e are ion and electron mass, the electron flux densities at the exterior of the Teal Ruby sensor would be in the range from 1 to 2 x 10^{11} electrons/cm^2/sec. For electrons to move to the interior of the sensor, they must also follow a tortuous path. Electron refractibility is quite high, however, and electrons can diffuse easily at high angles around material boundaries. For the expansion of the electrons to continue to be in-plasma, however, ions must accompany the electrons, and ion penetration into the sensor (and requiring plural refraction) has been previously examined and considered at extremely low levels. Electrons, thus, would have to proceed without the ions and under the influence of whatever electric fields may be within the sensor interior. It is not possible to state directly that sensor generated electric fields will be either present or absent in the sensor in that present descriptions of the sensor internal configurations are not available. It would be worthwhile to note, however, that these sensors must operate in the ambient space plasma and that electron flux densities in the ambient space plasma range from 10^{11} to 10^{13} electrons/cm^2/sec. For the sensors to operate in this plasma background will require the shielding of (possible) positive high voltages on exposed material surfaces and the shielding must be effective against electron flux densities in the ambient space plasma which can range to more than two orders of magnitude above the electron flux densities in the ion thruster plasma plume (at the sensor location). From this it may be concluded that simultaneous operation of the Teal Ruby sensor and the ion thruster will not result in significant interactive effects from electron drainage from the thruster plasma plume.

The ECOM-501 sensor located on the spacecraft zenith surface is somewhat closer to the thruster plasma plume and does not have the added protection of the umbra created by the thruster shield. This ECOM-501 sensor does have positive high voltages in the microchannel secondary electron multipliers. A view of the sensor internal construction, however, reveals that these positive high voltages are not on exposed surfaces but are in the most interior (and very shielded) regions of the sensor. In addition to this consideration, the inlet aperture of the ECOM-501 sensor has a transverse magnetic field of several hundred gauss to prevent space plasma electron entry into the sensor interior. From the combined factors of the very well shielded positive high voltages and the magnetic barrier at the sensor inlet, it may be concluded that simultaneous operation of the ion thruster and the ECOM-501 sensor will not have any significant interactive effects from electron drainage from the thruster plasma plume.

A final area of concern is the spacecraft solar array. The back surface of this array is ∿2 meters from the ion thruster at a polar angle of ∿90 degrees. For the fully operational ion thruster, the Group IV charge exchange plasma plume will be present in these angular regions and at these spatial separation distances. From previous fully operational thruster data, the electron flux densities in the thruster plasma plume will be ∿1 $\mu A/cm^2$ near the back surface of the solar array. These thruster plasma plume electron flux densities are comparable to the ambient space plasma electron flux densities.

The drainage of electrons from the thruster plasma plume to exposed elements of the solar array cannot occur on the back surface of the array but, instead, must occur on the front surface if it is to take place at any level. The solar array front surface is in the umbra region of the thruster plasma plume as created by the solar array back surface. There is, thus, considerable attenuation of the thruster plasma plume fluxes for locations over the front surface of the array. Moreover, and as noted previously, the various spacecraft systems and sensors must be operationally compatible with the ambient space plasma. From these several factors, then, it may be concluded that electron drainage from the thruster plasma plume to the solar array will not take place at any level of significance.

7. SUMMARY

This Special Report has examined both charged and neutral particle transport from an 8 cm mercury ion thruster to the surfaces of the P 80-1 spacecraft and to the Teal Ruby sensor and the ECOM-501 sensor in the experiment payload of that spacecraft. The study has examined both line-of-sight and nonline-of-sight particle transport modes, utilizing both laboratory measurements and analyses in carrying out the mass transport assessments.

The recirculation of Hg^+ ions in the magnetic field of the earth has been analyzed for spacecraft velocity vector and earth magnetic field vector configurations which are expected to occur in near earth, circular, high inclination orbits, such as the proposed P 80-1 orbit. For these magnetic field and orbit conditions and for expected ion release distribution functions, in both angles and energies, the recirculation/reinterception of weakly energetic ions on spacecraft surfaces has been evaluated. For a complete electric thruster mission of 10,000 hours of thruster operation, expected total levels of ion recirculation/reinterception are at approximately 10^{-3} monolayers. The study has concluded that these "$\vec{v}_+ \times \vec{B}_e$" nonline-of-sight ion transport modes do not result in any significant deposition effects for the P 80-1 spacecraft or its experiment payload sensors.

The second form of nonline-of-sight particle transport examined in the study is the refraction of weakly energetic ions in the electric fields of the thruster plasma plume and in the electric fields between this plasma plume and the material boundaries of the thruster, the thruster sputter shield, and the various spacecraft surfaces. The study has specifically examined the ion transport in this nonline-of-sight mode to the Teal Ruby sensor, the ECOM-501 sensor, and the spacecraft surface on that spacecraft face bearing the ion thruster. For the Teal Ruby sensor and for the thruster and thruster sputter shield configuration such that the sensor lies in the deep umbra of the beam shield, the study concludes that there are no significant ion deposition levels. For the ECOM-501 sensor located on the same spacecraft surface as the ion thruster and also for that spacecraft surface, the study concludes that it is very unlikely that significant ion deposition effects will result. The study does, however, recommend that additional laboratory measurements be carried out to determine the extent of refraction of weakly energetic ions over the edge of the thruster front ring by electric fields in the plasma plume near the front ring and between the plasma plume and the ring.

For the line-of-sight particle transport modes, the study has concluded that Group II Hg^+ and Group IV Hg^+ deposition on the rear surface of the spacecraft solar array (the only spacecraft surface possible for line-of-sight ion transport and deposition) will not be at levels of significance. The neutral particle transport modes of interest have been identified as sputtered metal atoms from the thruster accelerator grid and thruster front ring and sputtered material from the thruster beam shield. The study has recommended additional laboratory measurements of the sputtered thruster metal atom flux in the polar angle range near 90 degrees, and additional laboratory measurements of beam shield sputtered material in the polar angle range to ∿135 degrees. The surfaces of principal concern for those measurements are the rear surface of the spacecraft solar array and the P 80-1 spacecraft surface bearing the ion thruster. Material entry into the ECOM-501 sensor is not considered to be a significant problem in view of the limited cone of entry directions of that sensor which terminate on sensitive internal surfaces of the detector.

The study has also attempted to provide some perspectives on the uncertainties in particle/surface behavior for these "very low arrival rate" regimes. It has been suggested in the discussion of that section, that many processes may act to cause material removal from surfaces at rates which are comparable to or in excess of the arrival rates of potential contaminant materials and that actual accumulation of thruster generated materials is probably at much lower levels than even these small depositions which have been calculated for "upper boundary" assumption/conditions.

A final section of this report has examined the effects of electron deposition from the thruster plasma plume and has noted that the electron flux levels in the ambient space plasma are generally in excess of the electron fluxes in the thruster plasma for the possible locations of interest for electron drainage to spacecraft surfaces or sensor payload elements. The precautions taken by the spacecraft and sensor developers to avoid electron drainage effects from the ambient space plasma will, thus, assure that there are no significant electron drainage effects from the ion thruster plasma plume.

APPENDIX A

EFFLUX MEASUREMENTS OF CHARGED PARTICLES FROM AN 8-CENTIMETER MERCURY ION THRUSTER

CONTENTS

CONTENTS (Continued)

ILLUSTRATIONS

ILLUSTRATIONS (Continued)

ILLUSTRATIONS (Continued)

ILLUSTRATIONS (Continued)

APPENDIX A

EFFLUX MEASUREMENTS OF CHARGED PARTICLES FROM AN 8-CENTIMETER MERCURY ION THRUSTER

1. INTRODUCTION

This appendix will describe a series of measurements of the charged particle efflux from an 8-centimeter mercury ion engine. Three conditions of operation of the mercury ion thruster were examined. The first condition was for the operation of only the mercury hollow cathode plasma discharge neutralizer. The second condition was for the combined operation of both the plasma discharge neutralizer and the thruster electron bombardment discharge but did not include the application of acceleration voltages to the mercury ions created in the thruster discharge. The final condition was for a fully operational ion thruster.

The principal focus of emphasis in the charged particle measurements was the determination of the ion release patterns, including both current flux magnitudes and ion directional release properties, for the "weakly energetic" ion components. These weakly energetic ions, which includes the Group IV (charge transfer ions) are of particular interest in thruster/spacecraft integration analyses because of their susceptibility to trajectory refraction in the electric field structure in the plasma plume and in the electric field structure between the plasma plume, the ambient space plasma, and the surfaces of the spacecraft. Such ion trajectory refractions, if the refraction is of sufficient magnitude, can result in the deposition of an ion on spacecraft surfaces when such deposition would be dynamically forbidden for line-of-sight ion trajectories and for a given thruster/spacecraft configuration. Because the thrust ions from the ion engines are highly energetic and will not sustain significant levels of trajectory bending in the expected magnitudes of electric fields in the plasma plume, it is an acceptable procedure to carry out integration analyses between the thruster and the spacecraft based only on line-of-sight ion trajectory treatments. For such treatments, for example, the umbra region created by the thruster beam shield is completely devoid of thrust ions and sensitive spacecraft surfaces may be located in this umbra without fear of thrust ion impact.

When non line-of-sight considerations apply to ion trajectories, however, ion deposition can result upon even those spacecraft surfaces in the umbra regions, and estimates of the deposition levels must be obtained in order to determine if spacecraft surface properties will undergo significant levels of property alteration.

The bulk of the charged particle measurements to be described in this appendix were obtained with only the plasma discharge neutralizer in operation or for the combined operation of the thruster discharge and the discharge neutralizer but with no applied ion acceleration voltages. These operational conditions correspond to two of the three operational conditions for an ion thruster in space. The two operational conditions also result in a minimum level of "facility effect" fluxes of low energy ions which can obscure the presence and properties of the genuine weakly energetic ion fluxes. When ion acceleration voltages are applied these facility effect fluxes of low energy ions increase markedly and may create erroneous determinations of the weakly energetic particles. It is essential, however, that experimental techniques be derived for the reduction of facility effect fluxes for fully operational ion thrusters in laboratory testing chambers, and a portion of the experimental effort here has been directed to measurements of fully operational thrusters with a resulting advance in the general understanding of the plasma plume from such thrusters and of the interaction of this energetic ion plume with facility walls.

2. EXPERIMENT CONFIGURATION

The charged particle measurements were carried out in the 5- x 10-foot testing chamber. Figure 1 illustrates this testing facility. The diagnostic probes used in the measurements were the Spherical Langmuir Probe (SLP), the 1-1/2-inch J_+ probe, the 4 inch J_+ probe, and the Piggyback (PB) probe. Figure 2 illustrates the probe configuration relative to the thruster and Figures 3, 4, and 5 illustrate constructional details of the probes. The probe motion and mounting rod locations of the probes are further illustrated in Figure 6.

In addition to the upper and lower shrouds and beam collector in the testing chamber, the experimental configuration also included a cylindrical electrode termed the biasable surface. Figures 7 and 8 illustrate the

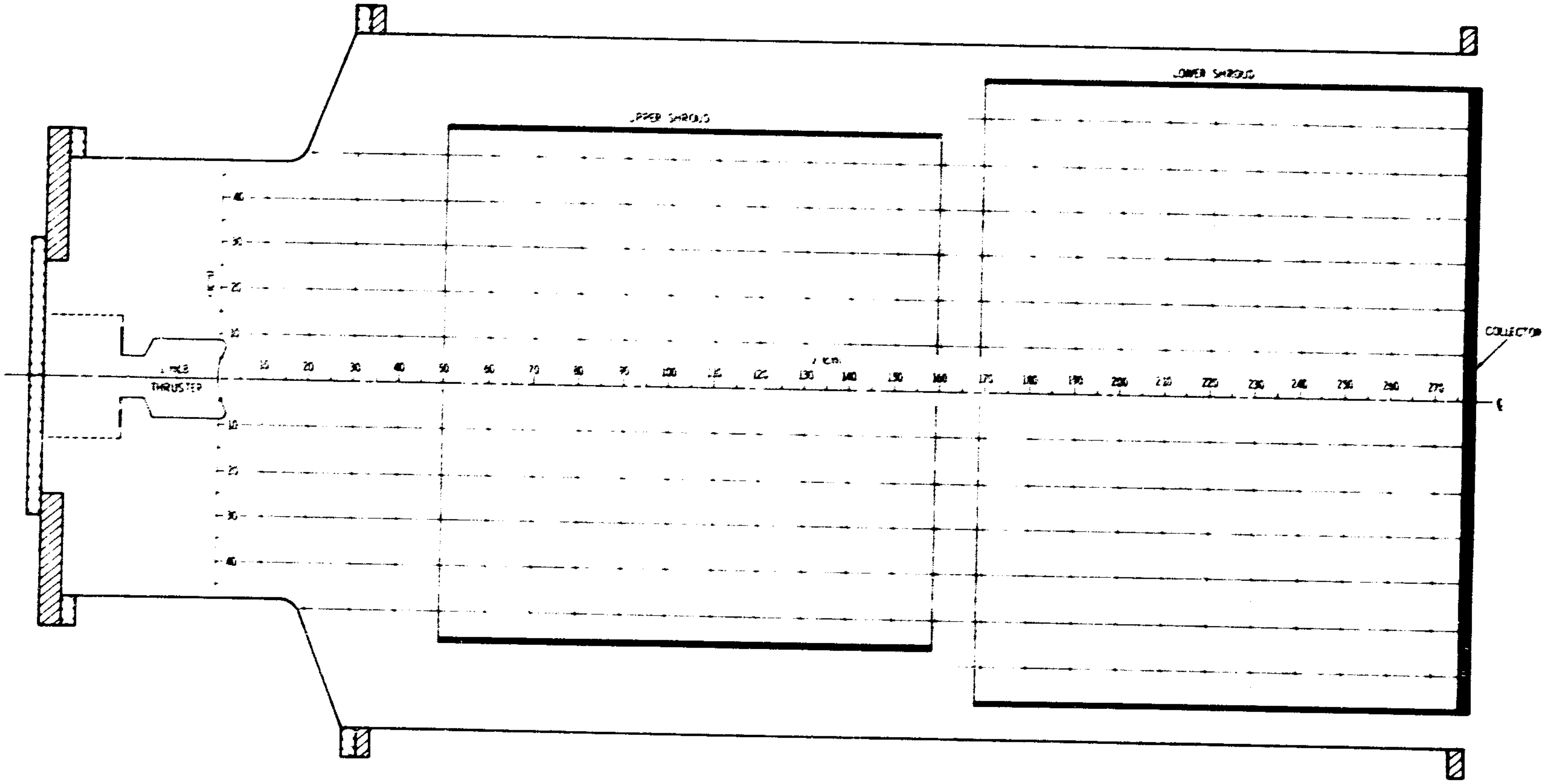

Figure 1. 5- by 10-foot Test Chamber Configuration

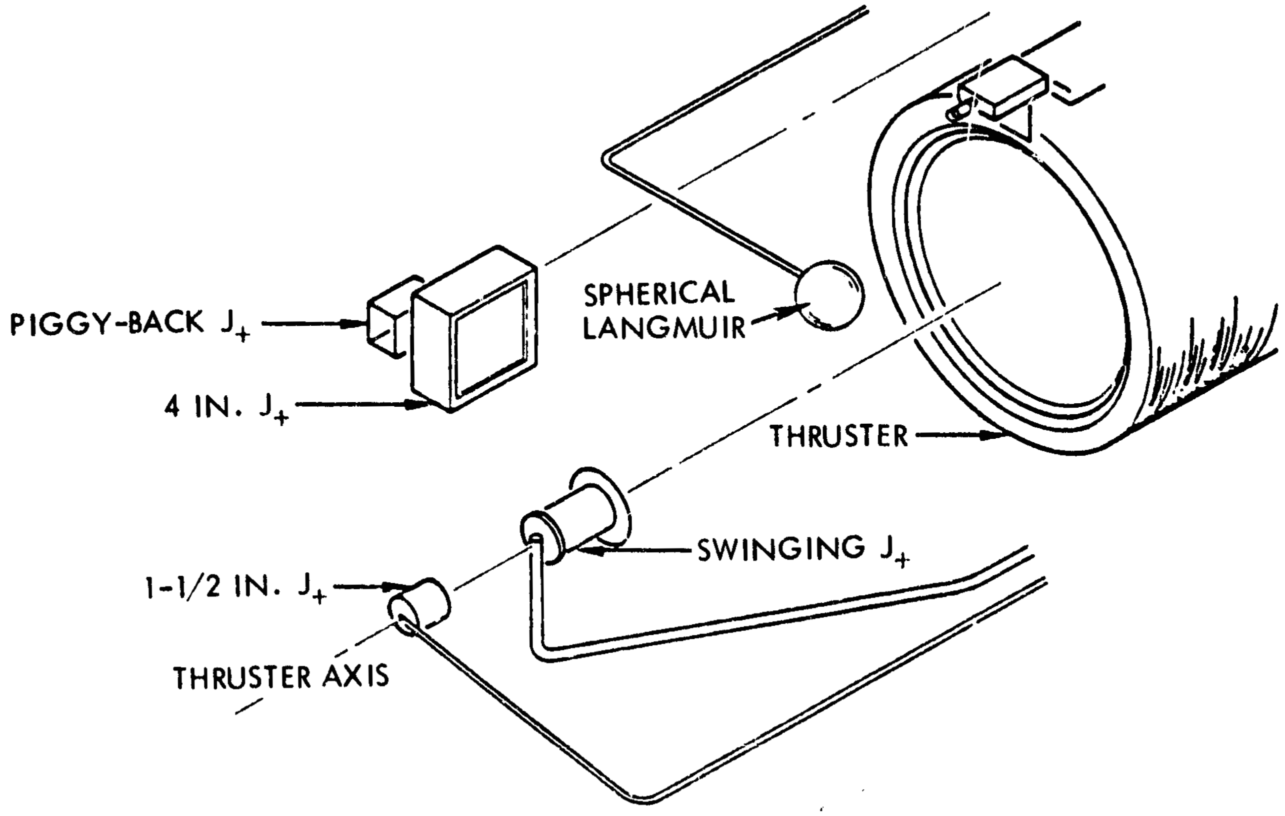

Figure 2. Diagnostic Probe Array for the Charged Particle Currents Tests

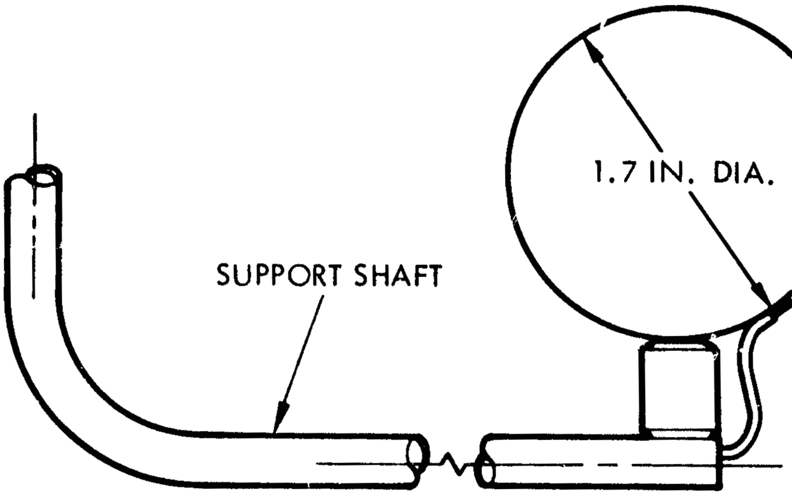

Figure 3. Spherical Langmuir Probe for the Charged Particle Currents Tests

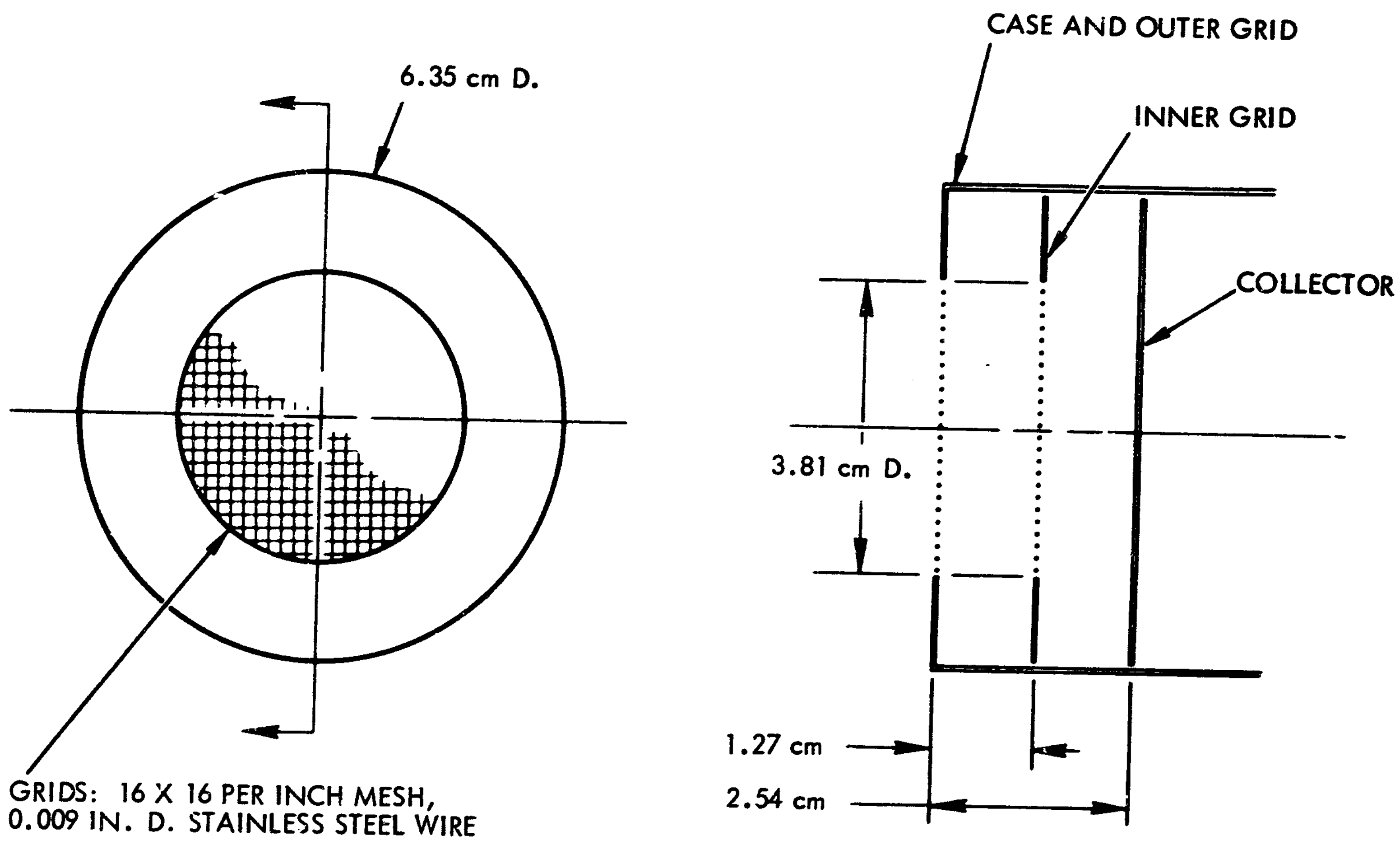

1-1/2-INCH J_+
EFFECTIVE COLLECTION AREA = 6.12 cm^2

AXIAL RANGE FROM
Z = 35 TO Z = 100 cm

Figure 4. 1-1/2-Inch J_+ Probe Dimensions

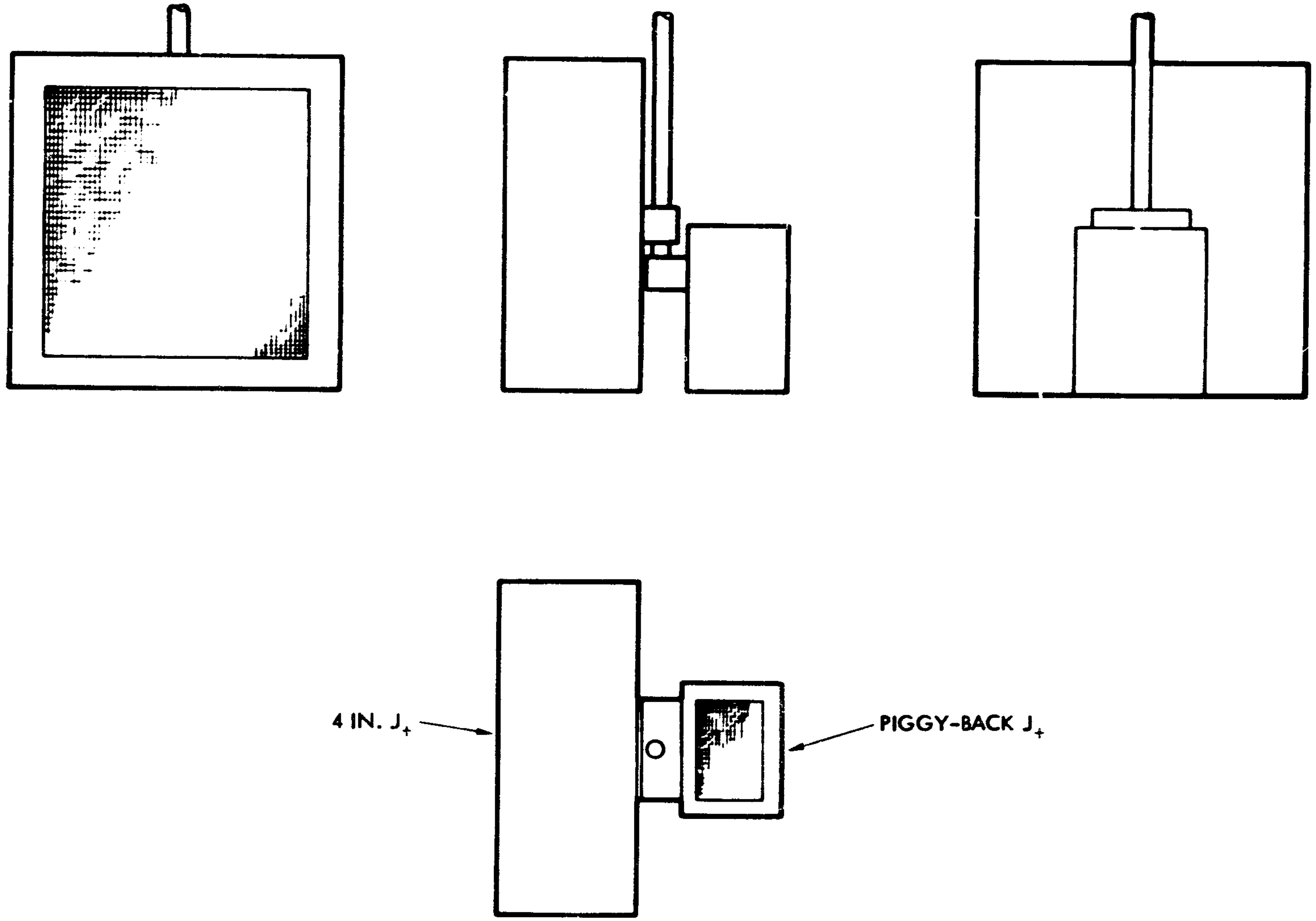

4 IN. J_+ AND PIGGY-BACK J_+ PROBE PACKAGE

Figure 5. 4-Inch J_+ and Piggyback Probe Dimensions

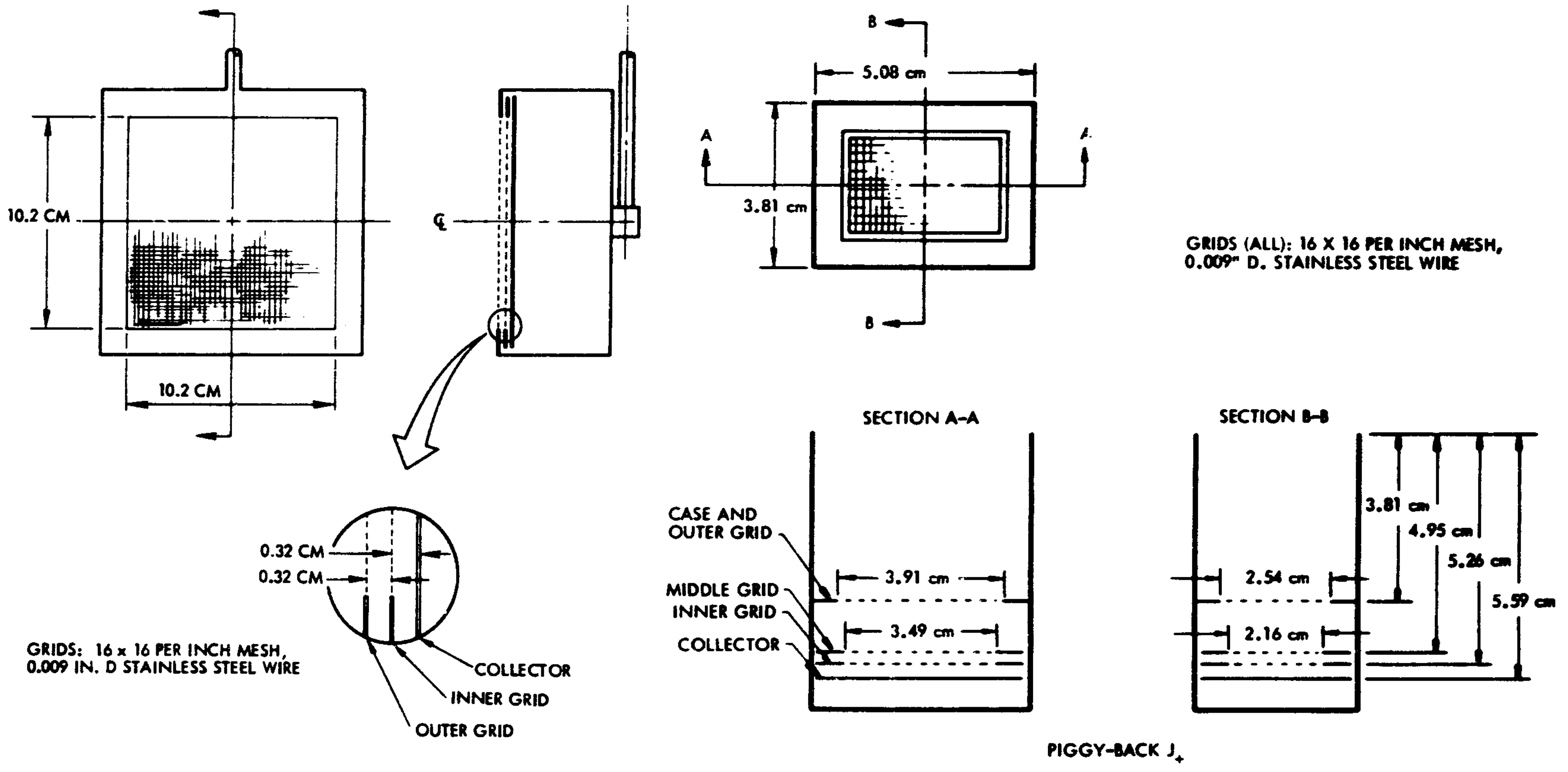

Figure 5. 4-Inch J_+ and Piggyback Probe Dimensions (Continued)

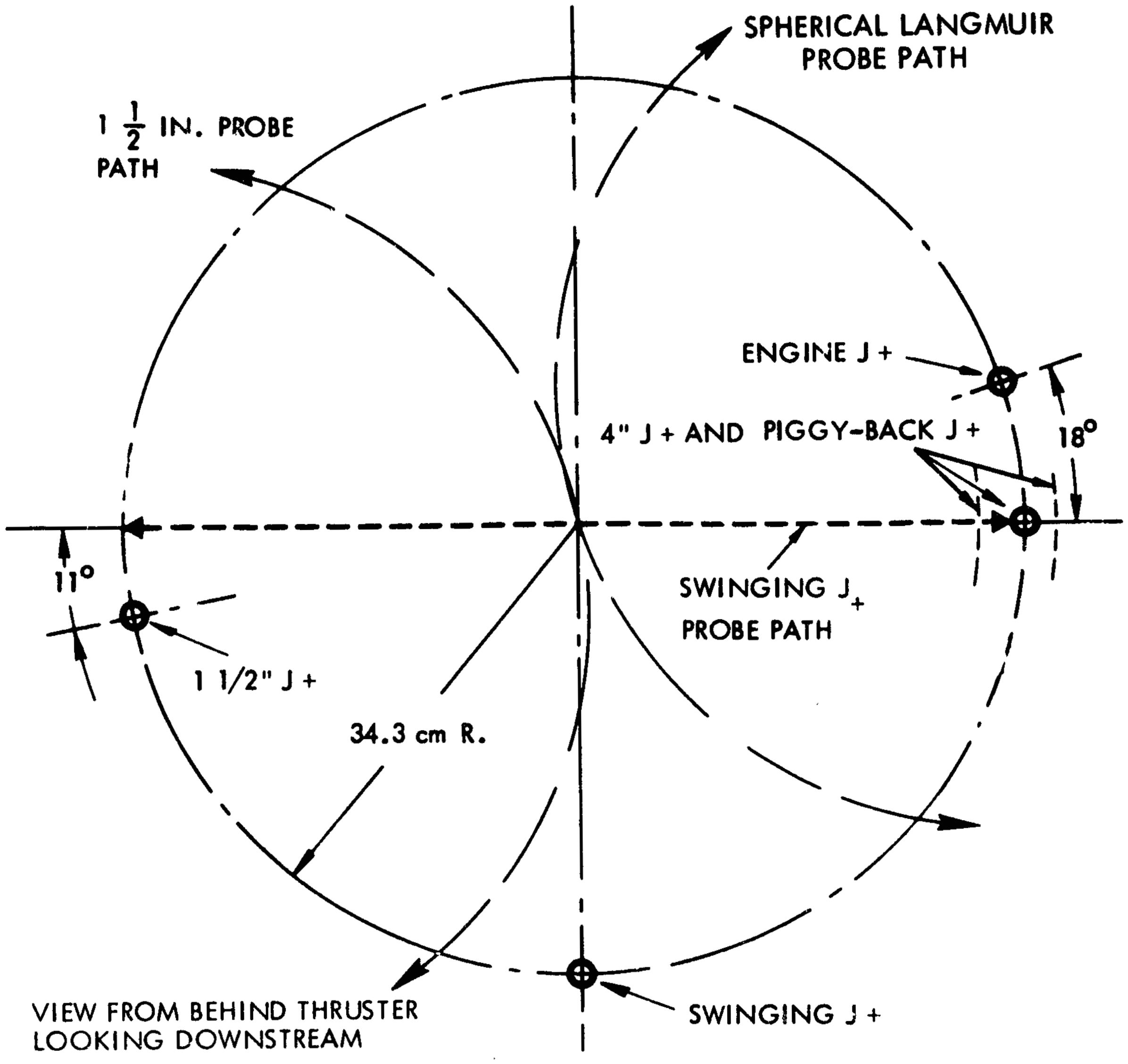

Figure 6. Probe Motion and Mounting Rod Locations

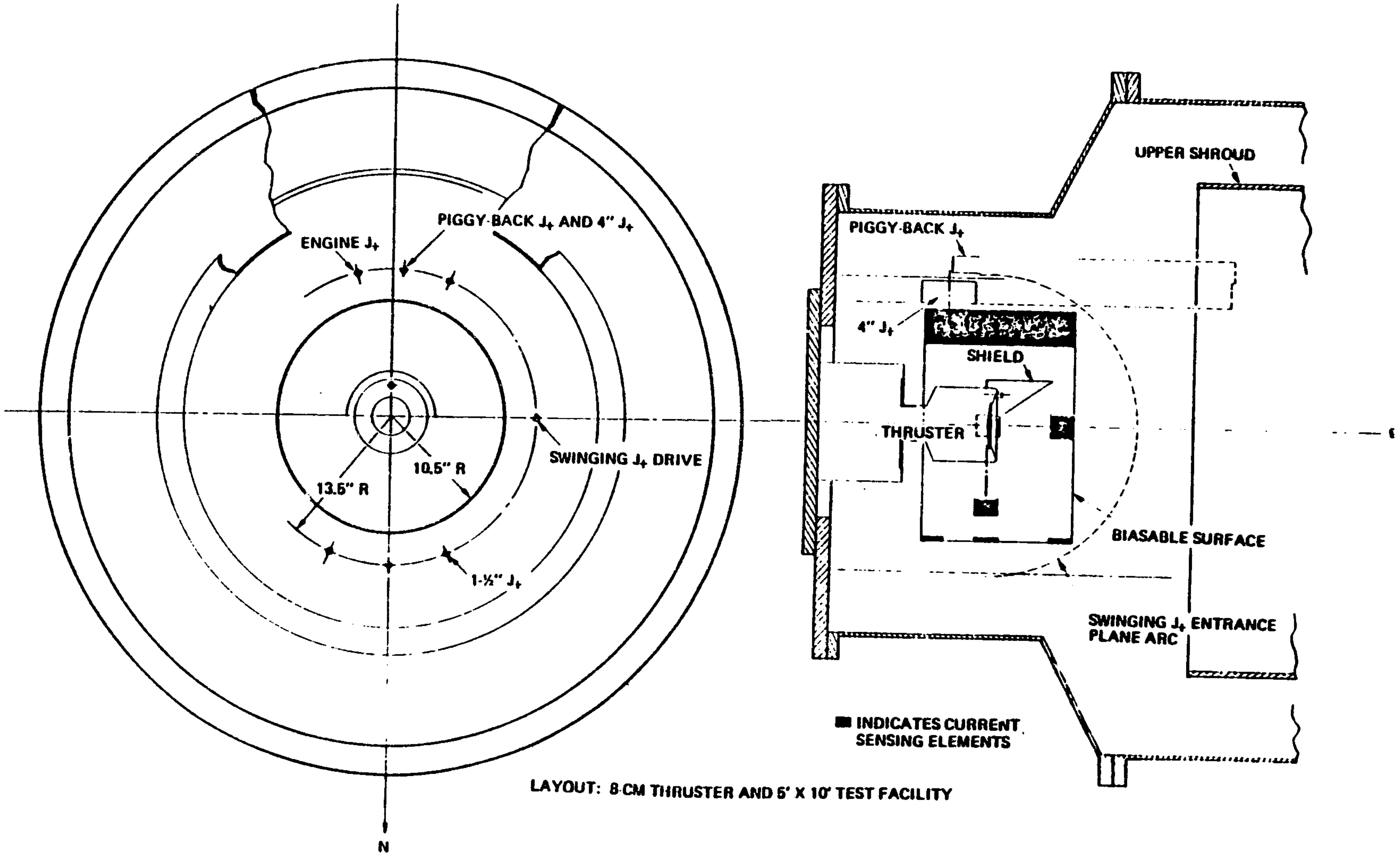

Figure 7. Overall Test Configuration for the Charged Particle Currents Tests

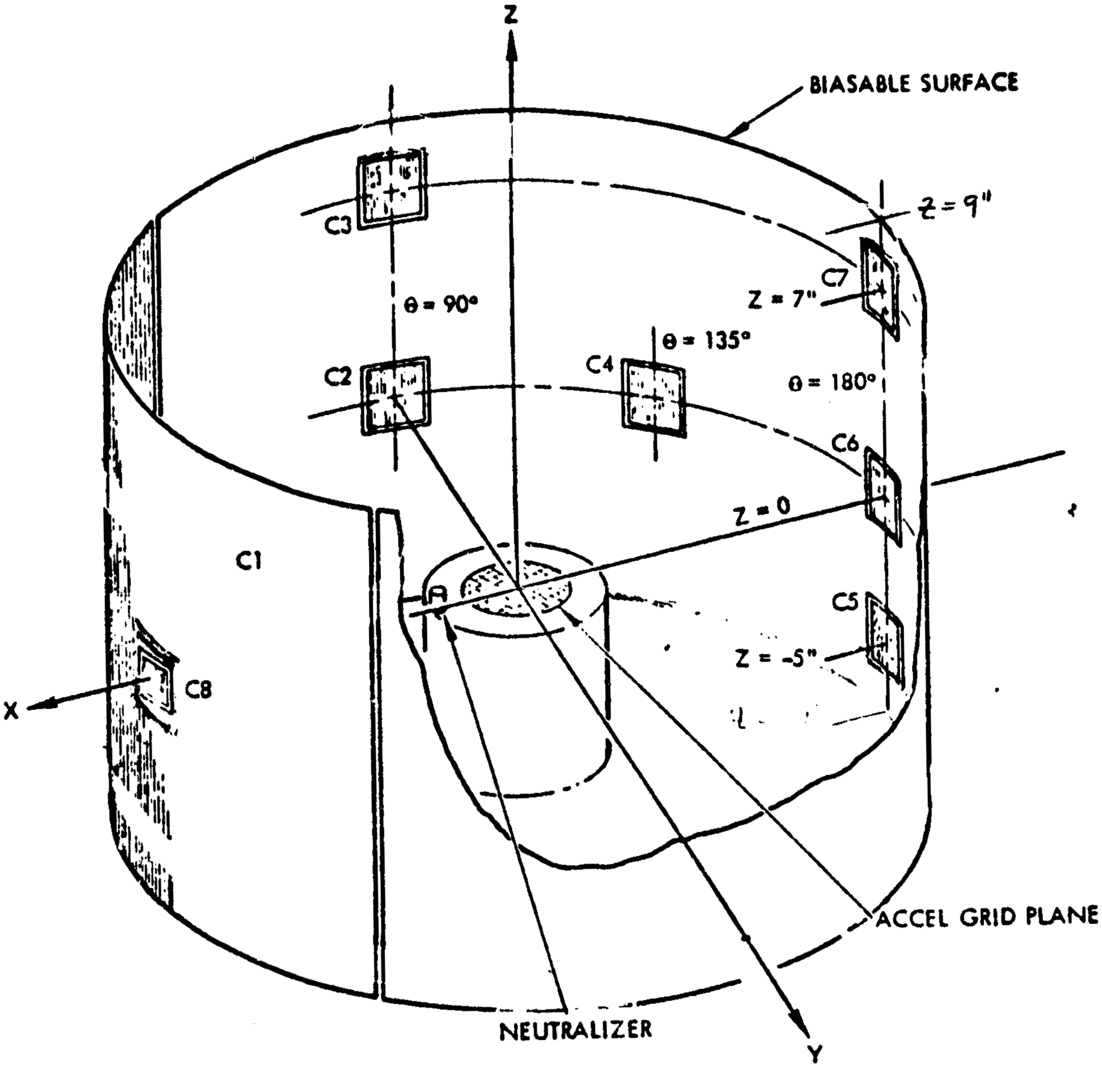

Figure 8. Arrangement of Current Sensing Elements on the Biasable Surface. [Collector C1 is rear quadrant on biasable surface. Collectors C2 through C8 are 2 x 2 inch (5 x 5 cm) surfaces. Thruster sputter shield was present during tests but not shown in drawing above for figure clarity].

position of this cylindrical electrode in the overall test configuration and provide details on the various sensing elements in the biasable surface.

The SLP and the 1-1/2-inch J_+, the 4-inch J_+, and the Piggyback probes are used in measurements of charged particle fluxes as functions of position and as functions of efflux direction of motion. Three of these probes (1-1/2-inch J_+, 4-inch J_+, and PB J_+) are also multi-gridded retarding potential analyzers and, thus, permit the determination of the energy spectrum of the charged particle fluxes. The exterior elements of the Faraday cup/RPAs can also be used as floating probes for the measurement of floating potentials in the various plasma plumes. The SLP may also be used for floating potential measurements.

The elements (C1, ..., C9) of the biasable cylinder are separately isolated and may be used for charged particle flux measurements and for floating potential measurements. The elements of the biasable cylinder may also be placed at a given electrical bias potential for the deliberate creation of an electric field structure between this element and the various plasma plumes from the several conditions of thruster operation. This creation and alteration of the electric field between a material boundary and the plasma plume permits a variation of the electric field refraction of weakly energetic particles moving in the regions near this structure, and the motion of the probes to various points relative to this material boundary then permits a determination of the degree to which this refraction causes the ion efflux to move into spatial regions which would not be occupied by ion fluxes for ions moving on straight line trajectories.

3. CHARGED PARTICLE MEASUREMENTS IN THE DISCHARGE NEUTRALIZER PLASMA PLUME

3.1 Spherical Langmuir Probe Measurements

3.1.1 Experiment Geometrical Considerations

Section 2 has stressed that a principal emphasis in the charged particle measurements will be to examine the refraction of weakly energetic ions by electric fields in the plasma plumes and in the regions between the plasma plumes and various material boundaries. To understand the geometrical considerations which are in effect here more fully, it is necessary to provide additional details, beyond that of Figures 1 through 8, of the probe and material boundary positions relative to the ion thruster. These additional configurational details are given in Figures 9 through 11.

Figure 9 is a view along the -Z axis of the thruster face and the spherical Langmuir probe position as a function of the rotation angle, θ_{SLP}, of the probe mounting rod. The convention here is that $\theta_{SLP} = 90$ deg for the SLP on the axis of the ion thruster. The usual range of probe positions is from $\theta_{SLP} = 30$ deg to $\theta_{SLP} = 150$ deg. Figure 9 also illustrates elements C1 and C9 of the biasable cylinder and the position of the thruster sputter shield and the ion thruster beam neutralizer. In addition, two cross-sectional planes, AA and BB, are illustrated.

Figure 10 is the cross-sectional view, AA, in Figure 9. For the view in Figure 10, the SLP has been placed such that its midpoint is the plane $Z = 26.0$ centimeters where $Z = 0$ is the plane of the origin of the accelerator grid. As the SLP moves from $\theta_{SLP} = 90$ deg to $\theta_{SLP} = 30$ deg it progresses into an umbra region created by the sputter shield for $\theta_{SLP} \sim 55$ deg, depending upon the point of location of the ions moving from the thruster face. Figure 10 illustrates several limiting straight line trajectories from the face of the accelerator grid and from the location of the ion thruster beam neutralizer. For $\theta_{SLP} \sim 58$ deg the SLP is in the umbra for line-of-sight ions from the discharge neutralizer while θ_{SLP} must go to ~49 degrees for ions released over the accelerator grid. These umbra locations in θ_{SLP} are, of course, also functions of the Z-plane of motion of the probe. For $\theta_{SLP} \sim 42$ degrees, the probe passes over the "south" edge of the biasable cylinder. This edge of the biasable cylinder may also be expected to cast shadows in the expanding flow of ions in the neutralizer discharge plasma plume. Figure 10 also illustrates the SLP position as a function of the probe Z setting for $\theta_{SLP} = 30$ degrees. Element C8 of the biasable cylinder is also illustrated in Figure 10.

Figure 11 illustrates the SLP positions as a function of probe rotation angle for the cross-sectional view BB. In this passage over the "east" edge of the biasable cylinder there is no intervention of the plasma plume by the sputter shield and the creation of an umbra region is by the biasable cylinder only. At $Z = 26$ centimeters, the SLP moves completely

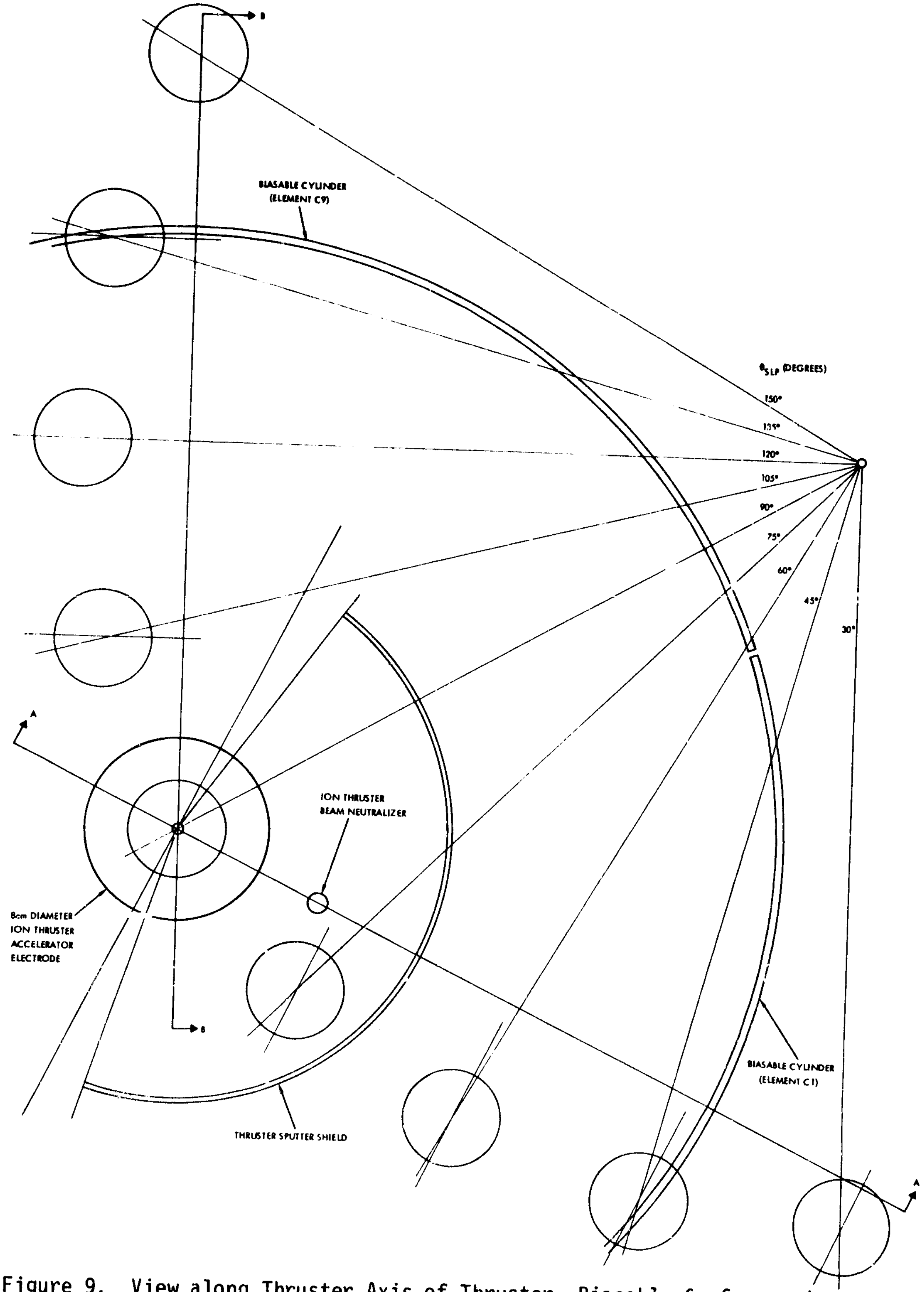

Figure 9. View along Thruster Axis of Thruster, Biasable Surface and Spherical Langmuir Probe, at Various Rotation Angle Positions

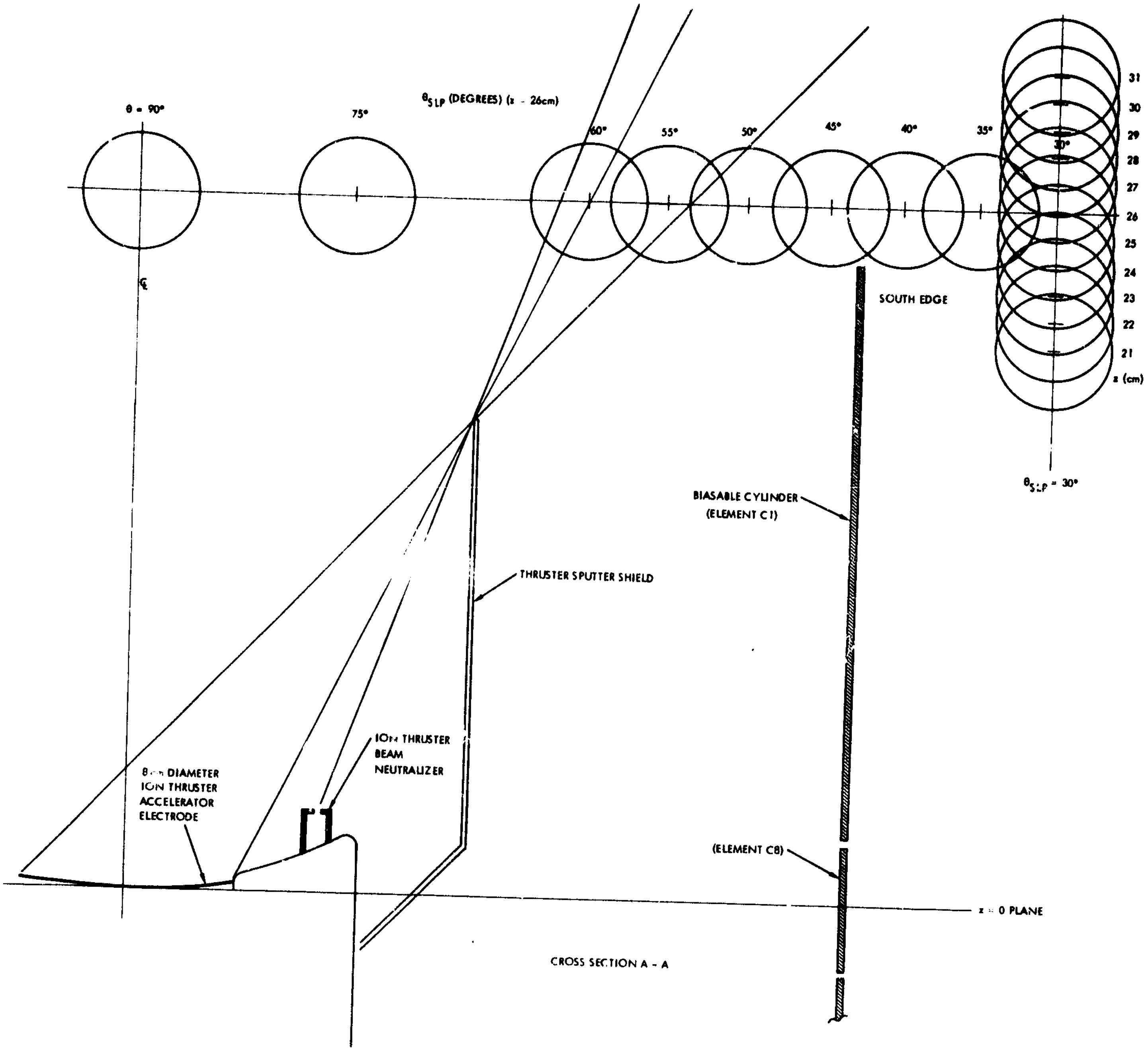

Figure 10. Cross-Sectional View in Plane A-A of Thruster, Biasable Surface and Spherical Langmuir Probe, at Various Rotation Angle and Axial Positions

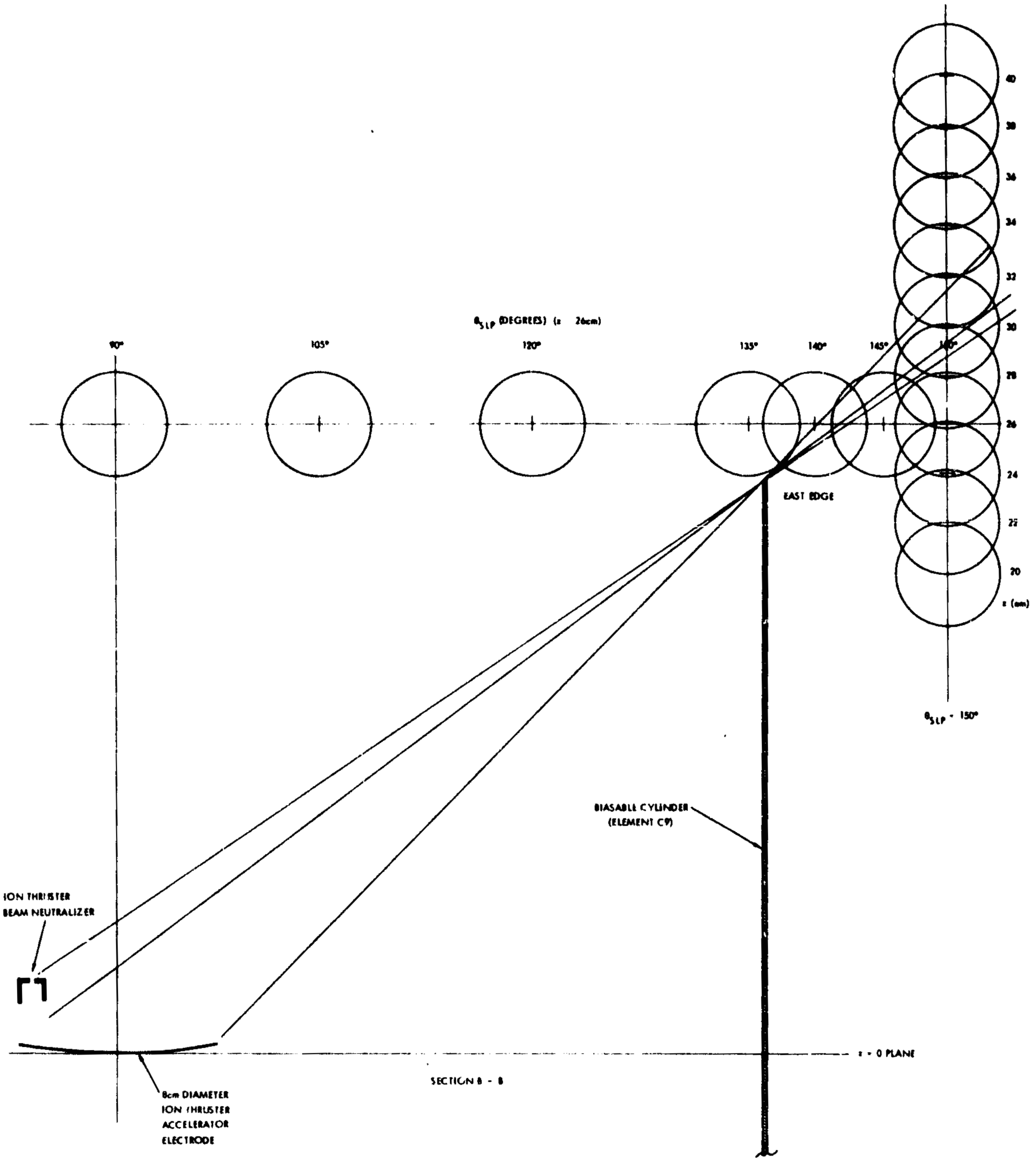

Figure 11. Cross-Sectional View in Plane B-B of Thruster, Biasable Surface and Spherical Langmuir Probe, at Various Rotation Angle and Axial Positions

into the umbra at θ_{SLP} ~150 deg. Figure 11 also illustrates the probe position as a function of Z placement for θ_{SLP} = 150 deg.

3.1.2 Floating Potential Measurements

Sections 3.1.3 and 3.1.4 will discuss the ion collection currents and the electron collection currents from the neutralizer plasma plume by the SLP. In order to selectively collect one or the other of the two charged species from the plasma, the SLP is biased either negatively or positively with respect to the plasma potential and a first requirement for the application of the probe bias voltage is the determination of the plasma potential. The determination of (exact) plasma potential by Langmuir probes can present some complications, particularly if the plasma density is sufficiently dilute that sheath growth comparable to the probe dimensions occurs for probe potentials at only minor potential differences from the plasma potential. In addition to these dilute plasma effects, there are also resistive surface film effects because of contaminant layers on the probe surfaces. For the reasons above and also for ease in experimentation, the less demanding measurement procedure of probe floating potentials will be used to estimate the plasma potentials.

With the SLP operating into a very high input impedance ($>10^{10}\Omega$) digital voltmeter, the electrical equilibration of this isolated material body in the plasma requires that the net ion and electron currents diffusing to the probe from the plasma shall be equal. This equality of electron and ion current deposition, in turn, acts to minimize the effects of possible resistive surface films on the probes because, on the average, electron and ion current densities are equal. When the SLP was placed in its floating mode, the data illustrated in Figure 12 was obtained. For these measurements, the neutralizer common is at ground potential (chamber wall), the keeper electrode is set in the range from 17 to 18 volts, keeper current is 0.5 amperes, and neutral mercury injection is ~7 milliamperes (equivalent).

Several features are of interest in the data of Figure 12. The first feature is that plasma floating potential is comparatively small compared to the known potentials (applied to the discharge neutralizer keeper electrode) at which it is believed that the neutralizer plasma plume is created.

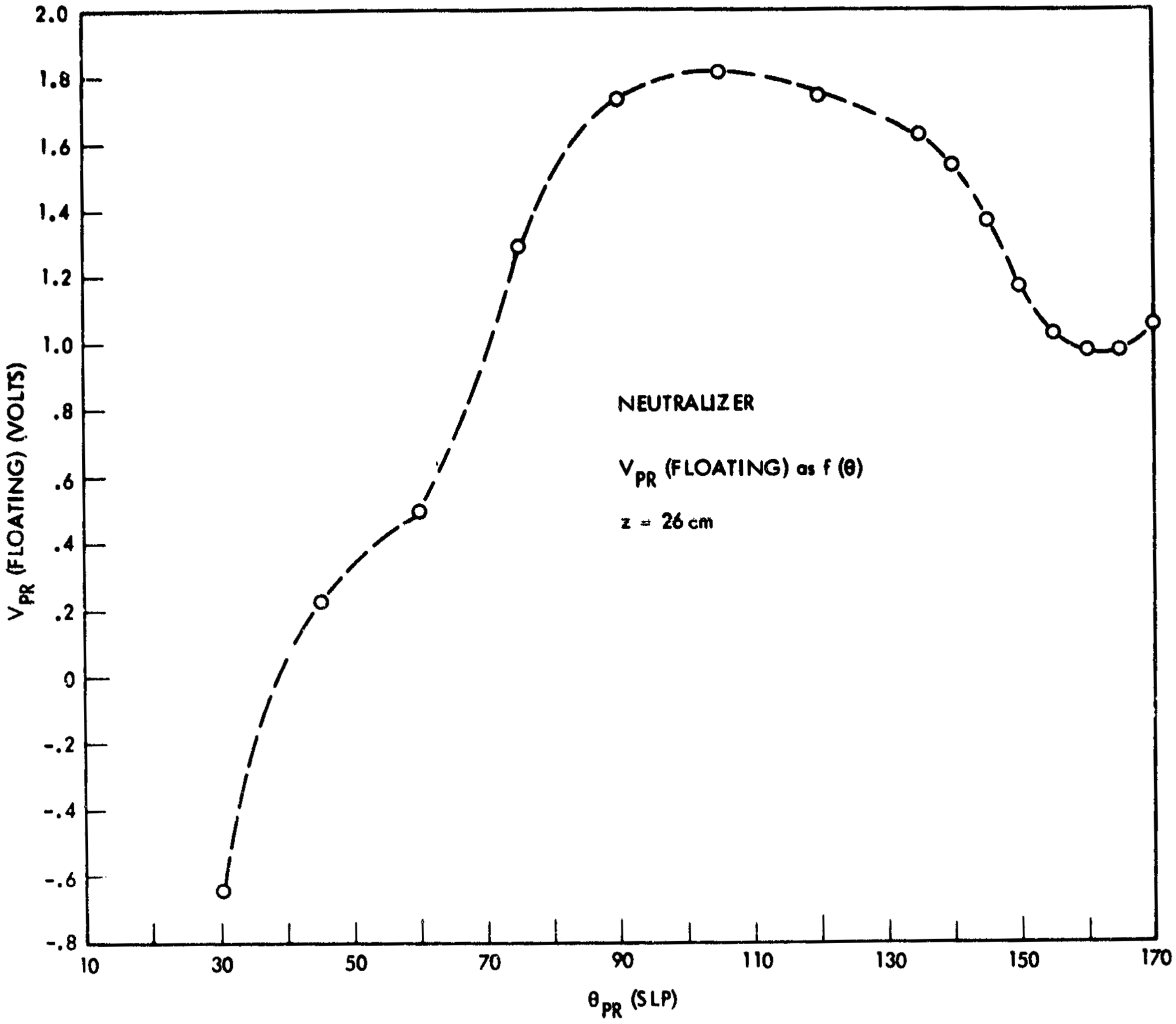

Figure 12. Spherical Langmuir Probe Floating Potential as a Function of Probe Rotation Angle in the Neutralizer Plasma Plume (biasable surface floating)

For neutralizer keeper potentials of the order of 18 volts, the very dense regions of the plasma plume (near the netralizer orifice and in the keeper electrode region) are believed to be at plasma potentials of approximately these levels. From the data of Figure 12, however, the (now) expanded plasma appears to be at much lower potentials. Potential gradients within a plasma are allowable, of course, if density gradients and (finite) electron temperatures also exist in the plasma (plasma potential moves in the negative direction ~ kT_e (in volts) for each exponential drop-off (by 2.72) in plasma density). The neutralizer plasma plume in moving from the neutralizer orifice to the probe location is in expansion and may fall off by as much as 10 orders of magnitude (from ~10^{16} ions/cm^3 to ~10^6 ions/cm^3) in moving over the present (~26 centimeters) source-to-probe separation distance. A large potential increment in the plasma plume over these particular separation distances is, thus, expected, and the data of Figure 12 would appear to support this model of plasma plume expansion.

The floating potentials in Figure 12 are not, of course, the plasma potentials at these locations. As a general rule, an electrically isolated body floats at a potential which is negative with respect to the actual plasma potential by several kT_e (because of differing ion and electron mobilities). Actual plasma potentials at the most dense portions of the SLP motion in Figure 12 (near θ_{SLP} = 90 deg) may be of the order of 5 or 6 volts, and, thus, potential increments from the neutralizer orifice to this probe location (at 26 cm and in the most dense portion of the plume at this Z setting) may be approximately 10 volts.

As the SLP moves to θ values where shielding of the plume expansion by the sputter shield can occur (θ_{SLP} ~60 deg) the floating potential of the probe does diminish. This evidence is the first direct indication that the presence of the sputter shield does cause regions of space in which plume density is reduced because of a blockage in those directions of the plume expansion. This effect is of fundamental importance in reducing ion transport and deposition on specifically sensitive surfaces and the present results indicate that some appeals can be made to ion trajectory shielding for even these weakly energetic (and presumably easily refractable) ions.

For probe motion to higher θ_{SLP} values than 90 degrees, floating potentials remain comparatively flat indicating that the plume expansion into these regions is not impeded. An examination of Figure 11 indicates that shadowing of the plasma flow by the east edge of the biasable cylinder should not occur until θ_{SLP} ~135 degrees. In point of fact, the floating potential results in Figure 12 do display a sharp drop-off in potential near this θ_{SLP} value, again confirming the earlier notions that material boundaries are capable of casting effective "shadows" in such expanding plasma plumes. The effectiveness of the shadows cast on the south edge passage (where both the sputter shield and the biasable cylinder are present) are superior to those cast on the east edge passage (biasable cylinder only). The data of Figure 12 would even appear to indicate successive shadowing effects of (first) the sputter shield and (then) the biasable cylinder for the south edge passage.

A final comment relative to the data of Figure 12 is the appearance of floating potentials which are negative with respect to V = 0, the chamber wall potentials. Such potentials are not forbidden by plasma considerations. Actual plasma potentials are, as noted, positive with respect to floating potentials, but negative values for either of these potentials can occur if sufficient density drop-off occurs (and for sufficient levels of electron temperature in the plumes). For the region of probe motion shown in Figure 12 and noting that actual plasma potentials are several kT_e positive with respect to floating, it is likely that the actual plasma potential is positive in even the most dilute regions of the plume under the present examination. This conclusion will be utilized in the setting of probe bias potentials for the ion collection measurements to be described in the following section.

3.1.3 Ion Extraction Current Measurements

3.1.3.1 Ion Extraction Current as a Function of SLP Bias Potential

The data in Figure 12 has indicated that plasma potential is positive, at least in most of the regions of the plasma. The exploration of the ion collection limb of the Langmuir probe characteristic, thus, should be possible for probe bias potential in the bias range below zero volts, and electron arrival at the probe for such potentials should be very much less than ion arrival, thus permitting a measurement of ion flux density in the neutralizer plasma plume. Figure 13 illustrates the SLP ion collection current in the bias range from 0 to -10 volts for SLP placement on the thruster axis at Z = 26 centimeters.

At 0 volts bias potential, the probe collects ~150 nanoamperes. If this probe current arrives over the entirety of the probe surface, then ion current density in the neutralizer plume would be approximately 3 nanoamperes/cm^2 at this position. If, on the other hand, the ion flow is largely ordered and is moving away from the neutralizer in a "spherical" expansion, the probe collecting area is reduced to the order of 10 cm^2 and ion flux density estimates must be raised to ~15 nanoamperes/cm^2 at this position.

The conclusions on ion flux density discussed above are further complicated, however, by the growth of collected signal as more negative probe bias voltages are applied. Growth in the collection signal for increased negative bias on the probe is, of course, predicted from probe theory because of growth in the sheath size for such dilute plasmas. Such probe theory, however, calls for a "knee" in the ion collection current limb with only modest increases in the collected ion current for bias voltages increased (negatively) beyond the knee. The presence of a positive curvature to the probe signal as bias voltage is increased, rather than the negative curvatures of Section 3.1.5, Probe Surface Film Effects, indicates some operational problems with the probe. In the discussion and experiments in Section 3.1.5, the existence of resistive surface films will be demonstrated and correction of the film effects will be carried out. This will result in an elevation of the collected ion signal for small negative bias potentials compared to the results in Figure 13. The general conclusions of the findings of the probe characteristics will, however, be found to remain the same, irrespective of the presence of resistive films. For this reason, Sections 3.1.3.2 and 3.1.3.3 will present data from probe experiments where such films are present and from other experiments in which the films, while present, have been significantly reduced by ion sputter cleaning. Comparisons of the data under the two conditions will be carried out and it will be shown that general conclusions of ion

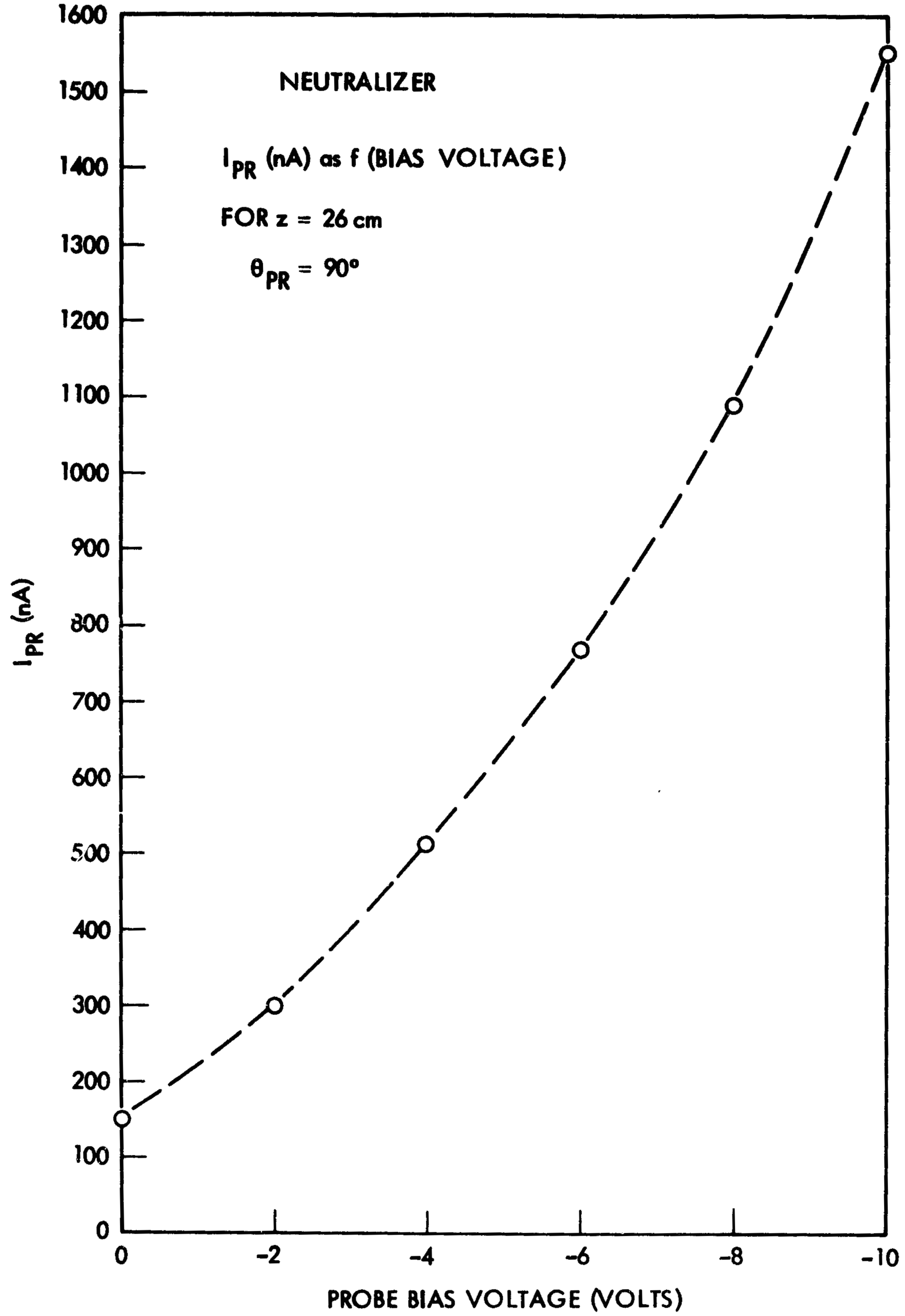

Figure 13. Ion Collection Current from the Neutralizer Plasma Plume to the Spherical Langmuir Probe as a Function of Probe Bias Voltage

trajectory refraction are the same for both conditions of probe operation, although the basic estimates of ion flux levels does change as the probes are cleaned. For present purposes, the data of Figure 13 will be taken to demonstrate that collected ion currents in the range from ~100 to ~1000 nanoamperes are observed for modest negative bias potentials and that estimates of ion flux density range from ~3 nanoamperes/cm^2 (randomly directed flux over the entire probe and "low" total signal level) to ~100 nanoamperes/cm^2 (essentially laminar ion flow for "high" total signal level).

3.1.3.2 Ion Extraction Current as a Function of Probe Position

Figure 14 illustrates the SLP collected ion signal for Z = 26 cm and as a function of probe rotation angle. Because of the concern over probe collection signal as a function of negative bias, discussed in the preceding section, the data given in Figure 14 has also been examined as a function of probe bias potential.

The results in Figure 14 illustrate significant diminutions in ion signal as the probe moves to the more protected regions of space in the probe passage. Particularly steep drop-offs are observed for probe angles less than ~75 degrees and in the region above ~135 degrees. Collection current drop-offs on either side of θ_{SLP} = 90 degrees are also present, however, and for angular positions for which shadowing by material boundaries should not be taking place. To illustrate the specific angular regions in which geometrical shadowing should be expected, Figure 15 has selected a specific curve of the Figure 14 data (-4 volts negative bias) and has presented the data in a parameter normalized to the signal at θ_{SLP} = 90 deg. Also shown on Figure 15, in the rectangular boxes, are the angular regions in which the probe should begin and should complete entry into the umbra.

From the data given in Figure 15 it cannot be stated that the drop-off rate is significantly larger for the umbra-entry condition than exists in other portions of the collection signal curve (although some apparent steepening of the drop-off does occur near θ_{SLP} ~145 degrees). The major fact to note, however, is that flux densities in the umbra region reach levels that are orders of magnitude less than the values obtained on the

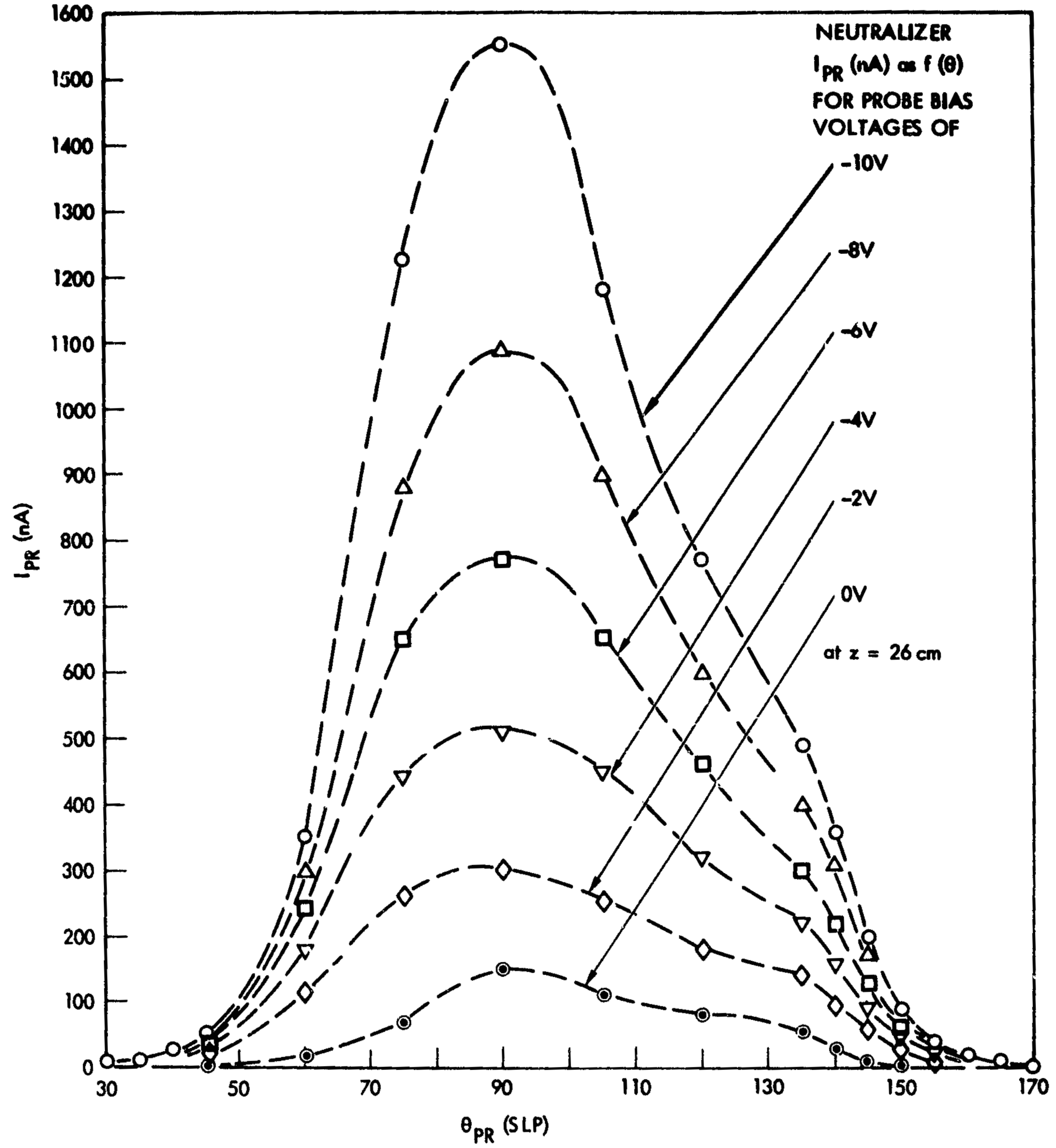

Figure 14. Ion Collection Current from the Neutralizer Plasma Plume to the Spherical Langmuir Probe as a Function of Probe Bias Voltage and Probe Rotation Angle (biasable surface floating)

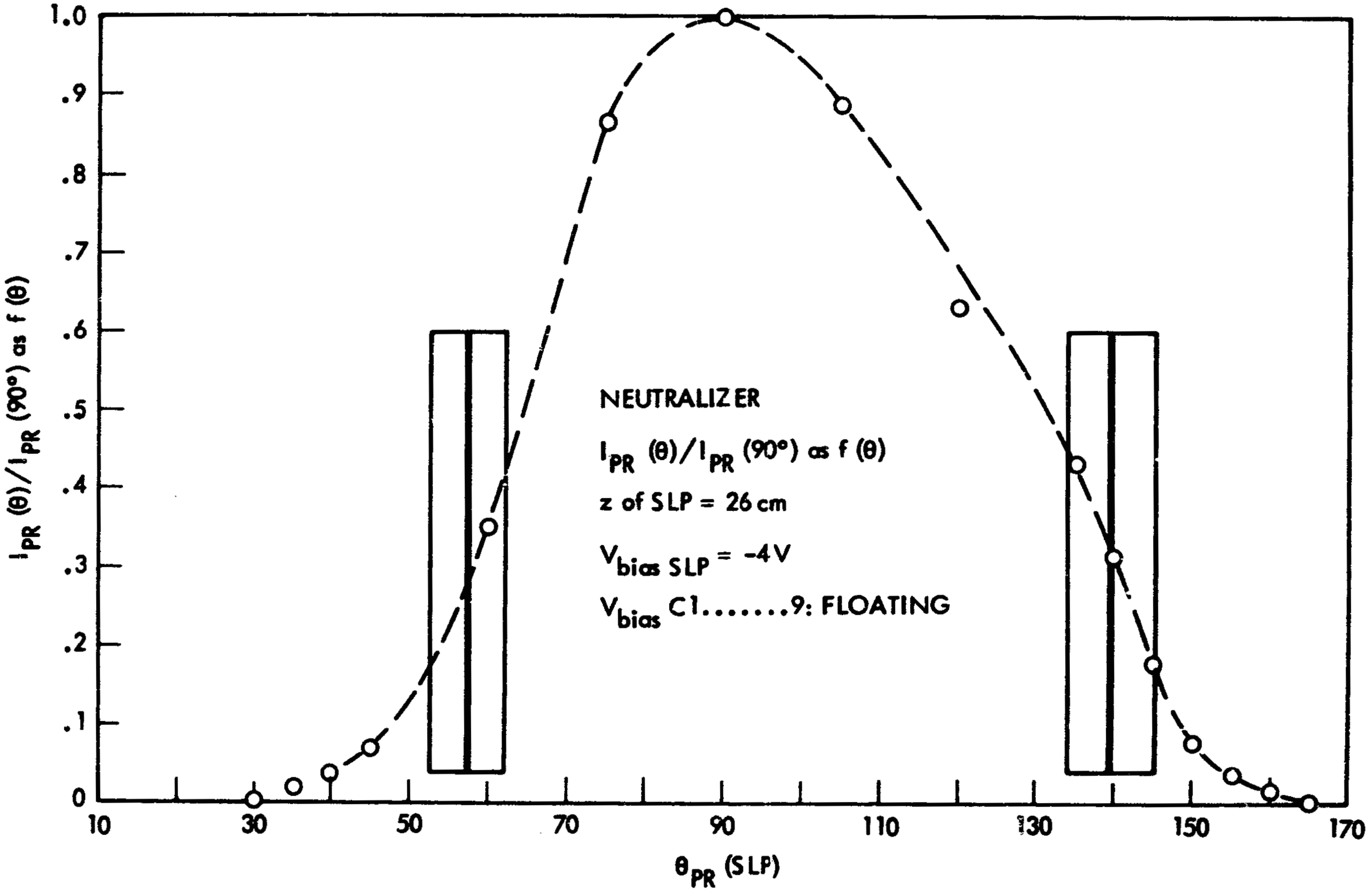

Figure 15. Ion Collection Current (Normalized to Value at θ_{PR} = 90^0) from the Neutralizer Plasma Plume to the Spherical Langmuir Probe as a Function of Probe Rotation Angle (biasable surface floating; boxes indicate "sunset" regions for optical illumination of the probe)

thruster axis. This satisfies the ultimately desired condition of low ion deposition levels in these protected regions.

A final experimental exercise in ion collection signal is to determine this signal drop-off for probe motion in the Z direction (θ_{SLP} fixed). Because the data in Figure 15 does indicate shadowing effects near θ_{SLP} = 145 degrees (corresponding to probe passage over the east edge), this region was chosen for the Z-variation experiment. Figure 16 illustrates the ion collection signal as a function of Z for θ_{SLP} = 150 degrees. For Z = 33 cm, the probe is fully in view of the neutralizer and near Z = 27 cm the probe is completely out-of-view of the neutralizer. Over the total Z range from 33 cm to 22 cm, probe signal falls by more than two orders of magnitude. The probe signal also exhibits a trail-off which follows approximately the illumination factor of a spherical probe of this given size for optical (line-of-sight) trajectories. The data presented in these figures then leads to three conclusions: the first conclusion is that ion deposition levels in "sheltered" regions are reduced to values which are very small compared to their on-axis levels. The second conclusion is that the shadows which material objects cast in the ion flow are effective and can reduce the deposition levels; and the final conclusion is that, in spite of these shadowing effects, ions can be collected in protected regions and that some levels of trajectory refraction must be present. Section 3.1.3.3 will examine this specific phenomenon, utilizing the capability of the biasable surface to alter ion trajectories by altering the potential difference between the surface and the neutralizer plasma plume.

3.1.3.3 Ion Extraction Current as a Function of Biasable Cylinder Potential

In the data given in Figures 13 through 16, the biasable cylinder (elements C1 ... C9) were electrically isolated and, thus assumed their floating potentials in the plasma. In Section 3.1.2 it was pointed out, however, that the floating potential of a material body is typically negative with respect to the plasma by potentials of the order of several kT_e. There are, thus, electric fields between the biasable cylinder elements and the neutralizer plasma plume, and weakly energetic ions, moving in

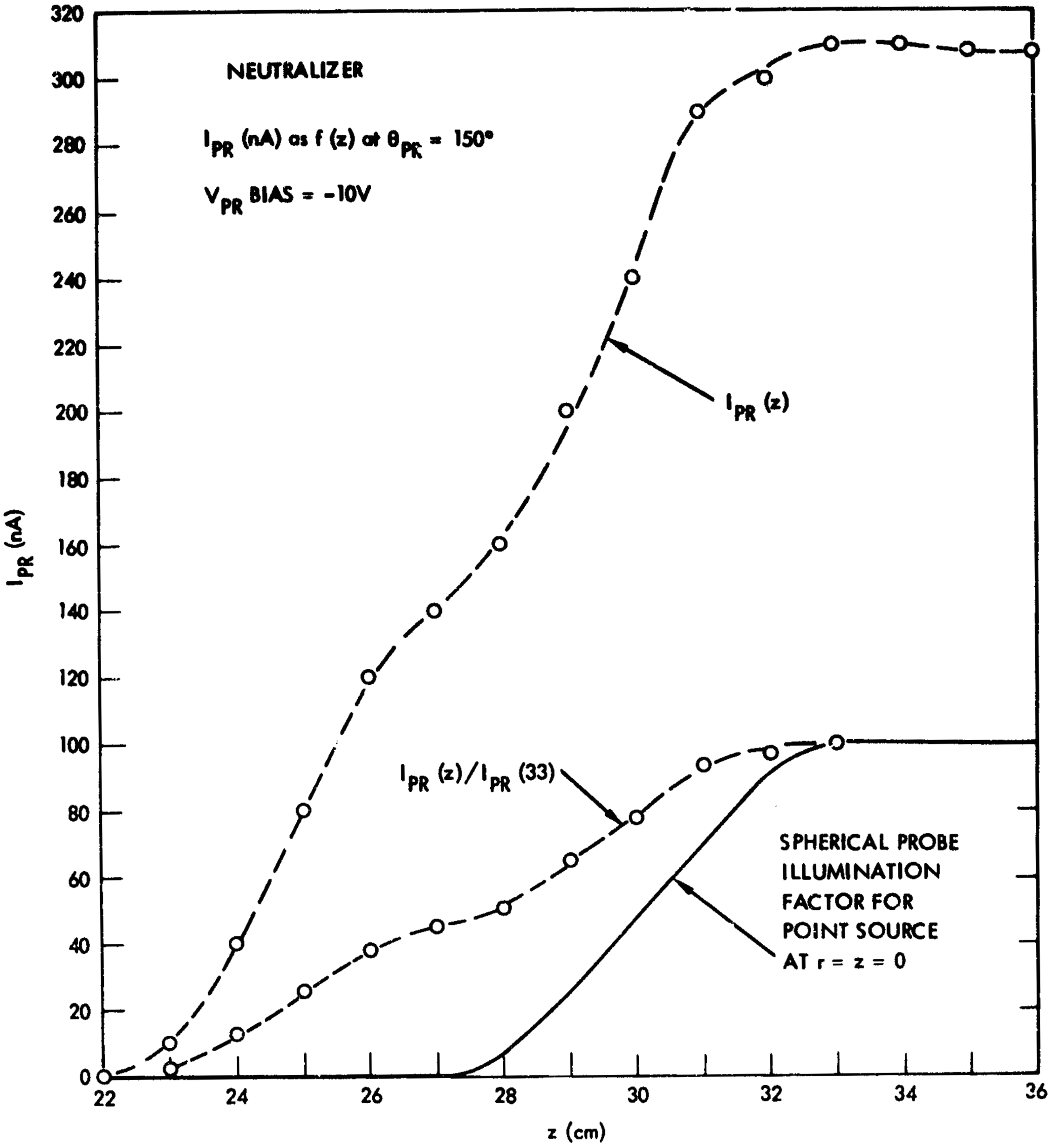

Figure 16. Ion Collection Current from the Neutralizer Plasma Plume to the Spherical Langmuir Probe as a Function of Probe Axial Position (biasable surface floating)

these electric fields will have non line-of-sight trajectories. Because the biasable cylinder is negative with respect to the plasma, ions moving past the cylinder will be attracted toward the cylinder and will be refracted into the umbra, and Figure 16 has exhibited evidence of such ion trajectories in the umbra.

To determine the degree to which ions may be refracted into protected regions by such electric fields, the SLP collection signal has been examined at a specific θ value as a function of biasable cylinder potential and over a range in θ for two values of cylinder bias. Figure 17 illustrates the probe collection signal at $\theta_{SLP} = 140$ degrees as cylinder bias moves from -4 volts to +6 volts. Some increase in the collected signal is evident for the more negative bias voltages on the cylinder indicating that ion trajectories are being bent to bring ions into a protected region. The signal increases seen here, however, are small, and a review of the probe configuration relative to the east edge and at $\theta_{SLP} = 140$ degrees (see Figure 11) indicates that major alterations in ion collected signal are not to be expected in view of the comparatively exposed probe position at this angle. More striking effects should be seen, however, for probe positions well into the umbra. Figure 18 does examine the ion collection signal over a range from $\theta_{SLP} = 50$ deg to $\theta_{SLP} = 150$ deg and for fixed bias potentials of +4 volts and -4 volts on the biasable cylinder elements. Over large portions of the angular range, no difference in collected ion signal is observed and should not be expected in view of the limited electric field penetration depth from the biasable cylinder and into the neutralizer plasma plume. For $\theta_{SLP} > 150$ deg, however, the difference in signal level between the two bias voltage conditions is striking. More than an order of magnitude in collected ion signal is present, for example, at $\theta_{SLP} = 155$ deg.

The results in Figures 17 and 18 illustrate that electric fields between the biasable cylinder and the plasma plume are at comparatively low levels for cylinder bias potentials of the order of +2 to +4 volts which tends to confirm earlier motions on the plasma potential in these regions. In addition to this, the results illustrate that the correct tailoring of the electric fields between a material boundary and the

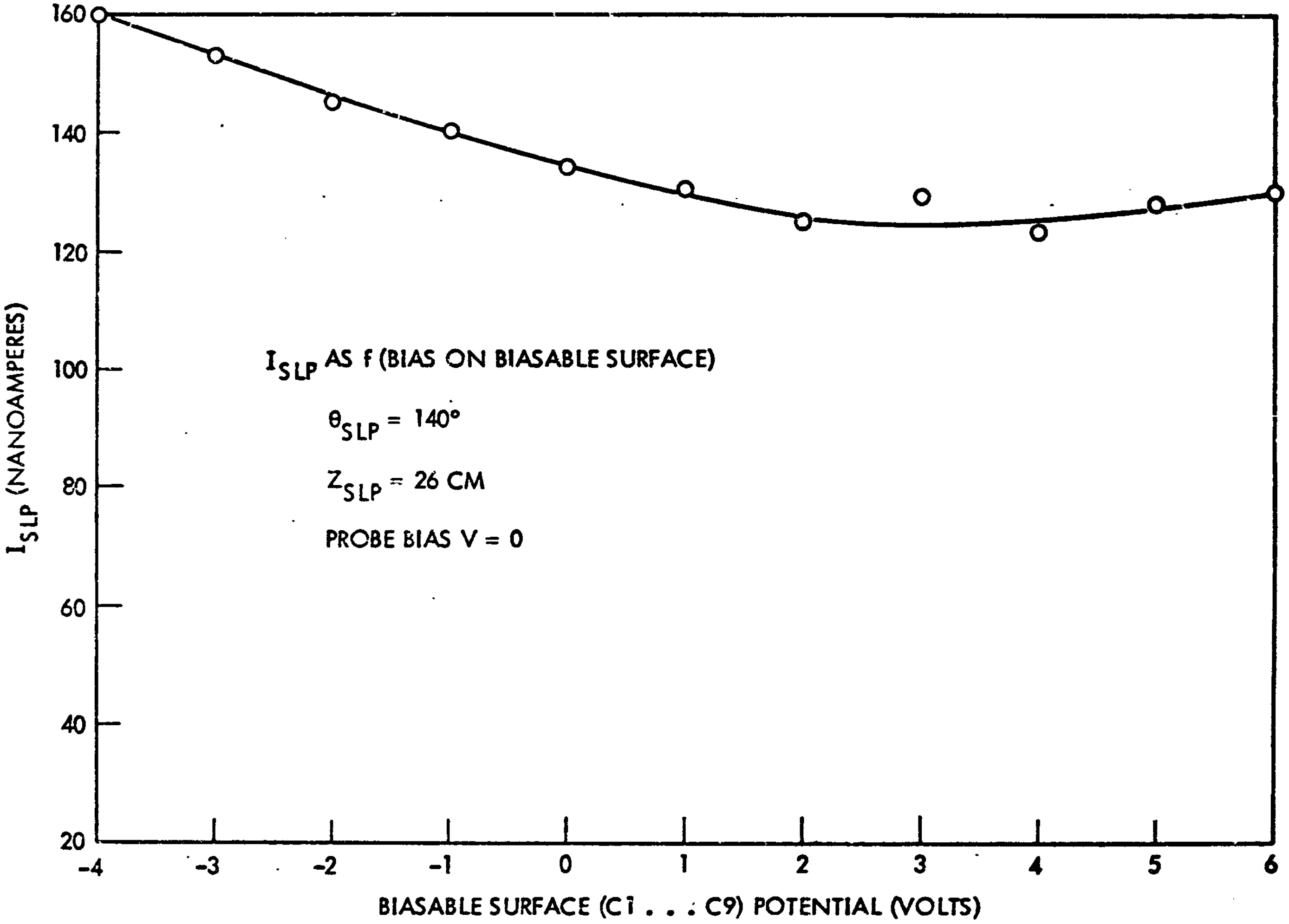

Figure 17. Ion Collection Current from the Neutralizer Plasma Plume to the Spherical Langmuir Probe as a Function of Biasable Surface Potential

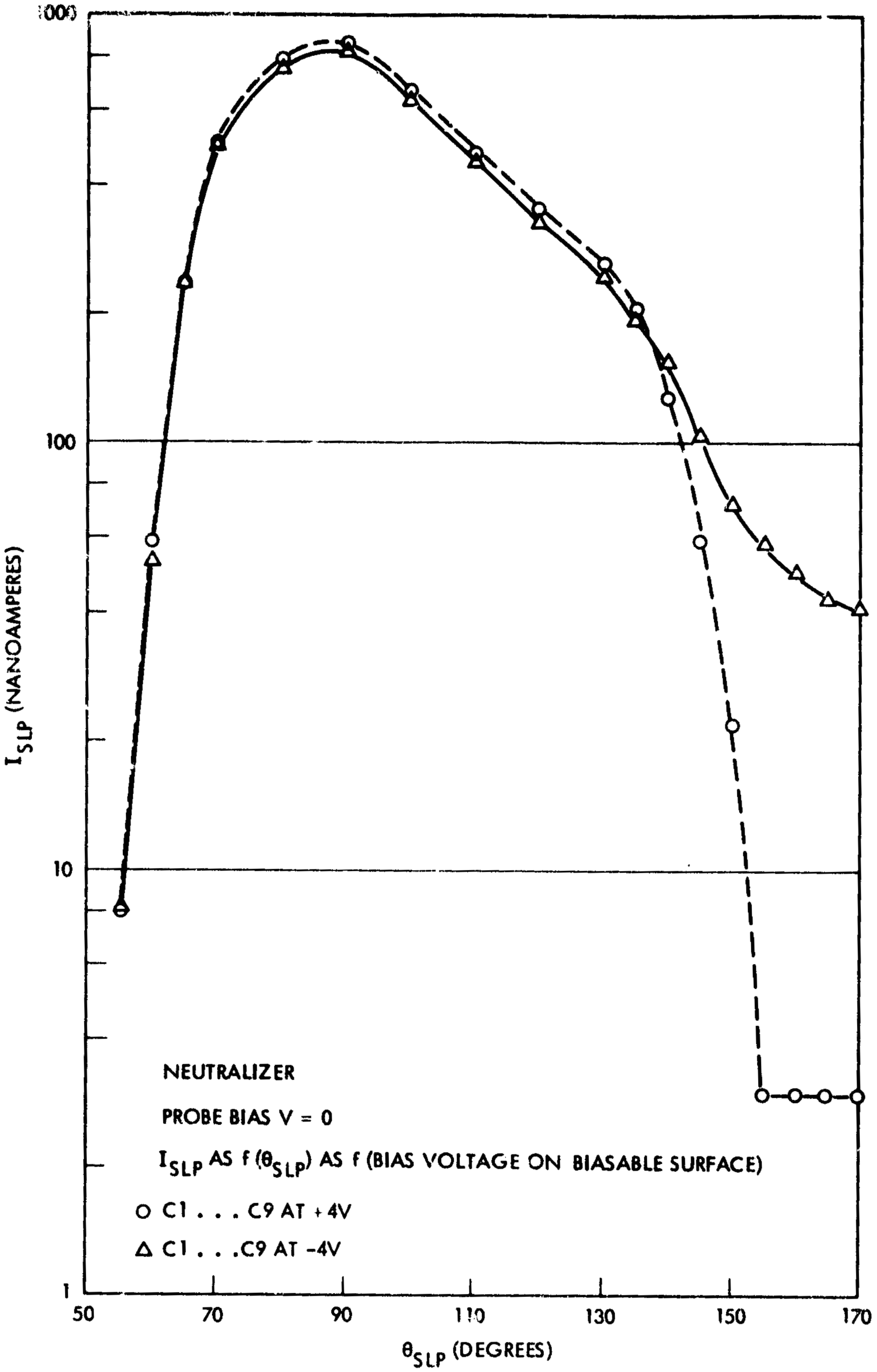

Figure 18. Ion Collection Current from the Neutralizer Plasma Plume to the Spherical Langmuir Probe as a Function of Probe Rotation Angle for Biasable Surface at +4V and -4V

plasma can dramatically reduce the level of ion refraction into protected regions. The alternative statement is that incorrect tailoring of these boundary conditions can enhance the refraction of ions and can introduce ion deposition onto surfaces in the protected regions. It follows that the diligent integration of ion thrusters into spacecraft must consider these boundary condition effects and attempt to so arrange them as to minimize ion transport refraction.

A final area to note in the data of Figures 17 and 18 is the level of ion signal throughout the various experiments. These signal levels are increased relative to the range of signals displayed in Figures 13, 14, and 15 (for comparable SLP bias voltages). The reason for this signal increase in Figures 17 and 18 is that ion sputter cleaning of the SLP has been carried out for this experiment. While such sputter cleaning of the probes has resulted in increased signal levels, the general conclusions on ion refraction from the probe data are not altered. The important features in all of this data are that ions are at significantly reduced levels in the umbra region and that even more significant reductions of these signals can be obtained if attention is paid to minimizing electric fields between material boundaries and the plasma plume.

3.1.4 Electron Extraction Current Measurements

Langmuir probes may be used in principle, for determinations of both the ion properties and the electron properties in plasma. In the present plasma, attempts were made to determine T_e by the shape of the electron collection limb of the probe. These attempts were not successful because of a continuous pattern of drifts in the collected electron signal. These drift patterns are considerably reduced in the ion limb current collection characteristics and the measurements there (Figures 13 through 18 and Figures 19 through 26) can be carried out with run-to-run stability. Because the electron currents rise so rapidly and because electron kinetic energies are suspected of being much lower than ion energies, only small fluctuations in probe surface characteristics can cause measurable drifting in electron collection.

The general indications from the Langmuir probe characteristics attempted for electron temperature measurement is that T_e is a fraction of

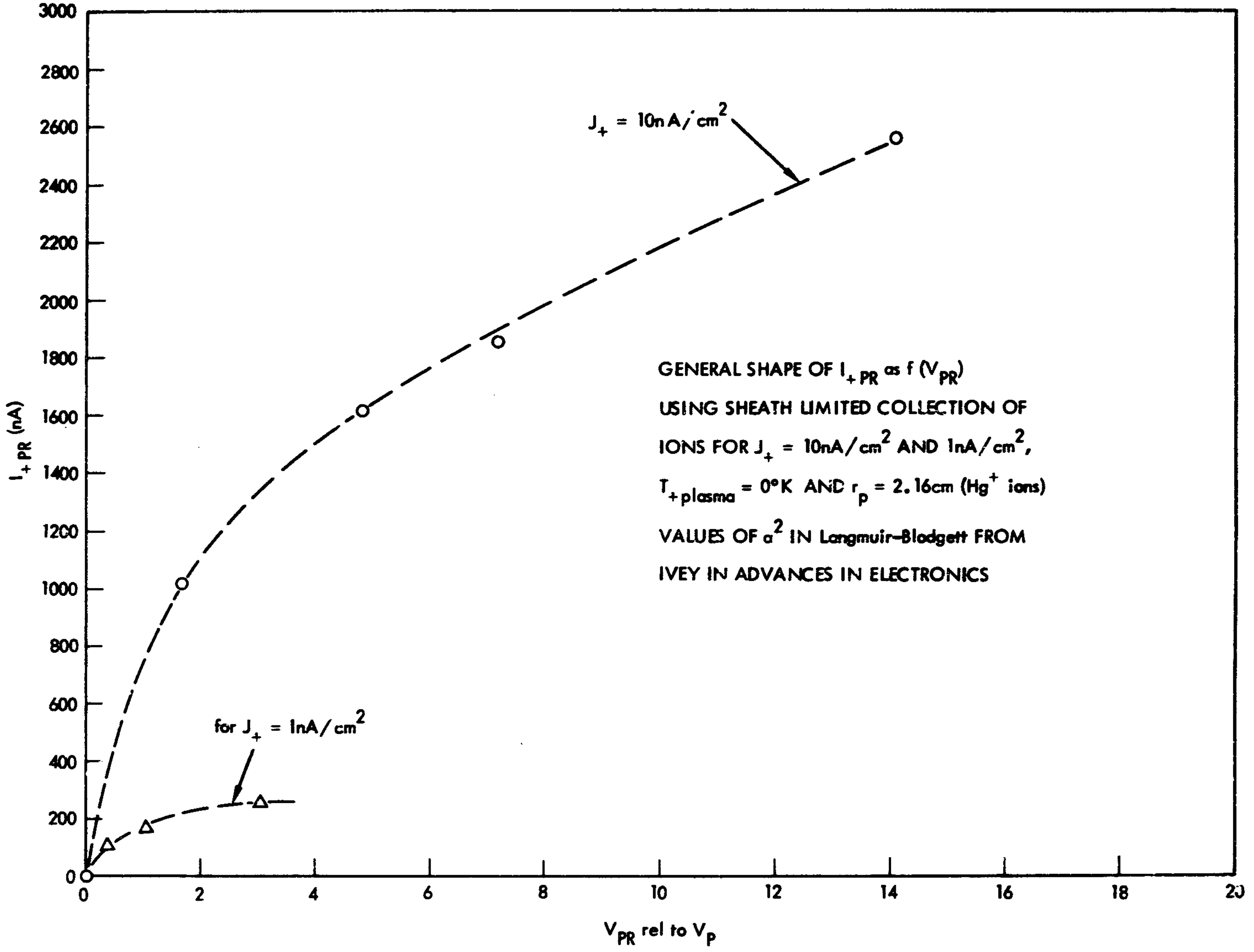

Figure 19. Computed Shape of the Expected Ion Collection Current from a Plasma as a Function of Probe Bias Potential

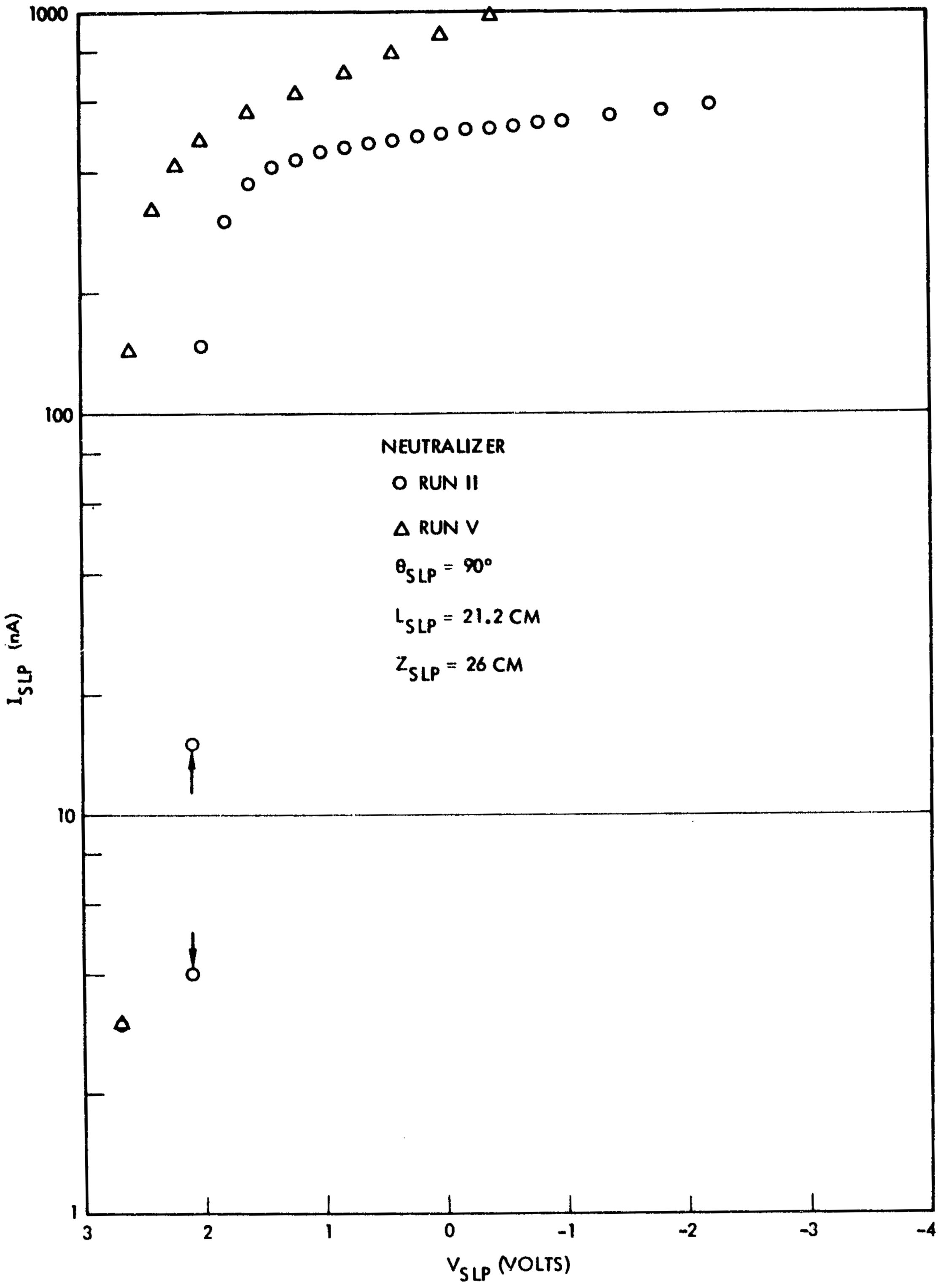

Figure 20. Ion Collection Current from the Neutralizer Plasma Plume to the Spherical Langmuir Probe as a Function of Probe Bias Voltage Following Ion Sputter Cleanings

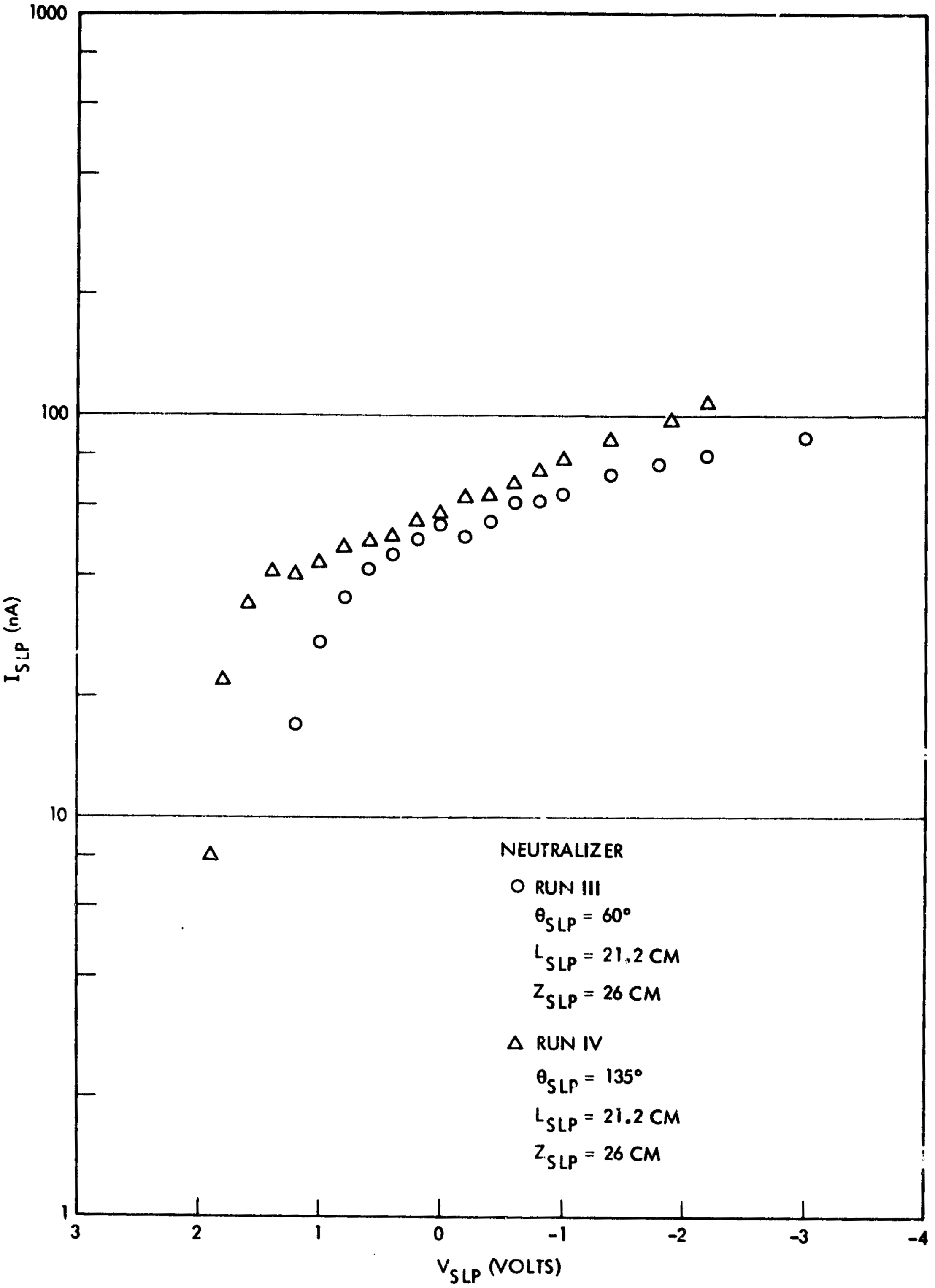

Figure 21. Ion Collection Current from the Neutralizer Plasma Plume to the Spherical Langmuir Probe (for off-axis probe locations and following ion sputter cleaning)

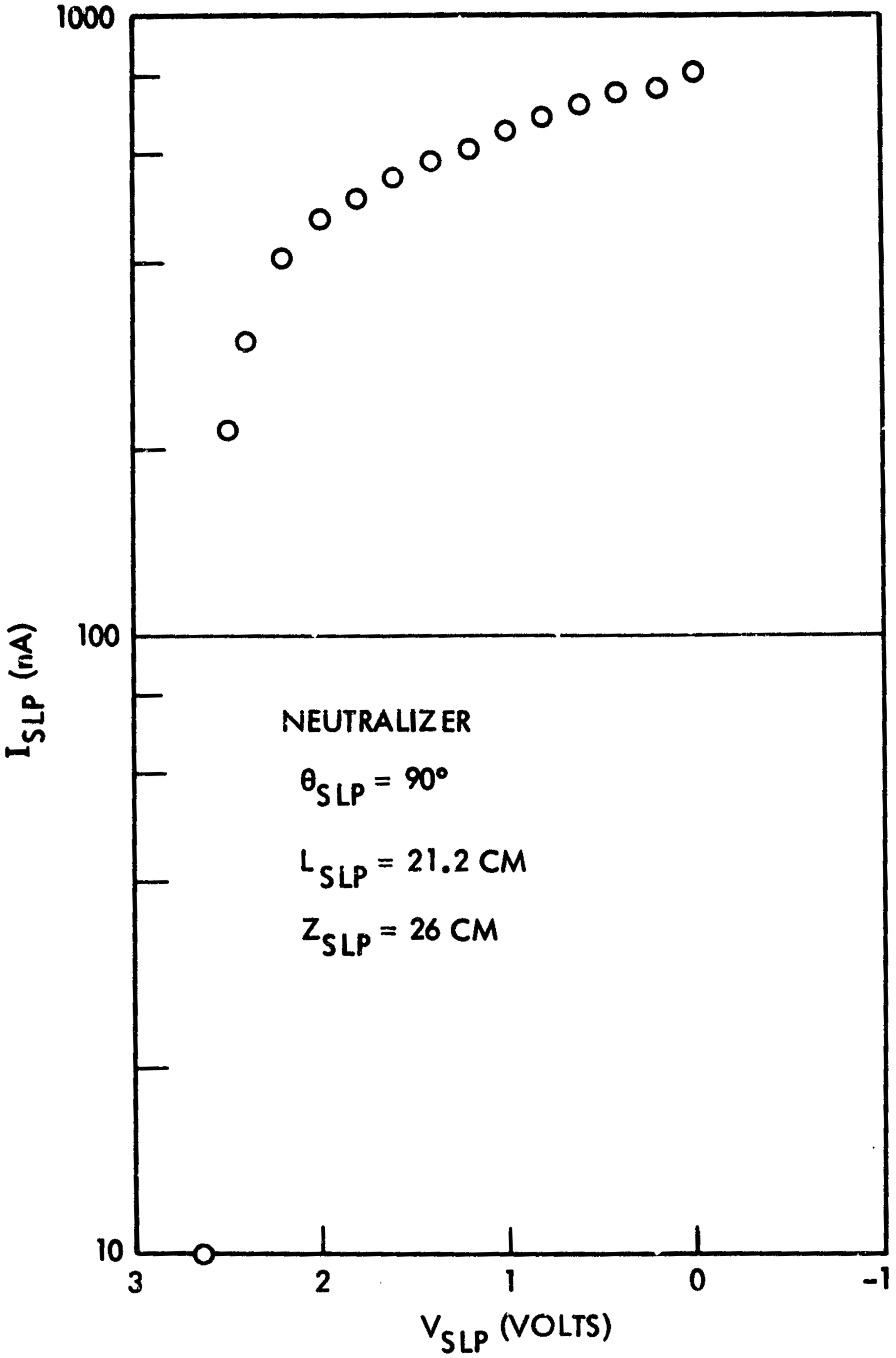

Figure 22. Ion Collection Current from the Neutralizer Plasma Plume to the Spherical Langmuir Probe (for continued ion sputter cleanings)

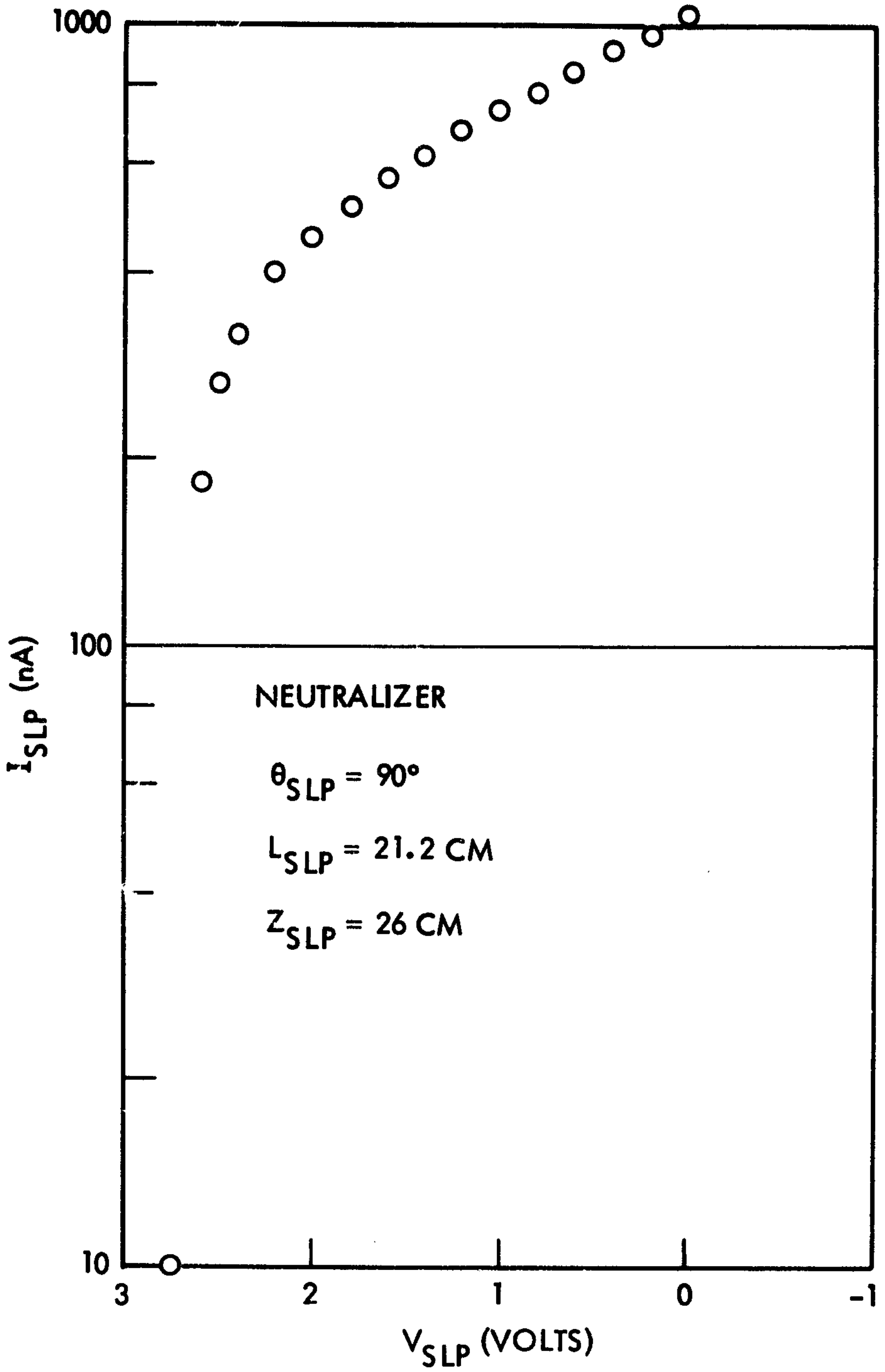

Figure 23. Ion Collection Current from the Neutralizer Plasma Plume to the Spherical Langmuir Probe (for continued ion sputter cleanings)

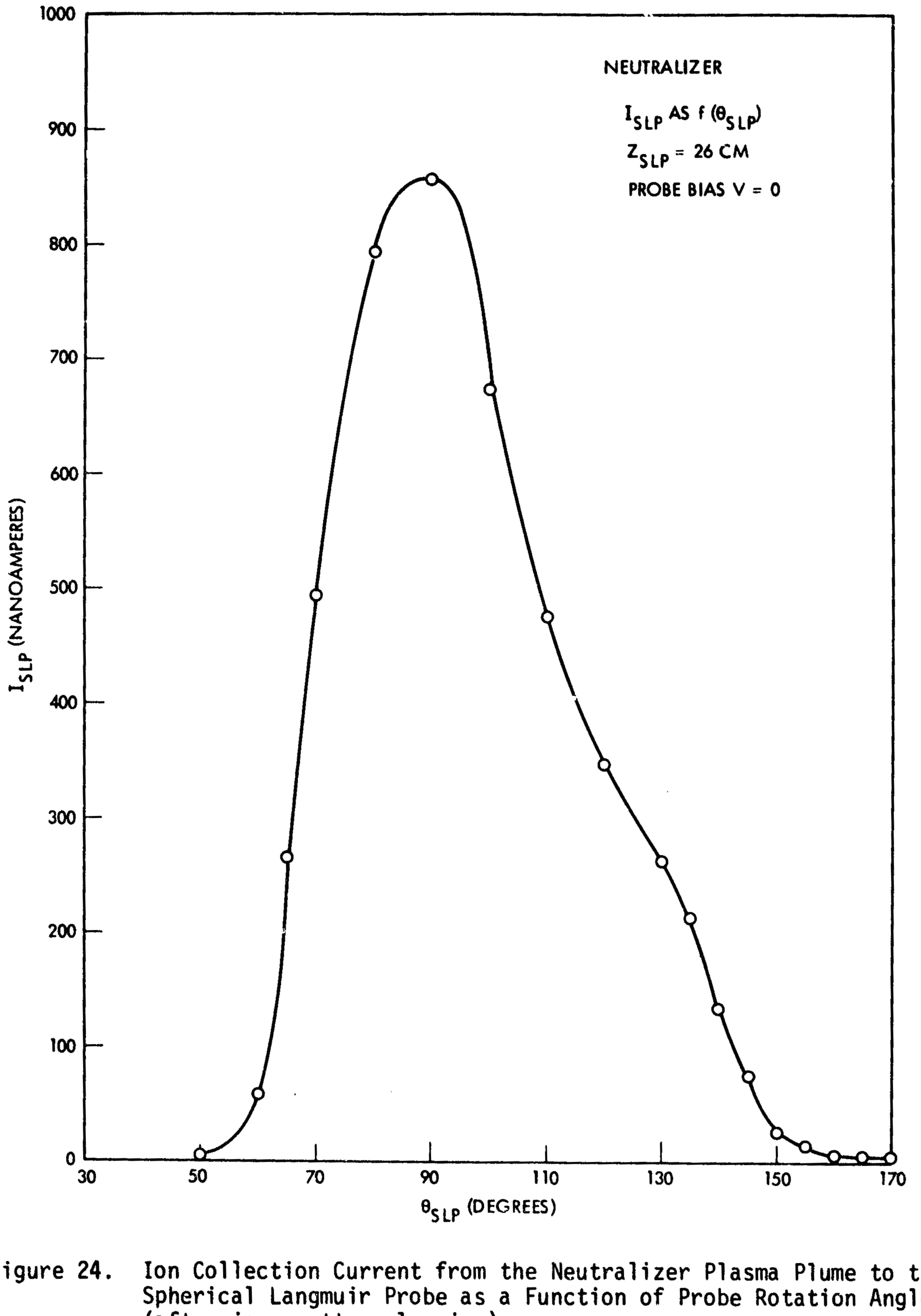

Figure 24. Ion Collection Current from the Neutralizer Plasma Plume to the Spherical Langmuir Probe as a Function of Probe Rotation Angle (after ion sputter cleaning)

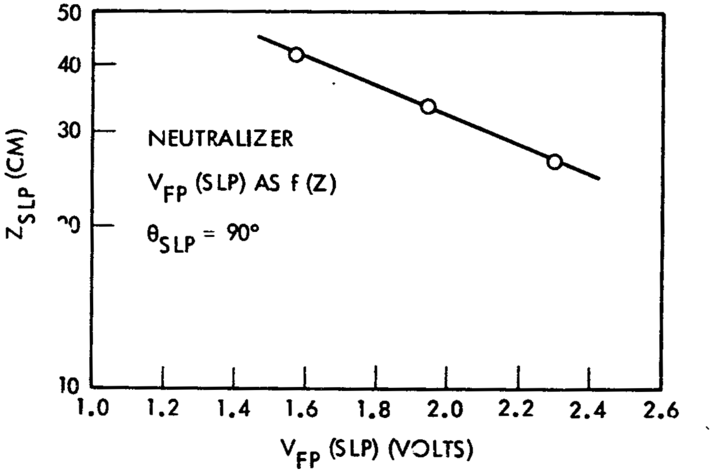

Figure 25. Floating Potential of the Spherical Langmuir Probe in the Neutralizer Plasma Plume, as a Function of Probe Axial Position

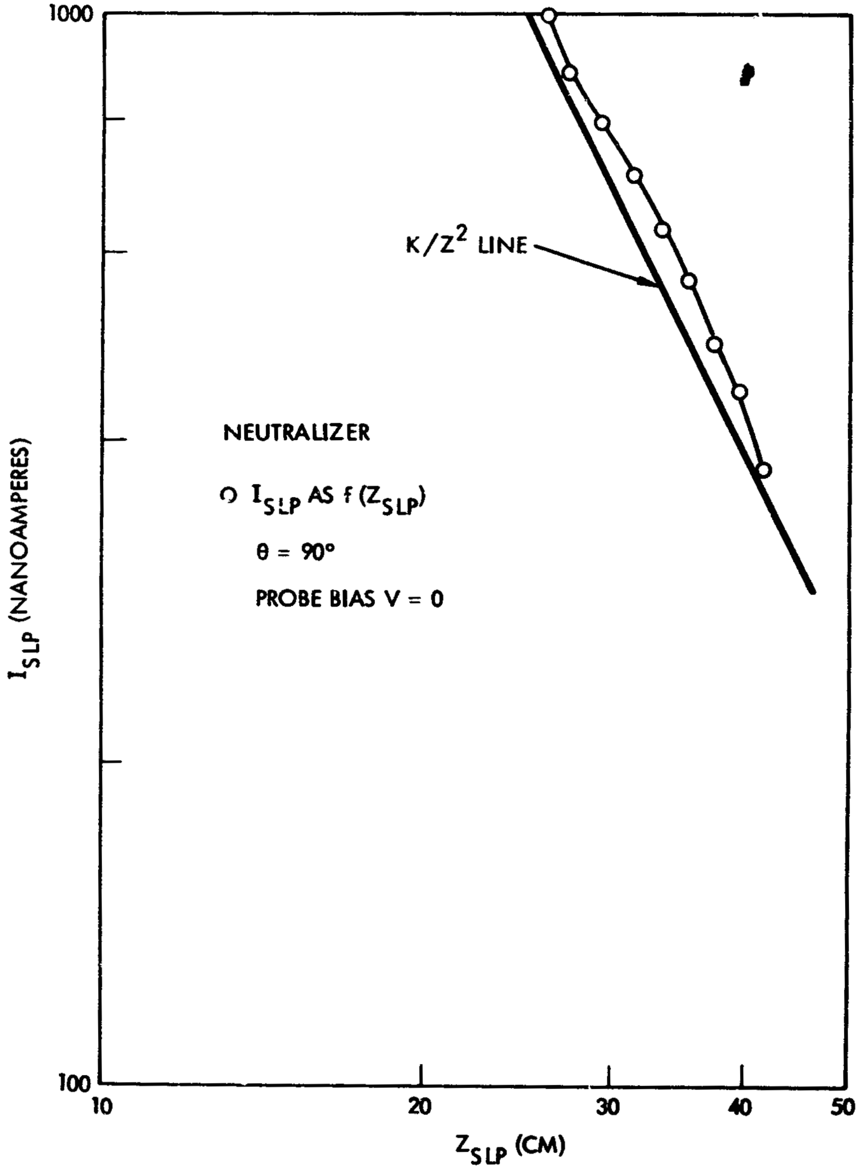

Figure 26. Ion Collection Current from the Neutralizer Plasma Plume to the Spherical Langmuir Probe as a Function of Probe Axial Position

an electron-volt, of order 0.5 eV. Definitive T_e measurements were not obtained, however.

3.1.5 Probe Surface Film Effects

The probe surface film effects discussed in Section 3.1.4 above do not rule out ion current collection limb measurements, although the current magnitudes observed at low negative bias potentials can be reduced because of resistive potential drops across the films. The presence of films is also suspected to be the cause of the positive curvature effect in ion collection in the data of Figure 13. A comparatively simple computation of expected probe ion collection, illustrated in Figure 19, displays a slight "knee" and the appropriate negative curvature in ion signal in the regions near the knee.

Because of the various evidence of film build-up, ion sputter cleaning of the probe was carried out by imposing a large (~400 volt) negative bias on the probe with respect to the discharge neutralizer plasma plume. Figure 20, Run II, illustrates the ion collection characteristic after this probe cleaning procedure. The "knee" is now visibly present and the collection characteristic in and near the knee is now of the expected shape. The magnitude of the ion signal at probe bias voltages in the general range of zero volts is now significantly larger than for the same bias condition in the earlier (non-cleaned probe) measurements. However, the level of ion signal at the knee is only 400 nanoamperes and even if the flow is laminar, J_+ is only of the order of 40 nanoamperes/cm^2 for the usual method of interpretation of Langmuir probe characteristics on ion "saturation current."

After Run II of the data shown in Figure 20, the data in Runs III and IV of Figure 21 were obtained in regions near the umbra for the sputter shield and for the east edge. The (now) cleaned probe exhibits the marked drop-off in ion signal between these angular settings and θ_{SLP} = 90 deg just as was previously observed with the noncleaned probe. This appears to confirm the statement made at the conclusion of Section 3.1.3.1 that both cleaned and noncleaned probes exhibit the same general behavior in ion plume expansion.

Following Run IV in the data of Figure 21, the probe was cleaned again and the data of Run V in Figure 21 was obtained. The "knee" of the curve is now less sharply defined and the knee position has now shifted as the possible result of even further surface film cleaning. The general agreement between the two probe characteristics is, however, good and the use of the knee as the ion saturation current would lead to almost exactly the same ion collection result for Runs II and V.

As a final exercise in possible surface film effects the probe was cleaned again before obtaining the collection characteristic in Figure 22 and once again before obtaining the collection characteristic in Figure 23. The level of ion signal at the knee remains fairly well fixed, although extracted current for more negative biases appears to be rising as the result of each successive cleaning operation. These latter changes are not, however, considered to be significant.

A final figure in this section, Figure 24, illustrates the SLP ion extraction current as a function of probe rotation angle for the (now) sputter cleaned probe. The data given in Figure 24 may be compared to the data in Figure 14 which was obtained prior to the ion sputter cleaning of the probe. As may be seen, the post-sputter cleaned probe in Figure 24 exhibits a higher level of ion collection than in Figure 14, for a comparable probe bias setting. The conclusions on ion refraction in the plasma plume expansion over the material boundaries remain unchanged. The growth in collected signal is partially due to the sputter cleaning and (it is believed) is partially due to the higher levels of neutral mercury injection (~15 mA, for example) for the (degraded condition) neutralizer in the later experiments. Neutral mercury injection with the neutralizer for the earlier probe measurements was ~7 milliamperes (equivalent).

3.1.6 Neutralizer Plume Expansion Measurements

A final experiment on the neutralizer discharge plasma plume with the SLP is an examination of the variation in probe floating potential for increasing axial separation, Z, and a measurement along this same path of the ion current collected by the probe. The results of these measurements are given in Figures 25 and 26. For increasing Z, floating potential continues to diminish and the sign of the electric field in the plasma is such as to continue to accelerate the outwardly moving ions. THe ion current density appears to be falling off as the inverse square of the distance from the neutralizer, thus undergoing an essentially "spherical" expansion. The pattern of behavior suggested here and by the previous data is that of a plasma in which the electric field is radially outward and is created by the plasma density gradients and by the finite electron temperature. Ions in such a potential configuration would acquire kinetic energy in the expansion, and, depending upon the scattering lengths for ion motion and possible ion energy loss mechanisms, could acquire kinetic energies much larger than kT_e, in that potential increments much larger than kT_e are present in the expansion plume of the plasma. If the ions acquire kinetic energy large compared to kT_e, their refraction by electric fields generated by plume expansion over more distantly removed material boundaries would be comparatively minor. To this point in the experimental series on neutralizer plume behavior the above description appears to match the apparent degree to which comparatively sharp shadows are cast by the biasable cylinder and by the sputter shield. Actual determinations of ion energy in the expansion plume cannot, however, be carried out with the Langmuir probe and will require the use of Faraday cup/Retarding Potential analyzers. These Faraday cup/RPA measurements will be described in the section which follows.

3.2 Faraday Cup/Retarding Potential Analyzer Measurements

3.2.1 Experiment Geometrical Considerations

The Faraday Cup/Retarding Potential Analyzer in use for this group of measurements is the 1-1/2-inch J_+ probe. This probe is illustrated in Figures 2 and 4 and details in the construction of the probe are given in Figure 4. The path of the probe for a rotational sweep through the plasma plume is illustrated in Figure 6. However, because geometrical considerations are of such importance in the probe response to plasma currents for the probe entry into umbra regions created by material boundaries, two additional figures have been prepared. Figure 27 illustrates the probe position relative to the thruster and the biasable cylinder in a view along

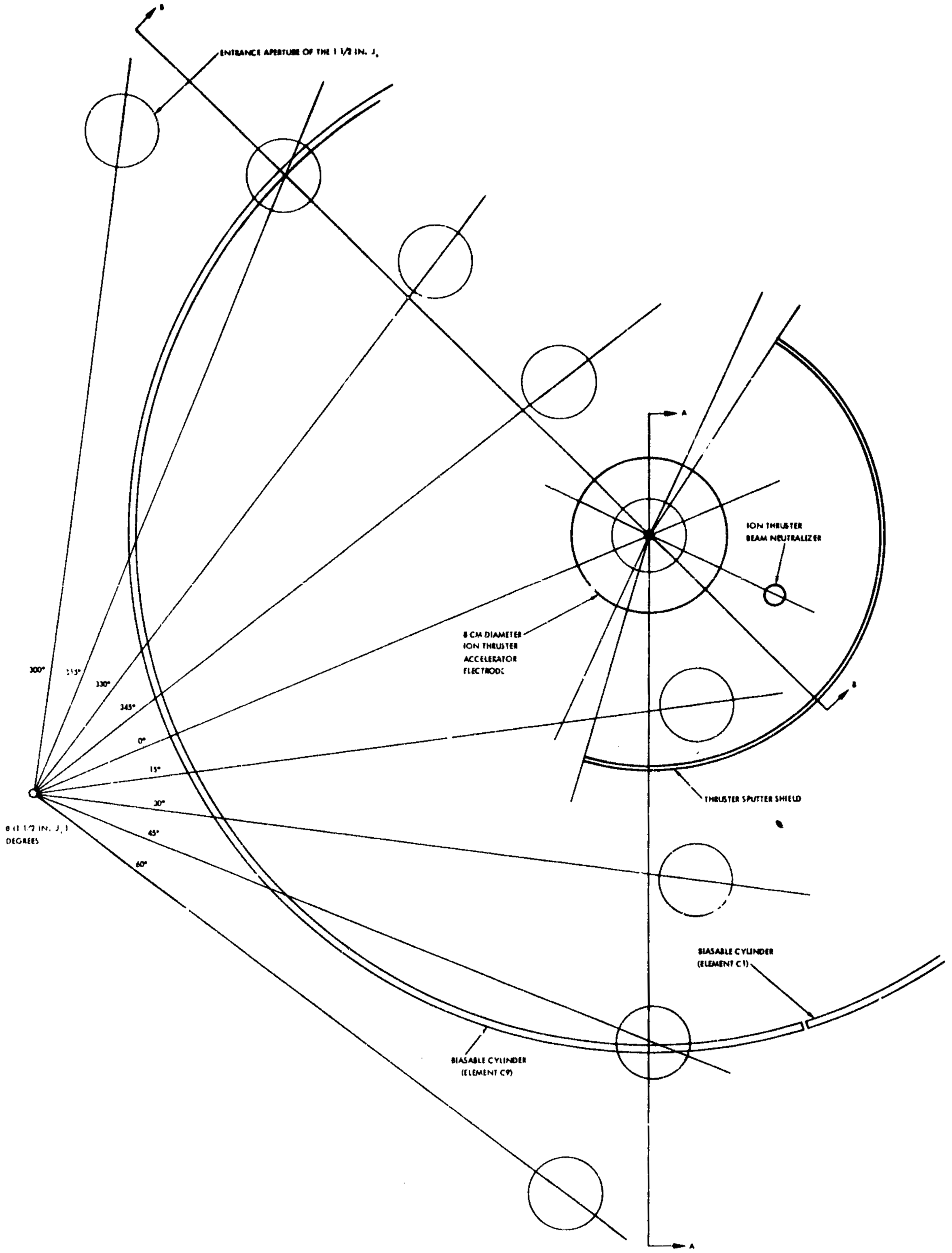

Figure 27. View Along Thruster Axis of Thruster, Biasable Surface, and 1-1/2-Inch J_+ Probe, at Various Rotation Angle Positions

the -Z axis. The entrance aperture of the 1-1/2-inch J_+ is shown there as a function of rotation angle, $\theta_{1\text{-}1/2\text{-inch } J+}$, around the probe mounting rod. The convention in the description of $\theta_{1\text{-}1/2\text{-inch } J+}$ is that $\theta_{1\text{-}1/2\text{-inch } J+}$ = 0 deg for the entrance aperture on the thruster axis. For $\theta_{1\text{-}1/2\text{-inch } J+}$ ~45 deg, the entrance aperture passes over the west edge of the biasable cylinder and for $\theta_{1\text{-}1/2\text{-inch } J+}$ ~315 deg, the entrance aperture passes over the northeast edge of the biasable cylinder.

Two cross sectional planes, AA and BB, are indicated in Figure 27. In the cross sectional plane BB the plasma plume from the neutralizer can expand in the direction of the northeast edge of the biasable cylinder without any shielding effect by the thruster sputter shield. This situation is somewhat more complicated in the cross sectional plane AA. Because of angle of cut in the thruster sputter shield the umbra of the sputter shield is generally reduced in its shielding effectiveness for probe movement toward the west edge of the biasable surface. Another complicating factor here is the off-axis location of the thruster neutralizer for measurements of the neutralizer plasma plume. The nearest passage of the 1-1/2-inch J_+ to the thruster neutralizer occurs for $\theta_{1\text{-}1/2\text{-inch } J+}$ ~8 deg. To assist in the general visualization of the shadow region created by the beam shield, the dashed lines in Figure 27 illustrate the intersection of the umbra for a point source at the midpoint of the ion thruster beam neutralizer with specific planes perpendicular to the Z axis of the thruster system.

Figure 28 illustrates a cross section of the 1-1/2-inch J_+ together with the position of the lines of sight from $r = z = 0$ to the biasable cylinder west edge. For the probe entrance aperture in the plane $z = 23.7$ centimeters and for a probe rotational angle of 50 degrees those portions of the entrance aperture which connect to the collector via straight line trajectories and at the appropriate angle are fully illuminated. For a movement of the probe rotation angle to ~51.3 degrees, the initiation of a "sunset" in the illuminated portions of the collector is encountered. This sunset is completed for a probe rotation angle of ~55 degrees.

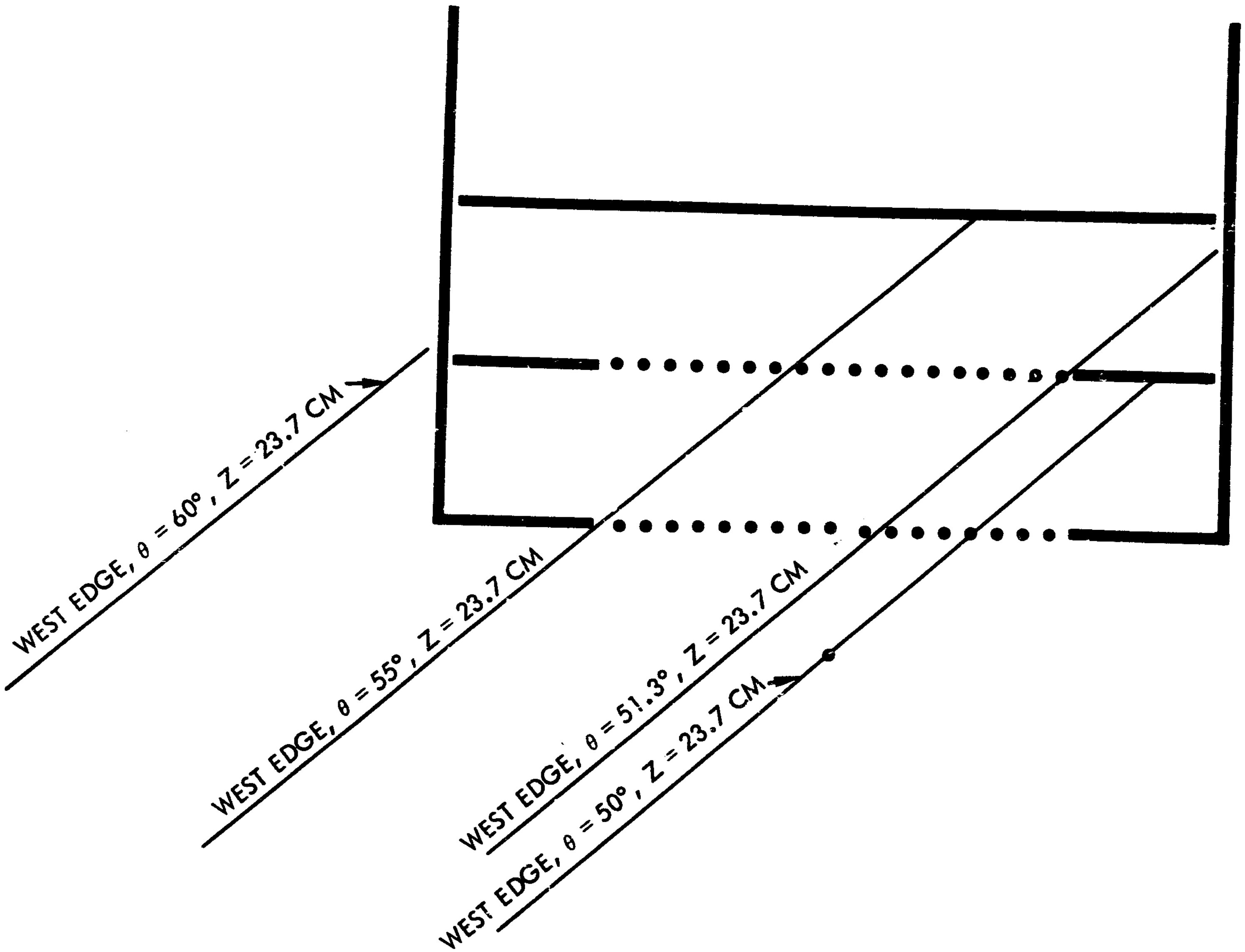

Figure 28. Expanded View of 1-1/2-Inch J_+ Probe Apertures, Grid Positions, and Collector Position, with Lines-of-Sight from $r = Z = 0$ to Biasable Surface West Edge for Various Probe Rotation Positions

The considerations above on collector illumination are based upon straight line trajectores initiated from $r = z = 0$ and making contact with the west edge of the biasable cylinder. Several factors act to complicate these geometrical considerations. The first of these factors is the off-axis location of the thruster neutralizer. A second factor is the shadowing created in the west edge direction by the sputter shield. A third, and important, complicating factor is the departure of ion trajectories from straight lines because of electric field refraction of these weakly energetic particles. As Section 3.1.3.3 has described, it is possible to cause ion refraction, to some extent, by alteration of the potential difference between the biasable cylinder and the plasma plume. Ion trajectory refraction can also occur because of electric fields between the plasma plume and the exterior surfaces of the measuring probe. It is possible, thus, for ions to appear at the collector of the 1-1/2-inch J_+ when such appearance would be dynamically forbidden on a basis of line-of-sight ion motion. If, however, it can be demonstrated that ion currents to the probe collector are markedly reduced as the probe moves into umbra regions, then it will have been demonstrated that refraction of the ions, while still present to some degree, is not of significant concern provided that sensitive surface placement in the umbra regions requires (even low level) multiple refractions for the ion to deposit on the sensitive surface.

3.2.2 Floating Potential Measurements

Before proceeding to the Faraday cup/RPA determinations of ion flux densities and ion energy spectra in the neutralizer plume, an examination will be made of the floating potential in the plasma plume. These measurements have been previously carried out using the spherical Langmuir probe (see Section 3.1.2), and the present measurements with the 1-1/2-inch J_+ can act to corroborate the previous findings as well as to explore possible new plume behavior along the specific motional path of this second probe. To carry out the floating potential measurements, all elements (exterior case, middle grid, and collector) are connected together and the entirety is then electrically isolated.

Figure 29 illustrates the floating potential of these probe elements as a function of probe rotation angle. The results shown there appear to agree qualitatively with the results given earlier in Figure 12. The

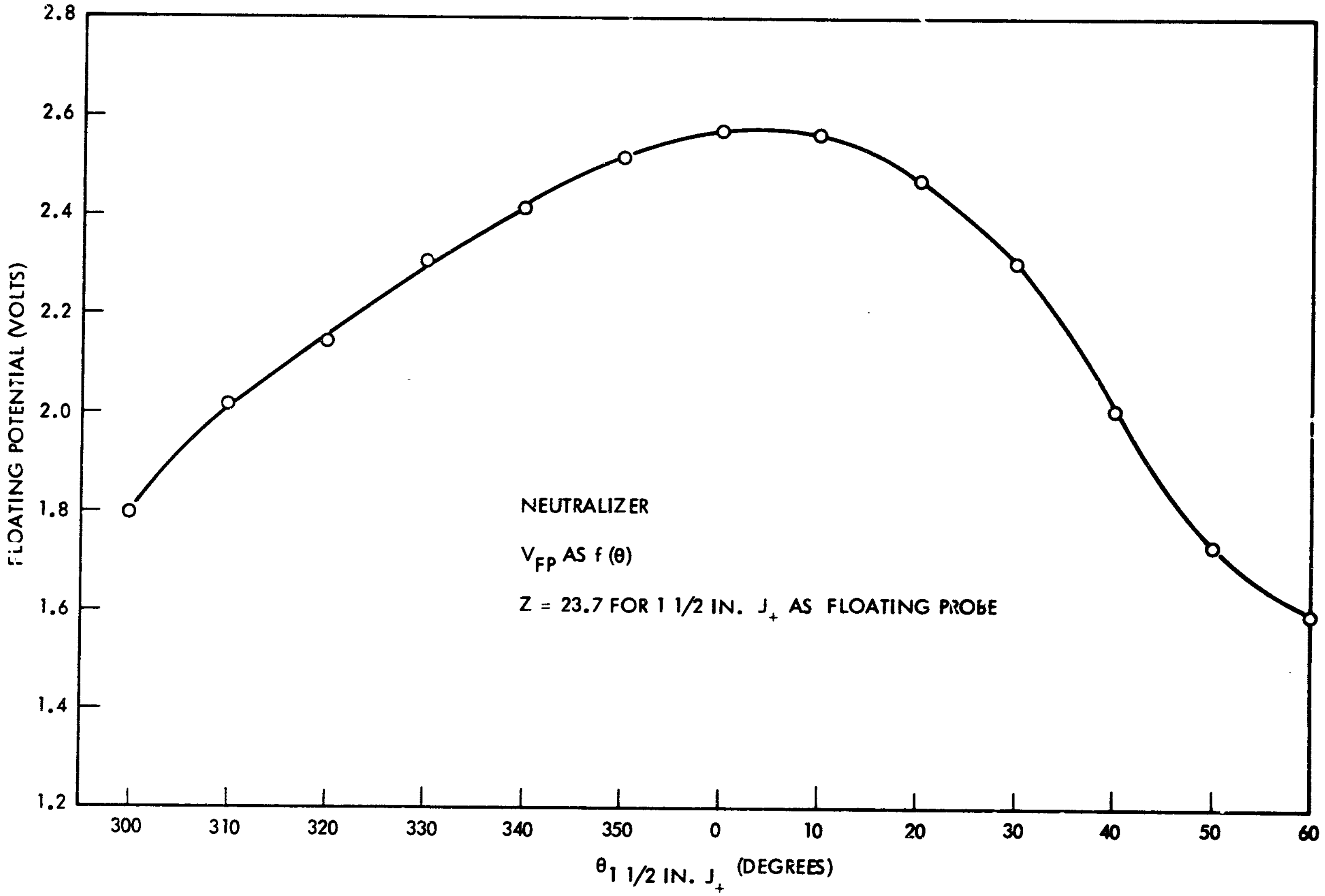

Figure 29. Floating Potential of the 1-1/2-Inch J+ Probe (used as a floating probe) in the Neutralizer Plasma Plume, as a Function of Probe Rotation Angle

floating potential reaches a maximum in the region from 0 to 10 degrees which corresponds to the point of nearest passage to the neutralizer location and which indicates maximum plasma density along the probe path of motion in this specific Z-plane. The drop-off in floating potential is more rapid in the range 20 deg $\leq \theta_{1\text{-}1/2\text{-inch } J_+} \leq$ 40 deg than for the range 320 deg $\leq \theta_{1\text{-}1/2\text{-inch } J_+} \leq$ 340 deg, indicating some action by the sputter shield in the reduction of plume density along this portion of the probe motional path in the west edge passage when compared to the northeast edge passage.

The data in the floating potential and the relationship of floating potential indicates that plasma potentials in the plume at this Z-plane probably range from ~6 volts, on the thruster axis, to ~4 volts near the biasable cylinder. In the measurements to be conducted with the probe as a Faraday cup/RPA, the entrance aperture will be set at V = 0 volts. This clearly establishes an electric field between the plasma plume and the entrance grid plane and such electric fields can cause trajectory bending of the ions into the Faraday cup. It is necessary, however, to exclude electron entry into the cup during both the Faraday cup and RPA measurements and the setting of the bias voltage on the cup exterior at V = 0 appears as the best configuration to exclude electrons and to minimize ion refraction. For the remaining measurements in Section 3.2, the biasable cylinder elements will be electrically isolated from ground and will assume their floating potentials. There will be, thus, a weak electric field structure between the biasable cylinder and the plasma plume and between the Faraday cup exterior and the plasma plume, It will be demonstrated that, despite the presence of such a weak electric field structure, the multiple refraction of weakly energetic ions with the Faraday cup will be at extremely low signal levels.

3.2.3 Ion Energy Spectrum Measurements

The principal factor in the degree to which ions in the neutralizer plume will be refracted is the relation of the kinetic energy of these ions relative to the electric fields which may exist in the plasma and between the plasma and various material boundaries. From the measured potentials in the plasma and the known potentials on the keeper electrode, it appears possible that ions could acquire kinetic energies considerably in excess of kT_e because of extremely large density drop-offs (estimated to be of the order of 10^{10}) between the neutralizer orifice and these comparatively dilute downstream plasma locations.

To determine the ion energy spectrum, the Faraday cup/RPA was placed at $\theta_{1\text{-}1/2\text{-inch } J_+} = 10$ deg (the point of nearest passage to the neutralizer) in the plane at $z = 23.7$ cm. Figure 30 illustrates the RPA characteristic obtained at this location and the energy spectrum of ions as that ion flow appears at the entrance plane (at $V = 0$ volts) of the analyzer. In the data given in Figure 30, most of the ions appear to have kinetic energies in the range from 12 to 18 eV with small spectrum content at higher and at lower energies. It is believed that some of the broadening of the ion energy spectrum is instrumental (including plasma density effects) and that the actual energy spectrum is even more narrowly defined than the result given in Figure 30.

The findings in Figure 30 are of considerable importance in explaining the comparatively sharp shadows cast by material boundaries in the plasma plume. The evidence given in Figure 30 indicates the great majority of the ions are created in a plasma region which is approximately at the neutralizer keeper potential. As the neutralizer plasma plume expands from this point in an ambipolar diffusion, the density gradients and the finite T_e combine to produce an electric field which continues to accelerate the ions. From the data in Figure 30 there is no evidence that ions undergo collisions or lose energy to any significant degree to such collisions. The ions in the plume, thus, acquire a kinetic energy which is approximately given by the difference in plasma potential between the ion generation region (plasma potential $\sim V_{NK}$) and the plasma potential at the specific point of interest in the plume. If the plume undergoes a considerable expansion between its creation region and the point at which the plume encounters a material boundary, then ions acquire kinetic energies in the region of that boundary which can be many times greater than kT_e/e. If the boundary is electrically floating, then a potential difference of several kT_e/e can exist between the boundary and the plasma. The electric fields can be described as

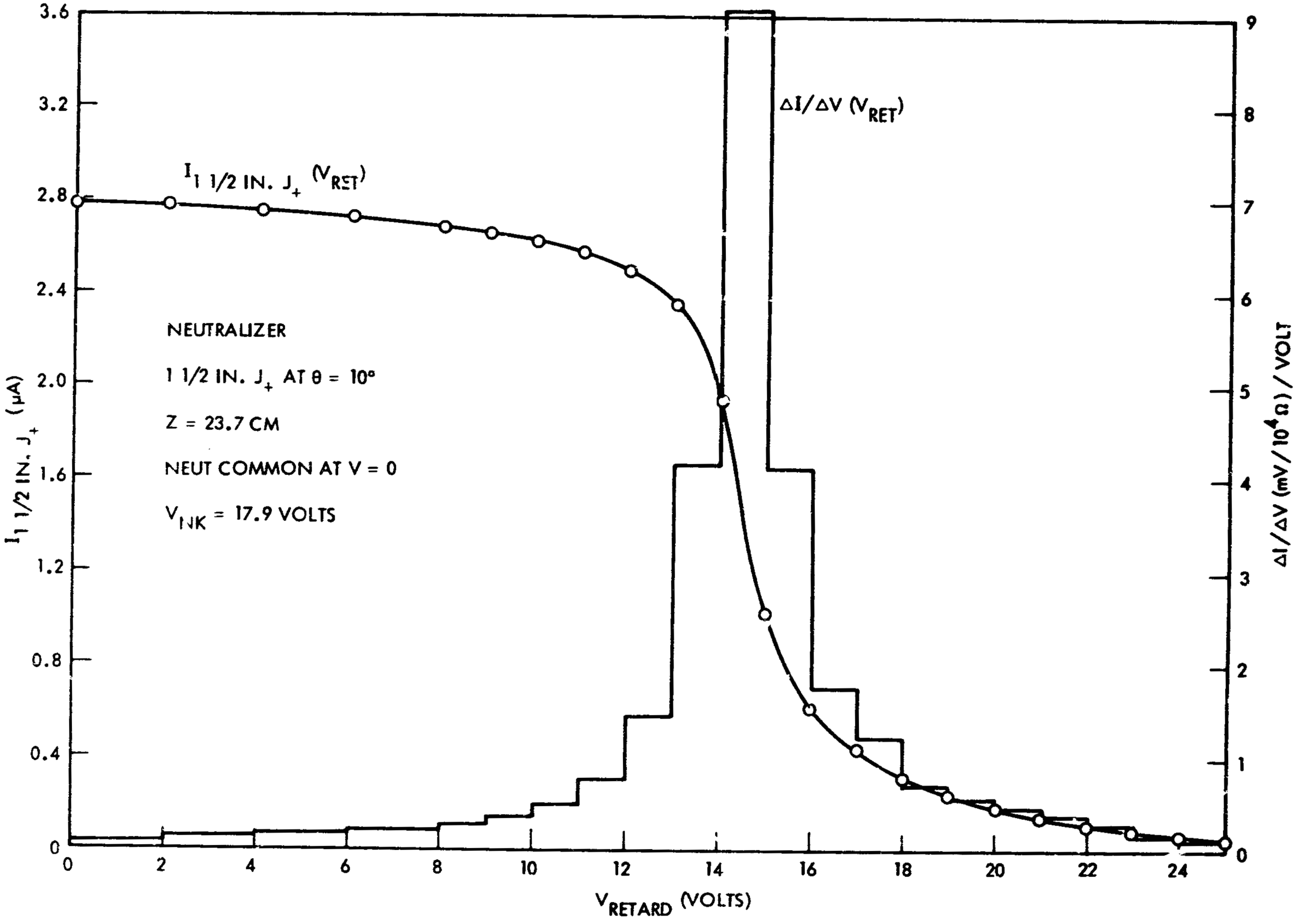

Figure 30. Ion Collector Current of the 1-1/2-Inch J+ Probe in the Neutralizer Plasma Plume as a Function of Retarding Potential on the Middle Grid, and Resultant Ion Energy Spectrum

$$\vec{E} \sim \frac{\xi \, kT_e}{e\lambda} \qquad (1)$$

where $\xi kT_e/_e$ is the potential difference between the boundary and the plasma and λ is the sheath thickness between the boundary and the plasma and the minimum radius of curvature of an ion moving in such an electric field will be

$$r \sim 2\lambda \, \frac{\gamma}{\xi} \qquad (2)$$

where γ is the ion energy at this point in the plasma in units of $kT_e/_e$. For the minimum bending radius given in Equation (2), the maximum value of the total ion refraction angle, $\theta_{r,max}$ can be estimated at

$$\theta_{r,max} \sim \frac{\xi}{2\gamma} \qquad (3)$$

using the notion that ion trajectory motion in the sheath region has a total path length of approximately the same distance as the sheath thickness. For values of $\xi \sim 5$ and $\gamma \sim 20$, $\theta_{r,max}$ is of the order of 0.1 radians. For this particular case and configuration, then, it should be expected that the material boundary will cast a comparatively sharp shadow in the plasma plume.

The derivation above has not considered the continued, long term, refraction of an ion which can occur, in principle, for that ion trajectory which happens to lie in the edge of the plasma plume expansion "fan" over a material boundary. It should be noted, however, that the electric fields in the edge of the expansion are generated by plasma density gradients. For an ion thruster in space, the plasma plume density falls, ultimately, to the density of the ambient space plasma and density gradient electric fields become vanishly small. For a spacecraft in a near-earth orbit, these ambient space plasma densities can range from 10^4 to 10^6 ions/cm^3 and an important factor then becomes the plasma plume density relative to these densities of 10^4 to 10^6 ions/cm^3.

One method of determining neutralizer plume plasma density is to use the measured current density in the Faraday cup and an average ion velocity for the ion flow.

Using the data of Figure 30 it can be estimated that the neutralizer plasma plume at this near on-axis location and Z-plane is

$$\rho_{+,\mathrm{plume}} \sim 6 \times 10^{6} \ \mathrm{ions/cm^{3}} \qquad (4)$$

Because of the relatively high neutral mass flow (~15 mA, e.g.) into the neutralizer for this (now degraded operation) neutralizer, an estimate of $\rho_{+,\mathrm{plume}}$ ($\theta = 0^{0}$, $z = 24$ cm) for a completely nominal neutralizer will be

$$\rho_{+,\mathrm{plume}} \ (\theta_{1\text{-}1/2\, J_{+}} = 10^{0}, \ z = 24 \ \mathrm{cm}) \sim 2 \times 10^{6} \ \mathrm{ions/cm^{3}} \qquad (4')$$

For probe positions near the biasable cylinder location (and for the centerline condition discussed in Equation (4) above) the plume density has dropped off still further to

$$\rho_{+,\mathrm{plume}} \ (\text{biasable cylinder edge}) \sim 10^{5} - 10^{6} \ \mathrm{ions/cm^{3}} \qquad (5)$$

The continued expansion of this plume must only proceed by levels of ~10^{4} ions/cm^{3} to drop to levels generally characteristic of the ambient space plasma for near-earth orbital conditions. There are, thus, strong reasons to expect that density gradient generated electric field regions will not continue to occur for substantially prolonged portions of the ion trajectories as they move beyond separation distances of ~1 meter and that the "continued" electric field refraction of ion trajectories will not significantly alter the earlier conclusions of comparatively sharply cast shadows by material boundaries in the plasma plume.

3.2.4 Ion Flux Density Distributions

The remaining measurements of interest with the 1-1/2-inch Faraday cup/RPA are the ion flux density distributions as a function of probe rotation angle for a fixed z-location of the probe. Figures 31 and 32 illustrate two such density distribution measurements, until the inclusion of the second figure for purposes of demonstrating run-to-run reproducibility in these measurements.

The peak current densities are, as expected, at $\theta_{1\text{-}1/2\text{-inch}\ J_+} \sim 10$ deg, which corresponds to the probe point of nearest passage to the neutralizer position. At this point and for the neutral vapor flow present in the (degraded operation) neutralizer, the ion current density reaches a level of ~ 4×10^{-7} A/cm^2. For the reduced mass flow for a nominal neutralizer, this peak current density would be reduced to ~ 2×10^{-7} A/cm^2. As the probe moves to rotation angles greater than 50 degrees and less than 310 degrees, the ion current density, for ions reaching the collector, falls to values less than 10^{-10} A/cm^2. For these calculations, the probe entrance area has been set at 6.12 cm^2, irrespective of probe position.

Figure 28 illustrated some of the ion trajectory considerations for probe placement near the biasable cylinder edge. The results in Figures 31 and 32 demonstrate conclusively that the plural refraction of ions, over the biasable cylinder edge and into the Faraday cup, produces an extremely low level of net ion transport for the refraction conditions required in these probe/cylinder/neutralizer configurations. Such low level transport is not the particular result of attempts to minimize electric fields between the material boundaries and the plasma. In this present experiment the biasable cylinder is at its floating potential and the probe entrance aperture is at V = 0. There are, thus, electric fields which can cause ion bending over the cylinder edge and into the cup, for the higher angle ($\theta \geq 50$ deg) cup placements. In spite of such electric fields, the plural refraction ion transport is at very low levels, and the previous experience (see Section 3.1.3.3 and Figures 17 and 18) on reduction of trajectory refraction by tailoring the boundary potentials to the potential of the local plasma indicates that still further reductions in ion transport can be achieved.

The data given above indicates that protection of sensitive surfaces can be carried out to very low deposition levels by suitable tailoring of boundaries and by the requirement that the ion trajectories must engage in

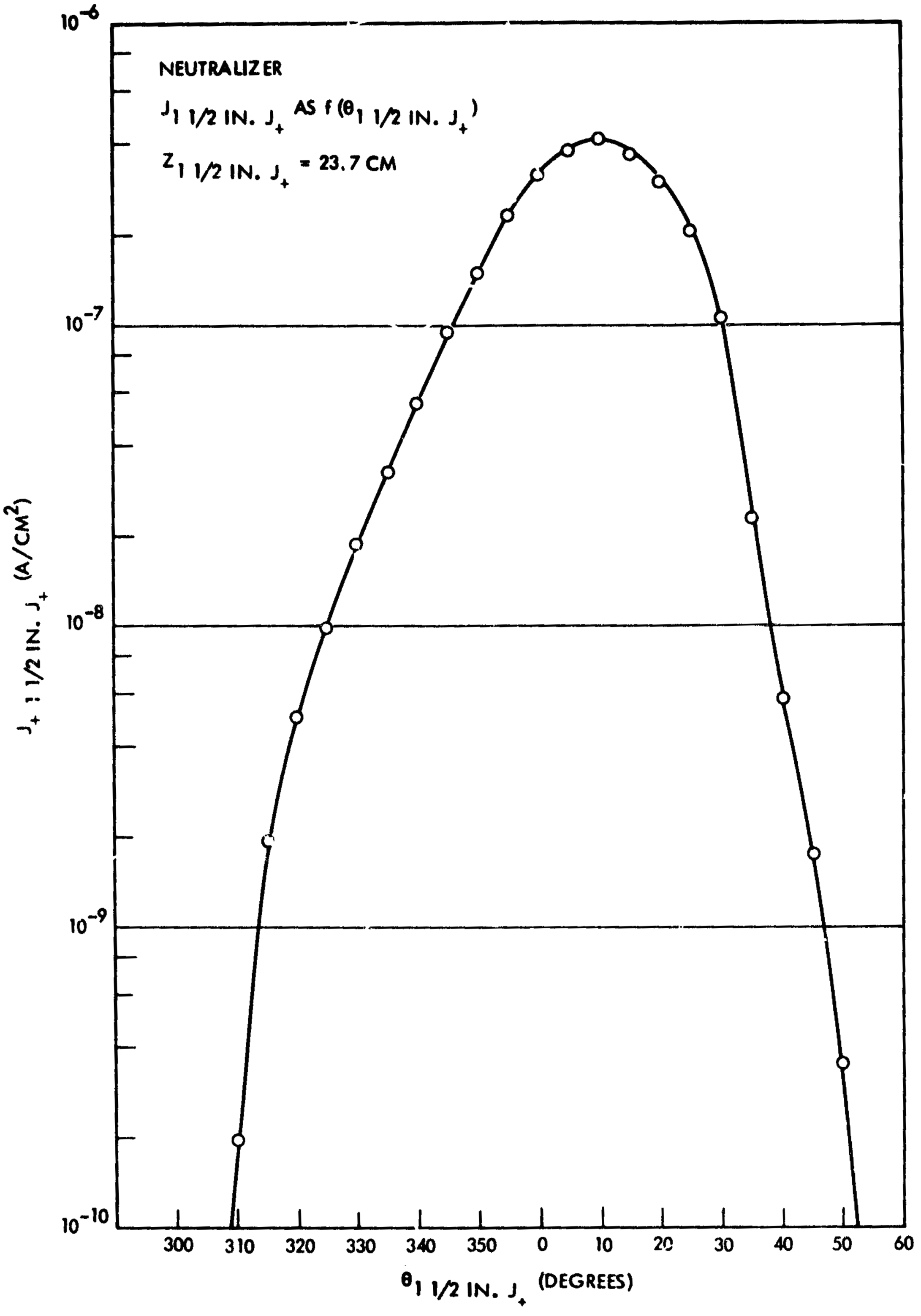

Figure 31. Ion Current Density in the 1-1/2-Inch J_+ Probe in the Neutralizer Plasma Plume, as a Function of Probe Rotation Angle

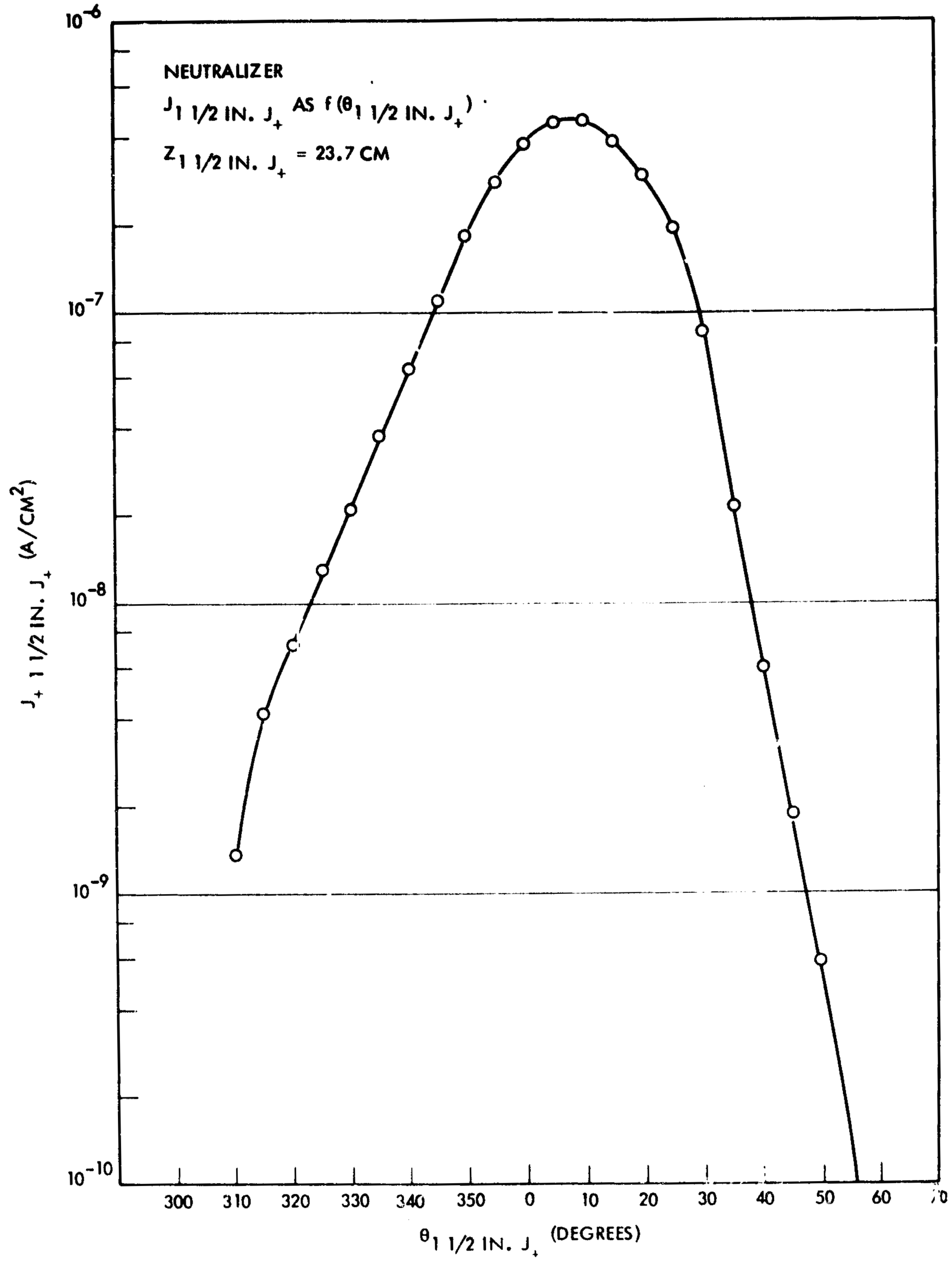

Figure 32. Ion Current Density in the 1-1/2-Inch J+ Probe in the Neutralizer Plasma Plume, as a Function of Probe Rotation Angle (second figure to illustrate run-to-run reproducibility)

plural refractions of some angular extent, in order to intercept the sensitive surface. Such tailoring of the geometrical and electrical properties of the boundary may not always be possible if the placement of the sensitive surface requires that it have a direct, line-of-sight, viewing angle to the thruster. If, however, the sensitive surface can be located in a total spacecraft/thruster/payload configuration which requires either single ion refraction at a high angle or plural ion refractions at somewhat lower angles, then, ion deposition rates can be reduced to extremely low levels. In the present instance, for example, ion deposition rates in the 1-1/2 J_+ cup collector are at levels from 6 x 10^8 cm^2/sec to less than 10^8 cm^2/sec for cup placement in the angular range from 52 to ~60 degrees. The z and r separations here are of the order of 24 centimeters and 25 to 30 centimeters. In spite of the small z and r separation values, the tortuous nature of the ion path required has reduced deposition levels to values of approximately 1 monolayer in 10^6 to 10^7 seconds. This is in the range of 1 monolayer per thousand hours for a comparatively near r and z placement. Even lower values of deposition rate could be obtained by increasing the separation distances. Throughout the whole procedure, however, the important feature in deposition reduction on the surface is the requirement of large angle single ion refraction or lower level angle plural refractions.

4. CHARGED PARTICLE MEASUREMENTS IN THE PLASMA PLUME OF THE THRUSTER DISCHARGE AND THE DISCHARGE NEUTRALIZER

4.1 Spherical Langmuir Probe Measurements

The condition of an operating thruster discharge and an operating discharge neutralizer occurs during normal thruster start-up in the interval just prior to the application of ion accelerator voltages (to the screen electrode and the accelerator electrode) and the FULL BEAM ON condition. In the laboratory measurements of the plasma plume from these two sources, the screen voltage and accelerator voltages are set at zero volts (chamber wall potential) and the cathode common leads of the neutralizer and the thruster discharge are set as before, at V = 0. The voltages and currents for the thruster discharge and the neutralizer keeper are set at nominal levels for this 8-cm thruster.

The geometrical considerations (locations of umbra relative to probe positions) are essentially the same for this "combined" discharge operation condition as for the neutralizer discharge only condition. An examination of Figures 9, 10, and 11 will illustrate that some shifting of the umbra boundaries does result because of the more extended source size in the combined discharge operation case compared to neutralizer only, but the "sunset" regions for direct line-of-sight illumination of the probes are essentially the same in the two conditions.

Figure 33 illustrates the SLP ion current as a function of probe rotation angle for probe bias potentials of -2, -4, and -6 volts and for biasable cylinder elements at their floating potentials. These SLP measurements were obtained without probe surface cleaning and probe behavior here generally follows the behavior for the data given in Figures 13 through 18 (the pre-cleaning period in the neutralizer discharge measurements). Probe currents in the combined discharge plume reach maximum levels approximately five times the level obtained for similar probe position and electrical bias for the neutralizer discharge only case. The peak intensities for the combined discharge case are shifted somewhat from the location of the peak intensity in the neutralizer only case. The sharp cut-offs of probe signal are located in the same angular intervals for combined discharge operation as for the neutralizer discharge only case.

The refractibility of ions in this combined discharge plume can be examined, as before, by probe placement in either a sunset region or in the umbra with variations in both probe and cylinder bias. Figure 34 illustrates SLP signal (at $z = 26.0$ cm and $\theta_{SLP} = 150$ deg) as a function of probe bias from -2 to -10 volts and with the biasable surface set at -10 volts and at +6 volts. Refraction of ions into this umbra region by negative electric fields from the cylinder and from the probe is demonstrated. Figure 35 illustrates this refraction effect, again, but with SLP bias fixed and with a continuous variation of the cylinder bias potential. These refraction effects remain as qualitative feature here in view of the size of the SLP and its ability to measure ion arrival from any and all directions. Subsequent data will demonstrate, however, that the general levels of the energies of the ions in the combined discharge plume are

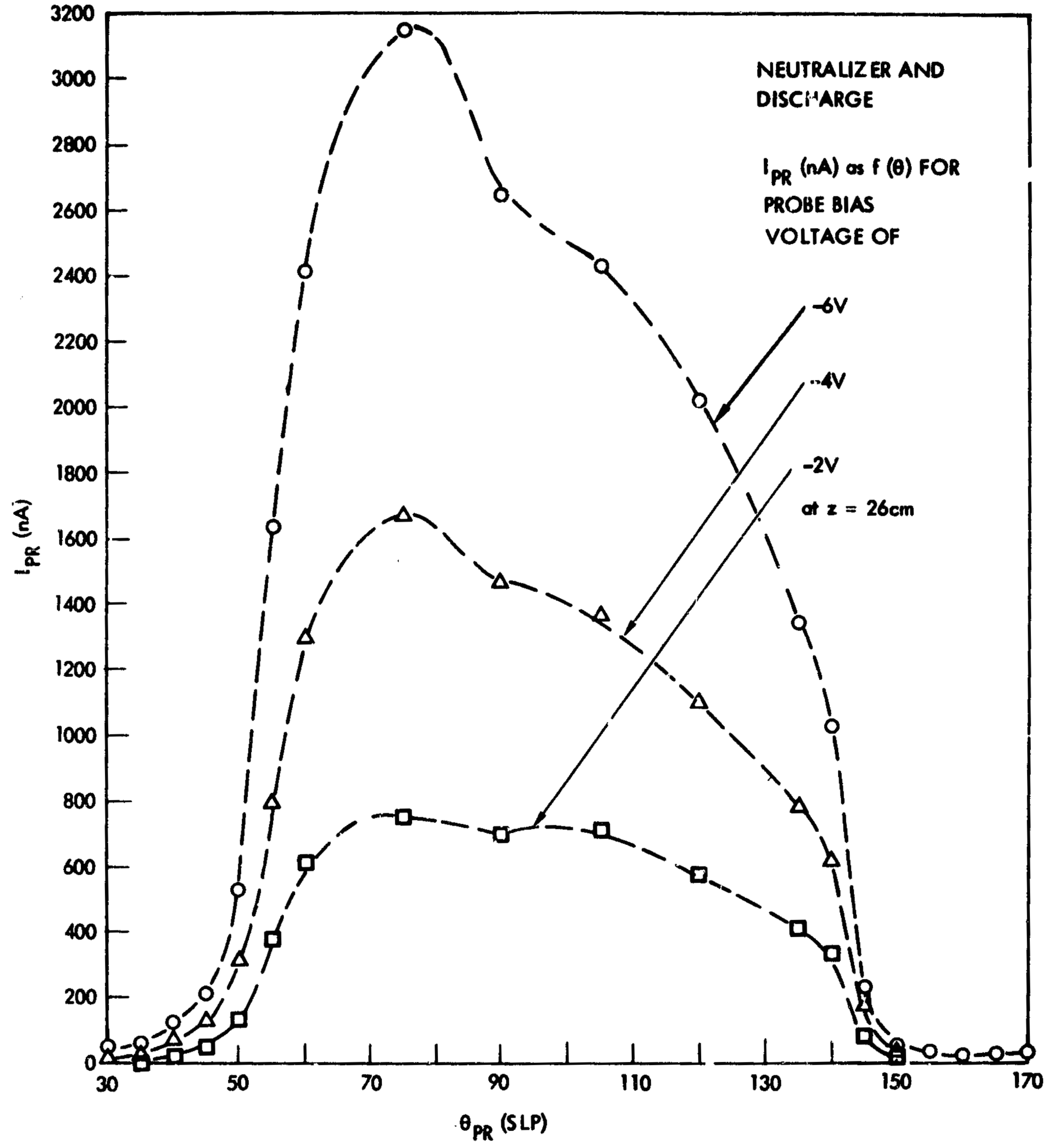

Figure 33. Ion Collection Current from the Combined Discharge Plasma Plume to the Spherical Langmuir Probe as a Function of Probe Bias Voltage and Probe Rotation Angle (biasable surface floating)

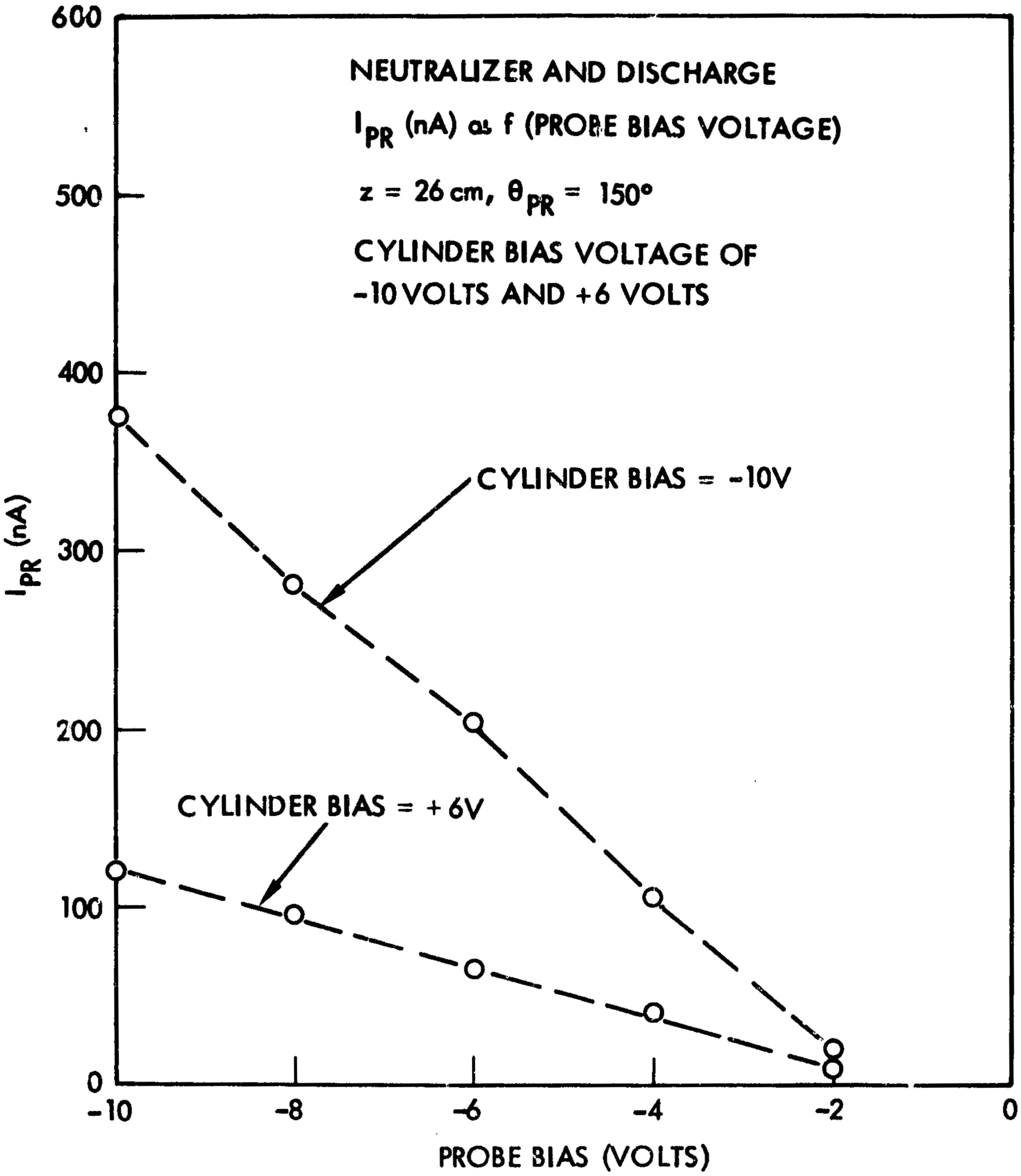

Figure 34. Ion Collection Current from the Combined Discharge Plasma Plume to the Spherical Langmuir Probe as a Function of Probe Bias Voltage and Biasable Surface at +6V and -10V

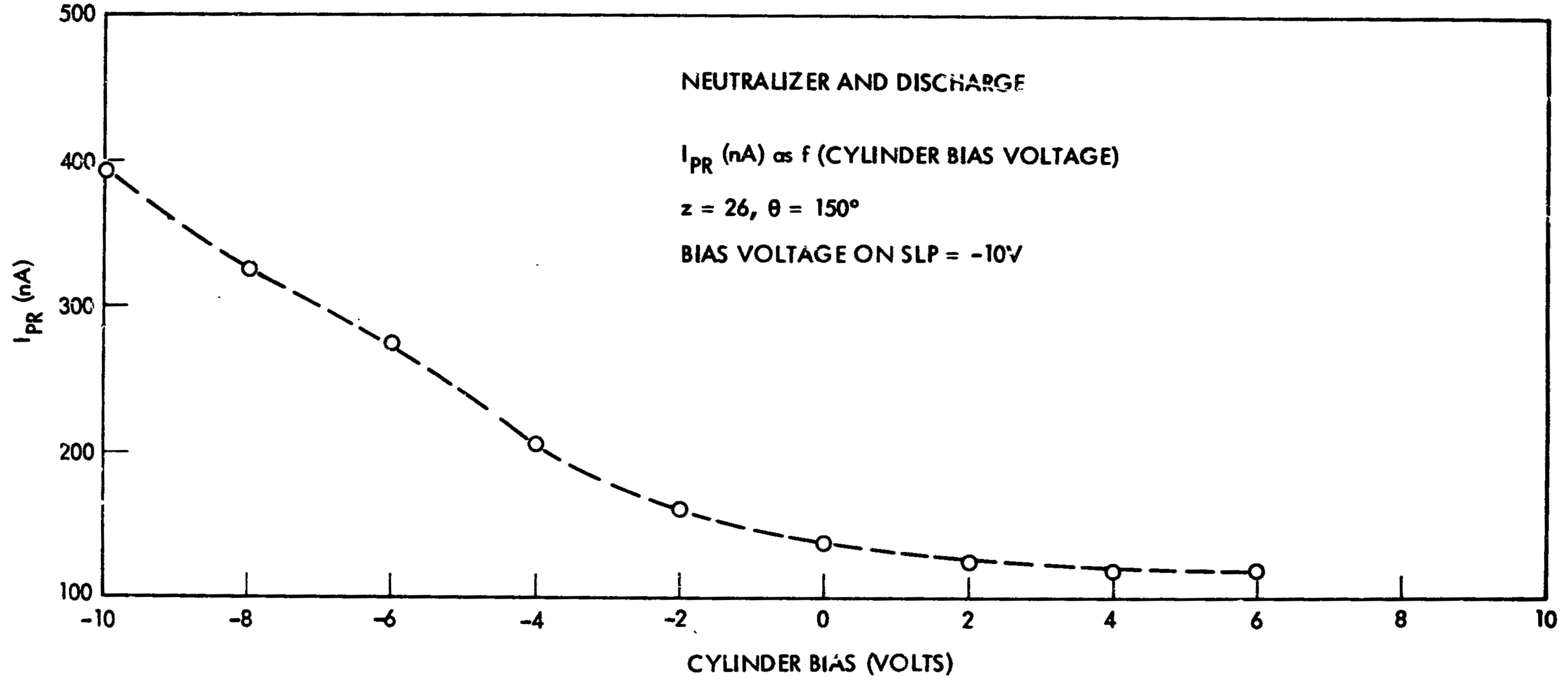

Figure 35. Ion Collection Current from the Combined Discharge Plasma Plume to the Spherical Langmuir Probe as a Function of Biasable Surface Potential

several times larger than those energies measured in the neutralizer discharge only case.

The flattening of the ion collection signal on the SLP in the range from +4 to +6 volts of biasable cylinder potential in Figure 35 indicates that plasma plume potential in the regions near the biasable cylinder are in this potential range. In the bulk of the remaining data to be given in this SLP section, the cylinder bias potential will be set at +6 volts, a minimized refraction condition. Figure 36 illustrates SLP ion collection signal as a function of probe angular position at z = 26 cm and for a probe bias of -4 volts. The current signal in Figure 36 is normalized to the probe signal at θ_{SLP} = 90 deg (on-axis to the thruster). The sunset regions for probe illumination by a line-of-sight source at r = z = 0 are also indicated in Figure 36. Strong signal cut-offs in those regions are evident, indicating that ion refraction, while present, is only through limited trajectory bending. Figure 37 presents an expanded version of probe signal as a function of angular position (now normalized to the value at θ_{SLP} = 135 deg, the onset of the sunset region) and also illustrates the probe illumination for line-of-sight ion flow from r = z = 0. Only a minor prolongation of the sunset is evident.

Figure 38 illustrates SLP ion signal as a function of axial position for fixed angular position. This permits another method of passage of the probe from its fully illuminated to its fully darkened state. Strong cut-off effects are evident, as in the Figure 37 data, and evidence of prolongation of the sunset by increased ion refraction over a boundary is again present for the data obtained with the biasable cylinder at V = 0 volts. Figure 39 provides an expanded presentation of probe signal, normalized to the value at z = 33 cm (fully illuminated), and the corresponding illumination factor.

In summary for this section, the behavior exhibited with the neutralizer discharge only plume is again present for the combined discharge condition. Ion flux levels have increased but ion refractibility remains at satisfyingly low levels.

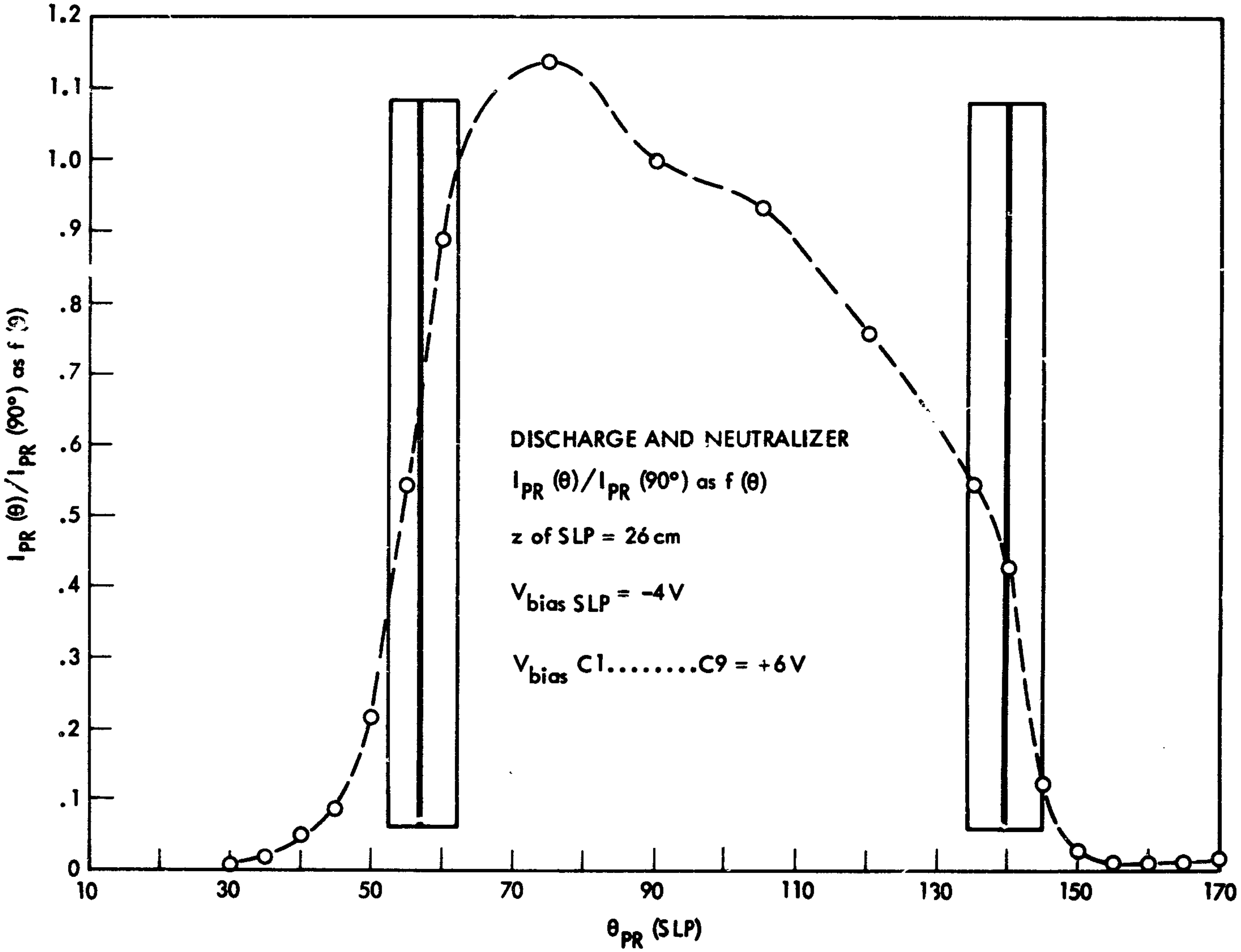

Figure 36. Ion Collection Current (Normalized to Value at 90 Degrees) from the Combined Discharge Plasma Plume to the Spherical Langmuir Probe as a Function of Probe Rotation Angle (boxes indicate "sunset" regions)

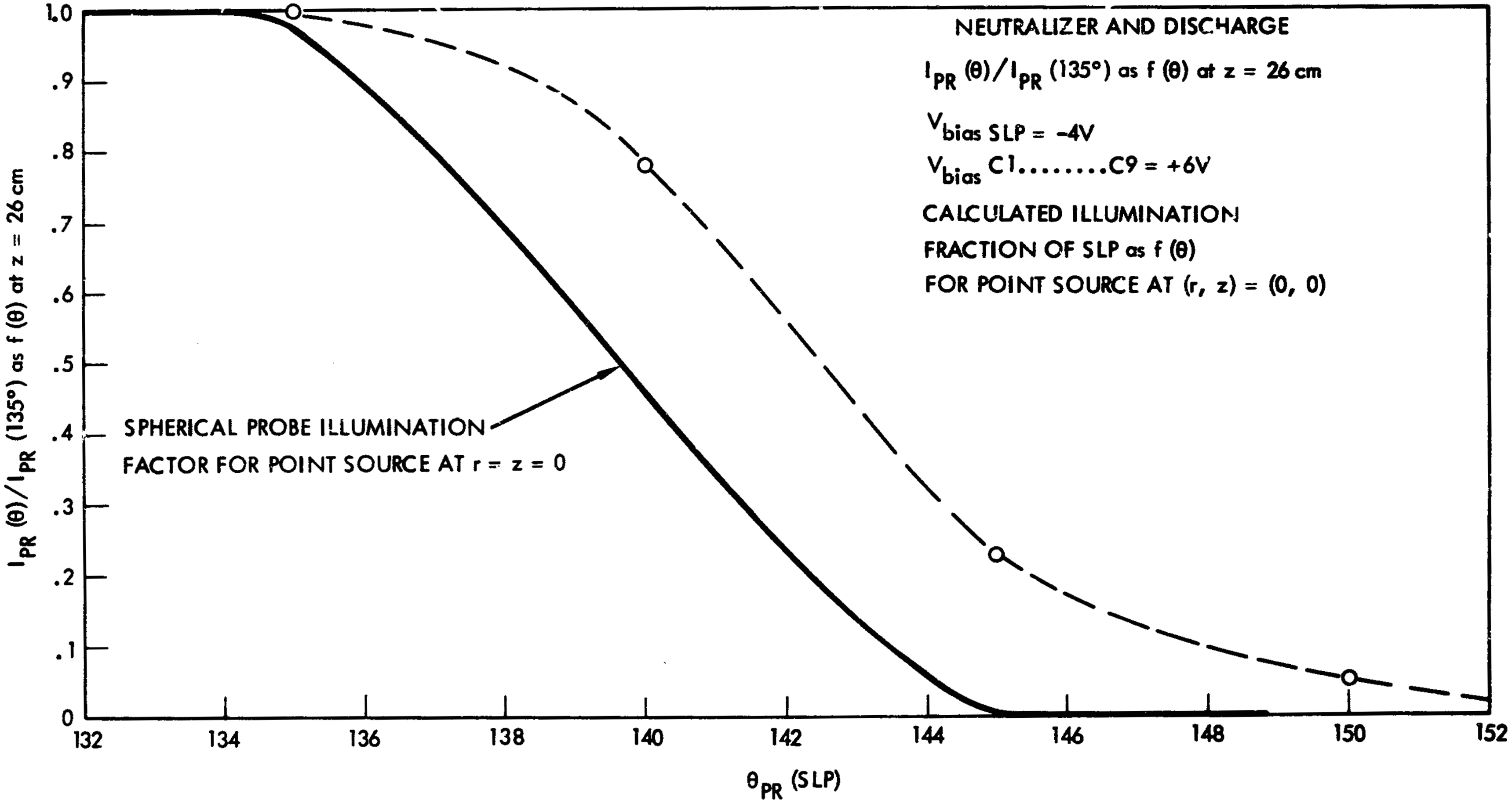

Figure 37. Ion Collection Current (Normalized to Value at 135 Degrees) from the Combined Discharge Plasma Plume to the Spherical Langmuir Probe as a Function of Probe Rotation Angle

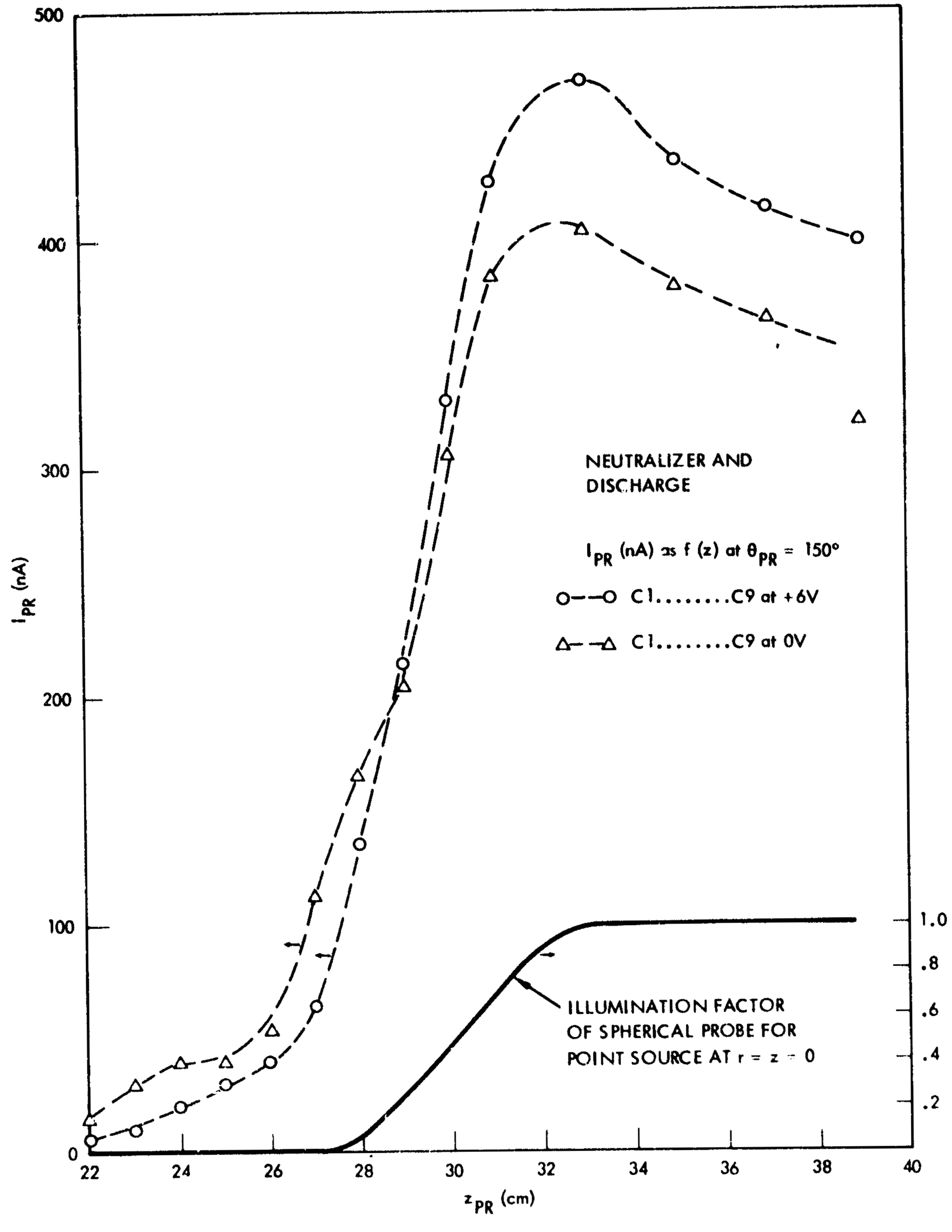

Figure 38. Ion Collection Current from the Combined Discharge Plasma Plume to the Spherical Langmuir Probe as a Function of Probe Axial Position and for Biasable Surface Potentials of +6V and 0V

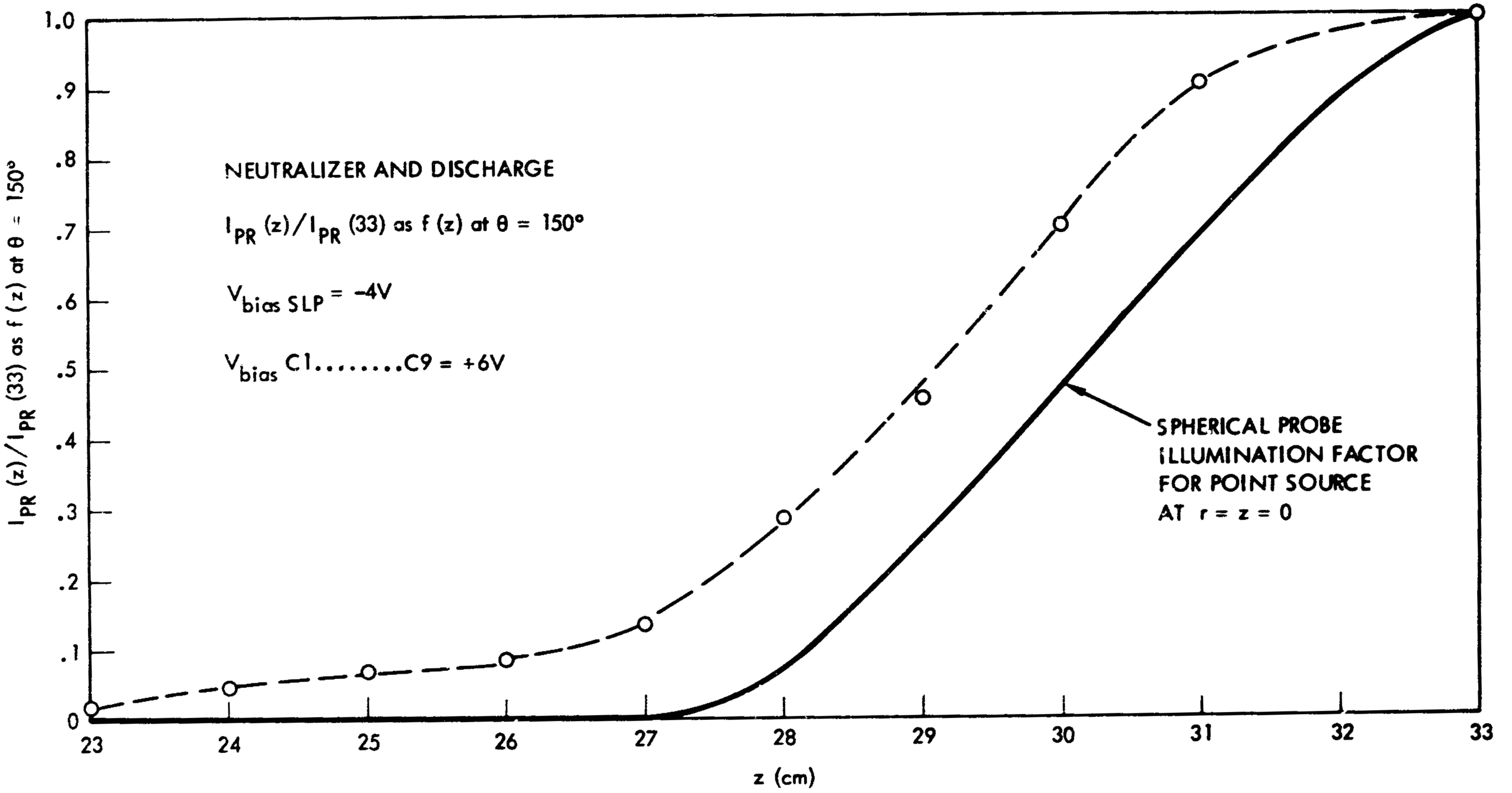

Figure 39. Ion Collection Current (Normalized to Value at 33 cm) from the Combined Discharge Plasma Plume to the Spherical Langmuir Probe as a Function of Probe Axial Position

4.2 Faraday Cup/Retarding Potential Analyzer Measurements

4.2.1 Floating Potential Measurements

Section 3.2.2 has described how the 1-1/2-inch J_+ probe can be used as a floating probe, and the data to be given in this section (4.2.1) will be obtained in the same manner. These floating potential measurements are required in order to set appropriate bias potentials on the probe entrance aperture. The floating potential measurements also provide data on the electric field structure in the plasma plume and in the regions near the plume and the material boundaries. Such data, combined with determinations of ion energy, allow the trajectory bending of the ions in these fields to be more accurately calculated.

Figure 40 illustrates the floating potential of the probe in the combined discharge plasma plume a function of probe rotation angle and probe axial position. Figure 41 provides a cross-plot of this data. For these measurements the biasable cylinder was allowed to float in the plasma plume.

The radial excursion as the probe is rotated through $\Delta\theta$ is approximately

$$\Delta r \text{ (cm)} = 0.6\ \Delta\theta \text{ (degrees)} \qquad (6)$$

using a probe rotation radius of 34.3 centimeters. For the $z = 23.7$ cm plane in Figure 40, the electric field in the radial direction is ~0.16 volts/cm. For $z = 28.7$, the average value of E_r is approximately 0.11 volts/cm while the average value of E_r at $z = 33.7$ cm has diminished to ~0.05 volts/cm. Comparatively strong axial electric fields are observed near $\theta_{\text{1-1/2-inch } J_+} = 55$ deg and in the 15.7 to 23.7 cm axial range.

To gain a better understanding of the location of various (θ,z) values relative to the biasable cylinder edge, Figure 42 illustrates the west edge of that cylinder and the location of the midpoint of the 1-1/2 J_+ entrance aperture for a given (θ,z) probe placement. Also shown in Figure 42 is the straight line trajectory from $r = z = 0$ to the downstream termination of the biasable cylinder west edge. Examining the data in Figures 40 and 41 with the position relative to the umbra line and the cylinder edge in Figure 42, it may be seen that the largest electric fields are near the

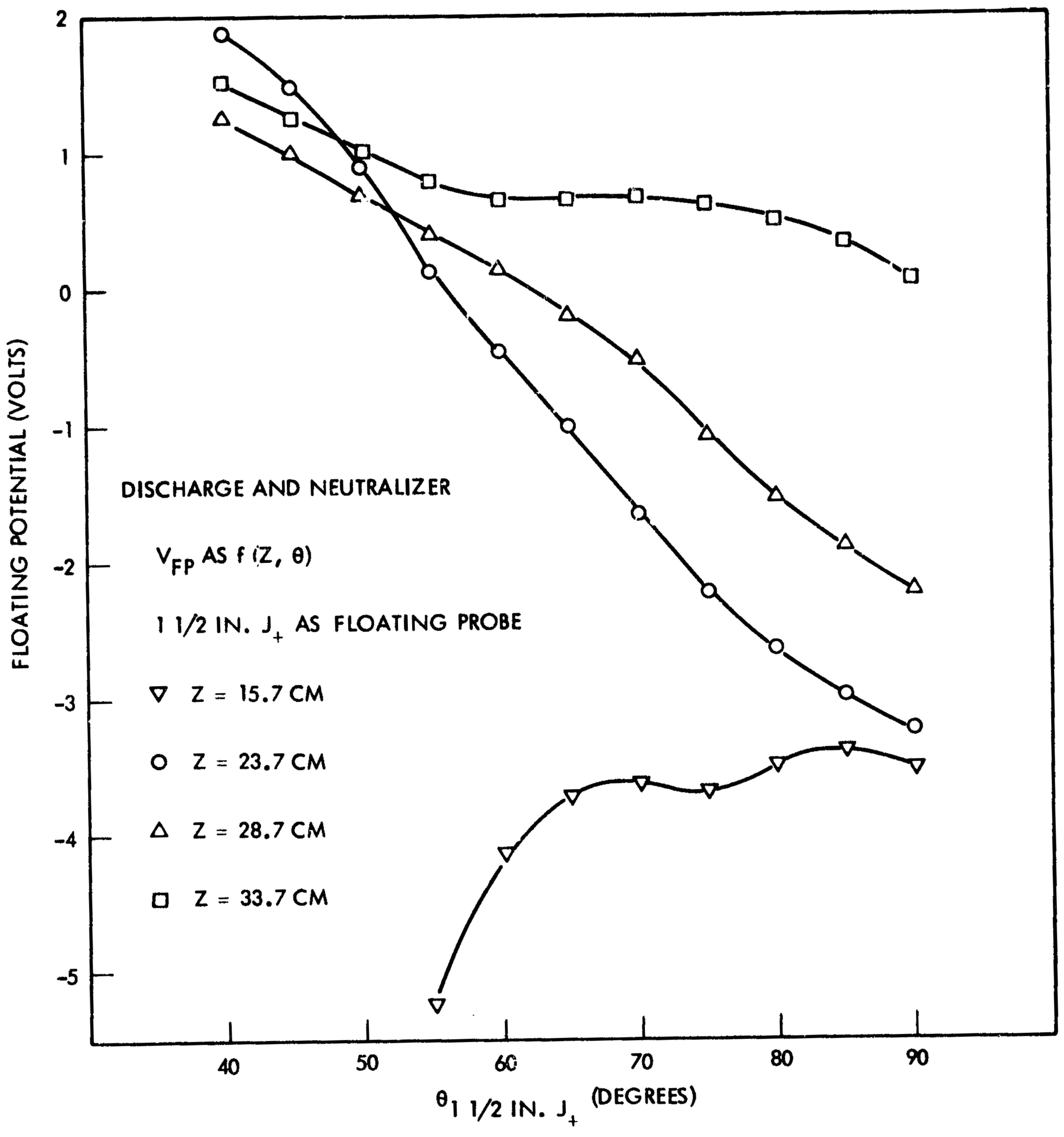

Figure 40. Floating Potential of the 1-1/2-Inch J+ (used as a floating probe) in the Combined Discharge Plasma Plume as a Function of Probe Rotation Angle and Probe Axial Position

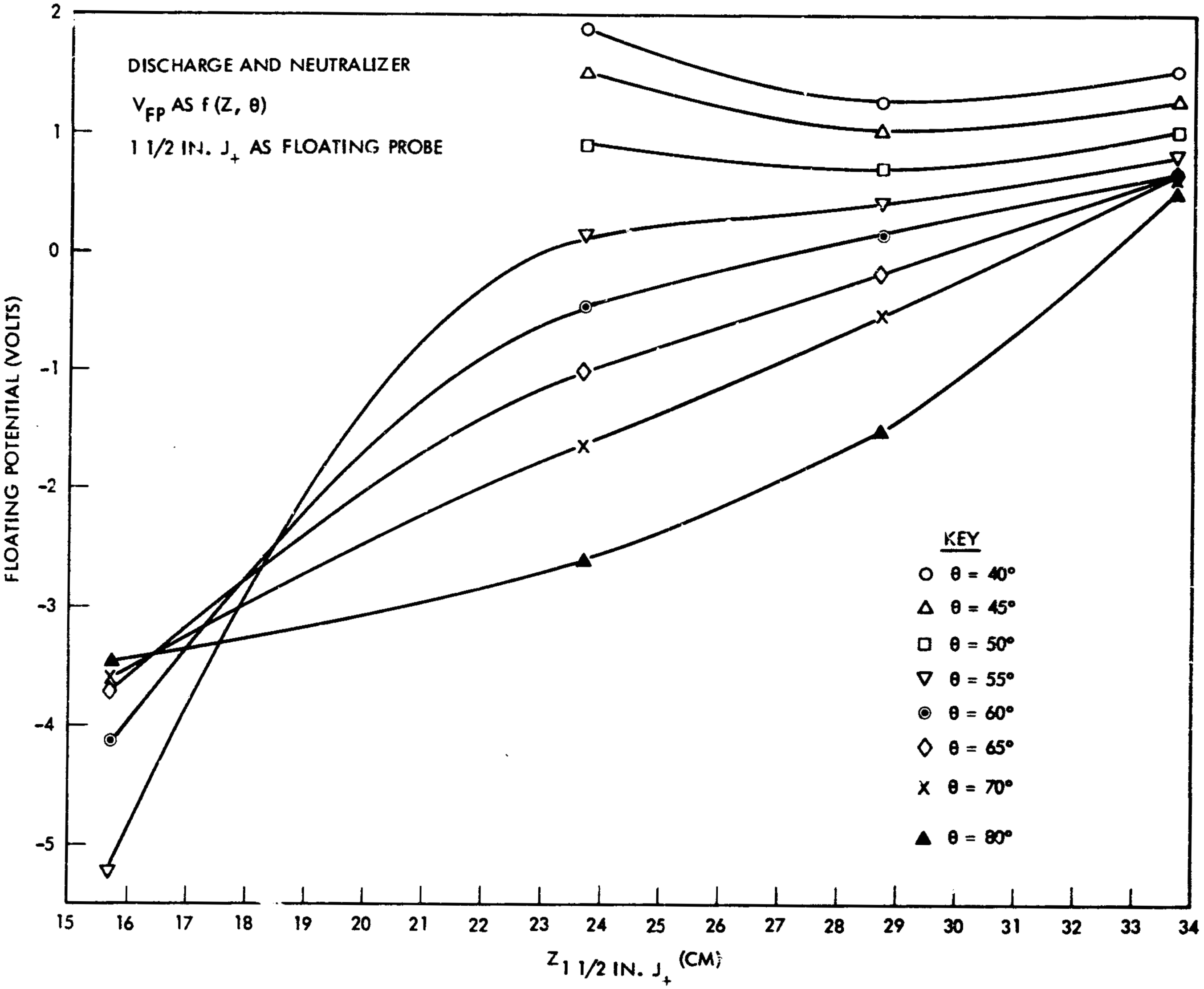

Figure 41. Cross-Plot of the Floating Potential Data of Preceding Diagram

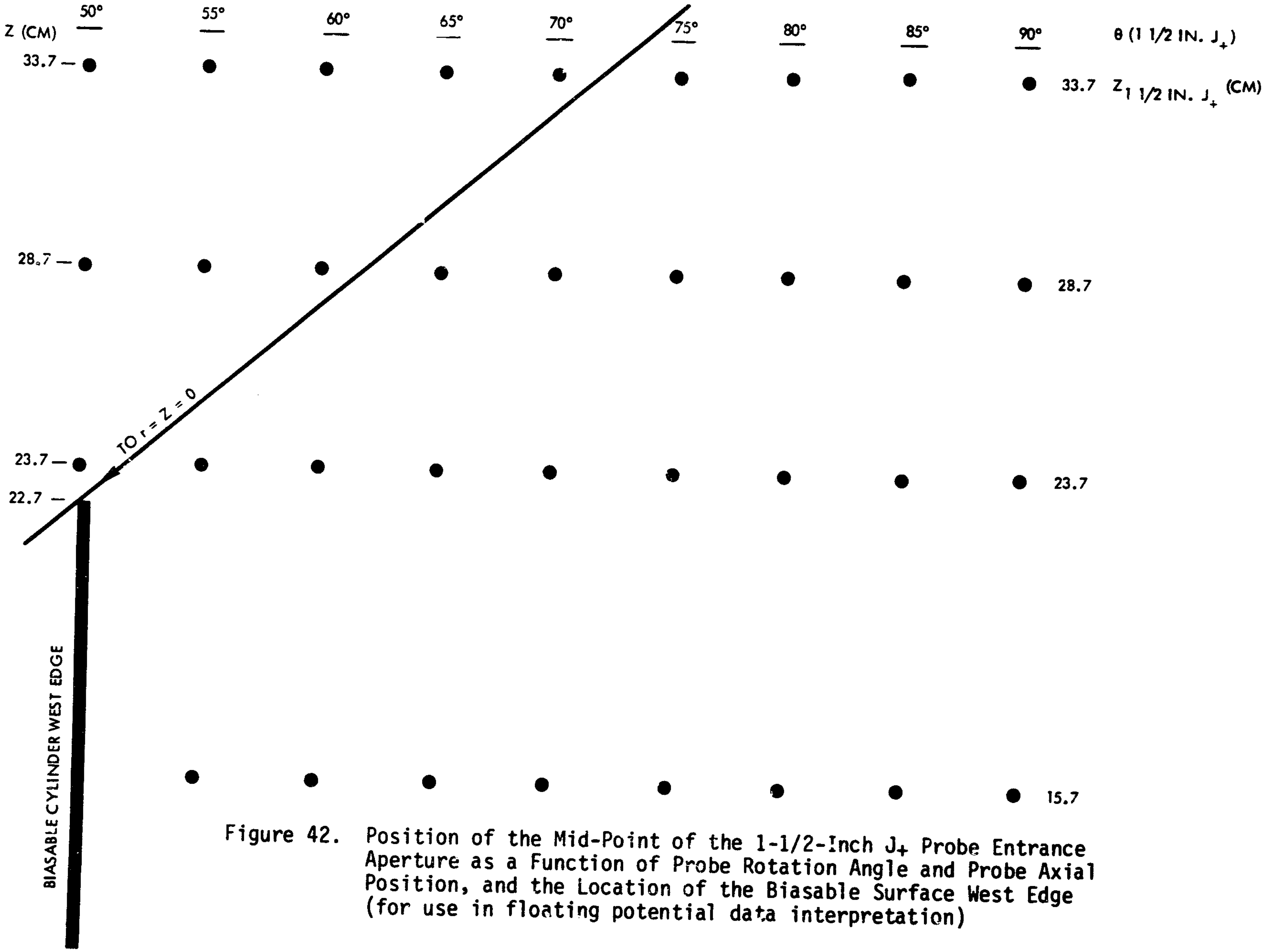

Figure 42. Position of the Mid-Point of the 1-1/2-Inch J_+ Probe Entrance Aperture as a Function of Probe Rotation Angle and Probe Axial Position, and the Location of the Biasable Surface West Edge (for use in floating potential data interpretation)

cylinder in the deep portions of the umbra where plasma density gradients (and, hence, also plasma potential gradients) are expected to be at their largest values. Across the umbra boundary at $z = 28.7$ cm the total electric field is ~0.12 volts/cm and is oriented at a polar angle of ~120 degrees. For $z = 23.7$ cm, the direction of the electric fields remains at ~120 degrees polar angle, but field magnitude increases to ~0.24 volts/cm. In Section 4.2.2, determinations of the ion energy in the combined discharge plasma plume will be given and these ion energies and the electric fields derived above permit a determination of the radius of curvature of the ions in their refraction into the umbra regions.

4.2.2 Ion Energy Spectrum Measurements

Figure 43 illustrates the ion collector current as a function of the retardation potential on the middle (retardation) grid of the Faraday cup/RPA. The upper curve is for cup placement on the thruster axis and the lower curve is for cup placement at 30 degrees probe rotation angle relative to the axis. The z plane of the measurements is 43.7 centimeters.

The results in Figure 43 indicate that the great majority of the ions in the combined discharge plasma plume have kinetic energies in the range from ~20 to ~26 eV. This indicates that most of the ions were created in the thruster discharge potential (which is approximately at anode potential) and are accelerated by a voltage difference of ~20 volts as they move from the interior of the thruster to the (exterior) plasma plume. Thus, even in the absence of a direct imposition of screen and accelerator grid potentials, the ions emerging into the plume constitute, in fact, a low energy ion beam. For an ion of this indicated energy and the electric field magnitude and orientation determined in Section 4.2.1 above, the radius of curvature of an ion moving along the umbra boundary (line from $r = z = 0$ to cylinder edge) will be ~2 meters, from Equation (2). There is, thus, only a minor bending of the ions by the plume density gradient generated electric fields in this region of the plasma. The modest bending derived from these measurements confirms the experimentally observed behavior of (comparatively) sharp shadows cast by the boundaries.

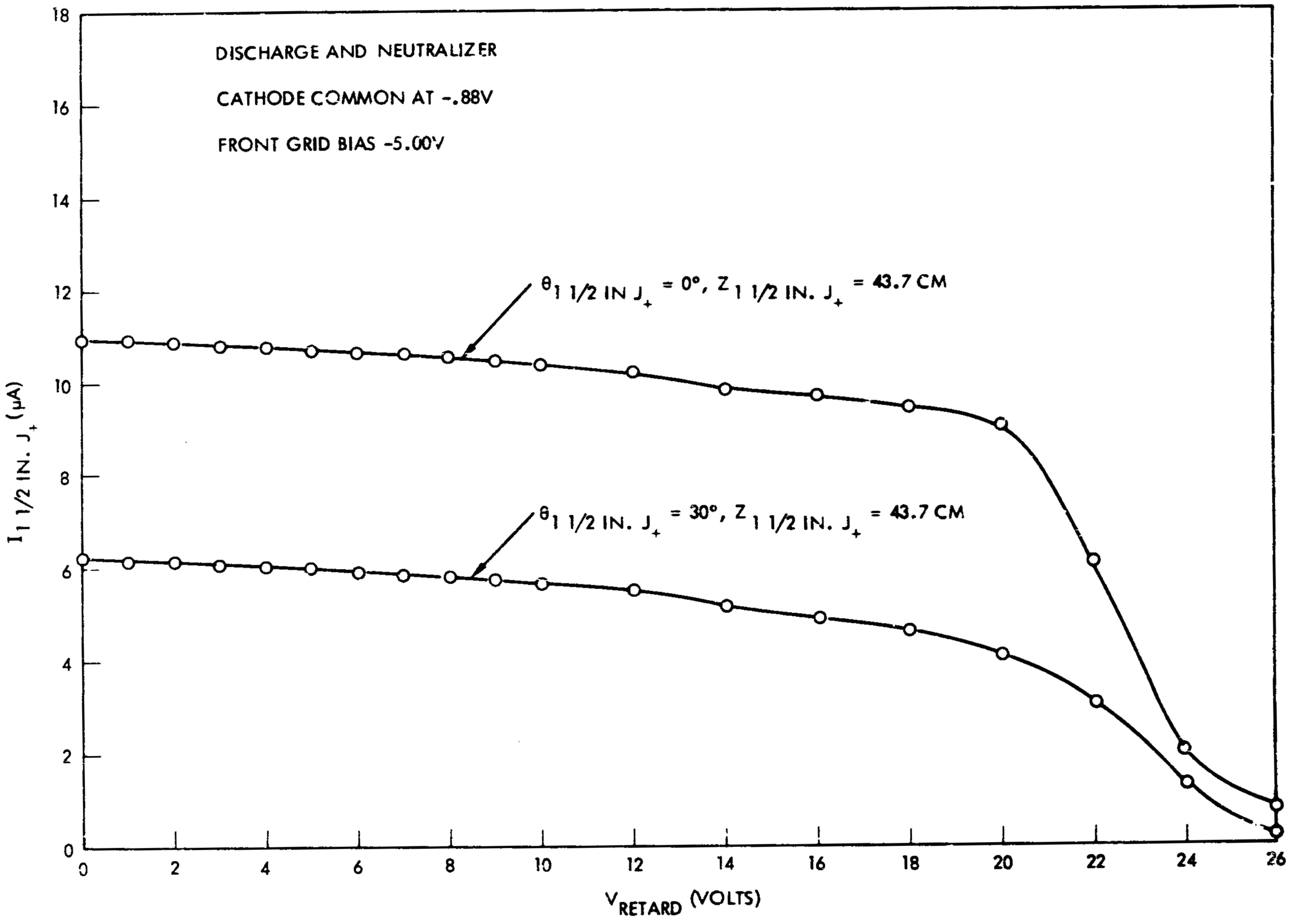

Figure 43. Ion Collector Current of the 1-1/2-Inch J_+ Probe in the Combined Discharge Plasma Plume as a Function of Retarding Potential on the Middle Grid

4.2.3 Ion Flux Density Measurements

Figure 44 illustrates the ion flux density in the combined discharge plasma plume as a function of probe rotation angle for the 1-1/2-inch J_+ in an axial plane at 24.7 cm. In the data shown there and for probe rotation angles within ~30 degrees of the thruster axis, flux density drop-offs of the order of 5 are observed which indicate, once again, that the ion thruster in this operational condition is, in effect, generating a weakly energetic, but nevertheless comparatively well defined, ion beam. For probe rotation angles beyond ~55 degrees from the thruster axis, the entrance aperture to the probe is within the umbra and flux drop-off of another three orders of magnitude (from the θ ~30 deg flux levels) are observed. Further increases in θ beyond the 55-degree point cause the flux levels to diminish below present system noise levels of ~10^{-11} A/cm^2. There is, thus, an extremely rapid cut-off of ion signal to the collector for probe positioning such that plural refraction of the trajectory is required for ion observation. Section 3.2.4 has discussed these plural ion refraction considerations and has noted that for sensitive surface placement such that plural refractions will be required through even modest bending angles, extremely low levels of ion deposition will be obtained on these surfaces.

A final determined parameter in the combined discharge plasma plume is plasma density. From the measured current density and the measured ion energy, the plasma density may be determined on the axis of the plasma plume and for z ~ 24 cm, this plasma density is ~ 6 x 10^7 ions/cm^3. Because the flow is comparatively well ordered, the plasma density of the plume diminishes considerably at the location of the biasable cylinder.

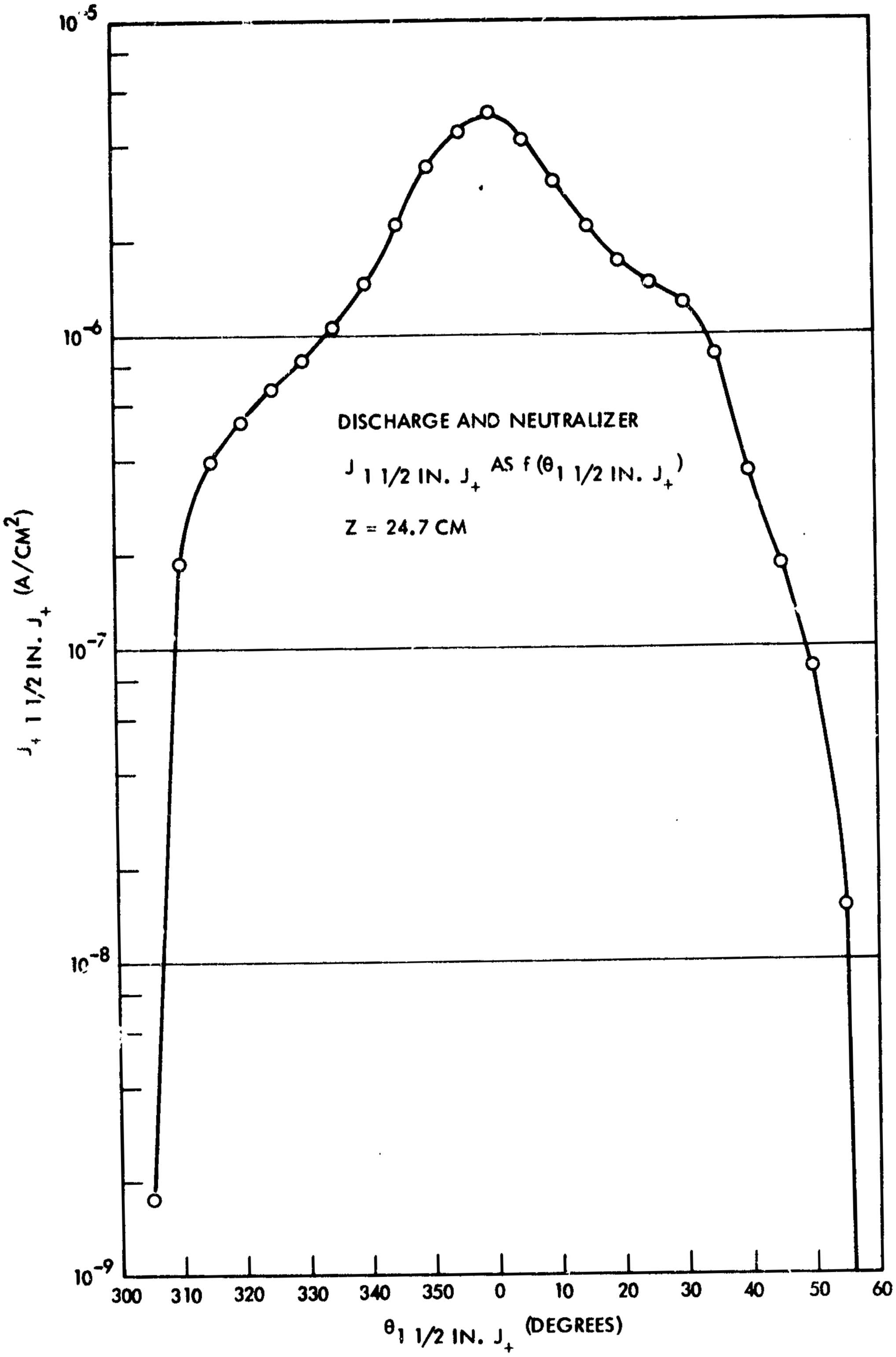

Figure 44. Ion Current Density in the 1-1/2-Inch J_{+} Probe in the Combined Discharge Plasma Plume as a Function of Probe Rotation Angle (biasable surface floating)

5. CHARGED PARTICLE MEASUREMENTS IN THE PLASMA PLUME OF A FULLY OPERATIONAL ION THRUSTER

5.1 Spherical Langmuir Probe Measurements

A previous report[1] contains extensive measurements on the charged particle effluxes of a fully operational ion thruster. The experiments to be described in Section 5 of this report have not attempted to reexamine all of the areas previously investigated. The measurements to be described here have been carried out, however, to provide additional details on "facility effect" particle effluxes and to determine if procedures can be devised to allow measurements of very low level charged particle currents from the thruster in the presence of these "wall-generated" particle currents.

Before proceeding to the probe measurement data, it will be of benefit to postulate the origins and general properties of the facility effect charged particles. In this discussion a facility effect particle will be defined as a particle whose measured presence in a detector is the result of the interaction of the ion thruster effluxes with the facility walls. A major element in this overall interaction occurs as a result of the thrust ion impact on the beam collector. This thrust ion impact on the collector leads to four principal reactions: These reactions are:

(1) Neutral Hg^0 release via a nonsticking incident ion. In this reaction, the incident energetic (keV) ion impacts on the collector but does not stick to the surface and rebounds as a weakly energetic neutral, moving in the backward hemisphere of directions.

(2) Sputtered Hg^0 release under energetic Hg^+ impact. In this reaction, the incident Hg^+ thrust ion sputters accommodated Hg^0 from the (LN_2 cooled) beam collector surface and causes the release of a weakly energetic Hg^0, moving in the backward hemisphere of directions.

(3) Sputtered metal atom release under energetic Hg^+ impact. In this reaction, the incident Hg^+ sputters a metal atom from the beam collector and causes, thus, the release of a weakly energetic neutral particle into the backward hemisphere of directions, and,

---

[1] "Ion Engine Auxiliary Propulsion Applications and Integration Study," NASA CR-135-312, July 1977.

(4) Rebounding ion release. In this reaction, the energetic Hg^+ impact results in a weakly energetic ion release into the backward direction with both mercury and metal ions as possible release species.

Of the reactions above, the major contributors to effluxes moving in the backward directions are reactions 1, 2, and 3. In all of these reactions, the species is (initially) neutral and will not cause an erroneous measurement in the charged particle detectors. The Hg^0 neutrals, however, can convert to Hg^+ via charge transfer reactions with the Hg^+ thrust ions. Charge transfer between metal atoms and Hg^+ may also occur, but the nonresonant nature of this charge transfer greatly reduces the charge transfer cross sections. The principal avenue for producing facility effect charged particles, thus, is the charge transfer of weakly energetic Hg^0, moving in the backward direction, to Hg^+ ions. From geometrical considerations these weakly energetic facility effect Hg^+ ions should be in motion within the polar angle range of directions from 90 to 180 degrees where 0 degrees in this coordinate frame is along the thruster axis. Because the facility effect ions are weakly energetic, their trajectories can be refracted in the electric field structure in the plasma plume and between the plasma plume and the various boundaries.

With the above discussion as a background for possible reaction processes, measurements with the spherial Langmuir probe were carried out with the fully operational ion thruster. Figure 45 illustrates the SLP current as a function of probe rotation angle for Z = 26 cm and for a probe bias potential of +10 volts. This probe bias voltage is set so that the SLP will be sufficiently negative with respect to the thrust beam plasma plume to repel electrons from the plasma but also at a sufficiently small potential increment with respect to the plasma to discourage excessive sheath growth on the ion collection limb (see also discussion in Section 5.3.1 on the floating potentials in the plasma plume of the fully operational ion thruster).

The data in Figure 45 illustrates a peak ion signal of approximately 15 milliamperes for the on-axis position of the SLP. Because the ion flow is well ordered here, the effective probe area is $\sim\pi r^2$ (which is $\sim$15 cm^2 for this 4.32 centimeter diameter spherical probe) and the current desnity of ions is approximately 1 mA/cm^2. This observed current density

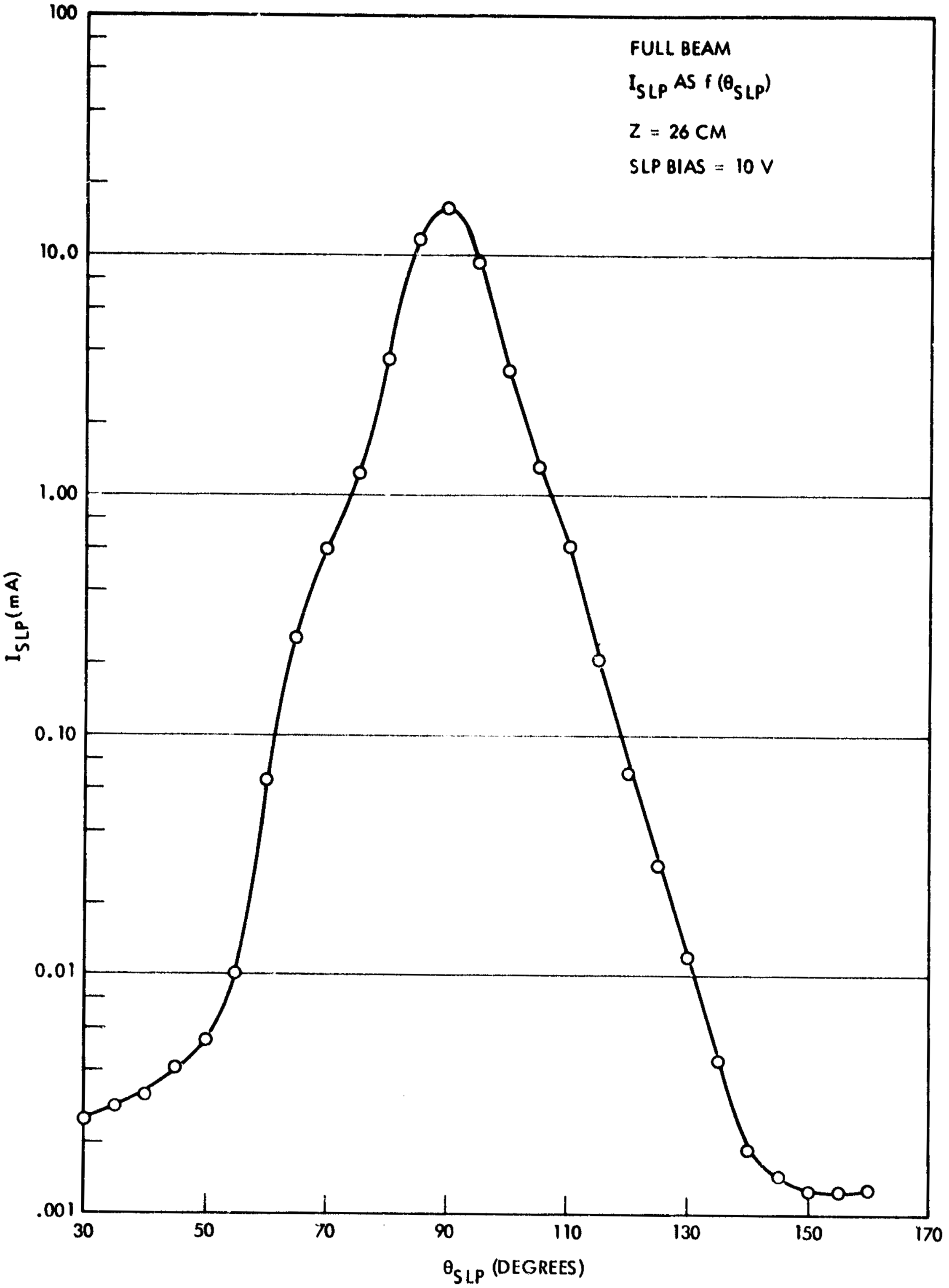

Figure 45. Ion Collection Current from the Full Beam Plasma Plume to the Spherical Langmuir Probe as a Function of Probe Rotation Angle (biasable surface floating)

obeys the typical fall-off for off-axis positions of the beam (exponential wing). For probe positions beyond $\theta_{SLP} \sim 140$ deg, however, the observed ion signal becomes approximately constant. Similar behavior is also observed for θ_{SLP} less than ∼ 50 degrees. A review of the probe and material boundary geometries (see Figures 9, 10, and 11) indicates the SLP is in the umbra regions created by the biasable cylinder for θ_{SLP} $\gtrsim$135 deg, and in the umbra created by both the sputter shield and the biasable cylinder for $\theta_{SLP} \lesssim 45$ deg. The SLP currents observed in these umbra locations are, thus, probably facility effect fluxes for the greater part. An estimate of the flux density in these umbra regions is $\sim 10^{-7}$ A/cm^2.

If the neutral Hg^0 release from the beam collector is $\sim J_B$, the thrust ion current, and if these neutrals are emitted over $\sim 2\pi$ steradians of solid angle, the flux density at such neutrals near the thruster would be

$$J\,(Hg^0) = \frac{J_B}{2\pi L^2} \tag{7}$$

where L is the distance from the beam collector to the probe location. For $J_B = 74$ milliamperes and $L \cong 200$cm, $J\,(Hg^0) \sim 3(10)^{-7}$ equivalent A/cm^2. For detection as an ion, however, charge transfer must occur and from the observed ion current densities on the SLP, the required conversion probability would be ∼30%. This is somewhat larger than the expected conversion probability. On the other hand, the neutral emission may be more confined than the 2π steradians assumed above. Also the release current of neutrals exceeds J_B in that both the arriving ion current and the sputtered Hg^0 from the beam collector (reactions 1 and 2 in the list of beam/collector interactions above) are in the Hg^0 release current. In view of these several factors, there is a comparatively good agreement between expected levels of facility effect ion fluxes and the ion fluxes observed on the SLP for probe locations in these umbra regions.

From the above discussion it would appear that because facility effect fluxes of the order of 10^{-7} A/cm^2 are present near the thruster, determinations of normalized efflux coefficients would be limited to regimes where $\epsilon \cong 10^{-6}$ cm^{-2}. As the subsequent discussion will demonstrate, however, substantial gains in signal-to-noise ratio can be achieved by limiting the cone of acceptance directions of a measuring probe. Because the Spherical Langmuir probe accepts particles over 4π steradians of directions, the measurements of charged particles with this probe are the most subject to the presence of facility effluxes. This statement on SLP capabilities should not be interpreted to mean that SLP measurements obtained with the neutralizer discharge only and with the combined neutralizer and thruster discharge plasma plume are significantly influenced by facility presence. In both of these previous operational conditions the ion energies are significantly reduced from their levels in the fully operational thruster case. Sputtering of materials from beam collectors and shrouds, thus, is not, generally speaking, present in these earlier operational cases. In addition, the total magnitudes of ion fluxes are greatly reduced for the first two operational conditions compared to ion fluxes levels for the fully operational thruster. The possibility of a neutral Hg^0 charge-transfer to the Hg^+ in a backward passage through the testing chamber is, thus, very small for the neutralizer discharge only and for the combined neutralizer and thruster discharges only.

A final measurement obtained with the SLP in the plume of the fully operational ion thruster is illustrated in Figure 46. In the data given there, the SLP is moved axially for a fixed probe rotation angle θ_{SLP} = 30 deg. In this motion to smaller Z values from larger Z values, the probe is increasingly withdrawn into a region bounded by the testing chamber wall on the one side and by the biasable cylinder on the other with the result that a diminishing fraction of all of the facility effect effluxes can intercept the probe surfaces. This demonstrates that attenuation of facility efflux levels is possible by appeals to geometrical considerations in material boundary placements, and that such boundary placements may be an important aspect of future test planning to assure that laboratory measurements of thruster effluxes become increasingly more accurate in their determinations of in-space efflux conditions.

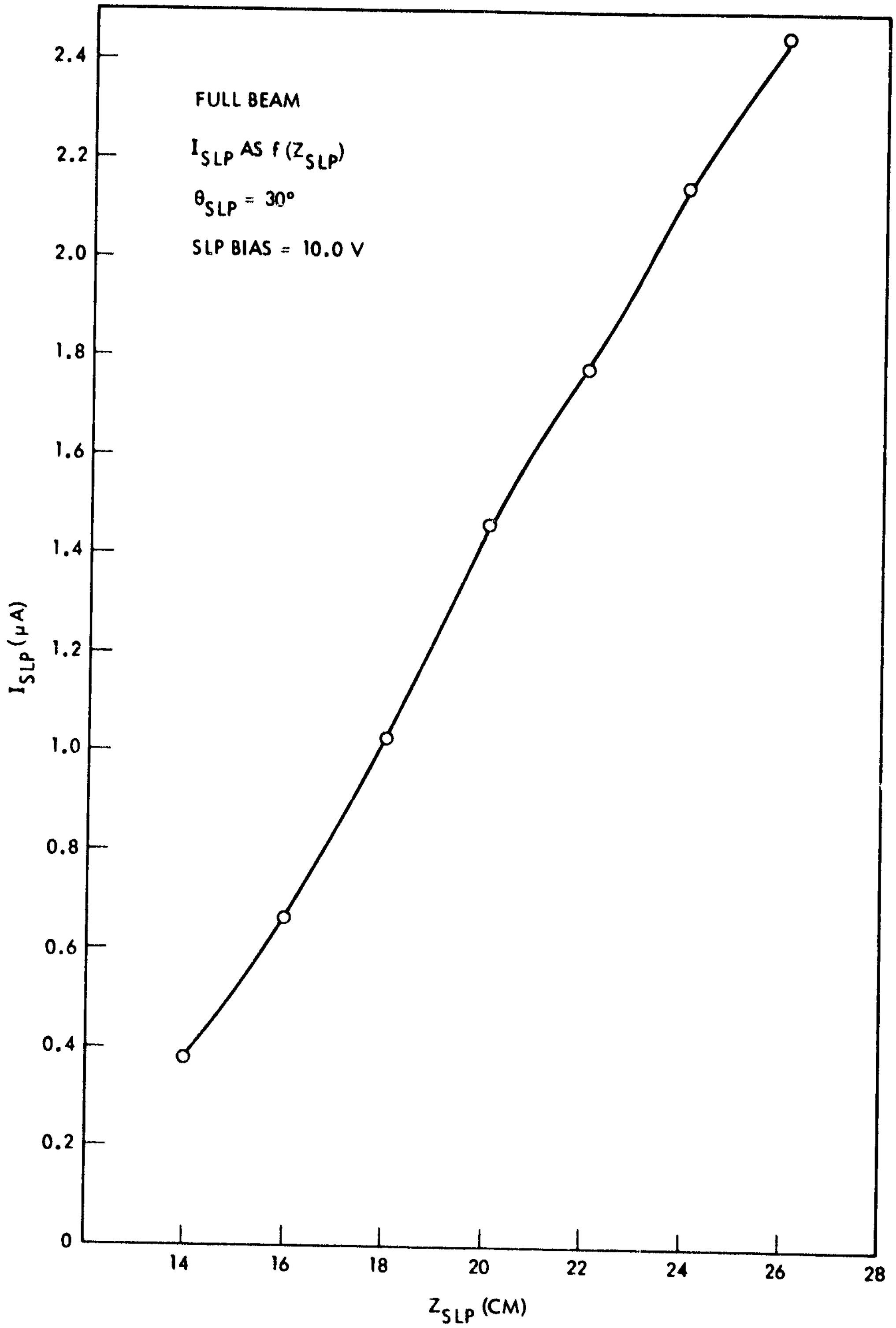

Figure 46. Ion Collection Current from the Full Beam Plasma Plume to the Spherical Langmuir Probe as a Function of Probe Axial Position (biasable surface floating)

5.2 Piggyback J+ and 4-Inch J+ Measurements

The Piggyback J_+ has its primary entrance axis along the polar angle direction $\theta = 180$ deg, where $\theta = 0$ deg is the thrust ion axis, and charged particles moving within ∿45 degrees of this entrance aperture axis can be intercepted on the probe collector. Figure 47 illustrates the measured ion current density into this Faraday cup as the probe is moved axially from Z values of the entrance plane from ∿65 to ∿5 centimeters. The ion thruster is in its fully operational condition and all grids of the probe are set at $V = 0$.

The current densities given in Figure 47 are obtained by dividing collector current by the area in the apertures immediately proceeding the collector. From the data given in Figure 47, the magnitudes of ion fluxes through these apertures and within the cone of acceptance directions are of the order of nanoamperes/cm^2. At $Z = 26$ cm the entrance plane of the PB J_+ is near the plane of the SLP measurements in Figure 45 and measured PB current density is ∿1 nA/cm^2. This may be compared to SLP current densities in this same Z plane and (cylindrical) radial displacement of ∿100 nA/cm^2. From this it would appear that, although the facility effect ions are moving in the backward directions, only a minor fraction of these effluxes are within a divergence cone of ±45 degrees around this $\theta = 180$ deg direction. The neutrals emanating from the beam collector and moving toward the thruster are, however, generally within such a directional range. Under such circumstances, then, it would appear that the current densities in the PB probe should be somewhat closer to the SLP current densities than presently demonstrated. An explanation of this difference in current densities may be in the bending of the charge exchange ion trajectories, away from the original Hg^0 direction, in the electric fields in the thruster plasma plume. Section 5.3.1 will present floating potential measurements which illustrate both radial and axial electric fields in the thruster plume. Because the facility effect neutrals are weakly energetic, the action of a radial electric field upon the (charge transfer produced) ion would be to deflect the ion into directional ranges which might lie outside of the acceptance cone of the PB J_+. This is, admittedly, a complicated interactive effect involving both radial and axial electric

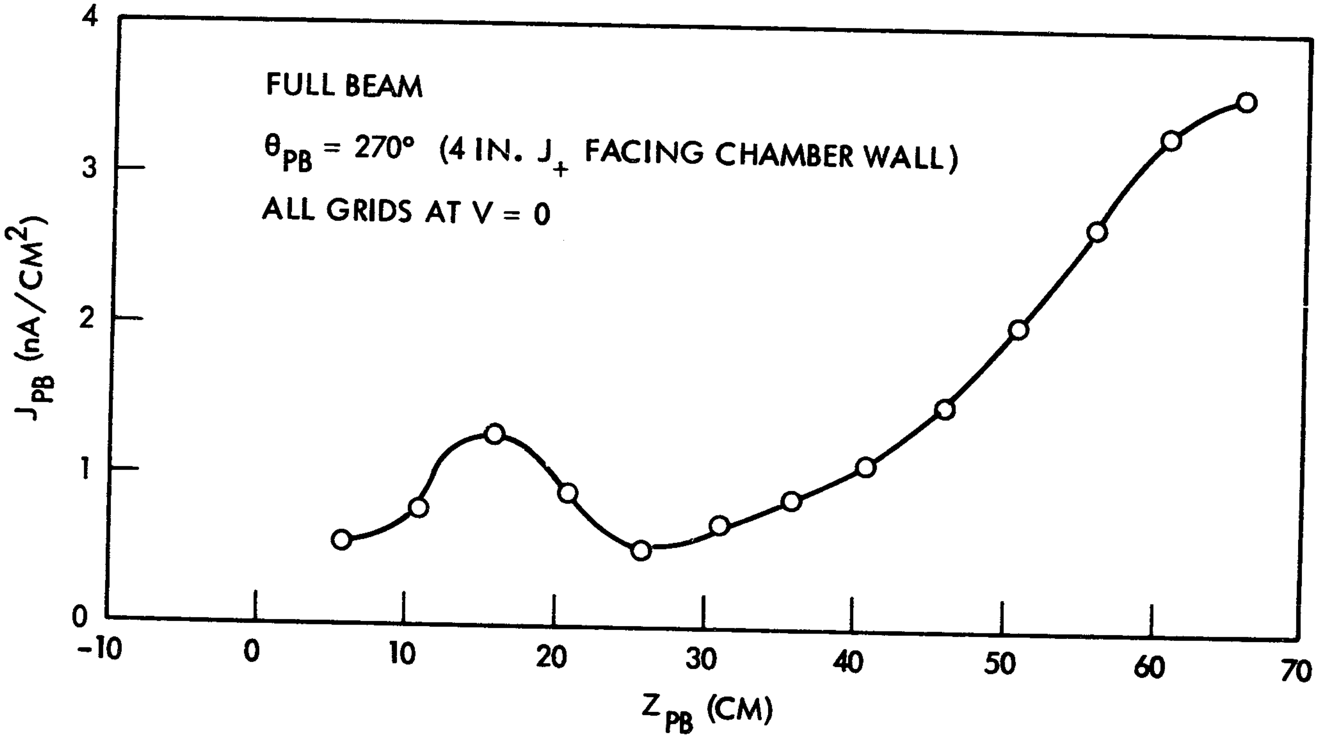

Figure 47. Ion Current Density from the Full Beam Plasma Plume to the Piggyback J_+ Probe as a Function of Probe Axial Position (biasable surface floating)

fields, initial neutral directions, charge exchange ion energies (which change along the path because of electric field actions), and the acceptance cones of entrance directions of the various probes. The results would appear to indicate, however, that appeals may also be made to such electric field actions on the facility effect ions as a means of reducing facility effect ion fluxes in the measuring probes. For certain probe measurements, of course, the probe orientation and the cone of acceptance directions will not lead to a clear exclusion of facility effect ions moving under the influence of the plasma plume electric fields in which case both "genuine" charged particle currents and "facility effect" charged particle currents will be detected at the collectors and inaccuracies will be present, to some degree, in the measured efflux coefficients.

A second facility effect measurement using the 4 inch J_+/PB J_+ is given in Figure 48. In the data given there, the 4 inch J_+ is oriented so that its entrance axis points radially outward toward the testing chamber walls. All probe grids were set at V = 0 volts and the probe is moved through the Z range from $\sim$55 to $\sim$-5 centimeters. Ion current densities are determined by dividing the probe current by the entrance aperture area.

The current densities in Figure 48 are reduced to levels below those given in Figure 47. The explanation for such reductions is that ion motion to enter the probe becomes even more difficult than for entry into the PB probe. Over portions of the 4 inch J_+ placement, electron currents, penetrating the grids at V = 0, exceed ion currents into the probe. This is not unexpected in view of the randomized directions in plasma plume electrons as compared to flow patterns (generally not randomized) in the weakly energetic ions as the result of radial and axial electric fields in the plasma plume. Electric fields between the plasma and the probe can, of course, cause some ion refraction into the probe, and care must be exercised in the assignment of probe grid potentials that ion entry into the probe is not being significantly increased by such electric fields. A second criterion in grid potential assignment is the exclusion of electrons (for measurements of ion effluxes) and a satisfactory solution of the required electron exclusion without ion refraction may not always

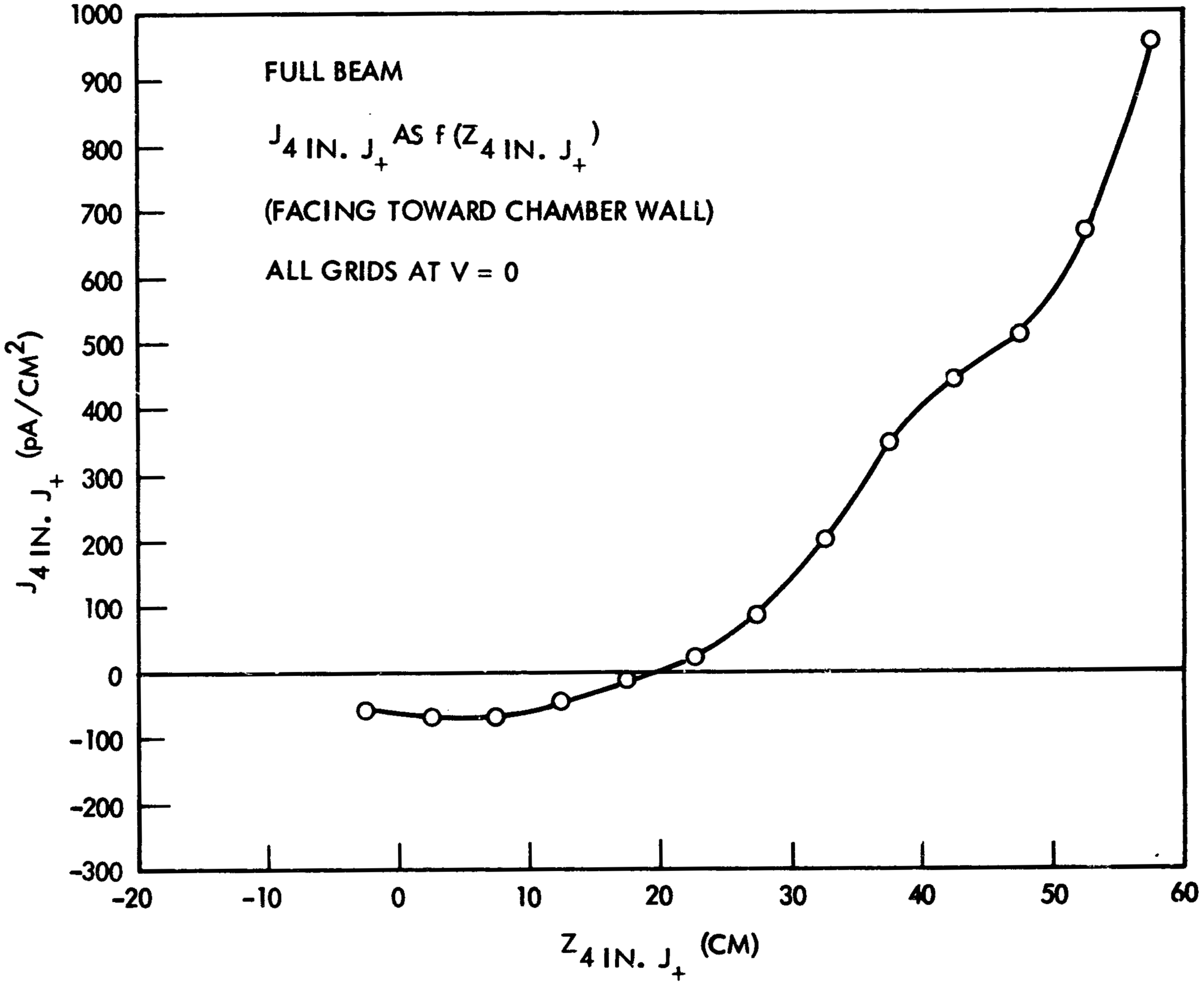

Figure 48. Ion Current Density from the Full Beam Plasma Plume to the 4-Inch J_+ Probe as a Function of Probe Axial Position (biasable surface floating)

be obtained. In the data of Figure 48, some ion refraction into the probe is probably present. The important aspect to note, however, is that ion signal levels below the nanoampere/cm^2 level are being obtained, in facility, for a fully operational ion thruster.

5.3 Faraday Cup/Retarding Potential Analyzer Measurements

5.3.1 Floating Potential Measurements

The 1-1/2 inch J_+ has been used as both a floating probe and as a Faraday Cup for measurements of the ion flux of a fully operational thruster. This section will describe the floating potential measurements and Section 5.3.2 will describe the Faraday cup measurements. Retarding potential analyses were not carried out. For probe locations in the thrust beam, the dominance of the very energetic thrust ions does not allow retarding potential analysis of weakly energetic ions. Also for probe locations in umbra regions, the (extremely small) signal levels (into the noise level) rule out further examination via retarding potential analyses.

Figure 49 illustrates the floating potential of the 1-1/2 inch J_+ probe as a function of probe rotation angle (noting that $\theta_{\text{1-1/2 inch } J_+} =$ 0 deg corresponds to probe placement on the thrust beam axis) and for the Z-planes of 23.7, 43.7, 63.7, and 83.7 centimeters. A cross-plot of this data is given in Figure 50.

Figure 50 illustrates a comparatively complex potential structure. The principal electric fields in this structure are radially outward with levels as high as 1.5 volts/cm being observed (see, for example, the Z = 23.7 cm scan in the angular range from 0 to $\pm\sim$40 degrees). The radial electric fields tend to diminish in magnitude for the Z-planes further downstream from the thruster. There are some regions that appear "anomalous" (310 deg $\leq \theta \leq$ 330 deg, Z = 43.7 cm) for which the radial electric field exists but would cause the inward radial motion of a weakly energetic ion created at such a location.

On the axis of the thrust beam the axial electric fields are in the downstream direction. These fields are at $\sim$0.5 volts/cm in the region

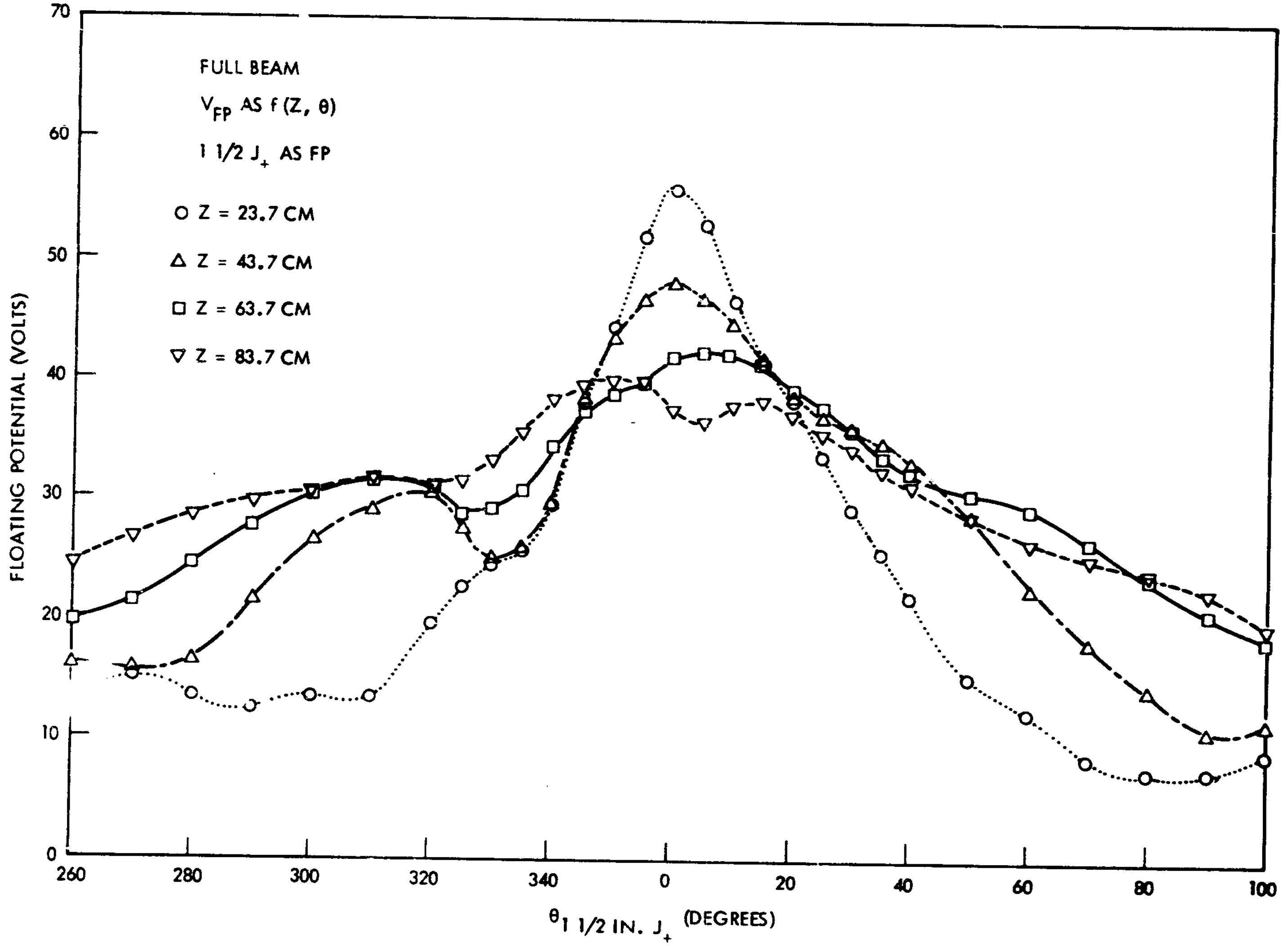

Figure 49. Floating Potential of the 1-1/2-Inch J+ Probe (used as a floating probe) in the Full Beam Plasma Plume and as a Function of Probe Rotation Angle and Probe Axial Position (biasable surface floating)

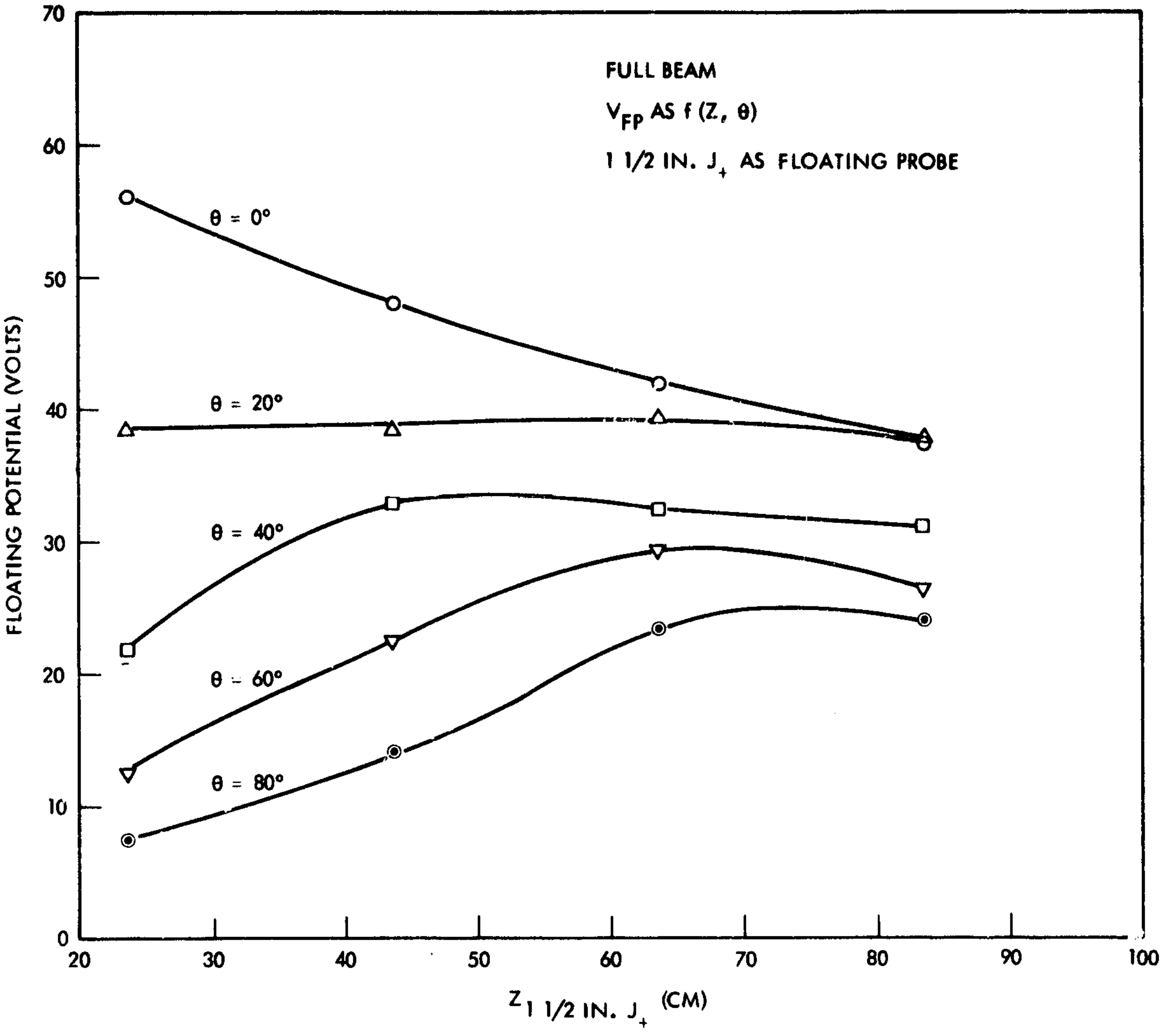

Figure 50. Cross-Plot of the Floating Potential Data of Figure 49

$23.7 < Z < 43.7$ cm and diminish for increasing Z. For off-axis locations, however, the axial electric may diminish to very small levels or may reverse directions to cause the backwards movement of a weakly energetic ion.

In addition to the complicating factors discussed above, there are the effects of wall potentials, shroud and beam collector potentials (floating), biasable cylinder potentials, and the effects of density gradients in the plasma plumes as the result of all of these material boundaries (with particular emphasis on the presence of the biasable cylinder). The trajectory of a weakly energetic ion created on such a complicated potential structure cannot be described with ease. The refraction of the ions in whatever E_Z fields are encountered along the ion pathway will depend upon the (accumulated) ion kinetic energy as it proceeds to "roll" down this rather tortuous potential "hillside." For the $\theta = 40$ deg region and Z $\sim$23.7 cm, the net electric field is $\sim$1.6 volts/cm and is oriented in the backward direction at a polar angle of $\sim$110 degrees with respect to the thrust axis. A charge exchange ion created at this point (and with, essentially, zero kinetic energy) would commence its motion in the polar angle direction of 110 degrees. A charge exchange ion moving from a creation point on the beam axis, however, could have acquired kinetic energies of the order of 40 eV, could be moving in the downstream direction as the result of previously encountered positively directed E_Z, and would have a radius of curvature of $\sim$50 cm at the ($\theta = 40$ deg, $Z = 23.7$ cm) example location from the calculated net $\vec{E}$ at that point and the (postulated) 40 eV of ion energy. Backward bending of the ion would be present but need not result in a backwardly directed ion motion if the previously acquired forward Z motion is at sufficient levels.

The example discussed above indicates weakly energetic ion motion in the plasma plume of fully operational ion thrusters remains as a less than completely understood phenomenon which should be examined in other material boundary and probe configuration conditions. An important element in such further examinations would be the demonstration that measurements of the weakly energetic ion fluxes for such configurations will not be materially altered by facility effect ion fluxes. The discussions in previous sections have indicated that appeals can be made to geometrical factors in the measuring probe construction and in material boundary placement in order to reduce the effects of facility presence to acceptably small levels.

5.3.2 Ion Flux Density Measurements

Figure 51 illustrates the measurements of ion current density for the angular rotation of the 1-1/2 inch J_+ probe in the $Z = 23.7$ cm plane and for a fully operational ion thruster. As the probe is rotated through $\theta_{1\text{-}1/2 \text{ inch } J_+} = 0$ deg, the thrust beam axis, the current density becomes slightly larger than 10^{-3} A/cm^2. This is in good agreement with the earlier current density measurements using the spherical Langmuir probe (see Figure 45). The major difference between the 1-1/2 inch J_+ probe and the SLP occurs as the Faraday cup/RPA moves into the umbra of the biasable cylinder. For $\theta > 55$ deg, for example, the current density (determined by cup collector current divided by entrance aperture area) diminishes to levels below 10^{-11} A/cm^2.

From the SLP results, the high rotation angle signals indicate facility effect fluxes on ions of $\sim 10^{-7}$ A/cm^2 (see Section 5.1). These ion fluxes, however, are clearly directed into the backward hemisphere of directions in that the 1-1/2 inch J_+ probe in these same regions perceives less than 10^{-11} A/cm^2. To enter the 1-1/2 inch J_+ probe requires a forwardly directed ion, generally within ~ 50 degrees of the polar direction angle of 0 degrees, and, from the observed results, less than 1 part in 10^4 of the facility effect flux in these umbra regions is within this cone of acceptance directions. From the Piggyback probe results (see Section 5.2 and Figure 47), it would also appear that only a small fraction of the facility effect fluxes in the umbra regions lie within the acceptance cone of directions for that probe. These combined observations, then, indicate a facility effect flux at $\sim 10^{-7}$ A/cm^2 in the total range of backward directions, $\sim 10^{-9}$ A/cm^2 in the cone of directions (half angle of 45 degrees) around 180 degrees of polar angle direction, and less than 10^{-11} A/cm^2 in the forward direction (cone half angle of ~ 50 degrees around the polar angle = 0 degrees direction). As has been previously

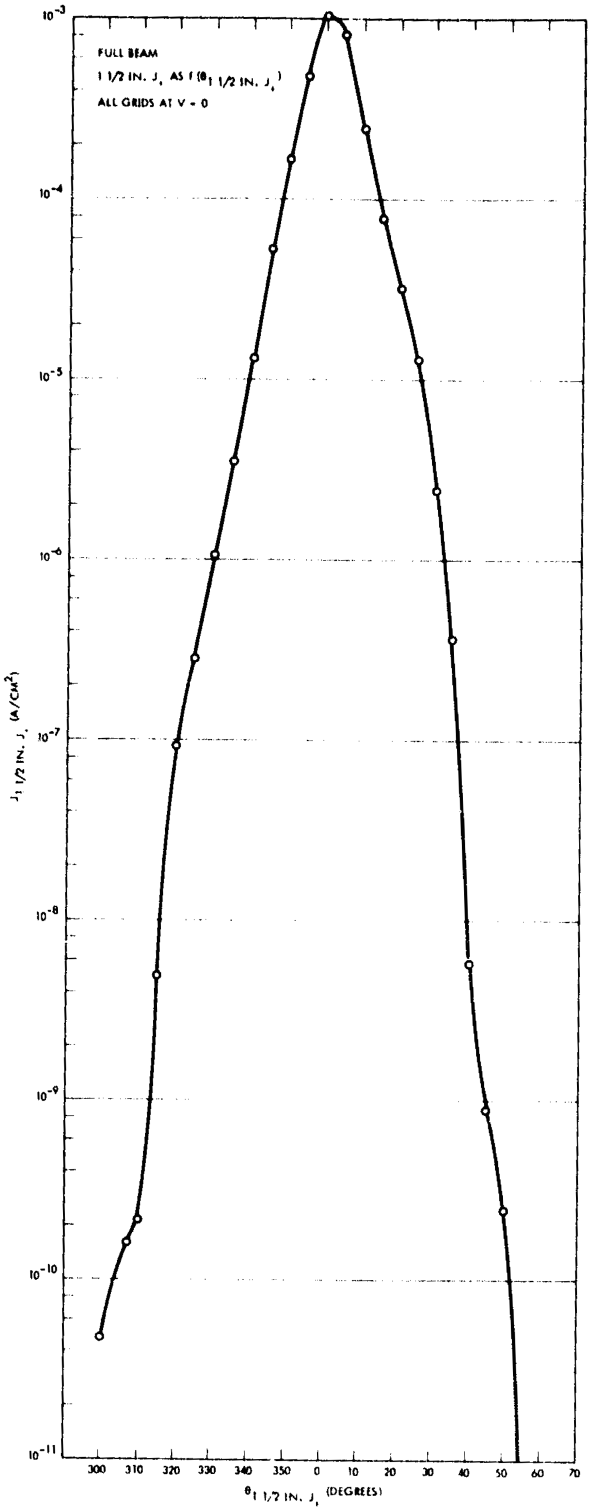

Figure 51. Ion Current Density in the 1-1/2-Inch J_+ Probe in the Full Beam Plasma Plume as a Function of Probe Rotation Angle (biasable surface floating)

noted, these qualities of the facility effect flux may be used to raise the signal-to-noise ratio between genuine particle effluxes and facility effect particle effluxes, provided that certain probe orientation directions and material boundary placements can be achieved.

6. TESTING CHAMBER PRESSURE EFFECTS

5.1 General Considerations

Section 5.1 has discussed the generation of a flow of weakly energetic ions as the result of neutral Hg^0 release from the beam collector and subsequent change exchange transfer of these Hg^0 atoms to Hg^+ ions. This specific reaction process is only one of several possible processes which may occur as the result of the presence of an ambient gas in the testing chamber, and the interest of this section will be to examine facility pressure effects as they may affect the results from the plasma discharge neutralizer experiments, from the experiments on the combined neutralizer and thruster discharges, and, finally, from the fully operational thruster experiments. Because the largest interactive cross section between the various particle species is the charge exchange cross section between Hg^0 and Hg^+ ($\sigma_{CX} \sim 5 \times 10^{-15}$ cm^2) the principal focus in the discussion of this Section will be upon ambient Hg^0 atoms.

Pressure measurements in the chamber are obtained with ionization gauges, located at the chamber walls, and it should be noted that such measurements are not specific in the partial pressures of the various gas species in the chamber. The gas species present can include N_2, O_2, CO_2, A, diffusion pump vapors, H_2O and mecury. Because of the extensive wall area of LN_2 cooled shrouds, strong cryopumping of diffusion pump vapors, H_2O, and Hg^0 is expected. The area of LN_2 cooled surface visible from the testing chamber midpoint is approximately 10.5 m^2, and, for total sticking of a (cryopumpable) gas at the wall, the atom pumping rate is 2×10^{19} atoms per second for an ambient chamber pressure of 10^{-6} torr. This atom pumping rate is equivalent to $\sim$3 amperes of injected neutral flow of cyropumpable gas. If the injection rate is lowered to 300 milliamperes (equivalent) of neutral gas, the chamber equilibrium pressure should be $\sim 10^{-7}$ torr.

As the discussion in the subsections to follow will indicate, the injected ion species from the thruster, under its various operation conditions, are not, in general, accommodated at the walls on the first encounter, and multiple traversals of these particles may be required before sticking of the particle to a cryopanel. Neutral particles leaving the thruster have temperatures of the order of a few hundred degrees Kelvin and will probably stick to the cryosurfaces on the first encounter. Mercury atoms sputtered from the beam collector by energetic thrust ions have energies in the range of several electron volts and may require more than a single encounter with the cryopanels to be accommodated. The density of mercury atoms in various regions of the chamber will be determined by the various rates of material injection from the several source regions and the traversals required before (ultimate) atom attachment to the cold surfaces. The density of noncryopumpable gases will tend to be more uniform over the chamber volume, and may constitute the major portion of observed chamber pressure under some of the thruster operational conditions. These noncryopumpable gases will probably not, however, be the principal source of interactive effects with Hg^0 and Hg^+ because of the generally reduced magnitudes of nonresonant charge transfer compared to resonant charge transfer.

6.2 Pressure Effects for Neutralizer Plasma Plume Measurements

For nominal operation, the neutralizer vapor feed rate is approximately 7 milliamperes (equivalent) of Hg^0. From the present J_+ data in the plume (see Figure 32, for example) the ion current created in the neutralizer discharge and expanding into the testing chamber is of the order of 300 microamperes. In the orifice of the thruster neutralizer, neutral pressures are of the order of 1 torr, but as the neutral flow moves away from the orifice, the density drops rapidly and at a distance of $\sim$3 centimeters from the orifice this mercury flux has densities which correspond to $\sim 10^{-6}$ torr pressure. The cryopumping of such neutrals probably occurs on the first wall encounter, and pressure in the testing chamber due to this mercury injection is at extremely low levels except, as noted, within very small distances from the neutralizer orifice. The densities of Hg^+

in the expanding plasma plume are reduced from Hg^0 densities by a factor of ∿200 (resulting from a factor of 20 in production rate and a factor of 10 in streaming velocity). In the combined Hg^0 and Hg^+ released from the neutralizer, thus, the pressure is at low levels throughout almost the entirety of the testing chamber. Sputtering of cryopumped Hg^0 from the cold walls under Hg^+ impact does not occur because of the relatively low (10-15 eV) energies of these neutralizer plume ions.

During the measurements of the neutralizer plasma plume, chamber pressures on the ionization gauge ranged from 8×10^{-7} to 1×10^{-6} torr. From the discussion above, it is apparent that those indicated chamber pressures cannot be the result of Hg^0 and Hg^+ release into the chamber. The most likely explanation for the observed ionization gauge readings is that this pressure is the chamber pumping state for the various non-cryopumpable gases (principally N_2 and O_2). The critical question then becomes the extent to which any of these chamber species can alter the observed fluxes and energies of the Hg^+ ions in the neutralizer plume.

The mean free path for ion charge transfer in the Hg^+, Hg^0 reaction is $\sim 6 \times 10^3$ centimeters for Hg^+ moving through 10^{-6} torr of Hg^0. Thus, even if the entirety of ion gauge reading, described above was due to Hg^0, less than 3% of the Hg^+ produced by the neutralizer would engage in a charge transfer for ion motion along the complete flight path from the thruster neutralizer to the distant beam collector and less than 0.3% would charge transfer in the space between the neutralizer and the general location of the measuring probes. Ion interactions with the noncryopumpable gases are at gas kinetic cross sections or less, for which the cross section magnitudes are of the order of 10^{-16} cm^2. For Hg^+ interaction with N_2 and O_2, thus, the mean free paths at 10^{-6} torr (now assuming that the entirety of the gauge reading of 10^{-6} torr is N_2 or O_2) would be 3×10^5 cm and only 1 part in 10^3 of the ions would engage in a scattering interaction for a traversal of the total chamber length.

From the discussion above, these are strong grounds to believe that pressure effects have not influenced the ion measurements for chamber pressures at this 10^{-6} torr figure. The experimental evidence from the

Faraday cup/RPA tends to confirm this finding. In the data of Figure 30, the ion energies are rather strongly peaked indicating that the great bulk of the ions are formed at the approximate potential of the neutralizer keeper and move in the electric field of the plasma plume, gaining energy as the plasma potential lowers. If ions moving in the electric fields of the plume were to engage in charge transfer with an Hg^0, the result would be a broadening of the ion energy spectrum and a shift of the spectrum to lower energies. The absence of such broadening and such shifts and the cross section arguments given above indicate that the neutralizer plume measurements described earlier have not been materially affected by facility pressure effects.

6.3 Pressure Effects for Thruster Discharge and Neutralizer Discharge Plume Measurements

For the operational condition in which the thruster discharge and the neutralizer discharge are in operation (but ion acceleration voltages are not applied), a substantial increase in the Hg^0 release occurs, compared to the previously examined, neutralizer discharge only, case. For this combined discharge plasma plume, the Hg^0 vapor feed is set at ∿100 milliamperes equivalent and nominal values of discharge current and voltage are established in both the thruster discharge and in the neutralizer discharge. Ions are produced in the thruster discharge and, even in the absence of applied acceleration potentials, a low energy "ion beam" is created (see data in Figure 43 and 44). The total current in the ion beam is only a small fraction of the neutral mercury injection, however, because of the limited current acceleration in the potential fall between the thruster discharge plasma and the screen and accelerator electrodes. From Figure 44, it may be estimated that the ion current in the weakly energetic beam is of the order of 2 to 3 milliamperes. The great bulk of the injected Hg^0 into the thruster discharge must, then, eventually emerge from the thruster in the still un-ionized state.

From the discussion of system cryopumping capability in Section 6.1, it may be seen that system equilibrium pressure to pump 100 milliamperes of Hg^0 from the total chamber volume would be much less than 10^{-7} torr. The neutral Hg^0 density in the chamber is more complicated than this simple calculation, however, because of source size effects and ordered flow effects. The release of ~100 milliamperes equivalent of Hg^0 from the 8 cm diameter of the ion thruster accelerator grid opening causes a local Hg^0 density of ~4 x 10^{11} atoms/cm^3 near the thruster exit plane, with subsequent neutral density fall-offs in the downstream regions because of neutral flow expansion. For a charge exchange cross section (Hg^+, Hg^0) of 5 x 10^{-15} cm^2, the mean free path of an Hg^+ ion against charge transfer is ~500 cm for the gas densities at the thruster exit plane. The mean free path for charge transfer increases very rapidly, however, in moving to downstream locations because of the neutral plume expansion, and it may be estimated that less than 2% of the Hg^+ ions released by the thruster will charge transfer in the space between the thruster and the general location (Z ~24 cm) of the measuring Faraday cup/RPA. From this low charge transfer probability, it would appear that the ion energy spectrum in the weakly energetic beam should correspond generally to the potential fall between the thruster discharge plasma and the exterior plasma plume region. The data of Figure 43 appears to confirm these conclusions.

The ions released in the weakly energetic beam have energies of the order of 20 to 30 eV and beam currents of the order of 2 to 3 milliamperes. These ions will probably not accommodate to the beam collector on the first impact and will probably require a second encounter with the cold walls in order to be cryopumped. Ions of those low energies cannot sputter, however, and the passage of several milliamperes of rebounding "hot" neutrals cannot substantially eliminate Hg^0 densities in the chamber. The observed chamber ion gauge readings for this operational condition remained at the 1.0 x 10^{-6} torr readings discussed earlier in Section 6.2 for operation of the neutralizer discharge only. As noted earlier, there are reasons to believe that these gauge readings represent, in general, the non-cryopumpable chamber gases.

From all of the above considerations it would appear that there are no materially significant facility pressure effects for these measurements of the plume of the combined thruster discharge and the neutralizer discharge.

6.4 Pressure Effects for Fully Operational Ion Thruster Measurements

For a fully operational ion thruster, the total Hg^0 injection into the thruster is the same as for the "combined discharge" plasma plume measurements discussed in Section 6.3, above. The application of ion acceleration potentials, however, causes the mass release from the thruster to change from a fractionally small weakly energetic ion beam to a fractionally large beam of energetic ions. These energetic ions are not cryopumpable on the first cold wall encounter. The impact of these energetic ions on the beam collector, moreover, causes the release of any previously cryopumped atoms. The "loss" of the beam collector area as an effective sink for Hg^0 and the presence in the testing chamber of a series of particle flows emanating from the downstream wall surfaces does cause an observable rise in chamber pressure (as seen by the ionization gauge) and does cause facility effect pressure reactions. A specific facility effect reaction has been previously discussed in Section 5.1, in the backwards directed weakly energetic ion fluxes. For the fully operational ion thruster, then, facility pressure effects do exist and influence the particle efflux measurements. These facility effects are, moreover, not subject to elimination by the simple procedure of additional pumping of either the conventional form or via cryopumping in that the particle currents and densities involved are dynamic releases from specific boundaries under energetic ion impact.

While it is not possible to eliminate facility pressure effects for the fully operational ion thruster, it is considered to be possible to reduce these effects through a variety of methods including the use of larger testing facilities, the introduction of additional material boundaries, and, finally, the use of measuring probes with more narrowly directionalized entrance apertures.

7. SUMMARY

This appendix has detailed a series of measurements on the plasma plumes from ion thrusters under various operational conditions. The first condition examined was that of the operation of the neutralizer discharge only. This plasma plume has a floating potential only a few volts positive with respect to ground for probe locations of the order of 20 to 30 centimeters from the neutralizer. The source of the ions in the plasma is approximately at neutralizer keeper potential. The potential difference between the source and these more dilute regions of the plume is in the direction of ion acceleration radially outward, and, if ion energy loss does not occur, would result in the generation of ion energies of the order of 10 to 15 electron volts in the dilute regions of the plume. Subsequent determinations of the ion energy spectra with retarding potential analyzers has demonstrated that these ion energies are present. These results not only validate the postulated model of the plasma plume electron-driven sheath potentials but also demonstrate that the presence of residual gas (at low pressures) in the testing chamber has not materially affected the ion flow properties.

Because the ion energies in the plasma are substantially greater than kT_e, for plasma expansion to the probe locations, the ion trajectories are only slightly bent as the result of plume expansion over material boundaries. These comparatively sharp shadows in the umbra created in the flow by material boundaries indicates that sensitive surface placement in the umbra can effectively act to reduce the deposition levels of mercury ions. The adjustment of the boundary potential (for conducting materials) can act to reduce the electric fields in the sheath region between the material and the plasma plume and can, thus, create even more effective (reduced deposition) umbra regions. Alternatively, the misapplication of potentials to boundaries in the plasma plume can result in ion refraction into the umbra regions and a reduction in the shielding effectiveness of the boundary.

The imposition of a requirement for plural refraction in the ion trajectory in order to deposit on a given surface has also been examined using probes with more narrowly defined cones of direction in the entrance aperture. For these probes and for selected probe and material boundary configurations such that plural refraction is required for ion transport to the collecting surfaces, extraordinarily low levels of ion collection are observed. This result demonstrates that protection of sensitive surfaces can be carried out to very high levels of required cleanliness by suitable placement of boundaries such that plural ion refraction is required in order to reach the surface. Specific examples have been described in the text and have Hg^+ ion deposition levels of the order of 1 monolayer per thousand hours of thruster operation in this condition and for comparatively near r and Z placement of the surface from the thruster. Still further reductions in these deposition levels will be obtained for more distant placement of surface from the thruster.

The second condition of thruster operation examined was the combined operation of the neutralizer discharge and the thruster discharge but without the application of acceleration potentials. For this second operational condition the Hg^0 and Hg^+ release levels are at $\sim$100 milliamperes (equivalent) and $\sim$2 to 3 milliamperes. Both of these levels are approximately one order of magnitude over the Hg^0 and Hg^+ release for the operation of the discharge neutralizer only. In spite of this increased Hg^0 and Hg^+ release rate, the data confirms that facility pressure effects have not altered the properties of the ion flow.

Measurements of the plasma potential in the exterior plume reveal a plasma which is positive by $\sim$1 to 2 volts with respect to the chamber walls. The ions in the plasma plume posses energies which correspond fairly accurately to the potential fall between the plasma discharge on the thruster interior and the exterior plasma plume. These potential increments (ranging from 20 to 30 volts) produce, thus, a weakly energetic ion "beam." The ion energies, though small, are, however, many times larger than kT_e and expansions of the plasma past material boundaries does not result in appreciable ion refraction. The conclusions stated above relative to sensitive surface protection for the plasma plume of the neutralizer discharge are, thus, equally valid for this combined discharge operation.

The final condition of operation examined in the experiments was a fully operational ion thruster. For this operational condition, it is apparent that the presence of facility walls does create particle fluxes which can interfere with and mask the particle current fluxes which would be observed for an ion thruster operating in an unbounded geometry. The principal form of these facility effect fluxes is a flow of weakly energetic ions in the backward direction. This backwards traveling efflux is primarily the result of Hg^0 release from the beam collector (either by sputtering or by impact and neutralization, without sticking, of a thrust ion) with subsequent charge transfer to Hg^+ via an (Hg^0, Hg^+) charge transfer reaction. The electric field structure in the plasma plume of the fully operational ion thruster has been determined and a general level of understanding of facility effect particle motion in these fields has been developed and described.

The results of the full beam ON measurements and the comments above do not lead to the conclusion that the measurement of the genuine particle effluxes cannot proceed beyond certain desirable lower levels. A specific example has been described in which current fluxes at the 10^{-11} and 10^{-12} A/cm^2 levels have been carried out in the testing facility and in spite of the presence of facility effect particles. These latter experiments, utilizing measuring probes with a reduced cone of ion acceptance directions, indicate that the use of specially configured probes and the use of specially configured material boundaries can reduce these facility presence effect fluxes. The use of even larger testing chambers appears also as a worthwhile direction of development in future testing.

In summary for the total series of measurements, the ion deposition levels for the neutralizer discharge only and for the combined discharges of the thruster and the neutralizer have been demonstrated to be at levels which can satisfy even the most stringent of spacecraft surface contamination requirements. These remain some unresolved questions on the extent and nature of facility effect particles for the fully operational thruster and methods for the reduction of these facility effect fluxes appear to be within the realm of possibility for comparatively modest extensions in present laboratory testing techniques.

APPENDIX B

RECIRCULATION OF ELECTRIC THRUSTER IONS IN THE MAGNETIC FIELD OF THE EARTH AND POSSIBLE ION REINTERCEPTION ON SPACECRAFT SURFACES

CONTENTS

ILLUSTRATIONS

ILLUSTRATIONS (Continued)

APPENDIX B

RECIRCULATION OF ELECTRIC THRUSTER IONS IN THE MAGNETIC FIELD OF THE EARTH AND POSSIBLE ION REINTERCEPTION ON SPACECRAFT SURFACES

1. INTRODUCTION

This appendix will consider the material transport of ions, released by a mercury ion thruster, in the magnetic field of the earth. Under certain circumstances, the $\vec{v}_+ \times \vec{B}_e$ force, where $\vec{v}_+$ is the ion vector velocity and $\vec{B}_e$ is the magnetic field of the earth, can cause a released ion to recirculate in such a manner as to reintercept the surfaces of the spacecraft bearing the electric thruster. The principal focus of this appendix will be the derivation of the expected levels of such material transport. These transport levels will be used, in turn, to determine if deposition levels of significance can occur during certain projected ion thruster missions.

The appendix will first examine the general conditions of ion recirculation and will identify those portions of a spacecraft orbit, for an earth orbiting spacecraft, in which ion recirculation/reinterception is dynamically allowed and those portions for which this transport is dynamically forbidden. For the dynamically allowed cases the "focus conditions" will be determined. Those focus conditions are the ion vector directions and energies such that the ion reintercepts the spacecraft at the precise point of the earlier departure of the ion. Realizable spacecraft, however, have finite surface areas and variations in the precise values of the ion direction angles and velocity are possible for ion trajectory reinterception over those broader regions of spacecraft surface. To determine the permissible range in angles and energies requires the derivation of the dispersion functions in the ion motion. The dispersion functions must be coupled, in turn, to the expected distribution functions, in direction and energy, of the released ions for the final calculations of the expected normalized efflux coefficients for this mode of material transport. Following these normalized efflux coefficient calculations, the appendix will summarize its findings in terms of expected interactive effects as the result of mercury ion transport and deposition on spacecraft surfaces.

2. DYNAMICALLY ALLOWED AND DYNAMICALLY FORBIDDEN REGIONS FOR ION RECIRCULATION/REINTERCEPTION ON SPACECRAFT SURFACES

The interest of this appendix will be for spacecraft in circular, near earth, orbits. Results of the analysis are generally applicable, however, and restriction of attention to this particular case is to focus the analysis on spacecraft orbit and magnetic field conditions which act to produce the highest possible levels of this mode of material transport. If it can be demonstrated that particle transport under these conditions is at tolerable levels, then extension of the findings to other (lower level transport) conditions will require no further analytical effort.

An ion released from the thruster will be subject to the forces stated in the Lorentz equation

$$\vec{f}_+ = q_+(\vec{E} + \vec{v}_+ \times \vec{B}) \qquad \text{(1)} \ \text{(MKS)}$$

where q_+ is the ion charge in coulombs, $\vec{E}$ is electric field in volts per meter, $\vec{v}_+$ is the ion velocity in meters per second, and $\vec{B}$ is magnetic field in webers per meter^2. In the MKS system used here, the force, $\vec{f}$, is in newtons.

The analysis will consider that the ion is sufficiently removed from the thruster neutralization (electron injection) regions that electric fields in these regions are no longer present and that the only force remaining is that due to the $\vec{v}_+ \times \vec{B}$ term in Equation (1). The analysis, thus, neglects any $\vec{E}$ fields in the space plasma. Also to be neglected in this analysis are coulomb scattering effects. The magnetic field to be used in Equation (1) will be $\vec{B}_e$, the magnetic field of the earth. Because the cyclotron orbits of the ions are small compared to the general dimensions of the earth's magnetic dipole, the $\vec{B}_e$ term remains fixed during the course of the initial ion recirculation motion.

With the assumptions above, Equation (1) becomes

$$\vec{f}_+ = q_+(\vec{v}_+ \times \vec{B}_e) \qquad \text{(1)}$$

and the ion motion is that of a helix. The velocity of the ion at the instant of its release from the thruster and into the $\vec{B}_e$ recirculation field has components $\vec{v}_{\parallel}$ and $\vec{v}_{\perp}$, both parallel and perpendicular to $\vec{B}_e$. The helical motion of the ion lies on a cylinder whose axis has the vector direction of $\vec{v}_{\parallel}$ and whose radius, R, is given by

$$R = \frac{M_+ v_\perp}{q_+ B_e} \qquad (2)$$

where M_+ is ion mass in kilograms, and $v_\perp$ is the magnitude of $\vec{v}_\perp$, the component of ion velocity perpendicular to $\vec{B}_e$. For the MKS system used, R is in meters.

Figure 1 illustrates the cylinder on which the helix of the ion motion in $\vec{B}_e$ is placed. The spacecraft position at the instant of ion release ($t = 0$) into $\vec{B}_e$ is denoted as point 0 on this cylinder. If the ion is to reintercept the spacecraft, then the spacecraft motion after $t = 0$ must be such as intercept the cylinder on which the ion trajectory is contained. Figure 1 illustrates three conditions of the spacecraft motion relative to this cylinder. In the first of these conditions the spacecraft motion subsequent to $t = 0$ does cause the spacecraft to reintercept the cylinder. In this case ion reinterception is dynamically allowed, and ion reinterception will occur provided that certain "focus" conditions in the ion direction angles and energy are satisfied. In Condition 2, ion reinterception on spacecraft surfaces is dynamically forbidden in that the spacecraft motion encounters the ion motion cylinder only at $t = 0$, the instant of release. Condition 3, included for generality, permits ion reinterception. Condition 3 is, however, of only limited interest in that precise alignment between the spacecraft velocity vector, $\vec{v}_s$, and $\vec{B}_e$ is required. While such alignment is, in principle, possible for a spacecraft in orbit, the periods of time for such alignment are vanishingly small for spacecraft in near-earth orbits.

The analysis to be conducted in the following sections will examine the spacecraft motion and ion motion configuration illustrated in Condition 1 of Figure 1. Before proceeding to these analyses, however, it is of interest to examine the relative periods of time during a spacecraft orbit in which ion recirculation/reinterception is dynamically allowed and dynamically forbidden.

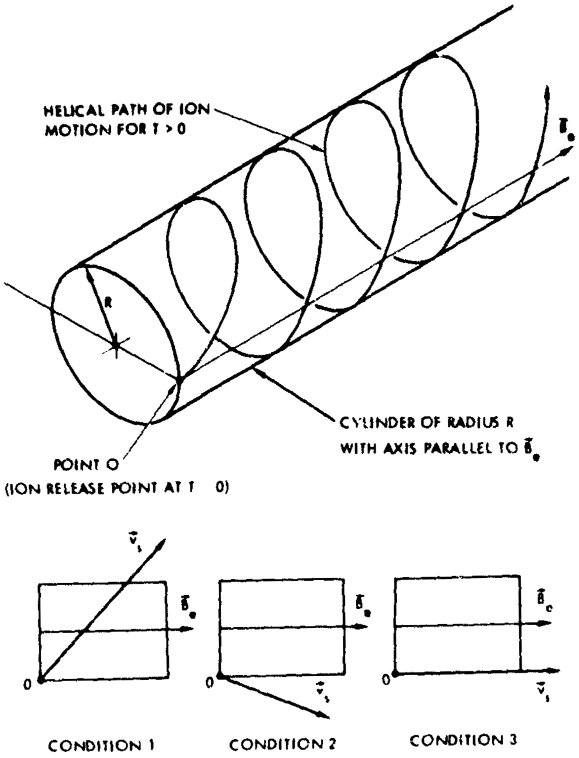

Figure 1. Helix of Ion Motion and Supporting Cylinder for Ion Recirculation in $\vec{B}_e$, and Three Possible Configurations of Spacecraft Velocity, $\vec{v}_s$, Relative to the Supporting Cylinder

3. ORBITAL AND MAGNETIC FIELD CONDITIONS FOR DYNAMICALLY ALLOWED AND DYNAMICALLY FORBIDDEN ION RECIRCULATION/REINTERCEPTION

It will be assumed in the initial discussion in this section that the magnetic field of the earth can be represented by a magnetic dipole. It will also be assumed that the axis of this magnetic dipole coincides with the axis of rotation of the earth. Figure 2 illustrates the orientation of the spacecraft velocity vector, $\vec{v}_s$, relative to $\vec{B}_e$ for a spacecraft in a circular equatorial orbit. In the Cartesian coordinate system shown there, the X axis coincides with $\vec{v}_s$, and the Z axis is along the (zenith) direction of the local vertical. For the circular equatorial orbit condition and the assumed dipole magnetic field and field alignment, $\vec{B}_e$ will be along the Y axis of this system throughout the course of an orbit.

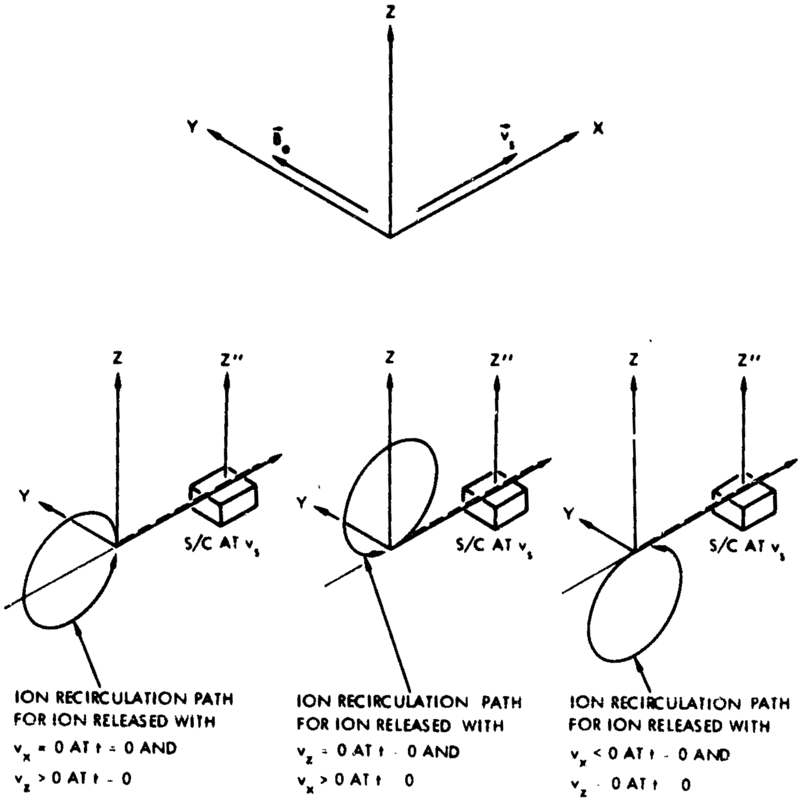

Figure 2. Orientation of $\vec{v}_s$ and $\vec{B}_e$ for a Spacecraft in a Circular Orbit at the Magnetic Equator and Ion Recirculation Trajectories (and Simultaneous Spacecraft Motion) for Ions Released by a Top-Mounted Thruster on the Spacecraft

For the spacecraft velocity and magnetic field configuration in Figure 2 and for a "top-mounted" thruster (thruster axis along the +Z axis), it can be demonstrated that it is dynamically forbidden for any thruster ion to recirculate in $\vec{B}_e$ and to reintercept the spacecraft. This follows from Equation (1) and the use of the ion velocity vector restrictions for the top mounted thruster. From Equation (1),

$$
\begin{aligned}
f_x &= -q_+ \, v_z \, B_e \\
f_y &= 0 \qquad\qquad (3) \\
f_z &= q_+ \, v_x \, B_e
\end{aligned}
$$

where $\vec{v}_+ = \vec{i}\, v_x + \vec{j}\, v_y + \vec{k} v_z$ in the Cartesian frame of Figure 2. Because $v_z \geq 0$ for all ions released by the top-mounted thruster, $f_x \leq 0$ for all ions. Because $f_x \leq 0$, the center of curvature for any ion released from the top-mounted thruster lies in the backward hemisphere of directions from the spacecraft velocity vector, $\vec{v}_s$, and the cylinders which contain the various helices for the trajectories of the ions circulating in $\vec{B}_e$ intersect the spacecraft path of motion at only the single point at $t = 0$ at which the ion was released. This corresponds to Condition 2 in Figure 1 (dynamically forbidden interception). For convenience Figure 2 illustrates several possible ion circulation patterns, demonstrating that reinterception of the spacecraft surfaces is forbidden in this present example.

The results illustrated in Figure 2 and discussed do not mean that reinterception is forbidden for all possible thruster mounting configurations for this equatorial orbit condition. A rear-mounted thruster and a bottom-mounted thruster both have dynamically allowed reinterception. Figure 3 illustrates several ion velocity conditions at the instant of release. For some conditions reinterception is allowed (cases where $v_z < 0$ at $t = 0$) and in other conditions, reinterception is forbidden. It should be emphasized that, even for allowed reinterception ($v_z < 0$ at $t = 0$), that other velocity conditions must also be met. In the present example of $\vec{v}_s$ along the X axis and $\vec{B}_e$ along Y, the ion must have zero velocity in the Y direction to recirculate and to reintercept the spacecraft. The ion must also have a specific magnitude of release velocity to reintercept the spacecraft. These focus conditions will be derived in Section 4 for reinterception of the ion with a "point"-sized spacecraft, and Section 5 will derive the conditions for reinterception on finite sized spacecraft.

The conditions illustrated in Figures 2 and 3 have been for an equatorial circular orbit, for a magnetic dipole representation of $\vec{B}_e$, and for the coalignment of the magnetic dipole axis with the axis of the spacecraft orbit. Another illustrative case is a polar orbiting spacecraft, with $\vec{B}_e$ again represented by a magnetic dipole. Figure 4 illustrates the direction of $\vec{B}_e$ during a complete polar orbit for a Cartesian coordinate system in which the X axis is the direction of spacecraft velocity, $\vec{v}_s$, and the Z axis is the upward direction along the local vertical. For this polar orbiting

ION ORBITS FOR REAR MOUNTED THRUSTER

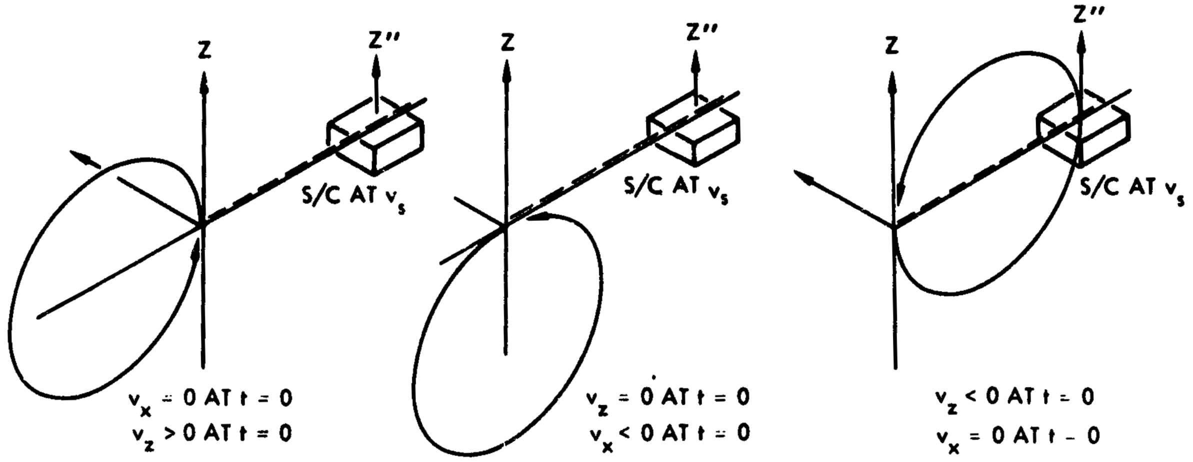

ION ORBITS FOR BOTTOM MOUNTED THRUSTER

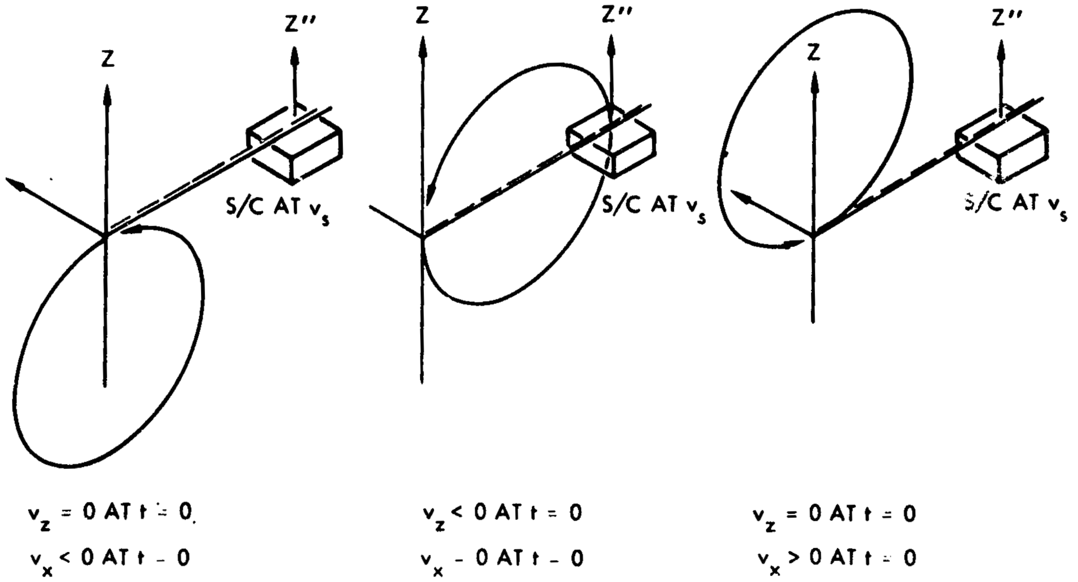

Figure 3. Ion Recirculation Trajectories for a Spacecraft in a Circular Orbit at the Magnetic Equator and for Ions Released from a Rear-Mounted Thruster and a Bottom-Mounted Thruster

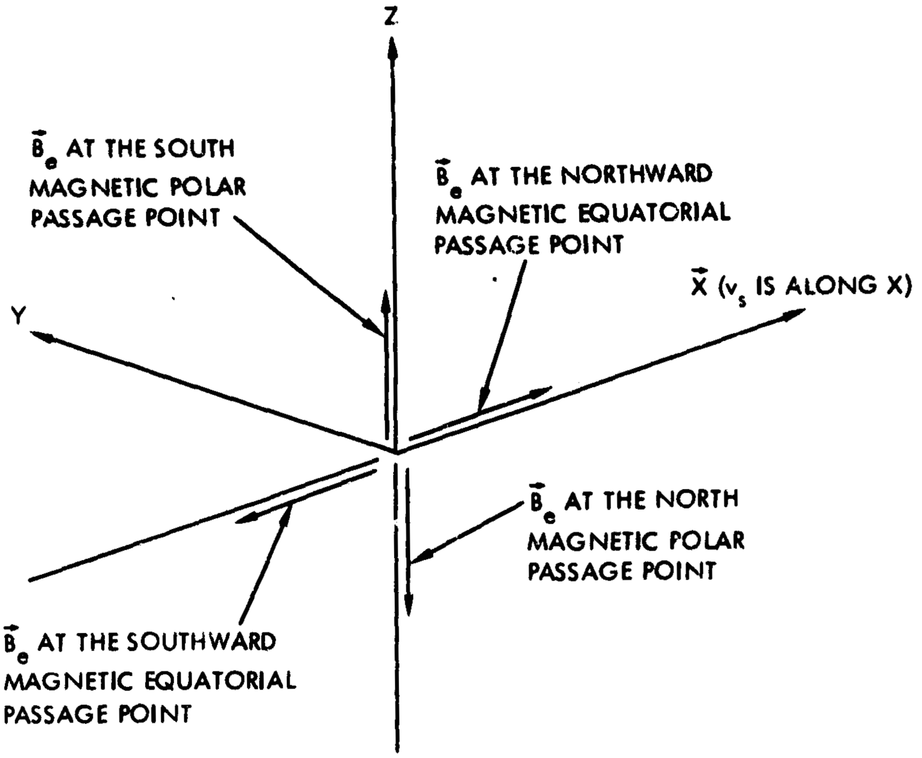

Orientation of $\vec{B}_e$ Relative to $\vec{v}_s$ in the Earth Frame Coordinate System for a Spacecraft in a Polar Orbit (magnetic field assumed as dipole with axis aligned with earth axis)

spacecraft, there are periods of the orbit in which specific ion release angles prevent reinterception and in which other ion release angles can result in reinterception. The general case here is more difficult to describe than for the equatorial orbit case described earlier. As a rule, however, and considering the entire orbit, half of all ion release angles lead to dynamically forbidden reinterception. Of the remaining half of all ion release angles (and which are dynamically in the "allowed" region), only a very small fraction can satisfy the focus conditions.

A particularly interesting condition for the polar orbiting spacecraft occurs during the magnetic equatorial passages. Figure 5 illustrates the condition of the northward equatorial passage during which $\vec{v}_s$ is parallel to $\vec{B}_e$. This parallel relationship between $\vec{v}_s$ and $\vec{B}_e$ corresponds to Condition 3 in Figure 1. In Condition 3 and in the configuration illustrated in Figure 5, all values of v_y and v_z in the ion velocity create helices whose supporting cylinders contain the spacecraft velocity vector. This would

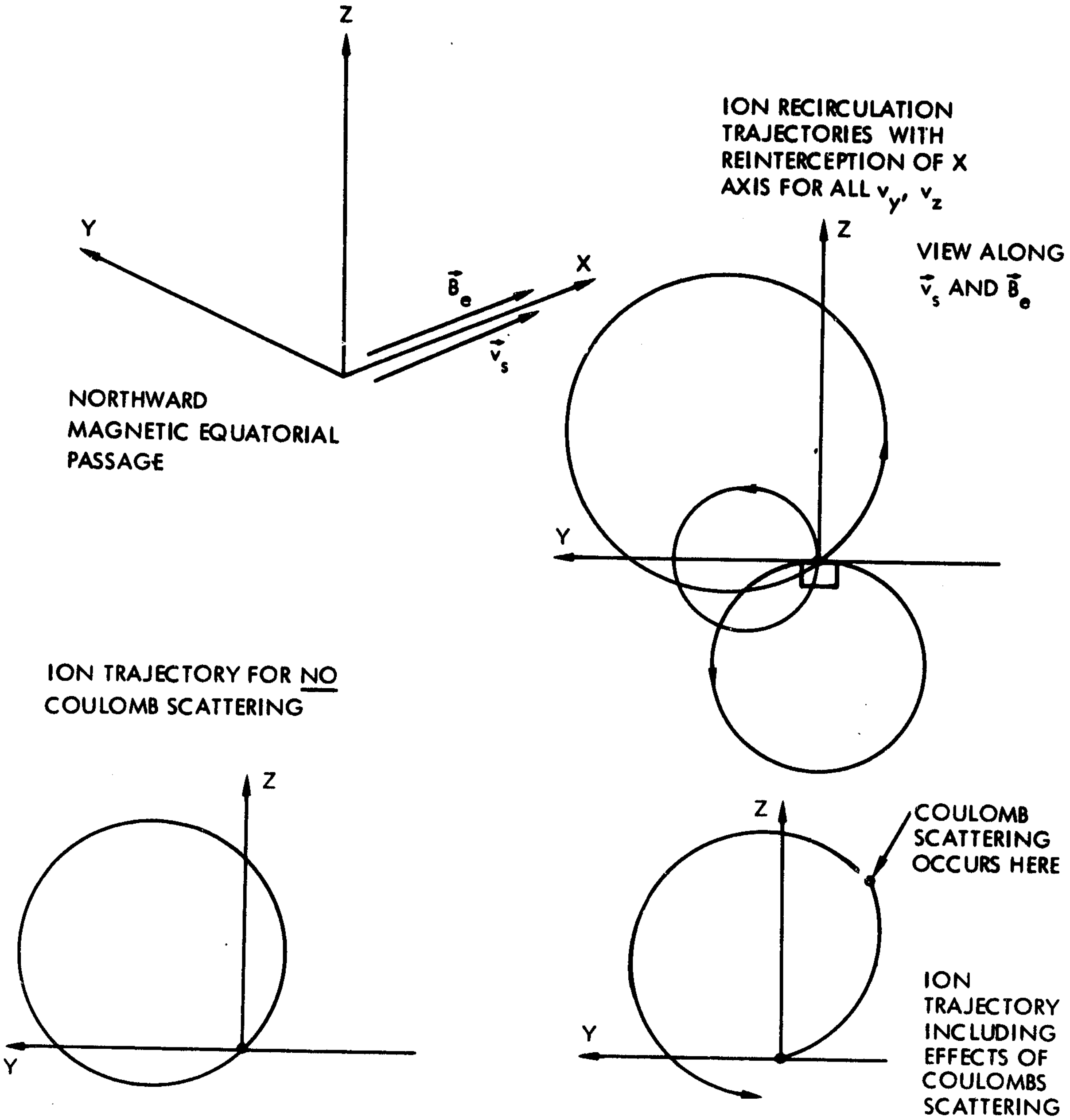

Figure 5. Ion Recirculation for the Northward Passage of the Magnetic Equator for a Polar Orbiting Spacecraft, Including Effects of Coulomb Scattering

appear to result in very high levels of reinterception with the spacecraft. It should be noted, however, that only those ions whose v_x at release equals v_s can reintercept the spacecraft, and only a small fraction of the released ions now lie within the acceptance band for reinterception. Two other factors also serve to mitigate the effects of ion recirculation in this special case. The first factor is that only minor coulomb scatterings of the ions as they make their (comparatively lengthy) helical motion through the space plasma are required to disperse the trajectories and thus to diminish the apparent focusing effects shown in Figure 5. These coulomb scattering interactions have not been included in the analysis of this appendix but should be reviewed in any dynamical situation in which perfect helical motion of many separate particle trajectories will be required to create a focusing effect. A second mitigating circumstance is that a condition of $\vec{v}_s \parallel \vec{B}_e$ within the required precision to produce the illustrated trajectories in Figure 5 is of only brief duration in the assumed polar orbit. The rate of change of magnetic field direction with respect to $\vec{v}_s$ is approximately 0.2 degree per second during equatorial passage, and the Condition 3 of Figures 1 and 5 is present for only small fractions of a second on any particular equatorial passage. A final, and more general condition is that $\vec{v}_s \parallel \vec{B}_e$ may never occur for lower inclination orbits in the actual magnetic field of the earth.

A final area of interest for this present examination of spacecraft velocity and magnetic field orientation effects is the expected orientation of $\vec{v}_s$ and $\vec{B}_e$ for a spacecraft in a high inclination orbit and for actual values and orientations of the earth's magnetic field. For a high inclination orbit (for example, at 60 degrees or greater inclination) the magnetic field at the maximum northerly and maximum southerly passage point is almost completely along the local vertical direction. As the spacecraft passes the magnetic equator (magnetic field in the local horizontal direction only) the minimum angle between $\vec{v}_s$ and $\vec{B}_e$ occurs. Because of declination effects (departure of the magnetic field from the true northerly direction) it is possible for $\vec{v}_s$ and $\vec{B}_e$ to be parallel for a brief period of time on occasional orbits and for sufficiently high orbital inclination. On the northern magnetic equatorial passage, and for sufficiently high orbital inclination, the range of $\vec{B}_e$ can include positive and negative B_y values as is illustrated in Figure 6. The southern magnetic equatorial passage also illustrated in Figure 6 can also include both positive and negative B_y values. These small angle conditions between $\vec{v}_s$ and $\vec{B}_e$ are of specific interest because of the possibly enhanced levels of transport in this configuration (see discussion above on Condition 3 configurations). Because a complete analysis of all orientations of $\vec{v}_s$ and $\vec{B}_e$ is not instructive, and because this examination of mass transport should focus on those configurations where the transport is expected to be at the larger of the possible range of values, attention will be devoted to the condition of magnetic equatorial passage and for a range of angles between $\vec{v}_s$ and $\vec{B}_e$ for that condition in which $\vec{B}_e$ lies in the X-Y plane, with a major component along the direction of the X axis, and with a minor component along the -Y' axis.

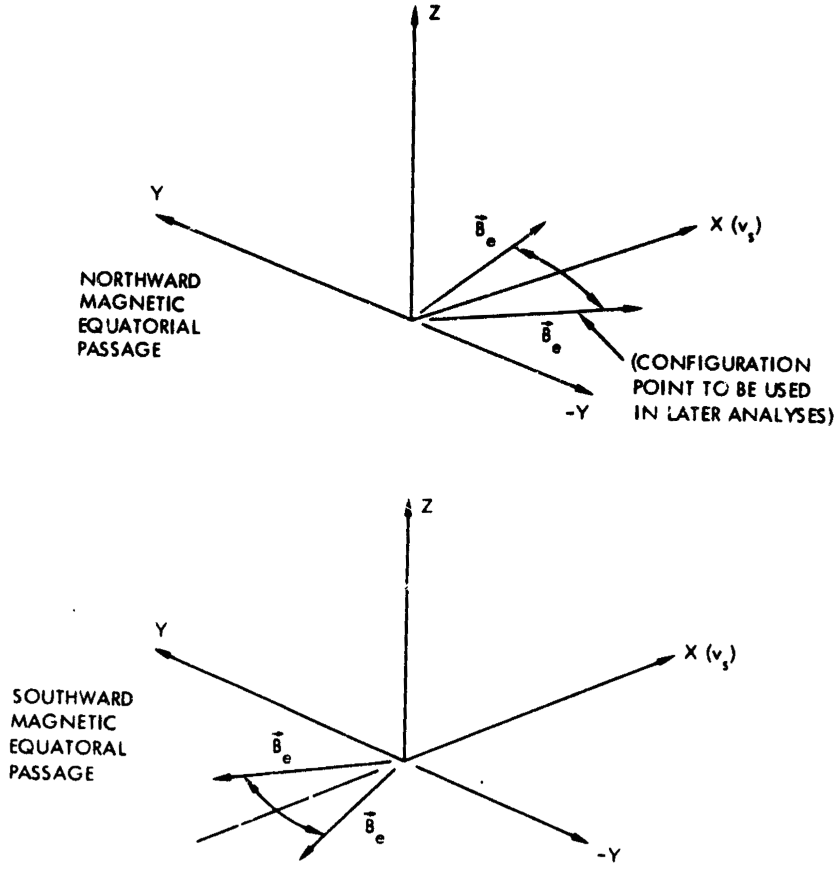

Figure 6. Possible Range of Orientation of $\vec{B}_e$ Relative to $\vec{v}_s$ for Magnetic Equatorial Passage of a High Inclination (Circular) Orbiting Spacecraft and with Actual Earth's Magnetic Field Declination Effects Included

4. POINT-TO-POINT ION RECIRCULATION FOCUS CONDITIONS

This section will derive the necessary ion angles of emission and ion emission energy such that the released particle will recirculate in the magnetic field and will reintercept the spacecraft at the precise point of the ion release. The configuration between the spacecraft velocity, $\vec{v}_s$, and the magnetic field of the earth $\vec{B}_e$, to be used in this "focus condition" derivation is illustrated in Figure 7. The choice of the configuration shown there follows from the discussion in the final portions of Section 3.

The Cartesian coordinate systems illustrated in Figure 7 will be termed the "earth frame" and the "magnetic field frame." The spacecraft velocity vector, $\vec{v}_s$, is along the X axis of the earth frame and the Z axis is the upward local vertical. The vector $\vec{B}_e$ lies in the X-Y plane ($B_{ex} > 0$, $B_{ey} < 0$) and is at angle, η, with respect to $\vec{v}_s$ in the earth frame. B_e also lies along the x' axis of the magnetic field frame.

The ion is released from the spacecraft at $t = 0$ at which time the spacecraft is at the origin (0, 0, 0) of the earth frame. Because the spacecraft moves along the X axis of this frame at v_s, the X-position of the spacecraft is

$$X_{S/C} = v_s\, t \tag{4}$$

while $Y_{S/C} = Z_{S/C} = 0$ for all t.

The ion motion in the $\vec{v}_+ \times \vec{B}_e$ force can be viewed more easily by an initial separation of the ion velocity, at release, into velocity components parallel and perpendicular to $\vec{B}_e$. Because the $\vec{v}_+ \times \vec{B}_e$ force vanishes along the $\vec{B}_e$ direction, ion velocity parallel to $\vec{B}_e$ remains constant. Denoting this parallel velocity component of $\vec{v}_+$ as $v_{||}$, it follows that the ion position at t, after its release at $t = 0$ must be in a plane whose distance from the origin is $v_{||}t$. Figure 7 illustrates this plane in a view along the -Z axis. Figure 7 also illustrates the plane containing the spacecraft at time t, viewed in this same direction. If the ion is to reintercept the spacecraft, it is required that these two planes must coincide at the time of reinterception T. This requires that

$$v_s(\cos \eta)\, T = v_{||}\, T$$

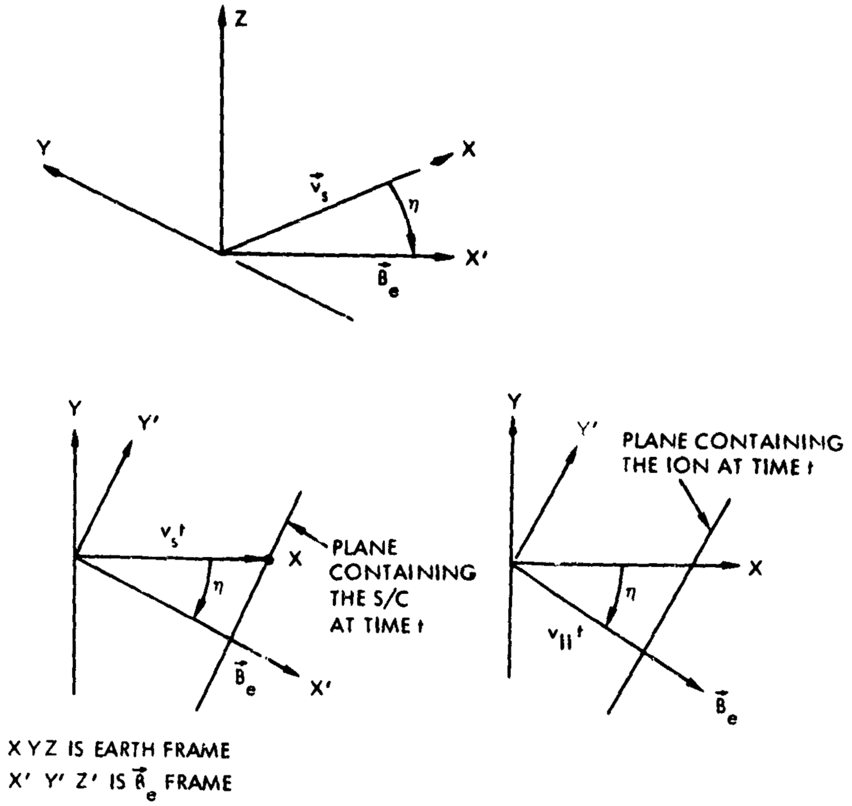

Figure 7. Earth Frame and Magnetic Field Frame Coordinate Systems and Planes Containing the Ion and the Spacecraft for t > 0 (Instant of Ion Release)

from which the first of the two focus conditions is given:

$$v_{||} = v_s \cos \eta \tag{6}$$

The second of the focus conditions is somewhat more difficult to visualize. Figure 8 provides a view in the direction of $\vec{B}_e$, of the spacecraft and ion motion. In this view (along the X' axis) the spacecraft has an apparent velocity along the Y' axis of

$$v_{S/C}\,(Y') = v_s \sin \eta \tag{7}$$

The ion velocity in this presentation is the perpendicular component, $v_\perp$, and the ion moves in a circle of radius

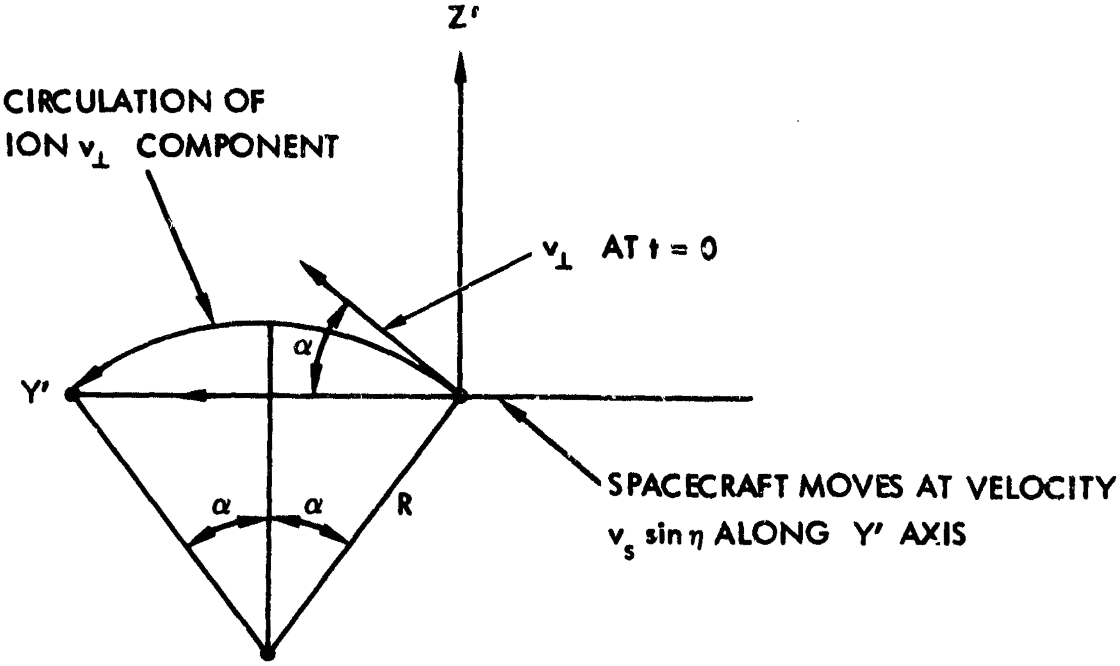

Figure 8. Ion Motion in $\vec{B}_e$ in a View Along the +X' Axis of the Magnetic Field Frame

$$R = \frac{M_+ \, v_\perp}{q_+ \, B_e} \qquad (2)$$

The angle α illustrated in Figure 8 is the angle between the plane containing $\vec{B}_e$ and $\vec{v}_\perp$ at t = 0 and the X'Y' plane.

The ion acquires a nonzero Z' coordinate during its rotation around $\vec{B}_e$. To reintercept the spacecraft, however, the ion must be at Z' = 0 because the spacecraft remains at Z' = 0. If the time of reinterception is T, it also is required that the Y' value of the ion at T be equal to the Y' value of the spacecraft at T. Now the arc-length along the segment of the circle is 2 Rα and the time for the ion to traverse this arc length at $v_\perp$ is

$$T = \frac{2 \, R\alpha}{v_\perp} \qquad (8)$$

The chord length from the origin of the Y'Z' origin is $2R \sin \alpha$ and the time required for the spacecraft to traverse this distance is

$$T = \frac{2R \sin \alpha}{v_s \sin \eta} \tag{9}$$

For reinterception to occur, the time, T, in Equation (8) must equal the time, T, in Equation (9). This leads to

$$\frac{2R \sin \alpha}{v_s \sin \eta} = \frac{2R\alpha}{v_\perp} \tag{10}$$

from which the second of the two focus conditions is given

$$v_\perp = v_s \sin \eta \left(\frac{\alpha}{\sin \alpha} \right) \tag{11}$$

The specification of v_s, η, and α thus determines the $v_\parallel$ and $v_\perp$ of the ion which determines the ion energy for a point-to-point reinterception and the required angles of emission for the reinterception. It should be emphasized that the angle α is a variable and, thus, a continuous range of ion energies and angles of emission are possible leading to reinterception. For a particular ion energy, however, only a single direction of release can lead to reinterception.

The specification of the focus conditions in Equations (5) and (11) does not allow an immediate recognition of the ion properties as viewed at the thruster locations. It should be emphasized that the $v_\parallel$ and $v_\perp$ stated thus far are relative to the magnetic field. The knowledge of the ion properties in the thruster plume, however, is in the thruster frame which is at rest with respect to the spacecraft but is in motion, at velocity v_s, with respect to the earth frame. Figure 9 illustrates these two coordinate systems. The spacecraft frame (in which the thruster is at rest) moves along the X axis of the earth frame at v_s. For a velocity transformation between the spacecraft frame and the earth frame

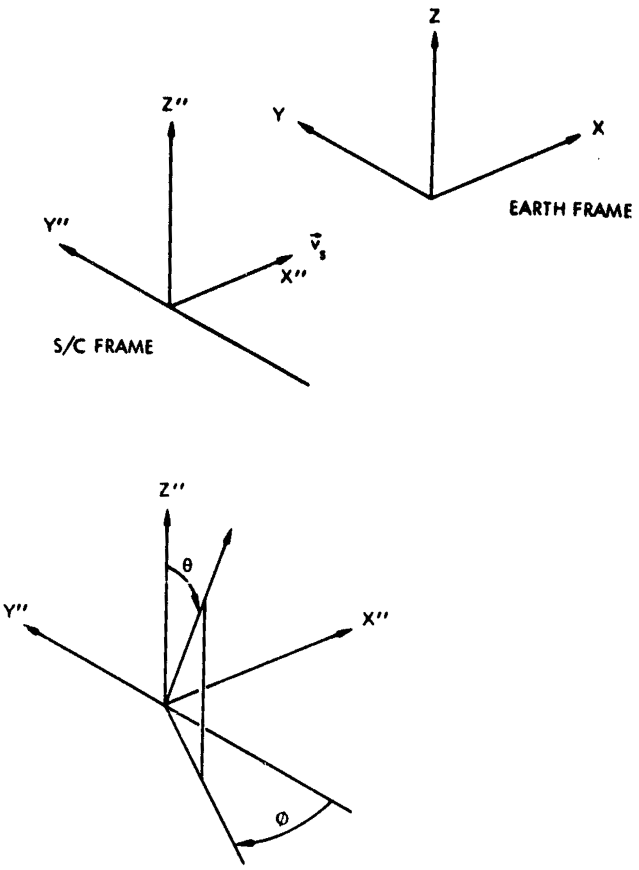

Figure 9. Spacecraft Frame (X", Y", Z") Orientation and Motion Relative to the Earth Frame (X, Y, Z). Also shown are the polar and azimuthal angles for ion recirculation in $\vec{B}_e$ with Reinterception on spacecraft surfaces.

$$
\begin{aligned}
v_{x''} &= v_x - v_s, \\
v_{y''} &= v_y, \\
\text{and} \quad v_{z''} &= v_z .
\end{aligned}
\tag{12}
$$

The knowledge of the ion velocity in the magnetic field frame ($v_\parallel$, $v_\perp$) and the orientation of the magnetic field frame with respect to the earth frame allows $v_\parallel$ and $v_\perp$ to be stated in the earth frame, and Equation (12) then allows the ion velocity to be stated in the spacecraft frame. Most ion thruster plume diagnostics, however, are carried in a polar coordinate system whose polar axis is the axis of the ion thruster. For a top-mounted thruster, the thrust axis is along the Z" direction and the polar and azimuthal angles are as illustrated in Figure 9, with a particular choice shown there for the origin and direction of the azimuthal angle, ϕ.

The burden of the mathematical action in the statement of the focus condition then becomes the transformation of $v_{\parallel}$ and $v_{\perp}$ (which are known relative to $\vec{B}_e$) to the earth frame, with a subsequent transform from the earth frame to the spacecraft (thruster) frame. These coordinate transformations will not be carried out in detail in this discussion, but Attachment 1 to this appendix will carry out the transformations and the subsequent use of these transforms in the calculations of dispersion coefficients.

The transformation which provides ion laboratory angles and energies from ion angles and energies in the spacecraft frame is

$$\gamma = \left(1 - 2\gamma'' \sin\theta \sin\phi + (\gamma'')^2\right)^{1/2} \tag{13}$$

$$\beta = \cos^{-1}\left(\cos\eta\left(\frac{1 - \gamma''(\sin\theta \sin\phi)}{\gamma}\right) + \sin\eta\left(\frac{\gamma'' \sin\theta \cos\phi}{\gamma}\right)\right) \tag{14}$$

and

$$\alpha = \sin^{-1}\left(\frac{\gamma''}{\gamma}\frac{\cos\theta}{\sin\beta}\right) \tag{15}$$

where θ and ϕ are the ion polar and azimuthal angles in the spacecraft frame, γ is the ion velocity in the earth frame normalized to v_s, γ'' is the ion ion velocity in the thruster frame normalized to v_s, the angles α and η have been previously defined, and β is the angle between $\vec{v}_+$ in the laboratory frame and $\vec{B}_e$ (see Attachment 2 for figures illustrating these angles and transforms). A reverse transformation (which derives γ'', θ, and ϕ from an initially stated η and α) also has been derived but will not be stated here.

The various transformations described above have been programmed into a computer and a series of transforms between initial α and η and the thruster frame have been carried out. Although these computational printouts will not be reported in detail in this appendix, it will be instructive to list a series of values of θ, φ, and ion energy in the thruster frame for stated η and α in the laboratory frame. These values are given in Table 1 for η = 30 degrees and α ranging from 5 to 165 degrees. Several features of these calculations are of interest. The first is that near the thruster axis ($\theta \rightarrow 0$ for the top-mounted thruster), the focus condition is for very weakly energetic ions (energies of the order of eV or less), while large θ values ($\theta \rightarrow 90$ deg) require ion energies in the ranges of kiloelectron volts. These focus conditions are of interest for this top-mounted thruster in that the expected ion properties in the thruster plume (very energetic ions at small θ, weakly energetic ions at large θ) directly reverses the focus condition. This indicates that the match-up between the ion release properties in the top-mounted thruster and the required focus properties is small and may be almost totally noninclusive. This, in turn, indicates a very low level of ion recirculation and reinterception on spacecraft surfaces.

Table 1 also lists values of θ, ϕ, and ion energy for η = 20 deg and 10 deg and for α ranging from 5 to 165 degrees. The behavior patterns shown earlier for the η = 30 deg case in Table 1 are also present for η = 20 deg and 10 deg. These data will also be used in the calculation of dispersion coefficients for various orientations between $\vec{B}_e$ and $\vec{v}_s$ (see Section 5).

A final area of interest in this section is to examine the findings in focus conditions in terms of a rear-mounted thruster. A rear-mounted thruster will have its thrust axis along the -X" axis and will, thus, have energetic ions emerging at large angles with respect to Z". The rear-mounted thruster will also have weakly energetic ions emerging at large angles with respect to X" which leads to some weakly energetic ions at small angles with respect to Z". From this it would appear that the match-up between ion release properties and the focus conditions is somewhat better for the rear-mounted thruster than for the top-mounted thruster. While this match-up may, in fact, be improved, the following sections will examine the expected ion transport for the top-mounted thruster and will demonstrate that this transport is at such reduced levels that the treatment of both top- and rear-mounted thrusters is not required. An additional point to note is that the treatment of the top-mounted thruster is mathematically simpler because the θ, ϕ angles stated with respect to Z" are

Table 1. θ, ϕ, and Ion Energy in the Thruster (Spacecraft) Frame as f(α) and η = 30, 20, 10 Deg
Assumed Spacecraft Velocity of 7.7 km/s

	Ion Angles and Energies for Point-to-Point Recirculation/Reinterception								
	$\eta = 30^0$			$\eta = 20^0$			$\eta = 10^0$		
α (deg)	θ (deg)	ϕ (deg)	E" (eV)	θ (deg)	ϕ (deg)	E" (eV)	θ (deg)	ϕ (deg)	E" (eV)
5	1.67	30	0.12	1.67	20	0.05	1.67	10	0.01
10	3.34	30	0.47	3.34	20	0.22	3.34	10	0.06
15	5.01	30	1.06	5.01	20	0.50	5.01	10	0.13
20	6.69	30	1.90	6.69	20	0.89	6.69	10	0.23
25	8.38	30	2.99	8.38	20	1.40	8.38	10	0.36
30	10.08	30	4.35	10.08	20	2.03	10.08	10	0.52
45	15.82	30	10.19	15.82	20	4.77	15.82	10	1.23
60	20.69	30	19.26	20.69	20	9.01	20.69	10	2.32
75	26.38	30	32.83	26.38	20	15.36	26.38	10	3.96
90	32.48	30	53.31	32.48	20	24.94	32.48	10	6.43
105	39.13	30	85.82	39.13	20	40.16	39.13	10	10.35
120	46.53	30	142.5	46.53	20	66.67	46.53	10	17.19
135	54.93	30	258.5	54.93	20	121.0	54.93	10	31.18
150	64.68	30	576.3	64.68	20	269.7	64.68	10	69.52
165	76.23	30	2249.3	76.23	20	1052.5	76.23	10	271.3

also the θ, ϕ angles used in the diagnoses of ion thruster plumes. For the rear-mounted thruster, however, an additional and complicated coordinate transform would be required to restate the θ, ϕ angles from the Z" axis to the -X" axis to correspond to the polar and azimuthal angles for ions released by this rear-mounted ion engine.

5. CALCULATION OF DISPERSION COEFFICIENTS FOR ION RECIRCULATION/ REINTERCEPTION ON A FINITE SIZE SPACECRAFT

The previous section has derived the required angles of emission and emission energies for an ion to recirculate in $\vec{B}_e$ and to reintercept the precise point of ion departure. The spacecraft bearing the ion thruster will, however, have a finite size and minor variations in the "focus" angles and energies can occur and still result in ion reinterception of the spacecraft.

The principal interest of this section will be the description of the dispersion coefficients for ion arrival/reinterception position as minor variations in the polar and azimuthal angles and minor variations in ion energy are carried out for the ion at the focus parameters in the spacecraft frame ion release.

In the derivation of a particular dispersion coefficient, the release point of an ion will be at X" = Y" = Z" = 0 where the X", Y", Z" notation indicates the spacecraft frame of reference. In the previous "point-to-point" recirculation calculations, the ion trajectory terminates at X" = Y" = Z" = 0. If, however, the polar and azimuthal angles of ion release are held fixed and the ion energy is increased $\Delta E''$ from the correct (point-to-point) value of E, the reinterception of the spacecraft surface will occur at some finite X" and Y". The physical limitations of the spacecraft surface will limit, in turn, the allowable level of $\Delta E''$, for θ and ϕ fixed. Dispersion of the ion points of impact can also be derived for minor variations in ϕ (with θ and E held fixed) and for minor variations in θ (with ϕ and E fixed).

The derivation of the dispersion coefficient formulae is carried out in Attachment 3 to this appendix and a computer program has been generated to calculate the various coefficients. The coefficients computed are:

X_θ: Variation in the x" value of ion impact for $\Delta\theta$ away from θ at the focus value (ϕ, E fixed)

X_ϕ: Variation in the x" value of ion impact for $\Delta\phi$ away from ϕ at the focus value (θ, E fixed)

X_E: Variations in the x" value of ion impact for ΔE away from E at the focus value (Θ, ϕ fixed)

Y_θ: Variations in the y" value of ion impact for $\Delta\theta$ away from θ at the focus value (ϕ, E fixed)

Y_ϕ: Variations in the y" value of ion impact for $\Delta\phi$ away from ϕ at the focus value (θ, E fixed)

Y_E: Variations in the y" value of ion impact for ΔE away from E at the focus value (θ, ϕ fixed)

The principal focus of attention after this computation is upon those particular dispersion coefficients which most severely limit the variation of either θ, ϕ, or E. The two coefficients of major interest are X_ϕ and Y_E. The variation of ϕ through a very narrow angular range causes the ion impact point to move to X" values which exceed the physical limits of the spacecraft in the X" direction. In a similar fashion, only small variations in E are required to cause the ion impact point to move to y" values which exceed the physical limits of the spacecraft. Table 2 illustrates the limitations in ion energy and the limitations in the total range of azimuthal angle, $\Delta\phi_{tot}$, for the η = 30 deg configuration of $\vec{B}_e$ relative to $\vec{v}_s$. Table 2 also provides similar values of energy range and azimuthal angle range for the η = 20 deg and η = 10 deg configurations. Some entries in the table are not listed because dispersion at that parameter configuration is not sufficient to exclude any value of the coordinate (for example, for very weakly energetic ions near θ = 0 deg, the dispersion in ϕ is small and all ϕ values are permissible). The discussion in Section 6 will demonstrate, however, that (for practical conditions in the ion release distributions) those angular and energy ranges are probably not significant.

Table 2. Allowable Total Range in Azimuthal Angle, $\Delta\phi_{tot}$, and Energy Half-Width, $E_{max} - E_{focus}$, for Hg^+ Ions Recirculating to a Spacecraft of Total X-Y Area of 2 x 2 Meters. Assumed spacecraft velocity of 7.7 km/s and assumed B_e of 0.33 gauss (0.33×10^{-4} webers per meter squared).

Ion Azimuthal Angular Range and Ion Energy Range for Recirculation and Reinterception on a Finite Sized Spacecraft

		$\eta = 30^0$		$\eta = 20^0$		$\eta = 10^0$	
α (deg)	θ (deg)	$\Delta\phi_{tot}$ (deg)	$E_{max} - E_{focus}$ (eV)	$\Delta\phi_{tot}$ (deg)	$E_{max} - E_{focus}$ (eV)	$\Delta\phi_{tot}$ (deg)	$E_{max} - E_{focus}$ (eV)
5	1.67	–	1.18	–	0.56	–	0.16
10	3.34	117.1	0.67	185.7	0.33	–	0.09
15	5.01	34.6	0.53	54.9	0.28	114.6	0.08
20	6.69	14.5	0.45	23.1	0.25	47.6	0.08
25	8.38	7.4	0.39	11.8	0.23	24.3	0.08
30	10.08	4.3	0.35	6.8	0.21	14.0	0.07
45	15.82	1.19	0.28	1.88	0.18	3.89	0.07
60	20.69	0.50	0.24	0.80	0.16	1.64	0.07
75	26.38	0.24	0.23	0.39	0.15	0.80	0.07
90	32.48	0.13	0.24	0.21	0.16	0.43	0.08
105	39.13	0.08	0.27	0.12	0.18	0.25	0.09
120	46.53	0.05	0.34	0.07	0.23	0.15	0.12
135	54.93	0.03	0.51	0.04	0.35	0.09	0.17
150	64.68	0.01	0.96	0.02	0.65	0.05	0.33
165	76.23	0.006	3.30	0.01	2.26	0.02	1.15

As an additional aid to one visualization of these dispersion properties, Figures 10 through 12 present the total azimuthal angular width, $\Delta\phi_{tot}$, the energy half-width, $E_{max} - E_{focus}$), and the focus energy for this case of a 2 x 2 meter (X-Y extent) spacecraft. The value of $\vec{B}_e$ used in these calculations is 0.33 gauss and v_s is set at 7.7 km/s (a near earth circular orbit condition).

The important features to note in the data of Table 2 and Figures 10 through 12 is that, except for very small θ, the allowable azimuthal angular range is quite small. The energy half-width for recirculation/reinterception on a finite sized spacecraft is also small, being generally fractions of an electron-volt. For reinterception to occur then, the ions must be emitted within very narrow angular and energy variations away from the "focus" conditions described earlier for point-to-point recirculation. The major question, then, becomes the population density of released ions in the angular and energy regions around the focus angles and energies. Section 6 will consider several forms of released ion distribution functions and will then calculate expected normalized efflux coefficients for this $\vec{v}_+ \times \vec{B}_e$ mode of ion transport and deposition.

6. CALCULATION OF THE NORMALIZED EFFLUX COEFFICIENTS FOR ION RECIRCULATION/REINTERCEPTION ON SPACECRAFT SURFACES

The previous sections have described the calculations of the point-to-point recirculation/reinterception focus conditions and allowable azimuthal and energy ranges, about these focus conditions, for interception on a finite sized spacecraft. This section will examine the specific calculation of the normalized efflux coefficient, ε, for ion transport from a top-mounted thruster to the top of the spacecraft for the $\vec{v}_s$, $\vec{B}_e$ configuration illustrated in Figure 7.

The normalized efflux coefficient, ε, is defined as the arrival ion current density (ions per square centimeter per second) normalized to the total thruster throughput (stated, essentially, as thrust ions per second and noting that the bulk of the material released by an ion thruster in nominal operation will be in the Group I (thrust ion) content). To calculate the ion current arrival over the spacecraft area, A, the fraction of all released ions within the azimuthal angular range and energy range and at a given polar angle must be determined. This, in turn, requires the

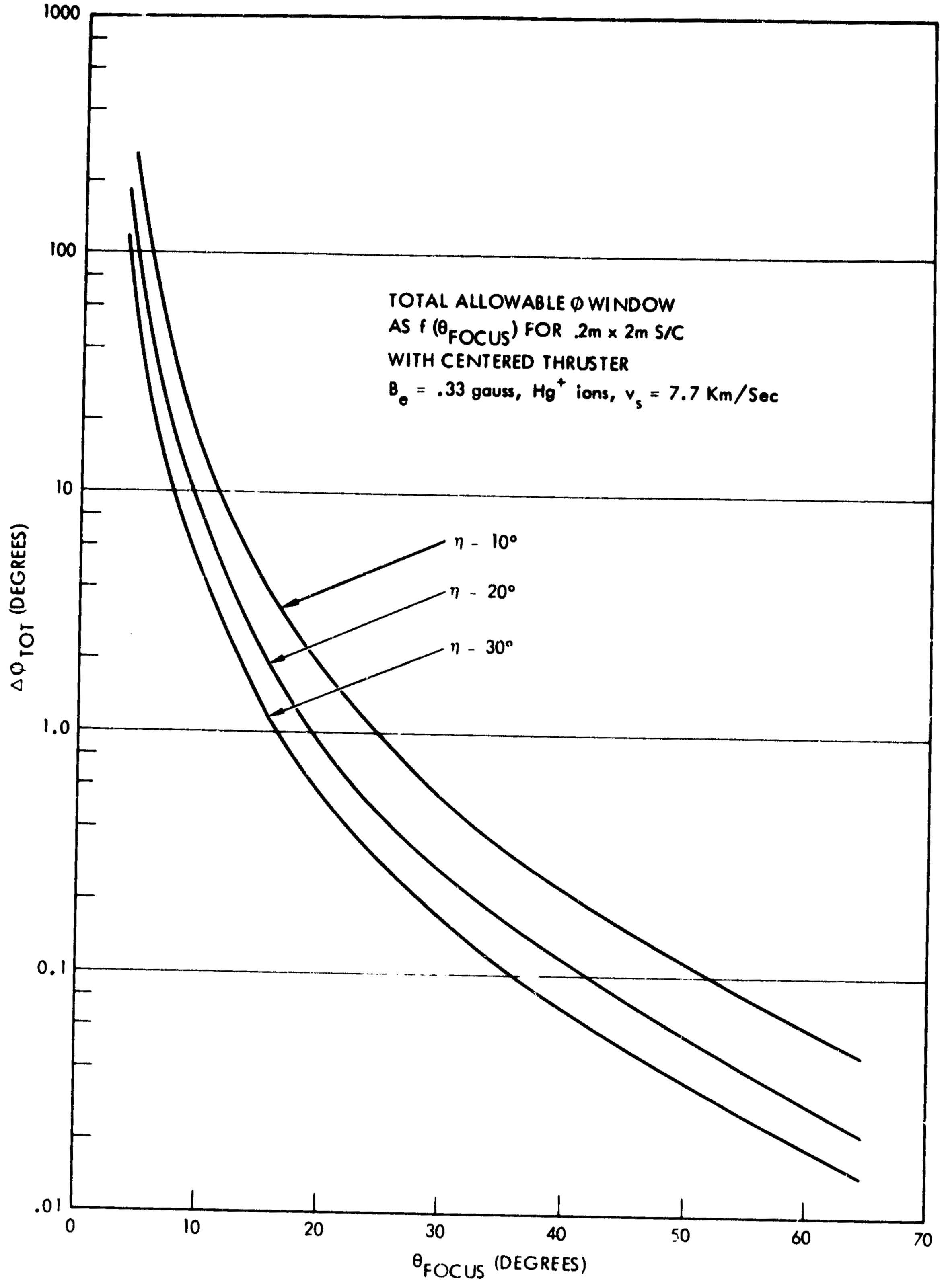

Figure 10. Total Allowable φ Window as a Function of the Focus Angle, θ

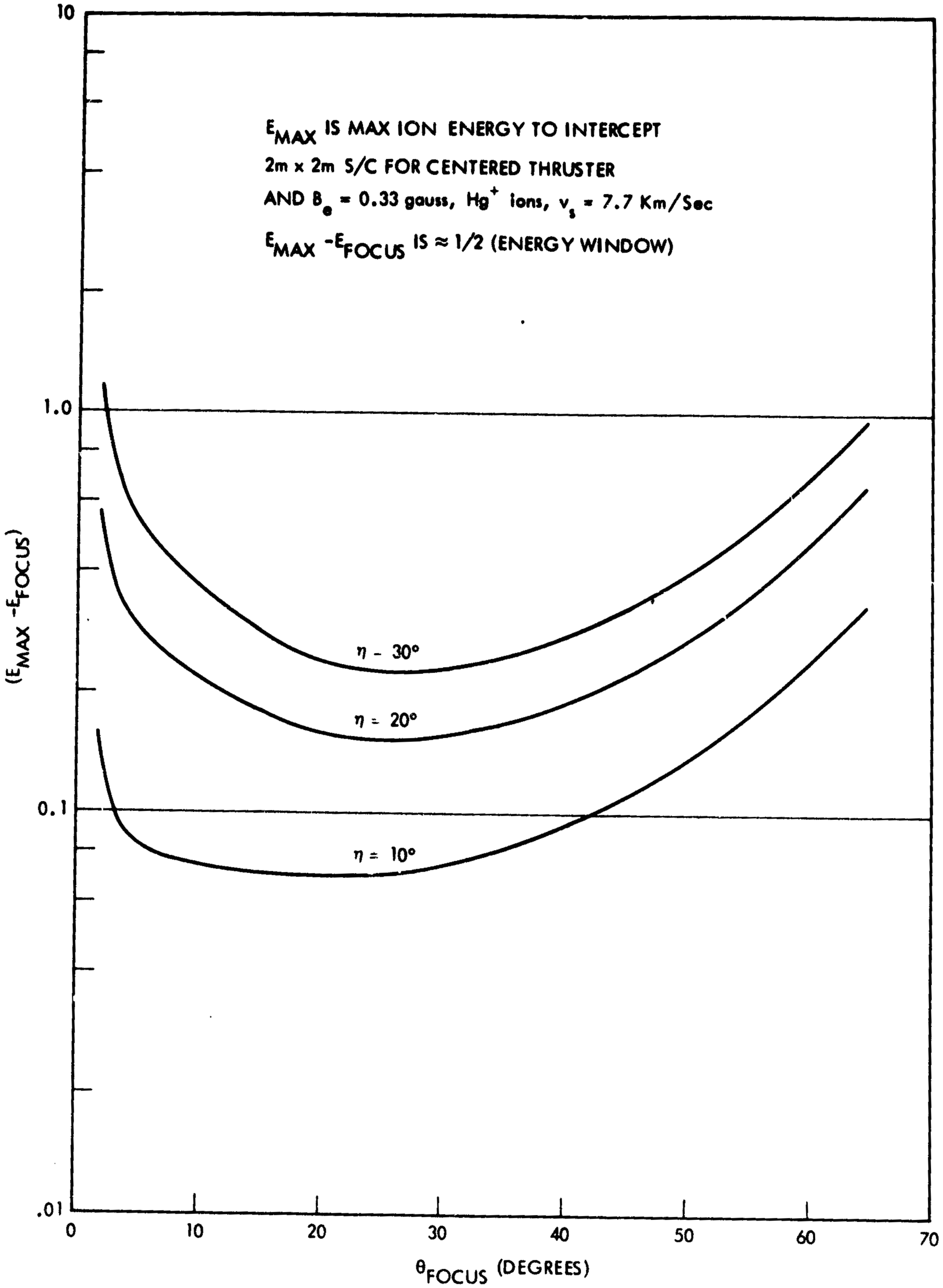

Figure 11. Energy Half-Window, $E_{max} - E_{focus}$, for Hg^+ Ions in B_e = 0.33 gauss, v_s = 7.7 km/sec

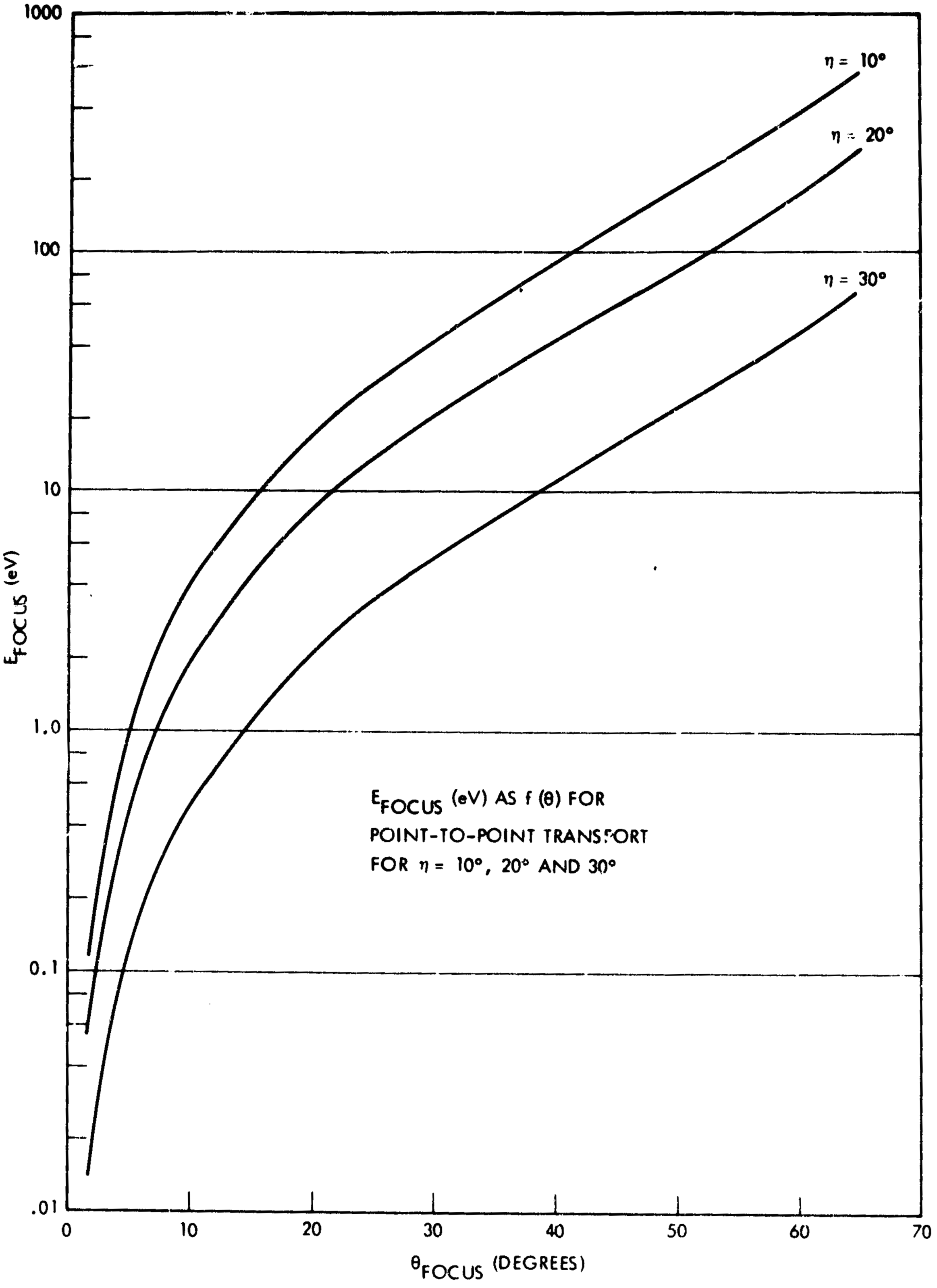

Figure 12. Focus Energy as a Function of Focus Angle, θ

formulation of the ion release distribution function, $f(\theta, \phi, E)$, where $f(\theta, \phi, E)$ is ions per steradian per energy width at θ, ϕ, E. In the present calculations a normalized distribution function will be used, i.e.,

$$\int_{\theta}\int_{\phi}\int_{E} f(\theta, \phi, E)\, d\Omega dE = 1 \qquad (16)$$

where the indicated integral is over the available solid angle and energy ranges for all the released ions.

The previous findings in Sections 4 and 5 have indicated that the principal participants in ion recirculation/reinterception for the top-mounted thruster and the $\vec{v}_s$, $\vec{B}_e$ configuration of Figure 7 will be weakly energetic ions emitted at relatively small values of θ and that thrust ion recirculation/reinterception will be at vanishingly small levels. The distribution function of interest, then, is $f_{+,we}(\theta, \phi, E)$ where the +,we designates weakly energetic ions. The total current of weakly energetic ions intercepting the spacecraft topside will be

$$I_{+,we,int} = I_{+,we}\int_{\theta}\int_{\phi}\int_{E} f_{+,we}(\theta, \phi, E) \sin\theta\, \Delta\phi\Delta E \qquad (17)$$

where $I_{+,we}$ is the release current of weakly energetic ions and the integral in θ, ϕ, E is now over the relevant θ and for the allowed $\Delta\phi_{tot}$ and ΔE for recirculation/reinterception. Table 2 and Figures 10 through 12 provide the relevant angular widths, energy widths, and angles and energies.

The final stage calculation of the normalized efflux coefficient for weakly energetic ion transport and deposition is

$$\varepsilon_{+,we} = \frac{I_{+,we}}{J_B\, A} \qquad (18)$$

where A is spacecraft area on the top side and J_B is the conventional representation of the thrust ion current in auxiliary ion thrusters.

A key element in the calculation of $\varepsilon_{+,we}$ is the function $f_{+,we}$. The most thorough recent determinations of the plume properties of the 8 cm thruster are described in Reference 1. Although the data given there is comparatively detailed, certain properties of the weakly energetic ion distribution have not been determined and there are strong reasons to believe that experimental measurements (beyond those presently described) will be difficult to obtain. The particular area of interest is in weakly energetic ions for small θ. For those small θ values the thrust ion currents are orders of magnitude above the weakly energetic ions and retarding potential analyses of the Faraday cup signals at small θ will probably not have sufficient signal-to-noise ratios to allow a positive determination of the current densities of weakly energetic ions in these angular ranges. The principal experimental evidence is that weakly energetic ions (largely Group IV) tend to emerge at large angles (in the range from 60 to 90 degrees, and there is a comparatively firm analytical basis for stating that emission of weakly energetic ions near $\theta = 0$ deg is unlikely because of the relative magnitudes of radial and axial electric fields in the thruster plasma plume. The strength of the observed electric fields in these plumes and the general knowledge of the formation point for Group IV ion creation (and the electric field strengths in these formation regions) also makes it unlikely that weakly energetic ions are created in any significant number in the range below a few electron volts.

While there is a comparatively firm basis for a description of $f_{+,we}$ with an emission peak at high angles and with an absence of ions below (say) 10 eV, the calculations of $\varepsilon_{+,we}$ should not be arbitrarily limited to this form of distribution function. A conservative approach to $\varepsilon_{+,we}$ calculations is to utilize assumed forms of $f_{+,we}$ and to examine the values of ion transport under each assumed distribution. For this reason two basic distribution functions will be used.

The first form of the distribution function is

$$f_{+,we} = \frac{1}{2\pi(E_1 - E_0)} \qquad (19)$$

---

1. "Ion Engine Auxiliary Propulsion Applications and Integration Study," NASA CR-135312, TRW 29999-6013-RU-00, July 7, 1977.

In this distribution function the ions are emitted uniformly over 2π steradians of solid angle and are emitted uniformly in energy from some minimum energy, E_0 to a maximum energy, E_1. The second form of the distribution function is

$$f_{+,we} = \frac{2 \sin \theta}{\pi^2 (E_1 - E_0)} \tag{20}$$

The emission of ions in the energy space from E_0 to E_1 remains uniform, as in the $f_{+,we}$ given in Equation (19) above. This second distribution, however, does have a preferential emission of ions at large angles when $\sin \theta$ has its more significant values. In both of the distributions, $0 \le \theta \le \pi/2$, and $0 \le \phi \le 2\pi$ for the polar and azimuthal angular ranges.

Figure 13 illustrates the calculated values of $\varepsilon_{+,we}$ as a function of the minimum energy, E_0, for the two forms of the distribution function. The value of E_1 used in these calculations is 53.3 eV, which approximates an expected upper end point to Group IV ion energies. The value of $I_{+,we}$ used in the ε calculations is 3×10^{-3} J_B, derived from the findings of Reference 1. The spacecraft area A is 4×10^4 cm^2. Because the allowable angular band for recirculation/reinterception scales with the basic scale size X of the spacecraft and the energy acceptance band scales with the Y of the spacecraft, the values of $\varepsilon_{+,we}$ in Figure 13 are independent of spacecraft scale size and spacecraft area is described here only in that the angular and energy acceptance bands, in the previous table and figures have been calculated for an example spacecraft whose upper face is 2 x 2 meters.

The results in Figure 13 illustrate a maximum value of $\varepsilon_{+,we}$ of 3.6×10^{-12} cm^{-2} for the uniform emission of weakly energetic ions from zero energy to E_1 and for an angular emission uniform over 2π steradians. For only very modest increases in E_0, however, the $\varepsilon_{+,we}$ values are significantly reduced and the inclusion of $\sin \theta$ effects in the angular emission (to favor higher angular emission of these ions) causes the $\varepsilon_{+,we}$ values to diminish still further. For a weakly energetic ion emission including $\sin \theta$ effects and with minimum ion energies of $\sim$10 eV, the $\varepsilon_{+,we}$ values are of the order of 5×10^{-14} cm^{-2}. These latter conditions

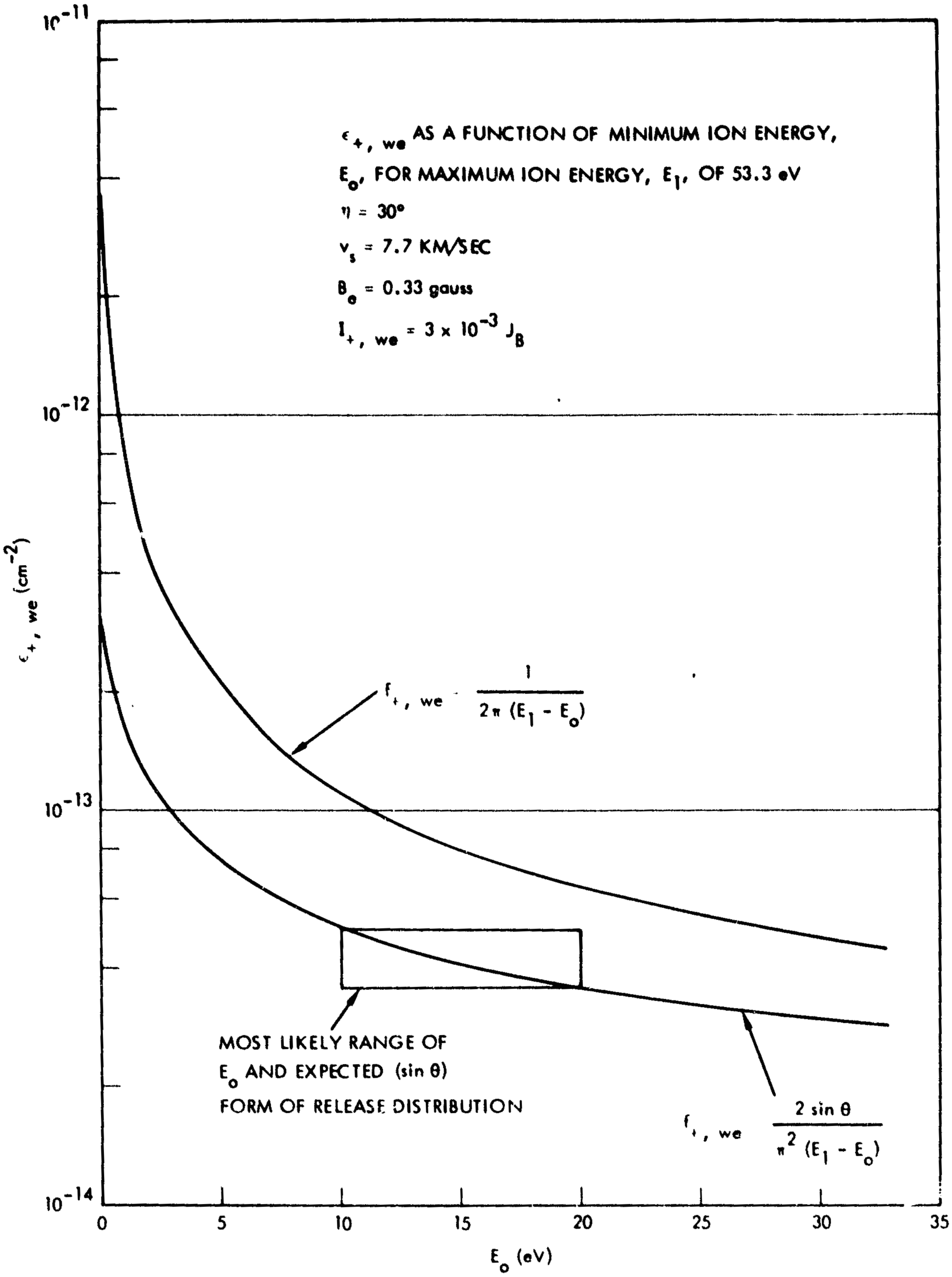

Figure 13. Normalized Efflux Coefficient $\epsilon_{+,we}$ for a Spacecraft at Magnetic Equatorial Passage and η = 30 deg for Two Forms of Ion Distribution Function in the Weakly Energetic Ion Release

(sin θ weighting in the angular emission, and $E_0 \lesssim 10$ eV) corresponds to the distribution most expected to occur in view of the previously obtained laboratory data on the electric field structures within the thruster plasma plume.

A final area of interest in this section is to examine the possible behavior of $\epsilon_{+,we}$ as the angle η between $\vec{v}_s$ and $\vec{B}_e$ varies. Table 3 lists values of product of the total azimuthal angular acceptance band for recirculation/reinterception times the half energy acceptance band for values of η = 30, 20, and 10 deg and for various values of polar angle emission of the ions. This product, 1/2 $(\Delta E_{allowed})$ $(\Delta\phi_{allowed})$, generally describes the possibility that released ions in $f_{+,we}$ will be recirculated and will reintercept the spacecraft, and, from the data in Table 3, this reinterception possibility is only weakly dependent upon the value of η. This net weak dependence results from counteracting effects in the allowable energy and angular windows as η varies. (See Table 2 for the separate values of the energy and angular windows.) The important feature of this weak dependence in the total energy and angular acceptance window product is that the findings of $\epsilon_{+,we}$ values for η = 30 deg can now be accepted as generally valid for even smaller values of η, and there are no anticipated singularities in the recirculation/reinterception calculations for the small η angle regime.

7. GENERALIZATION OF DERIVATION OF REQUIRED POLAR AND AZIMUTHAL ANGLES FOR ION RECIRCULATION IN $\vec{B}_e$ AND REINTERCEPTION ON THE SPACECRAFT

Figure 7 (see Section 4) has illustrated a $\vec{v}_s$, $\vec{B}_e$ configuration which may occur for a spacecraft in a high inclination, circular earth orbit during the magnetic equatorial passage. The results of Sections 5 and 6 have been in terms of this specific $\vec{v}_s$, $\vec{B}_e$ configuration. As Section 3 has pointed out, however, a widely ranging series of configurations of $\vec{v}_s$ and $\vec{B}_e$ occur during the total orbit for a high inclination orbit. The interest of this section will be to generalize the angular transformations used in Section 4 to the total range of $\vec{v}_s$, $\vec{B}_e$ configurations.

Table 3. Product of 1/2 Energy Window X Total Azimuthal Angular Window as f(η) for $0 \le \theta \le 76.226$ deg. $B_e = 0.33$ gauss and $v_s = 7.7$ km/s

α (deg)	θ (deg)	$\eta = 30^0$ $(E_{max} - E_{focus})$ $\Delta\phi_{tot}$ (eV deg)	$\eta = 20^0$ $(E_{max} - E_{focus})$ $\Delta\phi_{tot}$ (eV deg)	$\eta = 10^0$ $(E_{max} - E_{focus})$ $\Delta\phi_{tot}$ (eV deg)
5	1.67	–	–	–
10	3.34	78.552	62.114	–
15	5.01	18.366	15.426	9.456
20	6.69	6.538	5.808	3.718
25	8.38	2.906	2.700	1.837
30	10.08	1.488	1.432	1.033
45	15.82	0.328	0.344	0.276
60	20.69	0.120	0.126	0.114
75	26.38	0.056	0.060	0.057
90	32.48	0.0314	0.0338	0.0338
105	39.13	0.0206	0.0222	0.0228
120	46.53	0.0154	0.0168	0.0173
135	54.93	0.0132	0.0144	0.0151
150	64.68	0.0138	0.0150	0.0156
165	76.22	0.0204	0.0222	0.0231

Figure 14 illustrates the three coordinate frames used in previous sections. These are the earth frame (X, Y, Z), the magnetic field frame (X', Y', Z'), and the spacecraft frame (X", Y', Z"). The X and X" axes are determined by the vector direction $\vec{v}_s$ at the specific instant in the orbit path for which the ion recirculation is under examination. The X-Y plane is then determined by locating that plane which contains $\vec{v}_s$ and $\vec{B}_e$, with the choice of Y axis direction such that the y component of $\vec{B}_e$ is along the -Y direction. This completely determines the orientation of (X, Y, Z) and X", Y", Z". The X' axis is determined by the $\vec{B}_e$ at the specific instant in the orbital path for which the ion recirculation is to be examined. The angle η between $\vec{v}_s$ and $\vec{B}_e$ must be in the range from

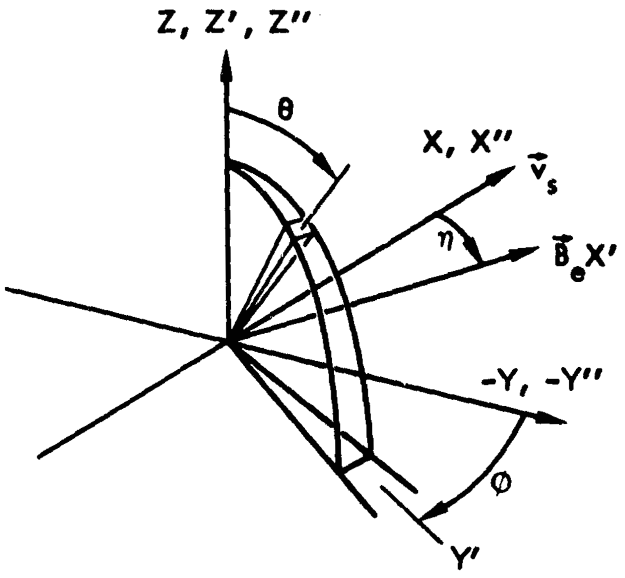

Figure 14. Orientations of Magnetic Field Frame, Earth Frame, and Spacecraft Frame Axes and the Polar and Azimuthal Angles for Ion Recirculation and Reinterception. Indicated $\Delta\theta$ and $\Delta\phi$ is for ion reinterception on a finite sized spacecraft.

0^- to π radians. The choice of Y' direction is such that the angle between +Y and +Y' is also η.

Figure 14 also illustrates a polar angle θ and an azimuthal angle ϕ. Both θ and ϕ are determined by the transformation equations given in Attachment 2 to this appendix. For a finite sized spacecraft variations in θ and ϕ are permissible with one trajectory impact point remaining on the spacecraft surface.

While Figure 14 illustrates a θ, ϕ condition which will lead to an ion recirculating in $\vec{B}_e$ and reintercepting the spacecraft, there is, as yet, no assurance that the ions released by the thruster will be emitted in these directions. In the earlier example in Section 4 of a top-mounted thruster (thrust axis along the +Z" axis) there is a match-up between the cone of directions for the released ions and the required directions of emission for recirculation/reinterception. However, for a bottom-mounted thruster (axis along the -Z" axis) no such match up exists and recirculation with reinterception falls into the dynamically forbidden condition cited earlier (Section 3).

As the spacecraft moves over its complete orbit, the direction of the Z" axis relative to the spacecraft will change, noting that (Z , Z', Z") are determined by orientations of $\vec{v}_s$ and $\vec{B}_e$. The Z" axis may, then, emerge over any one of the six faces of the spacecraft and the cone of acceptance directions for reinterception may or may not include the cone of directions of ion release. In general, some sort of match up of the two cones might be expected over about 50% of the time in a complete orbit, while some configurations (top-mounted thruster in equatorial orbit and forward face-mounted thruster in equatorial orbit) are dynamically forbidden in reinterception over the entirety of the orbit while other configurations (bottom-mounted thruster in equatorial orbit and rear face-mounted thruster in equatorial orbit) have dynamically allowed interception over the entirety of the orbit.

The importance of the generalization conditions described above is that the ε values calculated earlier (Section 6) must be multiplied by another "orbit-averaging factor." If reinterception is dynamically allowed for the entirety of the orbit, the ε values determined in Section 6 are multiplied by unity. If reinterception is dynamically allowed over $\sim$50% of the orbit, the ε values of Section 6 are to be multiplied by 0.5, and if reinterception is forbidden over the entirety of the orbit, then the ε values are multiplied by zero. Now the range of $\varepsilon_{+,we}$ for the various $f_{+,we}$ ion distribution functions ranged from 3.6×10^{-12} cm^{-2} to 2.8×10^{-14} cm^{-2}. Applying an orbit averaging factor of 0.5 causes these $\varepsilon_{+,we}$ to diminish to a range given by

$$1.4 \times 10^{-14} \text{ cm}^{-2} \leq \langle \varepsilon_{+,we} \rangle \leq 1.8 \times 10^{-12} \text{ cm}^{-2} \tag{21}$$

For a mission in which the total ion release in a thruster is $\sim 2 \times 10^{25}$ thrust ions, the integrated ion interception over the total mission life would range from

$$2.0(10)^{11} \text{ ions/cm}^2 \leq \int_0^T J_{+,we}\, dt \leq 3.6(10)^{13} \text{ ions/cm}^2 \tag{22}$$

which may be expressed as

$$0.0002 \text{ monolayers} \leq \int_0^T J_{+,we}\, dt \leq 0.036 \text{ monolayers} \qquad (23)$$

In the discussion of Section 6 the expected $f_{+,we}$ leads to $\varepsilon_{+,we}$ of 5.0×10^{-14} cm^{-2} and for this expected ion release condition, the integrated ion deposition over the mission would be 10^{12} ions/cm^2 which represents an integrated deposition of 10^{-3} monolayers per mission.

8. SUMMARY

This appendix has examined the recirculation of ions from the ion thruster in the magnetic field of the earth and the possible reinterception of these ions on spacecraft surfaces. It has been demonstrated that this reinterception is dynamically allowed under some conditions in the arrangement of $\vec{v}_s$ (spacecraft velocity), $\vec{B}_e$ (the magnetic field of the earth), and the axis of the ion thruster, while for other arrangements, reinterception is dynamically forbidden.

A specific, dynamically allowed, configuration in $\vec{v}_s$, $\vec{B}_e$ and thruster orientation has been examined. For this specific case, the particles which are the more apt to match the required emission angles and energies are the weakly energetic ions. Several forms of the distribution function of such weakly energetic ions were convolved with the angular and energy acceptance windows and normalized efflux coefficients, $\varepsilon_{+,we}$, have been determined. These $\varepsilon_{+,we}$ values have ranged from 2.8×10^{-14} cm^{-2} to 3.6×10^{-12} cm^{-2}. The "most likely" value of $\varepsilon_{+,we}$ (for $f_{+,we}$ of expected angular and energy dependences) is 1.0×10^{-13} cm^{-2}. For a general orbit, averaging over the orbit reduces this figure of $\varepsilon_{+,we}$ to 5.0×10^{-14} cm^{-2} which would result in 10^{-3} monolayers per mission (integrated ion deposition over the mission) for a total thruster throughput of 2×10^{25} thrust ions during the mission. These integrated deposition figures are comfortingly small and indicate that $\vec{v}_+ \times \vec{B}_e$ recirculation of ions will not lead to any significant alterations of spacecraft surface properties.

Because of the very low levels of these depositions and because surface thermal reevaporation of the ions (to reduce surface buildup) has not been invoked, it follows that recirculation/reinterception deposition of ions does not lead to significant surface alteration irrespective of the values of surface temperature.

ATTACHMENT 1

ION VELOCITY TRANSFORMS FROM THE SPACECRAFT FRAME TO THE EARTH AND MAGNETIC FIELD FRAMES

Figure 1-1 illustrates the spacecraft frame and the ion polar and azimuthal angles. Also illustrated is the direction of spacecraft motion for the ultimate transformation of coordinates and angles into the earth frame.

The ion velocity vector is a "normalized" vector where the normalization velocity is v_s. Thus

$$\vec{v}''_+ = \vec{i}''\, v''_x + \vec{j}''\, v''_y + \vec{k}''\, v''_z$$

has all of its components (v''_x, v''_y, v''_z) normalized relative to v_s. From the definition

$$\gamma'' = \left| \frac{\vec{v}''_+}{v_s} \right| \tag{1-1}$$

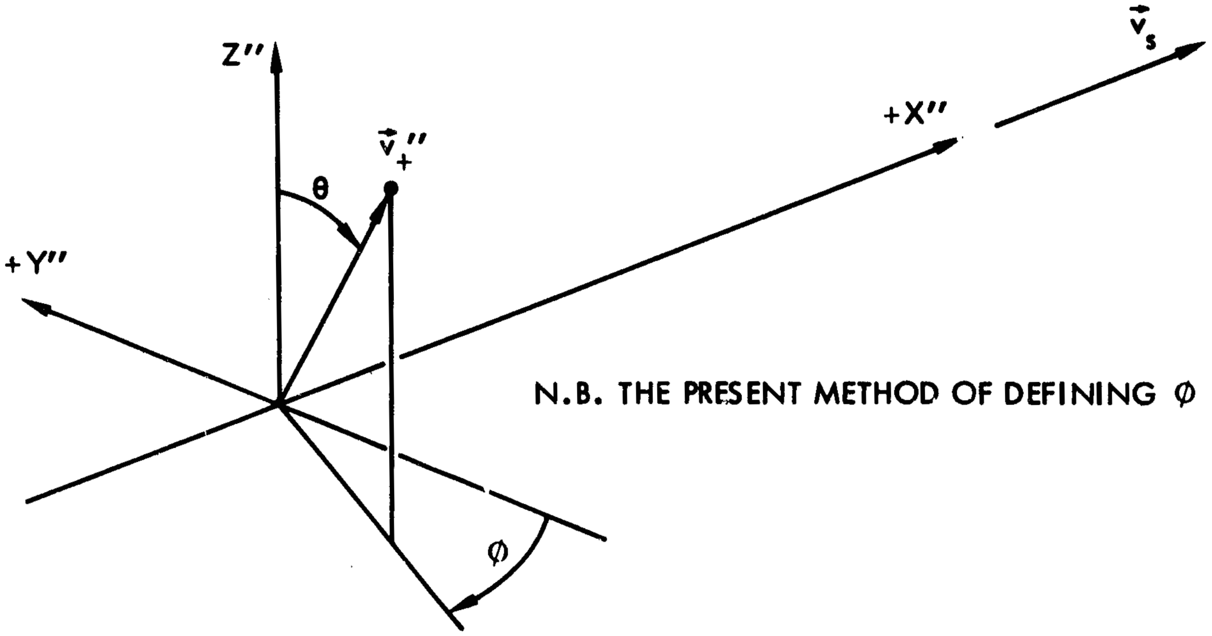

Figure 1-1. Spacecraft Frame and Ion Angles

$$\vec{v}_+'' = \gamma'' (\vec{i}'' (-\sin\theta \sin\phi) + \vec{j}'' (-\sin\theta \cos\phi) + \vec{k}'' (\cos\theta)) \quad (1\text{-}2)$$

defines the ion velocity vector in the spacecraft frame.

When the vector in (1-2) is transformed into the laboratory frame the vector will be denoted as $\vec{v}_+$. Because of the v_s orientation along x" and the normalization to v_s,

$$\begin{aligned}\vec{v}_+ = {} & \vec{i} (\gamma'' (-\sin\theta \sin\phi) + 1) \\ & + \vec{j} (\gamma'' (-\sin\theta \cos\phi)) \\ & + \vec{k} (\gamma'' (\cos\theta))\end{aligned} \quad (1\text{-}3)$$

The next calculation is to determine the angles β and α between $\vec{v}_+$ and $\vec{B}_e$ and between the plane containing $\vec{v}_+$ and $\vec{B}_e$ and the X-Y (horizontal) plane. Figure 1-2 illustrates the orientation of $\vec{B}_e$ in the earth (X,Y,Z) frame. Also illustrated in Figure 1-2 is the $\vec{B}_e$ frame (denoted as the X', Y', Z' frame). Note that $\vec{B}_e$ is in the X-Y plane at angle η with respect to the X axis.

To determine the angle between $\vec{v}_+$ and $\vec{B}_e$, the dot product of v_+ and B_e may be used, i.e.,

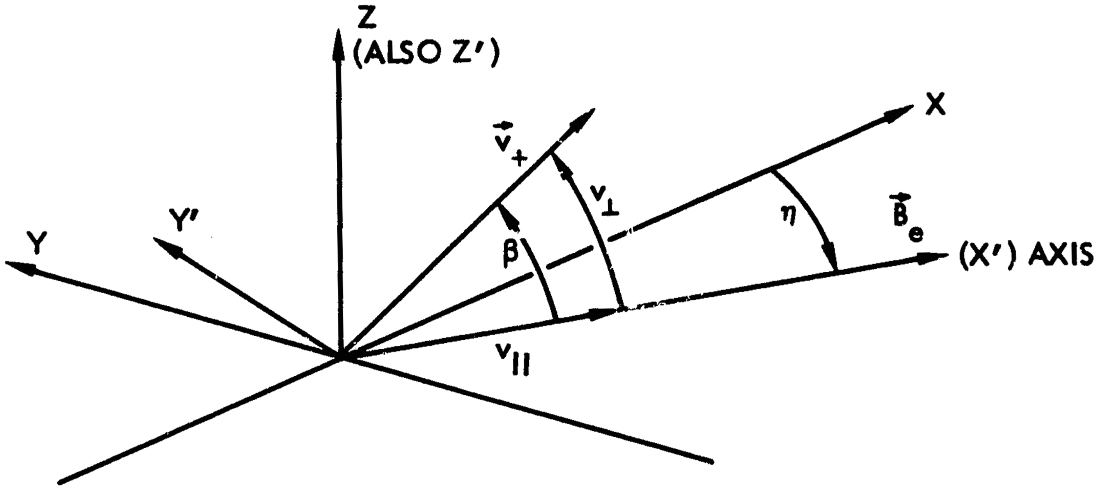

Figure 1-2. Earth Frame and $\vec{B}_e$ Frame

$$\beta = \cos^{-1}\left\{\frac{\vec{v}_+ \cdot \vec{B}_e}{|v_+|\ |B_e|}\right\} \tag{1-4}$$

Because it is easier to work with unit vectors in this calculation, the following unit vectors will be calculated:

Unit vector for $\vec{B}_e$ is $\vec{B}_{e,uv}$

$$\vec{B}_{e,uv} = \vec{i}\ (\cos \eta) - \vec{j}\ (\sin \eta) \tag{1-5}$$

The magnitude of $\vec{v}_+ = (\vec{v}_+ \cdot \vec{v}_+)^{1/2}$ and will be denoted as γ where

$$\gamma = \left[(\gamma''\ (-\sin\theta \sin\phi) + 1)^2 + (\gamma''\ (-\sin\theta\cos\phi))^2 + (\gamma''\cos\theta)^2\right]^{1/2}$$

and

$$\gamma = \left(1 - 2\gamma''\sin\theta\sin\phi + (\gamma'')^2\right)^{1/2} \tag{1-6}$$

and

$$\begin{aligned}\vec{v}_{+,uv} = {} & \vec{i}\left(\frac{1 - \gamma''\ (\sin\theta\sin\phi)}{\gamma}\right)\\ & + \vec{j}\left(\frac{-\gamma''\ (\sin\theta\cos\phi)}{\gamma}\right)\\ & + \vec{k}\left(\frac{\gamma''\cos\theta}{\gamma}\right)\end{aligned} \tag{1-7}$$

from which β may now be calculated, i.e.,

$$\beta = \cos^{-1}\left\{\cos\eta\left(\frac{1 - \gamma''\ (\sin\theta\sin\phi)}{\gamma}\right) + \sin\eta\left(\frac{\gamma''\ (\sin\theta\cos\phi)}{\gamma}\right)\right\} \tag{1-4'}$$

From angle β, $v_{||}$, the component of ion velocity, $\vec{v}_+$, which is parallel to $\vec{B}_e$ may be calculated. Using

$$v_{||} = |\vec{v}_+| \cos \beta \qquad (1\text{-}8)$$

and, recalling that $|\vec{v}_+| = \gamma$ leads to

$$v_{||} = \cos \eta \, (1 - \gamma'' (\sin \theta \sin \phi)) + \sin \eta \, (\gamma'' \sin \theta \cos \phi) \qquad (1\text{-}9)$$

noting that this is a normalized velocity (to v_s) as are all other velocities in these calculations. The remaining component of ion velocity to calculate is $v_\perp$, the component of $\vec{v}_+$ perpendicular to $\vec{B}_e$, and noting that

$$\begin{aligned} v_\perp &= |\vec{v}_+| \sin \beta, \\ v_\perp &= \gamma \sin \beta \end{aligned} \qquad (1\text{-}10)$$

The remaining angle to calculate is the angle α, illustrated in Figure 1-3, which is the angle between the plane containing $\vec{v}_+$ and $\vec{B}_e$ and the X-Y plane. From this figure it can be seen that

$$v_\perp \sin \alpha = v_z' \qquad (1\text{-}11)$$

and, because $v_z' = v_z$

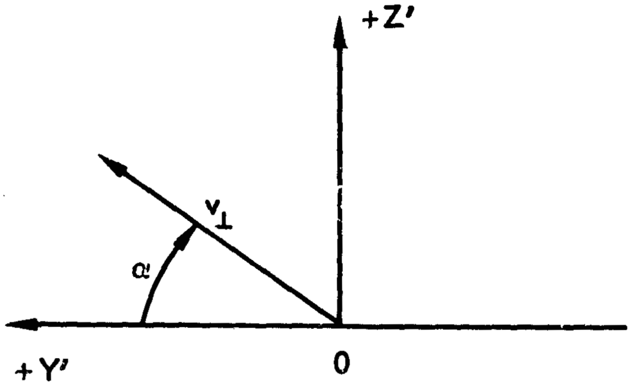

Figure 1-3. Angle α in $\vec{B}_e$ Frame

$$\alpha = \sin^{-1}\left\{\frac{v_z}{v_\perp}\right\}$$

$$\alpha = \sin^{-1}\left\{\frac{\gamma'' \cos \partial}{\gamma \sin \beta}\right\} \qquad (1\text{-}12)$$

All of the processes above merely allow the calculation of the various angles and velocity components. The next step is to calculate the dispersion coefficients. These dispersion coefficients will be derived in Attachment 3.

ATTACHMENT 2

ION VELOCITY TRANSFORMS FROM THE MAGNETIC FIELD FRAME TO THE SPACECRAFT FRAME

The focus conditions have required that

$$v_{\parallel} = v_s \cos \eta \tag{2-1}$$

and

$$v_{\perp} = v_s \sin \eta \left(\frac{\alpha}{\sin \alpha}\right) \tag{2-2}$$

In normalized velocities, to be used throughout the remainder of this transformation

$$v_{\parallel} = \cos \eta \tag*{(2-1)'}$$

and

$$v_{\perp} = \sin \eta \left(\frac{\alpha}{\sin \alpha}\right) \tag*{(2-2)'}$$

the total ion velocity, normalized to v_s, is given by

$$\gamma = \left(v_{\parallel}^2 + v_{\perp}^2\right)^{1/2} \tag{2-3}$$

and

$$\gamma = \left(\cos^2 \eta + \sin^2 \eta \left(\frac{\alpha}{\sin \alpha}\right)^2\right)^{1/2} \tag{2-4}$$

where γ has been previously defined (1-6).

The angle α is a specified quantity. The angle β, defined as the angle between $\vec{v}_+$ and $\vec{B}_e$ is given by

$$\beta = \tan^{-1}\left\{\frac{\sin\eta\left(\frac{\alpha}{\sin\alpha}\right)}{\cos\eta}\right\} \tag{2-5}$$

The vector components of $\vec{\gamma}$ in the magnetic field frame are (normalized)

$$\begin{aligned} v_x' &= \cos\eta \\ v_y' &= \sin\eta\left(\frac{\alpha}{\sin\alpha}\right)\cos\alpha \end{aligned} \tag{2-6}$$

and

$$v_z' = \alpha\sin\eta$$

and the vector components of γ in the earth frame are (normalized)

$$\begin{aligned} v_x &= \cos^2\eta + \sin^2\eta\left(\frac{\alpha}{\sin\alpha}\right)\cos\alpha \\ v_y &= \sin\eta\cos\eta\left(\frac{\alpha\cos\alpha}{\sin\alpha} - 1\right) \end{aligned} \tag{2-7}$$

and

$$v_z = \alpha\sin\eta$$

The velocity transformation into the thruster (spacecraft) system is comparatively simple (relative velocity on only one axis) and yields

$$\begin{aligned} v_x'' &= \sin^2\eta\left(\frac{\alpha\cos\alpha}{\sin\alpha} - 1\right) \\ v_y'' &= \sin\eta\cos\eta\left(\frac{\alpha\cos\alpha}{\sin\alpha} - 1\right) \\ v_z'' &= \alpha\sin\eta \end{aligned} \tag{2-8}$$

From the definition of the azimuthal angle ϕ used in the earlier figures (Figure 1-1)

$$\phi = \tan^{-1}\left\{\frac{v''_x}{v''_y}\right\} = \tan^{-1}(\tan \eta)$$

from which it follows that

$$\phi = \eta \, , \tag{2-9}$$

an interesting result which is helpful in terms of visualizing the focus conditions. The total ion velocity in the spacecraft frame is denoted as γ'' (normalized) where

$$\gamma'' = \sin \eta \left(\left(\frac{\alpha \cos \alpha}{\sin \alpha} - 1\right)^2 + \alpha^2\right)^{1/2} \tag{2-10}$$

and the remaining quantity of interest, the polar angle θ in the spacecraft frame is given by

$$\theta = \cos^{-1}\left\{\frac{\alpha}{\left(\left(\frac{\alpha \cos \alpha}{\sin \alpha} - 1\right)^2 + \alpha^2\right)^{1/2}}\right\} \tag{2-11}$$

An interesting feature to note here is that ϕ is not a function of α but is determined by the value of η, while θ is a function of α only and does not depend on the choice of η. These features can be used for simplifying the visualization of ion point-to-point recirculation conditions.

ATTACHMENT 3

DERIVATION OF THE DISPERSION RELATIONS IN X' AND Y' FOR VARIATIONS IN ION POLAR AND AZIMUTHAL ANGLES AND FOR VARIATIONS IN ION ENERGY

To calculate the dispersion in X' and Y' for variations in the ion angles of emission and variations in ion energy, the general conditions for the point-to-point recirculation/reinterception must first be stated. For the ion at the precise α, β, γ for reinterception:

$$v_{\|} = \cos \eta$$

and

$$v_{\perp} = \sin \eta \left(\frac{\alpha}{\sin \alpha}\right) \tag{3-1}$$

and

$$\gamma = \left(\cos^2 \eta + \sin^2 \eta \left(\frac{\alpha}{\sin \alpha}\right)^2\right)^{1/2}$$

is required for point-to-point recirculation and reinterception. The time to have reinterception is also known for the point-to-point case and is

$$T = \frac{2r_{\perp} \alpha}{\hat{v}_{\perp}} \tag{3-2}$$

where $r_{\perp}$ is the radius of curvature in B_e for an ion of velocity $\hat{v}_{\perp}$ and the "hat" indicates a dimensional (nonnormalized) velocity. Denoting T_{ci} as the period for an ion cyclotron orbit in $\vec{B}_e$ for an ion of Hg^+, then

$$T = \left(\frac{\alpha}{\pi}\right) T_{ci} \tag{3-3}$$

From Equations (3-3) and (3-1), and Figure 1-2 it can be seen that a variation in θ which causes an α variation of $d\alpha$ will cause a variation in T, and can also cause variations in $\hat{v}_\perp$, $r_\perp$ and β. Concentrating first on the effects of dispersion along the X' axis caused by variations in $\hat{v}_{||}$ the quantity $\Delta X'$ will denote the X' distance between the ion as it recrosses the X'Y' plane and the position of the spacecraft midpoint (point of release of the ion). The spacecraft midpoint at T is

$$X'_{S/C\ MP} = \hat{v}_s\ T \tag{3-4}$$

and

$$dX'_{S/C\ MP} = \hat{v}_s\ dT \tag{3-5}$$

The X' value of the ion as it recrosses the X'Y' plane is

$$X'_{ion\ recross} = \frac{\hat{v}_{||}\ T}{\cos\ \eta} \tag{3-6}$$

and

$$dX'_{ion\ recross} = \frac{1}{\cos\ \eta}\ (d\hat{v}_{||}\ T + \hat{v}_{||}\ dT) \tag{3-7}$$

From (3-4) and (3-7), $\Delta X'$ is given by

$$\Delta X' = \frac{1}{\cos\ \eta}\ (d\hat{v}_{||}\ T + \hat{v}_{||}\ dT) - v_s\ dT \tag{3-8}$$

but

$$\Delta X' = \frac{d\hat{v}_{||}\ T}{\cos\ \eta} \tag{3-9}$$

noting that $\hat{v}_{||} = \cos\ \eta\ \hat{v}_s$ thus,

$$\Delta X' = \hat{v}_s\, T \left(\frac{dv_{||}}{\cos \eta}\right) \tag{3-10}$$

$$\Delta X' = \hat{v}_s\, T_{ci} \left(\frac{\alpha}{\pi}\right) \left[\frac{dv_{||}}{\cos \eta}\right] \tag{3-11}$$

From Equation (1-9)

$$\frac{v_{||}}{\cos \eta} = (1 - \gamma'' (\sin \theta \sin \phi)) + \tan \eta\, \gamma'' (\sin \theta \cos \phi)$$

From this the dispersion may be rather easily calculated for variations in γ'', θ, and ϕ. First, examining $dv_{||}/d\theta$,

$$\frac{1}{\cos \eta} \frac{dv_{||}}{d\theta} = - \gamma'' (\cos \theta \sin \phi) + \tan \eta\, \gamma'' (\cos \theta \cos \phi)$$

and

$$\frac{\Delta X'}{d\theta} = \hat{v}_s\, T_{ci} \left(\frac{\alpha}{\pi}\right) \{\gamma'' \cos \theta (- \sin \phi + \tan \eta \cos \phi)\} \tag{3-12}$$

is the dispersion in X' for $d\theta$ changes in the ion parameters. The dispersion in $\Delta X'$ for $d\phi$ is

$$\frac{\Delta X'}{d\phi} = \hat{v}_s\, T_{ci} \left(\frac{\alpha}{\pi}\right) \{\gamma'' \sin \theta (- \cos \phi - \tan \eta \sin \phi)\} \tag{3-13}$$

and

$$\frac{\Delta X'}{d\gamma''} = \hat{v}_s\, T_{ci} \left(\frac{\alpha}{\pi}\right) \{\sin \theta (- \sin \phi + \tan \eta \cos \phi)\} \tag{3-14}$$

Turning now to the somewhat more difficult derivation of the dispersion in the Y' direction, it should be noted that the midpoint of the spacecraft has a Y' value as a function of t which is

$$Y'_{S/C\ MP} = \hat{v}_s \sin \eta\, t \tag{3-15}$$

and, at T (the reinterception time)

$$Y'_{S/C\ MP} = \hat{v}_s \sin \eta\, T \tag{3-16}$$

The Y' value of the ion as it recrosses the X'Y' plane is

$$Y' = 2r_\perp \sin \alpha \tag{3-17}$$

Now a change of ion parameters will effect $r_\perp$, α, and t and

$$\Delta Y' = (2dr_\perp \sin \alpha + 2d\alpha\, r_\perp \cos \alpha - v_s \sin \eta\, dT) \tag{3-18}$$

where $dr_\perp$, $d\alpha$, and dT must then be evaluated for a given $d\theta$, or $d\phi$, or $d\gamma''$. Now $T = \alpha/\pi\, T_{ci}$ from Equation (3-3) so that

$$dT = \frac{d\alpha}{\pi} T_{ci} \tag{3-19}$$

Another relation is that

$$\hat{v}_s \sin \eta \left(\frac{\alpha}{\pi}\right) T_{ci} = 2r_\perp \sin \alpha$$

for the point-to-point reinterception case so that, using

$$\hat{v}_s \sin \eta' \left(\frac{\alpha}{\pi}\right) T_{ci}$$

in Equations (3-18) and (3-19)

$$\Delta Y' = \left(2dr_\perp \sin \alpha + 2d\alpha\, r_\perp \cos \alpha - 2r_\perp \sin \alpha \left(\frac{d\alpha}{\alpha}\right)\right) \tag{3-20}$$

or

$$\Delta Y' = 2r_\perp \sin \alpha \left(\frac{dr_\perp}{r_\perp} + d\alpha \cot \alpha - \frac{d\alpha}{\alpha}\right) \tag{3-20)'$$

or

$$\Delta Y' = 2r_\perp \sin \alpha \left(\frac{dr_\perp}{r_\perp} + d\alpha \left(\frac{\cos \alpha}{\sin \alpha} - \frac{1}{\alpha}\right)\right) \tag{3-20)"$$

or

$$\Delta Y' = \hat{v}_s \sin \left(\frac{\alpha}{\pi}\right) T_{ci} \left(\frac{dr_\perp}{r_\perp} + d\alpha \left(\frac{\cos \alpha}{\sin \alpha} - \frac{1}{\alpha}\right)\right) \tag{3-21}$$

to place the equation in a form somewhat more similar to that used in Equations (3-11) and (3-14).

To determine $\Delta Y'/d\theta$, $\Delta Y'/d\phi$, and $\Delta Y'/d\gamma''$ now requires the appropriate derivatives of $r_\perp$ and α with respect to θ, ϕ, and γ''. Now

$$r_\perp = \frac{M_+}{q\, B_e} \hat{v}_\perp \tag{3-22}$$

from $M_+ \hat{v}_\perp^2/r_\perp = q\, \hat{v}_\perp B_e$ (Lorentz force equation). Thus

$$dr_\perp = \frac{M_+}{q\, B_e} dv_\perp$$

and

$$\frac{dr_\perp}{r_\perp} = \frac{\dfrac{M_+}{q\, B_e} \dfrac{d\, \hat{v}_\perp}{\hat{v}_\perp}}{\dfrac{M_+}{q\, B_e}} = \frac{d\hat{v}_\perp}{\hat{v}_\perp}$$

It is also known that

$$v_{\perp} = \gamma \sin \beta$$

Equation (1-10) and γ and β are defined in Equations (1-4) and (1-6). It is required, thus, to determine $dv_{\perp}$ where

$$\frac{dv_{\perp}}{v_{\perp}} = \frac{d\gamma \sin \beta}{\gamma \sin \beta} + \frac{\gamma \cos \beta \, d\beta}{\gamma \sin \beta}$$

$$\frac{dv_{\perp}}{v_{\perp}} = \frac{d\gamma}{\gamma} + \frac{\cos \beta \, d\beta}{\sin \beta}$$

and

$$\frac{dr_{\perp}}{r_{\perp}} = \frac{\frac{M_{+}}{q \, B_{e}}}{\left(\frac{M_{+}}{q \, B_{e}}\right)} + \left(\frac{d\gamma}{\gamma} + \frac{\cos \beta \, d\beta}{\sin \beta}\right)$$

$$\frac{dr_{\perp}}{r_{\perp}} = \left(\frac{d\gamma}{\gamma} + \frac{\cos \beta \, d\beta}{\sin \beta}\right) \qquad (3\text{-}23)$$

Neither these quantities nor the $d\alpha$ terms in Equation (3-21) are simple enough to encourage a direct, closed, formulation. What is desirable, instead, is the calculation of γ, α, β for a given γ'', θ, ϕ and then the calculations of $d\alpha$, or $d\beta$, or $d\gamma$ as a variation of $d\theta$, $d\phi$, or $d\gamma''$ is imposed.